

THE UNIVERSITY OF CHICAGO

RATIONAL DESIGN OF MULTIFUNCTIONAL FRAMEWORK MATERIALS FOR  
SYNERGISTIC CATALYSIS

A DISSERTATION SUBMITTED TO  
THE FACULTY OF THE DIVISION OF THE PHYSICAL SCIENCES  
IN CANDIDACY FOR THE DEGREE OF  
DOCTOR OF PHILOSOPHY

DEPARTMENT OF CHEMISTRY

BY  
YINGJIE FAN

CHICAGO, ILLINOIS

AUGUST 2024

© 2024

YINGJIE FAN

ALL RIGHTS RESERVED

# TABLE OF CONTENT

<b>LIST OF FIGURES .....</b>	<b>ix</b>
<b>LIST OF TABLES .....</b>	<b>xiii</b>
<b>LIST OF ABBREVIATIONS .....</b>	<b>xv</b>
<b>ABSTRACT.....</b>	<b>xx</b>
<b>ACKNOWLEDGEMENT .....</b>	<b>xxii</b>
<b>Chapter 1. Framework Materials for Synergistic Catalysis .....</b>	<b>1</b>
1.1 Framework Materials and Their Characterization .....	1
1.2 Metal-Organic Layers for Synergistic Catalysis .....	2
1.3 Covalent-Organic Frameworks for Synergistic Catalysis .....	6
1.4 Assessment of Synergy in Framework Materials for Photoredox Catalysis .....	8
1.5 References .....	9
<b>Chapter 2. A Substrate-Binding Metal–Organic Layer Selectively Catalyzes Photoredox Ene-Carbonyl Reductive Coupling Reactions.....</b>	<b>11</b>
2.1 Introduction .....	11
2.2 Results and Discussion.....	13
2.2.1 Synthesis and Characterization of Hf-IrF-OTf.....	13
2.2.2 ECRC Reactions and Mechanistic Studies.....	16
2.2.3 Substrate Scope .....	20

2.3 Conclusion.....	22
2.4 Methods.....	23
2.4.1 Material synthesis.....	23
2.4.2 Catalytic Reactions.....	24
2.5 References.....	32
<b>Chapter 3. Site Isolation in Metal-Organic Layers Enhances Photoredox Gold Catalysis .</b>	<b>35</b>
3.1 Introduction.....	35
3.2 Results and Discussion.....	37
3.2.1 Synthesis and Characterization of Hf-Ru-Au.....	37
3.2.2 Cross-Coupling Reactions of Unsaturated Carbon-Carbon Bonds .....	41
3.2.3 Mechanistic Studies.....	44
3.3. Conclusion.....	48
3.4. Methods.....	49
3.4.1 Material synthesis.....	49
3.4.2 Catalytic Reactions.....	51
3.5 References.....	62
<b>Chapter 4. Sequential Modifications of Metal-Organic Layer Nodes for Highly Efficient Photocatalyzed Hydrogen Atom Transfer.....</b>	<b>66</b>
4.1 Introduction.....	66
4.2 Results and Discussion.....	68



4.2.1 Synthesis and Characterization of Zr-OTf-EY .....	68
4.2.2 HAT Reactions and Mechanistic Studies .....	71
4.2.3 Substrate Scope .....	75
4.3. Conclusion.....	78
4.4. Methods .....	78
4.4.1 Material synthesis.....	78
4.4.2 Catalytic Reactions .....	79
4.5 References .....	90
<b>Chapter 5. Metal-Organic Layers with Photosensitizer and Pyridine Pairs Activate Alkyl Halides for Photocatalytic Heck-type Coupling with Olefins .....</b>	<b>94</b>
5.1 Introduction .....	94
5.2 Results and Discussion.....	96
5.2.1 Synthesis and Characterization of Hf-IrF-PPA .....	96
5.2.2 Heck-Type Coupling Reactions .....	99
5.2.3 Mechanistic Studies.....	102
5.3. Conclusion.....	106
5.4. Methods .....	106
5.4.1 Material synthesis.....	106
5.4.2 Catalytic Reactions.....	109
5.5 References .....	115

## **Chapter 6. Molecular Engineering of Metal-Organic Layers for Sustainable Photocatalysis**

..... 118

6.1 Introduction ..... 118

6.2 Results and Discussion ..... 120

6.2.1 Synthesis and Characterization of MOLs ..... 120

6.2.2 Reaction Optimization and Mechanistic Insights ..... 124

6.2.3 Substrate Scope ..... 127

6.2.4 Gram-Scale Synthesis and Catalyst Recycle ..... 129

6.3 Conclusion ..... 131

6.4 Methods ..... 132

6.4.1 Material synthesis ..... 132

6.4.2 Catalytic Reactions ..... 135

6.5 References ..... 143

## **Chapter 7. Biomimetic Active Sites on a Metal-Organic Layer for Artificial Photosynthesis**

..... 146

7.1 Introduction ..... 146

7.2 Results and Discussion ..... 149

7.2.1 MOZs for Photocatalytic Carbon Dioxide Reduction ..... 149

7.2.2 MOZs for Photocatalytic Water Oxidation ..... 161

7.2.3 MOZs for Photocatalytic Total Carbon Dioxide Reduction ..... 168

7.3 Conclusion.....	170
7.4 Methods.....	171
7.4.1 Material synthesis.....	171
7.4.2 Catalytic Reactions.....	172
7.5 Supplementary Data .....	174
7.6 References .....	177
<b>Chapter 8. Energy Transfer in a Two-Dimensional Sp<sup>2</sup> Carbon Conjugated Covalent Organic Framework for Photo-Excited Nickel Catalysis.....</b>	<b>183</b>
8.1 Introduction .....	183
8.2 Results and Discussion.....	185
8.2.1 Synthesis and Characterization of CN and NiCN .....	185
8.2.3 Borylation and Trifluoromethylation Reactions.....	188
8.2.3 Mechanistic Studies.....	191
8.3 Conclusion.....	194
8.4 Methods.....	195
8.4.1 Material synthesis.....	195
8.4.2 Catalytic Reactions.....	197
8.5 References .....	207
<b>Chapter 9. A Spirobifluorene-Based Covalent Organic Framework for Dual Photoredox and Nickel Catalysis.....</b>	<b>210</b>

9.1 Introduction .....	210
9.2 Results and Discussion.....	211
9.2.1 Synthesis and Characterization of SCN and NiSCN.....	211
9.2.2 Sp <sup>2</sup> C-N and C-O Coupling Reactions and Mechanistic Studies .....	214
9.2.3 Substrate Scope .....	217
9.3 Conclusion.....	220
9.4 Methods.....	220
9.4.1 Material synthesis.....	220
9.4.2 Catalytic Reactions.....	222
9.5 References .....	229

## LIST OF FIGURES

Figure 1-1. Schematic presentation of MOF and COF structures. ....	1
Figure 1-2. Two modification strategies for the design and synthesis of MOF catalysts.....	3
Figure 1-3. Synthetic scheme for a Hf <sub>12</sub> -based MOL. ....	5
Figure 1-4. Effects of building block geometries on COF photoactivities. ....	7
Figure 2-1. Substrate-binding strategy.....	12
Figure 2-2. Structural model and characterization of Hf-IrF-OTf.....	14
Figure 2-3. <sup>19</sup> F NMR of digested Hf-IrF-TFA (top) and Hf-IrF-OTf (bottom).....	15
Figure 2-4. Mechanistic studies of Hf-IrF-OTf-catalyzed ECRC reactions. ....	19
Figure 2-5. Catalyst reuse experiments.....	22
Figure 3-1. Dual photoredox and gold-catalyzed cross-coupling reactions. ....	37
Figure 3-2. Schematic showing the synthesis of Hf-Ru-Au. ....	38
Figure 3-3. EXAFS fitting (left) and UV-vis analysis (right) of Hf-Ru-Au.....	39
Figure 3-4. <sup>1</sup> H NMR spectrum of digested Hf-Ru-Au in DMSO- <i>d</i> <sub>6</sub> . ....	39
Figure 3-5. <sup>31</sup> P NMR spectrum of digested Hf-Ru-Au in DMSO- <i>d</i> <sub>6</sub> . ....	40
Figure 3-6. Morphology and structure of Hf-Ru-Au. ....	41
Figure 3-7. <sup>31</sup> P NMR study of cross-coupling reaction between 3.1c and 3.6a.....	47
Figure 3-8. Proposed mechanism for Hf-Ru-Au catalyzed cross-coupling reaction. ....	48
Figure 4-1. Direct HAT reactions. ....	68
Figure 4-2. Schematic showing the synthesis of Zr-OTf-EY. ....	69
Figure 4-3. <sup>1</sup> H NMR spectrum of digested Zr-OTf-EY in DMSO- <i>d</i> <sub>6</sub> . ....	70
Figure 4-4. Characterization of Zr-OTf-EY.....	70
Figure 4-5. Reactivity and stability of Zr-OTf-EY.....	73

Figure 4-6. Activation of 4.2a with Zr-OTf-EY. ....	74
Figure 4-7. Proposed mechanism for Zr-OTf-EY-catalyzed HAT coupling reaction. ....	75
Figure 5-1. Radical generation from dithiocarbamates (top) and pyridinium salts (bottom). ....	95
Figure 5-2. MOL design for biomimetic CO <sub>2</sub> reduction (left) and haloalkane activation (right). 96	
Figure 5-3. Morphologies of Hf-IrF and Hf-IrF-PPA.....	97
Figure 5-4. PXRD patterns of Hf-IrF and Hf-IrF-PPA.....	98
Figure 5-5. <sup>1</sup> H NMR spectrum of digested Hf-IrF-PPA.....	98
Figure 5-6. Mechanistic studies. ....	104
Figure 5-7. Proposed mechanism for Hf-IrF-PPA-catalyzed Heck-type coupling reactions. ....	105
Figure 5-8. Synthetic scheme of Ir(C <sup>N</sup> ) <sub>3</sub> . ....	108
Figure 6-1. Dehydrogenative coupling reactions catalyzed by MOLs comprising photosensitizers and cobaloximes.....	120
Figure 6-2. Synthetic schemes of MOLs. ....	121
Figure 6-3. Characterization of Hf-Ir-Co-PPA. ....	122
Figure 6-4. <sup>1</sup> H NMR spectrum of digested Hf-Ir-Co-PPA in DMSO- <i>d</i> <sub>6</sub> .....	123
Figure 6-5. Proposed mechanistic cycles for photochemical aniline synthesis. ....	125
Figure 6-6. Stern-Völmer plots of PSs quenched by enamine (left) and amine (right). ....	126
Figure 6-7. Gram-scale synthesis of vesnarinone. ....	130
Figure 6-8. Catalyst recycle. ....	131
Figure 7-1. Design of biomimetic MOZs. ....	147
Figure 7-2. Schematic showing diversification, selection, and optimization of MOZs. ....	148
Figure 7-3. MOZ construction and optimization for CO <sub>2</sub> RR. ....	150
Figure 7-4. Characterization of MOZs.....	151

Figure 7-5. Morphology characterization of MOZ-2 and MOZ-3.....	152
Figure 7-6. $^1\text{H}$ NMR of digested MOZs. ....	153
Figure 7-7. $\text{CO}_2\text{RR}$ product. ....	155
Figure 7-8. TONs for $\text{CH}_4$ of MOZ-1, AA-modified MOZs, and Ur-modified MOZ. ....	156
Figure 7-9. Representative model structures of $\text{Fe}^{\text{II}}\text{CO}_2^{2-}$ and $\text{Fe}^{\text{I}}\text{CHO}$ in MOZ-3 and MOZ-4.	157
Figure 7-10. $\text{CO}_2\text{RR}$ reactivity of MOZs.....	158
Figure 7-11. $\text{CO}_2\text{RR}$ by MOZs with artificial ligands.....	160
Figure 7-12. Sunlight-driven $\text{CO}_2\text{RR}$ and catalyst recycle.....	161
Figure 7-13. MOZ construction and optimization for WOR.....	162
Figure 7-14. Characterization of MOZ-5 and MOZ-6.....	164
Figure 7-15. Photocatalytic WOR by MOZs.....	166
Figure 7-16. Am-R ligands for WOR.....	167
Figure 7-17. Photocatalytic total $\text{CO}_2\text{RR}$ .....	169
Figure 7-18. TONs of photocatalytic total $\text{CO}_2\text{RR}$ .....	170
Figure 8-1. Schematics showing energy transfer catalysis by a $\text{sp}^2$ -carbon conjugated COF....	185
Figure 8-2. Synthetic scheme of NiCN.....	186
Figure 8-3. Characterization of CN.....	187
Figure 8-4. Catalyst recycle and reuse.....	191
Figure 8-5. Proposed mechanism for NiCN-catalyzed borylation reactions.....	193
Figure 8-6. Mechanistic studies.....	194
Figure 9-1. Schematic showing photocatalysis by CN (left) and NiSCN (right). ....	211
Figure 9-2. Synthetic scheme of NiSCN.....	212
Figure 9-3. Characterization of SCN.....	214

Figure 9-4. Mechanistic studies.....	216
Figure 9-5. Synthetic application of NiSCN.....	219



## LIST OF TABLES

Table 2-1. Photoredox ECRC reactions catalyzed by Hf-IrF-OTf and homogeneous controls. ..	17
Table 2-2. Substrate scope of Hf-Ir-OTf catalyzed photoredox ECRC reaction.....	21
Table 3-1. Hf-Ru-Au-catalyzed cross-coupling of allenates with aryldiazonium salts.....	42
Table 3-2. Hf-Ru-Au-catalyzed cross-coupling of alkenes with aryldiazonium salts.....	43
Table 3-3. Hf-Ru-Au-catalyzed cross-coupling of alkynes with aryldiazonium salts.....	44
Table 3-4. Control experiments for Hf-Ru-Au catalyzed cross-coupling reactions.....	45
Table 4-1. HAT reactions and control groups.....	71
Table 4-2. Zr-OTf-EY-catalyzed HAT C-C coupling reactions.....	76
Table 4-3. Zr-OTf-EY-catalyzed HAT C-N coupling reactions.....	77
Table 5-1. Nucleophile screening for homogenously catalyzed reactions.....	99
Table 5-2. Nucleophile, additive and solvent screening for MOL-catalyzed reactions.....	100
Table 5-3. Substrate scope for MOL-catalyzed Heck-type radical coupling reactions.....	101
Table 5-4. Control experiments.....	103
Table 6-1. Reaction optimization for photochemical aniline synthesis.....	124
Table 6-2. Reaction optimization for Heck-type coupling reactions.....	127
Table 6-3. Substrate scope for photochemical aniline synthesis catalyzed by Hf-Ir-Co-PPA. ..	128
Table 6-4. Substrate scope for Heck-type coupling reaction catalyzed by Hf-Ir-Co-PPA.....	129
Table 7-1. Summary of photocatalytic CO <sub>2</sub> RR with different catalytic systems.....	174
Table 7-2. Summary of photocatalytic WOR with different catalytic systems.....	176
Table 7-3. Summary of photocatalytic total CO <sub>2</sub> RR with different catalytic systems.....	177
Table 8-1. Substrate scope for NiCN-catalyzed borylation reactions.....	189
Table 8-2. Substrate scope for NiCN-catalyzed trifluoromethylation reactions.....	190

Table 8-3. Control experiments for NiCN-catalyzed borylation reactions.....	192
Table 9-1. Control experiments for NiSCN-catalyzed amination reactions. ....	215
Table 9-2. Substrate scope of NiSCN-catalyzed $sp^2$ C-N and C-O coupling reactions. <sup>a</sup> .....	218

## LIST OF ABBREVIATIONS

2D	Two dimensional
AA	Amino acid
AFM	Atomic force microscopy
AQ	4-(9,10-Dioxo-9,10-dihydroanthracen-2-yl)benzoic acid
B <sub>2</sub> pin <sub>2</sub>	Bis(pinacolato)diboron
BET	Brunauer–Emmett–Teller
BIH	1,3-Dimethyl-2-phenyl-2,3-dihydro-1H-benzo[d]-imidazole
BPY	4',6'-Dibenzoato-[2,2'-bipyridine]-4-carboxylate
bpy	Bipyridine
bpy-Br	5,5'-Bis(bromomethyl)-2,2'-bipyridyl
bpy-CN	2,2'-([2,2'-Bipyridine]-5,5'-diyl)diacetonitrile
BTB	4-[3,5-Bis(4-carboxyphenyl)phenyl]benzoate
CO <sub>2</sub> RR	Carbon dioxide reduction reaction
cod	Cyclooctene
COF	Covalent-organic framework
Cp <sup>*</sup>	Pentamethylcyclopentadienyl

CV	Cyclic voltammetry
DABCO	1,4-Diazabicyclo[2.2.2]octane
DBB	4,4'-Di(4-benzoato)-2,2'-bipyridine
DCA	Dichloroacetic acid
DCM	Dichloromethane
dF(CF <sub>3</sub> )ppy	2-(2,4-Difluorophenyl)-5-(trifluoromethyl)pyridine
DFT	Density functional theory
DIPEA	Di( <i>iso</i> -propyl) ethyl amine
DLS	Dynamic light scattering
DMA	Dimethyl acetamide
DMAP	<i>N,N</i> -dimethylamino pyridine
dme	Ethylene glycol dimethyl ether
DMF	<i>N,N</i> -dimethylformamide
dmgh	Dimethylglyoxime
DMSO	Dimethyl sulfoxide
dppf	1,1'-Bis(diphenylphosphino)ferrocene
dtbbpy	Di( <i>tert</i> -butyl)bipyridine

ECRC	Ene-carbonyl reductive coupling
EDS	Energy-dispersive X-ray spectroscopy
EXAFS	Extended X-ray absorption fine structure
EY	Eosin Y
FFT	Fast Fourier Transform
FM	Framework material
GC	Gas chromatography
GC-MS	Gas chromatography-mass spectrometry
HAADF	High-angle annular dark-field
HAT	Hydrogen atom transfer
HEH	Bis(2-methoxyethyl) 2,6-dimethyl-1,4-dihydropyridine-3,5-dicarboxylate
H-MBA	2-(4'-Methyl-[2,2'-bipyridin]-4-yl)acetic acid
HNTf <sub>2</sub>	Bistriflimidic acid
HRTEM	High resolution transmission electron microscopy
ICP-MS	Inductively coupled plasma mass spectrometry
IR	Infrared (spectroscopy)
MOF	Metal-organic framework

MOL	Metal-organic layer
MOZ	Metal-organic-zyme
NMA	<i>N</i> -methylacridone
NMR	Nuclear magnetic resonance spectroscopy
OTf	Triflate
PAPA	3-(Methyl-4-pyridylamino)propionic acid
PCET	Proton-coupled electron transfer
PPA	Pyridine propionic acid
PPA <sup>+</sup>	4-(2-Carboxyethyl)- <i>N</i> -(ethoxycarbonylmethyl)pyridinium bromide
ppy	Phenylpyridine
PS	Photosensitizer
PXRD	Powder X-ray diffraction
py-Br	1,3,6,8-Tetrakisbromopyrene
py-CHO	1,3,6,8-Tetrakis(4-formylphenyl)pyrene
QT	Quantum yield
SBU	Secondary building unit
sp	Spirobifluorene

sp-Br	2,2',7,7'-Tetrabromo-9,9'-spirobifluorene
sp-CHO	4,4',4'',4'''-(9,9'-Spirobi[fluorene]-2,2',7,7'-tetrayl) tetrabenzaldehyde
ssNMR	Solid-state nuclear magnetic resonance spectroscopy
TBADT	Tetrabutylammonium decatungstate
TCSPC	Time-correlated single-photon counting
TEM	Transmission electron microscopy
TEMPO	2,2,6,6-Tetramethyl-1-piperidinyloxy
TFA	Trifluoroacetic acid
TFE	Trifluoroethanol
THF	Tetrahydrofuran
TMS	Trimethylsilyl
TON	Turnover number
UV-vis	Ultraviolet-visible light
WOR	Water oxidation reaction
XAS	X-ray absorption spectroscopy
XAT	Halogen atom transfer
XPS	X-ray photon spectroscopy

## ABSTRACT

Yingjie Fan: Rational Design of Multifunctional Framework Materials for Synergistic Catalysis

Under Direction of Professor Wenbin Lin

Framework materials (FMs), including metal-organic frameworks (MOFs) and covalent organic frameworks (COFs), have risen to prominence over the last two decades in the field of chemistry. The rigidity, structural regularity, and tunability of FMs allow precise molecular control on their structures, providing an ideal platform for developing heterogeneous catalysts with unique reactivities. My doctoral research aims at designing FMs with multiple active sites for synergistic catalysis. Specifically, I have designed and synthesized two types of FMs, metal-organic layers (MOLs) and COFs, to mediate photocatalytic synergistic reactions for fine chemical synthesis and energy conversion, with enhanced efficiency and selectivity.

Chapter 1 describes the fundamental concepts about FMs and elucidates their design strategies for synergistic catalysis. Their structural features, characterization techniques, and functionalization methods are examined to provide the basis for the subsequent discussion on how to achieve FM-catalyzed synergistic reactions.

The first part of the thesis, including chapters 2 through 5, focuses on elaborating on how the design of MOL catalysts can enhance the reactivities and selectivities of photoredox-catalyzed reactions. Four photocatalytic reactions including Giese addition, gold-catalyzed cross-coupling reactions, hydrogen atom transfer (HAT), and radical Heck-type coupling were studied with MOL catalysts comprising photosensitizers (PSs) in combination with a Lewis acid, a gold-phosphine



complex or a nucleophilic pyridine. Control experiments and mechanistic studies revealed that the strategic pre-organization of catalytic sites within MOLs greatly facilitated the kinetics of targeted reactions.

The second part of the thesis, including chapters 6 and 7, focuses on the application of MOL catalysts in laboratory-scale reactions of pharmaceutical and energy interest. Systematic optimization of the components in MOLs resulted in MOL catalysts with durability, recyclability, and superior reactivities for both photocatalytic dehydrogenative coupling reactions and artificial photosynthesis, showcasing their potential in synthetic transformations and energy conversion.

The third part of the thesis, including chapters 8 and 9, describes the exploration of photocatalytic properties of COF catalysts in the nascent stage. A significant reactivity difference between a planar COF and a non-planar COF embedded with nickel-bipyridine active sites was uncovered. The planar COF demonstrated efficiency in photocatalytic borylation and trifluoromethylation of aryl halides via energy transfer catalysis, while the non-planar COF catalyzed photocatalytic C-N and C-O coupling reactions of aryl halides via photoredox catalysis.

## ACKNOWLEDGEMENT

I feel profoundly grateful for the past five years spent as a doctoral student at the University of Chicago. Looking back, I am surprised by what I have achieved and would like to extend my sincere gratitude to my mentors, colleagues, and families who keep supporting me along my scientific journey.

First and foremost, I want to express my deepest appreciation to my research advisor, Prof. Wenbin Lin. As the ancient essayist, Yu Han, once wrote, ‘A teacher is the one who could propagate doctrine, impart professional knowledge, and resolve doubts.’ Wenbin epitomizes this ideal; he has been the ‘teacher’ throughout my doctoral studies, shaping my scientific ethos and fostering my academic growth.

In our daily interactions, he has instilled in me his scientific doctrine, emphasizing the imperative of addressing real-world problems. Wenbin is a scientist who does not limit himself to laboratory research, possessing a broader vision and an ambitious drive to translate his research and discoveries into practical technologies. Honestly, this is extremely challenging. His passion and dedication have inspired me, among other students, to pursue this noble scientific goal with lifelong commitment. Furthermore, his incisive perspective and critical thinking have equipped me with the acumen to navigate my future academic endeavors with confidence and clarity.

Wenbin started his career as an inorganic chemist. Later, he branched his research into the field of catalysis and cancer therapy. In the Lin Lab, I am very fortunate to have the opportunity to learn the fundamentals about inorganic chemistry, organic chemistry, and biology in the interdisciplinary projects led by Wenbin. This is not an opportunity within easy reach, which has broadened my horizons and deepened my understanding of diverse scientific disciplines.

Moreover, I am indebted to Wenbin for imparting me with invaluable research skills. I started in my first year with a superficial understanding of chemistry research. Through biweekly meetings with Wenbin, where we discuss experimental results and plans in detail, I have gained invaluable insights and guidance from him, allowing me to refine and enhance my experiments. This iterative learning process has built my capabilities in selecting appropriate techniques and planning rigorous experiments to probe unknown chemistry. When preparing for publications, Wenbin reviewed and edited every single sentence in the drafts I wrote, which significantly strengthened my skills in scientific writing, undoubtedly, at the expense of considerable time and effort on his part. There are too many examples to include in the acknowledgement, which all underscores Wenbin's role as the most committed 'teacher', dedicated not only to advancing scientific knowledge but also to educating and training the younger generation, me included.

Lastly, I want to thank Wenbin for choosing me as his graduate student and for his strong support of my career development. 'There are many swift horses, but very few can spot them.' Despite not being the best student at Peking University, Wenbin recognized my potential and brought me from Beijing to Chicago. To me, this was a life-changing decision, not only exposing me to the forefront of scientific research but also facilitating a cultural and personal evolution that I shall forever cherish. Moreover, Wenbin has provided me with insightful career advice and has offered me strong recommendations for fellowship, awards, and research opportunities to facilitate my success, for which I am deeply grateful.

I extend my deepest gratitude to Professor Wenbin Lin for his mentorship, guidance, and unwavering support. The past five years have been a transformative chapter in my life, and I am immensely fortunate to have shared this journey with him.

I am deeply grateful for the invaluable support from the faculty members in the Department of Chemistry. I extend my heartfelt appreciation to Prof. John Anderson and Prof. Anna Wuttig for being my dissertation committee members. Prof. Anderson has always been kind and generous in offering me constructive research suggestions and support to my career development. Prof. Wuttig has provided me with invaluable career advice, and her unwavering passion for science serves as a deep source of encouragement, motivating me to pursue an academic career path. Their expertise in the field of inorganic chemistry has provided me with many insights and guidance, for which I am deeply thankful. I also wish to express my gratitude to Prof. Guangbin Dong, Prof. Dimitri Talapin, and Prof. John Anderson once again for being my candidacy exam committee members. Their rigorous examination of my research project in my second year challenged me to delve deeper into my work and future direction. I also enjoyed and learned a lot from the courses taught by Prof. Dong and Prof. Talapin on organometallic chemistry and material chemistry, respectively. In addition, I would like to thank Prof. Mark Levin and Prof. Stephen Kent for teaching me physical organic chemistry and enzyme catalysis, respectively.

I would like to express gratitude to my lab mentors, colleagues, and friends, Prof. Guangxu Lan and Prof. Yuanyuan Zhu. In my first year, Guangxu taught me the fundamental experimental skills essential for laboratory work. His generous sharing of scientific insights and strategic approaches to advancing research projects proved invaluable, laying a strong foundation for my future work. As a dedicated and impassioned researcher, he has exemplified the qualities of a successful young scientist I would like to emulate. I am particularly thankful for the support he has provided. Dr. Zhu instructed me when I worked at the Lin Lab in 2018 summer, during which for the first time I experienced the satisfaction of contributing to a research project. His sharing of

his anecdotes and experiences in his academic journey offered me a fresh perspective on being a scientist.

During my doctoral studies, I've been immensely grateful to have met numerous talented and warm-hearted colleagues. Dr. Haifeng Zheng and Dr. Dongwon Kang joined the Lin lab in my second year, and our close collaboration has marked the most productive time of my PhD career. Their unparalleled dedication and expertise in organic methodologies and covalent-organic frameworks have propelled our research endeavors forward. Dr. Taokun Luo and Dr. Xiaomin Jiang have been my closest friends since my first year in Chicago. They have offered me tremendous help intellectually, explaining everything I was unfamiliar with in material chemistry and cancer therapy. Together, we have explored events in Chicago, even during the pandemic, cherishing invaluable moments in restaurants, orchestra halls, and lakeside grasslands. I extend my heartfelt gratitude for their companionship and support.

I am also indebted to the senior members of the lab who kindly offered their guidance and assistance, including Dr. Wenyao Zhen, Dr. Jing Liu, Dr. Wenjie Shi, Dr. Yangjian Quan, and Dr. Qingyun Guo. Collaborations with them on interdisciplinary projects have broadened my horizons and resulted in exciting research breakthroughs. Furthermore, I extend my appreciation to Dr. Yang Song, Dr. Xuanyu Feng, Dr. Ziwan Xu, Dr. Geoff Nash, Dr. Zhibei Zhou, and Dr. Chenghua Deng for their help with my research projects.

Undergraduates, including Steven Labalme, Abbie Blenko, and Eric You, have made indispensable contributions to our research projects. Their diligence and curiosity have invigorated every project we've undertaken, inspiring me to delve deeper. Additionally, I am grateful for insightful feedback provided by graduate students, Zitong Wang and Jinhong Li. I have been

working closely with Zitong in the last half of my PhD and together we have advanced many projects, helping each other along the way.

I would also like to express my gratitude to friends, including Rui Zhang, Di Wang, Junjie Xia, Ruihan Huang, and Ge Sun, for their support and suggestions, both in my research and personal life. Furthermore, I extend my thanks to the dedicated staff members at the University of Chicago, including Dr. Alexander Filatov, Dr. Josh Kurutz, Yimei Chen, Dr. Qiti Guo, and Dr. Justin Jureller, for their assistance with instrument training and access. Besides, I am grateful for the support from by Dr. Yu-Sheng Chen and Dr. Yujia Ding at Argonne National Lab, as well as Dr. Fengyuan Shi at the University of Illinois Chicago, in experiments. I am thankful to Melinda Moore, Debrah Morgan, Dr. Vera Dragisich, and Dr. Valerie Keller for their help with administration and teaching.

I would like to thank my partner, Xinyi Long, for her steadfast support in my life. We met and formed a bond at UChicago, where we have spent four years navigating the challenges and opportunities that come our way. Despite our differing personalities and career paths, she has consistently shown patience, communicating with me, and working alongside me to overcome any obstacles we encountered. Her presence has brought color and depth to my doctoral experience. I am deeply grateful for her support, which has enriched my doctoral experience in countless ways.

Throughout my doctoral studies spanning five years, I have been away from home. Yet I want to conclude my acknowledgment with my deepest gratitude for the support from my parents thousands miles away. Every strength and virtue that propelled me towards success traces its roots back to their nurturing guidance. They taught me to proactively organize my life to stay focused and energized. Their enduring commitment to their endeavors instilled in me a similar resilience. Their curiosity about the world ignited my own, shaping my intellectual pursuits. Furthermore,

they have consistently been my unwavering support and my strongest backup. In my challenging times, they would tell me I was always welcome home, regardless of circumstances, alleviating burdens and steeling my resolve. I feel very fortunate to have been born into a family full of love and I am forever indebted to them for their boundless and selfless support.

# Chapter 1. Framework Materials for Synergistic Catalysis

## 1.1 Framework Materials and Their Characterization

Framework materials (FMs), including metal-organic frameworks (MOFs) and covalent-organic frameworks (COFs), are porous crystalline materials constructed by periodic bonding between either metal and ligands or organic building blocks (**Figure 1-1**). The concept of MOFs was first proposed three decades ago,<sup>1-2</sup> followed by the construction of the first COF reported ten years later.<sup>3</sup> The diversity in building blocks and structures of FMs has allowed chemists to design functional FMs for different applications.<sup>4-5</sup> Particularly, in catalytic applications, FMs have provided a platform for developing heterogeneous catalysts more tunable and characterizable than traditional heterogeneous catalysts.

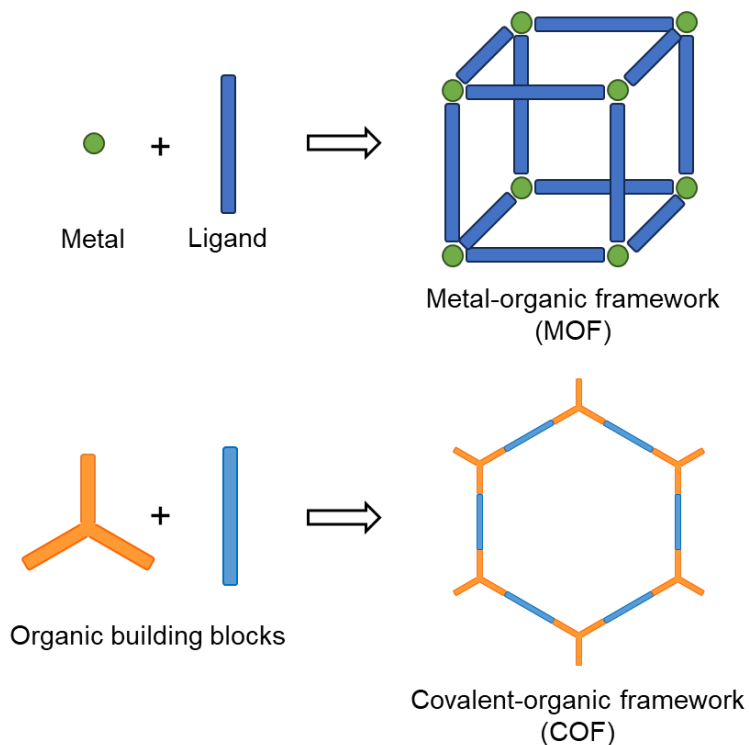


**Figure 1-1.** Schematic presentation of MOF and COF structures.



To achieve rational design of functional FMs, direct and indirect methods have been used to analyze their structures and chemical compositions. Direct methods include single-crystal X-ray crystallography, powder X-ray diffraction (PXRD), and gas sorption, which provide structural insights into FMs. Additionally, chemical compositions of FMs can be studied with infrared spectroscopy (IR), X-ray photoelectron spectroscopy (XPS), X-ray absorption spectroscopy (XAS), and solid-state nuclear magnetic resonance spectroscopy (ssNMR). Indirect methods use chemical reagents to digest FMs into separate building blocks, which are subsequently characterized with quantitative solution-based spectroscopy, such as NMR, ultraviolet-visible light spectroscopy (UV-vis), and inductively coupled plasma-mass spectrometry (ICP-MS). Controlling digestive conditions allows determination of chemical components of FMs at either molecular or atomic level.

Furthermore, morphology control significantly influences the potential efficacy of FMs in catalytic applications. For example, materials used in this thesis exhibit at least one dimension within 200 nm to facilitate substrate diffusion in catalytic reactions. The morphology of FMs is controlled by systematic optimization of synthetic conditions and can be assessed by transmission electron microscopy (TEM) and atomic force microscopy (AFM).

## 1.2 Metal-Organic Layers for Synergistic Catalysis

Over 90000 MOFs have been synthesized, resulting from the diversity of metals, ligands, and topology in MOF structures.<sup>6</sup> Functionalization of the metals (so-called secondary building units, SBUs) and bridging ligands in MOFs provide two primary strategies to design and synthesize MOF catalysts. For example, the metalation of a  $Zr_6$  SBU in a UiO-69 type MOF with  $MgMe_2$  affords an active solid catalyst for hydroboration and hydroamination reactions (**Figure**

**1-2a).**<sup>7-8</sup> The incorporation of a metal-bipyridine complex, an active catalytic site for a variety of reactions, onto ligands in a similar MOF can be achieved either through post-modification of a MOF synthesized with uncoordinated bipyridine ligands or via MOF synthesis starting from pre-functionalized metal-bipyridine ligands (**Figure 1-2b**).<sup>9</sup>

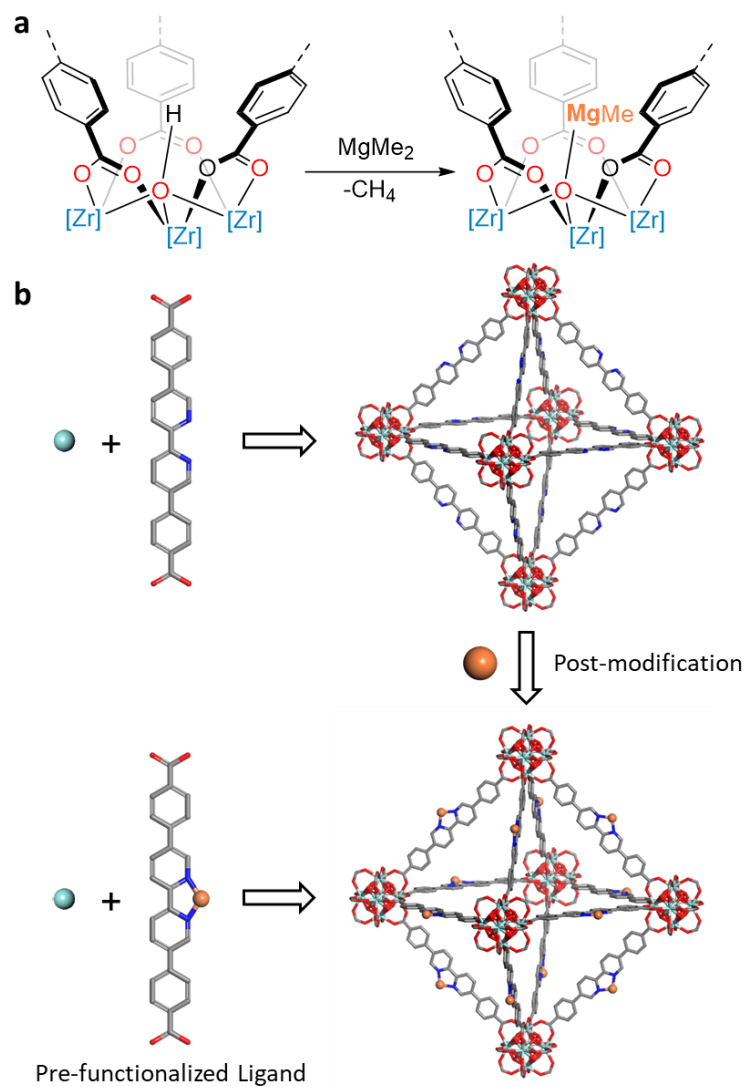


**Figure 1-2.** Two modification strategies for the design and synthesis of MOF catalysts.(a) SBU modification strategy. (b) Ligand modification strategy. Gray, C; blue, N; indigo, Zr; orange, catalyst precursor.

The strategies outlined above vastly expand the chemical landscape available for MOF catalyst design. However, the pore size inherent to MOFs imposes constraints on the incorporation of catalytic sites and slows down the diffusion of substrates and products. While this limitation is inconsequential for small molecule chemistry, such as CO<sub>2</sub> reduction and H<sub>2</sub> evolution, it presents a substantial hurdle in MOF-catalyzed fine chemical synthesis.

To address this issue, our research group has pioneered the synthesis of metal-organic layers (MOLs), a two-dimensional (2D) version of MOFs.<sup>10-12</sup> We specifically focus on MOLs constructed with Hf or Zr-based SBUs, renowned for their stability under catalytic conditions. The method involves the addition of modulating acids as competing reagents alongside linear dicarboxylate ligands,<sup>13</sup> achieving precise control over the thickness and diameter of MOL nanoplates. A detailed growth mechanism of a Hf<sub>12</sub>-based MOL, extensively employed in this thesis, is pictured in **Figure 1-3**. Initially, excess modulating monocarboxylates bind Hf<sup>4+</sup> ions and form SBUs at elevated temperatures. The resulting SBUs then undergo a reversible ligand exchange with linear dicarboxylate ligands, affording MOLs with a diameter of around 200 nm and a thickness ranging from 1.5 to 2 nm. The MOLs have demonstrated catalytic efficiency with substrates as large as 1 nm and have exhibited enhanced accessibility in both catalytic and biomedical applications.<sup>12, 14</sup>

Dimensional reduction from MOFs to MOLs introduces an additional advantage: a method for hierarchical assembly of multiple active sites. The surface of a MOL is covered by modulating monocarboxylates, substitutable with catalyst-attached carboxylates. Leveraging the two strategies for MOF catalyst design, catalytic components can be incorporated into MOLs in two different stages, ligand pre-functionalization and SBU post-modification (**Figure 1-3**). Moreover, the proximity between SBUs and ligands within MOLs facilitates efficient electron and mass transfer

between the two distinct catalytic sites,<sup>15</sup> providing a platform for rational design of synergistic catalysts. These methods have been explored in chapters 2 through 5 to achieve unique activities inaccessible to homogeneous analogs and in chapters 6 and 7 for systematic optimization of MOL catalysts for targeted chemical transformations.

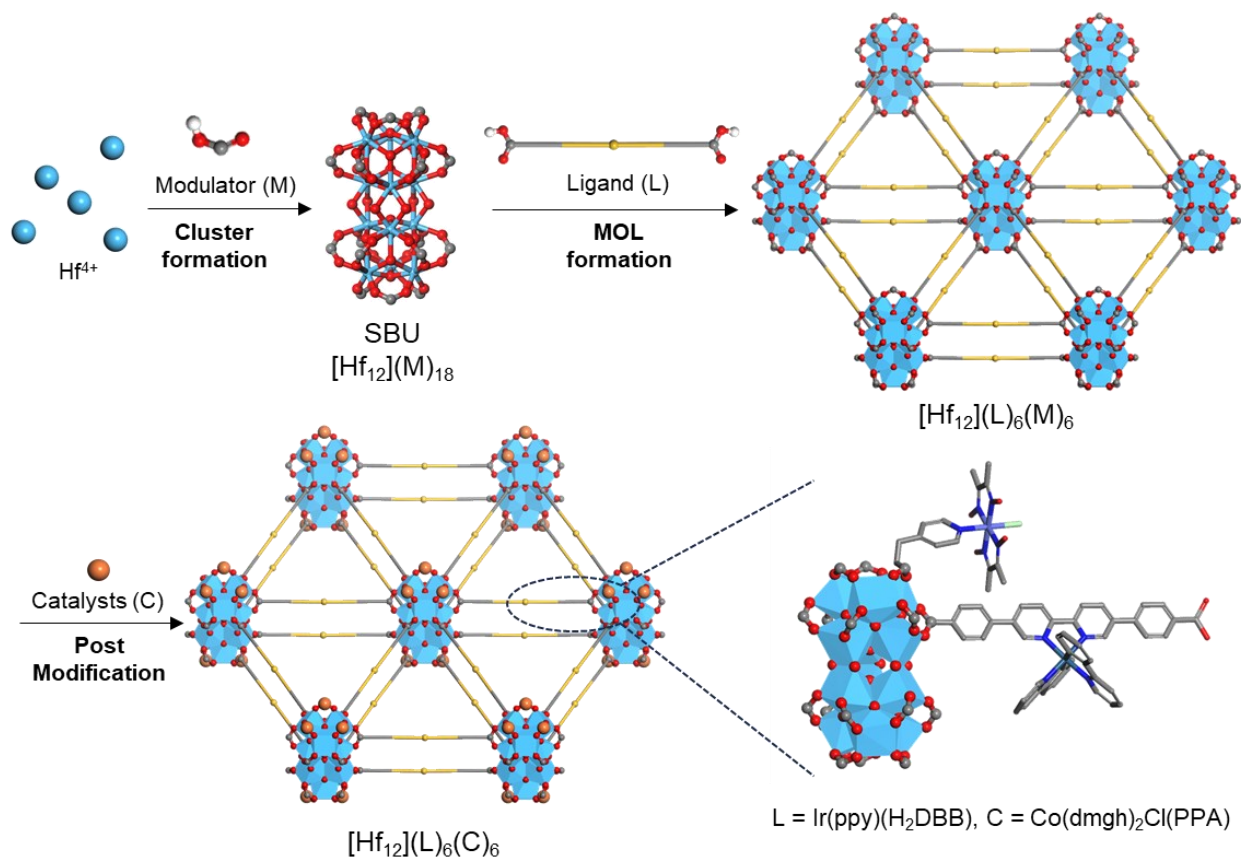


**Figure 1-3.** Synthetic scheme for a Hf<sub>12</sub>-based MOL. Gray, C; blue, N; sapphire, Hf; yellow, pre-functionalized ligand; orange, catalyst precursor. The zoomed-in image is an example of the catalyst assembly with an iridium-based PS and a cobaloxime dehydrogenation catalyst (see Chapter 6).

### 1.3 Covalent-Organic Frameworks for Synergistic Catalysis

Similar to MOFs, COFs represent another example of an extended porous structure achieved through reticular synthesis. However, COFs are constructed with covalent bonds between organic building blocks without SBUs. Saturation in covalent bonds decreases the bonding capacity of the organic building blocks, thus limiting the possible topology that a COF can adopt. Catalytic moieties can be incorporated into COFs through either pre-synthetic or post-synthetic modification of the building block. In this thesis, we specifically focus on the design of 2D COFs, owing to their structural simplicity and ease of synthesis.

2D COFs are unique in three different ways. First, unsaturated or heteroatom-based linkages in the COF extend the conjugation of the building blocks to the entire framework, enhancing in-plane electron and energy transfer. Second, the same structural feature amplifies electric conductivity and light absorption efficiency, which paves the way for the design of non-metal-based COF photosensitizers. Third, strong aggregation induced by  $\pi$ - $\pi$  interaction among COF nanoplates drives the formation of a secondary structure and facilitates interlayer energy and electron transfer. In catalysis, these features can be finely tuned through linkage chemistry or building block design to promote targeted chemical transformations and inhibit side reaction pathways.

Synergy in COF catalysts, therefore, hinges on the rational design of the conjugated system to modulate the kinetics of both in-plane and through-plane electron and energy transfer. The principle is exemplified with two case studies in chapters 8 and 9, demonstrating how variations in building block geometry can influence the photoactivity of 2D COFs to tailor them for different chemical reactions (**Figure 1-4**). The planar COF, incorporating pyrene and nickel-bipyridine components, facilitates excited-state nickel catalysis by enhancing energy transfer. In contrast, the

non-planar COF comprising spirobifluorene and nickel-bipyridine structures, disrupts in-plane conjugation and aggregation, accelerating electron transfer for dual photoredox and nickel catalysis.

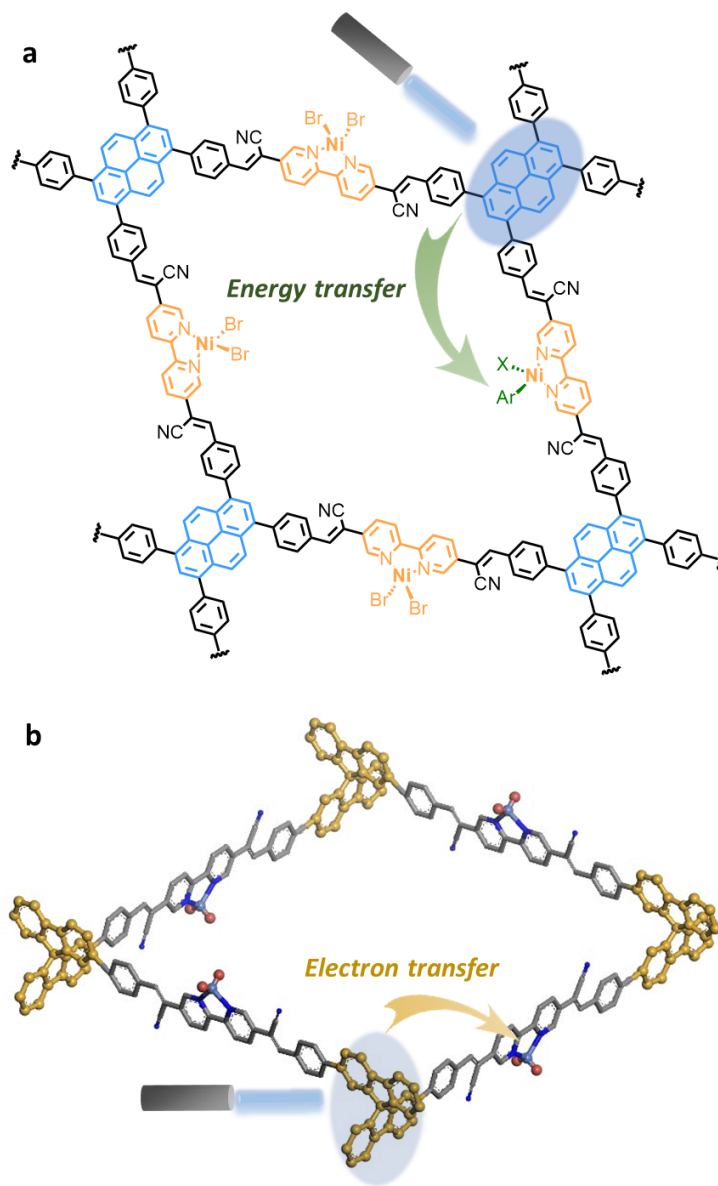


**Figure 1-4.** Effects of building block geometries on COF photoactivities.(a) Pyrene-based COF, NiCN, for enhanced energy transfer catalysis. (b) Spirobifluorene-based COF, NiSCN, for dual photoredox catalysis. Gray, C; blue, N; lavender, Ni; brick red, Br; yellow, spirobifluorenyl units.

## 1.4 Assessment of Synergy in Framework Materials for Photoredox Catalysis

FM-based catalysts, as described, are heterogeneous catalysts with well-characterized catalytic sites. This offers an advantage to FM-based catalysts over traditional heterogeneous catalysts, which typically feature ambiguous active sites, in elucidating reaction mechanisms. The mechanistic insights can subsequently guide the rational design of enhanced FM catalysts for targeted reactions, while also contributing to a general rule for achieving high reactivity and selectivity in heterogeneous catalyst design for analogous reactions.

However, a detailed examination of reaction mechanism necessitates a comprehensive analysis of reaction intermediates and supporting calculation results. Analyzing catalyst synergy is even more challenging and often requires in-situ ultrafast spectroscopy. We therefore direct our research focus towards photoredox catalysis, where readily available emission spectroscopy can provide kinetic insights into the photochemistry.

The major feature of photoredox catalysis is the use of a photosensitizer, which upon irradiation, transitions to an excited state with potent oxidizing and reducing potentials. Seminal work from the Macmillan group has demonstrated that the synergistic combination of photoredox catalysis and transition metal catalysis can broaden the scope of coupling partners in cross-coupling reactions.<sup>16-17</sup> FMs, therefore, serve as an ideal platform to integrate both photosensitizers and transition-metal complexes (and in some cases, Lewis acids) to enhance the synergy between the catalyst duo, which can be evaluated by comparing the yield or selectivity of reactions catalyzed by FMs and their homogeneous counterparts. Photoluminescence spectra, along with other characterization techniques outlined in section 1.1, can be utilized to probe the photochemistry in FM-based catalysts. Notably, Stern-Völmer plots offer a straightforward means

to measure the efficiency of electron or energy transfer from the excited photosensitizer to the transition-metal complex or the reaction substrate.

In the following chapters, while reaction yield is the major focus of the reaction optimization, efforts in mechanistic studies exemplify how material design of FMs can enhance catalytic performance through several key strategies: 1) enhancing electron and energy transfer between catalyst components; 2) binding substrates to increase kinetics of productive pathways; and 3) isolating catalytic sites to prevent deactivation pathways through ligand redistribution. We hope these studies will provide insights into the catalysis community and inspire rational design of other heterogeneous catalysts.

## 1.5 References

1. Yaghi, O. M.; Li, G.; Li, H., Selective binding and removal of guests in a microporous metal–organic framework. *Nature* **1995**, *378* (6558), 703-706.
2. Li, H.; Eddaoudi, M.; O’Keeffe, M.; Yaghi, O. M., Design and synthesis of an exceptionally stable and highly porous metal-organic framework. *Nature* **1999**, *402* (6759), 276-279.
3. Côté, A. P.; Benin, A. I.; Ockwig, N. W.; O’Keeffe, M.; Matzger, A. J.; Yaghi, O. M., Porous, Crystalline, Covalent Organic Frameworks. *Science* **2005**, *310* (5751), 1166-1170.
4. Song, Y.; Feng, X.; Lin, W., 9.10 - Metal-Organic Frameworks for Catalytic Applications. In *Comprehensive Coordination Chemistry III*, Constable, E. C.; Parkin, G.; Que Jr, L., Eds. Elsevier: Oxford, 2021; pp 228-259.
5. Xu, Z.; Luo, T.; Lin, W., Nanoscale Metal–Organic Layers for Biomedical Applications. *Accounts of Materials Research* **2021**, *2* (10), 944-953.
6. Moosavi, S. M.; Nandy, A.; Jablonka, K. M.; Ongari, D.; Janet, J. P.; Boyd, P. G.; Lee, Y.; Smit, B.; Kulik, H. J., Understanding the diversity of the metal-organic framework ecosystem. *Nat. Commun.* **2020**, *11* (1), 4068.
7. Feng, X.; Song, Y.; Lin, W., Transforming Hydroxide-Containing Metal–Organic Framework Nodes for Transition Metal Catalysis. *Trends in Chemistry* **2020**, *2* (11), 965-979.
8. Manna, K.; Ji, P.; Greene, F. X.; Lin, W., Metal–Organic Framework Nodes Support Single-Site Magnesium–Alkyl Catalysts for Hydroboration and Hydroamination Reactions. *J. Am. Chem. Soc.* **2016**, *138* (24), 7488-7491.
9. Drake, T.; Ji, P.; Lin, W., Site Isolation in Metal–Organic Frameworks Enables Novel Transition Metal Catalysis. *Acc. Chem. Res.* **2018**, *51* (9), 2129-2138.
10. Cao, L.; Lin, Z.; Peng, F.; Wang, W.; Huang, R.; Wang, C.; Yan, J.; Liang, J.; Zhang, Z.; Zhang, T.; Long, L.; Sun, J.; Lin, W., Self-Supporting Metal–Organic Layers as Single-Site Solid Catalysts. *Angew. Chem. Int. Ed.* **2016**, *55* (16), 4962-4966.



11. Lan, G.; Quan, Y.; Wang, M.; Nash, G. T.; You, E.; Song, Y.; Veroneau, S. S.; Jiang, X.; Lin, W., Metal–Organic Layers as Multifunctional Two-Dimensional Nanomaterials for Enhanced Photoredox Catalysis. *J. Am. Chem. Soc.* **2019**, *141* (40), 15767-15772.
12. Luo, T.; Fan, Y.; Mao, J.; Yuan, E.; You, E.; Xu, Z.; Lin, W., Dimensional Reduction Enhances Photodynamic Therapy of Metal–Organic Nanophotosensitizers. *J. Am. Chem. Soc.* **2022**, *144* (12), 5241-5246.
13. Schaate, A.; Roy, P.; Godt, A.; Lippke, J.; Waltz, F.; Wiebcke, M.; Behrens, P., Modulated Synthesis of Zr-Based Metal–Organic Frameworks: From Nano to Single Crystals. *Chem. Eur. J.* **2011**, *17* (24), 6643-6651.
14. Feng, X.; Song, Y.; Lin, W., Dimensional Reduction of Lewis Acidic Metal–Organic Frameworks for Multicomponent Reactions. *J. Am. Chem. Soc.* **2021**, *143* (21), 8184-8192.
15. Kent, C. A.; Mehl, B. P.; Ma, L.; Papanikolas, J. M.; Meyer, T. J.; Lin, W., Energy Transfer Dynamics in Metal–Organic Frameworks. *J. Am. Chem. Soc.* **2010**, *132* (37), 12767-12769.
16. Zuo, Z.; Ahneman, D. T.; Chu, L.; Terrett, J. A.; Doyle, A. G.; MacMillan, D. W. C., Merging photoredox with nickel catalysis: Coupling of  $\alpha$ -carboxyl  $sp^3$ -carbons with aryl halides. *Science* **2014**, *345* (6195), 437-440.
17. Chan, A. Y.; Perry, I. B.; Bissonnette, N. B.; Buksh, B. F.; Edwards, G. A.; Frye, L. I.; Garry, O. L.; Lavagnino, M. N.; Li, B. X.; Liang, Y.; Mao, E.; Millet, A.; Oakley, J. V.; Reed, N. L.; Sakai, H. A.; Seath, C. P.; MacMillan, D. W. C., Metallaphotoredox: The Merger of Photoredox and Transition Metal Catalysis. *Chem. Rev.* **2022**, *122* (2), 1485-1542.

## Chapter 2. A Substrate-Binding Metal–Organic Layer Selectively Catalyzes Photoredox Ene-Carbonyl Reductive Coupling Reactions

### 2.1 Introduction

Photoredox reactions have provided powerful methods to generate and use radicals over the past decade.<sup>1-3</sup> For ene-carbonyl reductive coupling reactions, conventional methods rely on stoichiometric amounts of strong reductants, such as SmI<sub>2</sub>,<sup>4</sup> Mg,<sup>5</sup> and Zn,<sup>6</sup> to generate ketyl radicals, which react with olefinic substrates to afford the coupling products. By using mild reductants such as Hantzsch ester to generate ketyl radicals for addition to olefins, photoredox ene-carbonyl reductive coupling (ECRC) reactions increase functional group compatibility. The photoredox strategy has been successful in intramolecular addition of ketones to olefins<sup>7</sup> and imines<sup>8</sup> and coupling of alkenylpyridines<sup>9-10</sup> or allyl sulphone<sup>11</sup> with aldehydes and imines,<sup>9</sup> as well as for some reactions under continuous flow conditions.<sup>12</sup> However, intermolecular photoredox ECRC reactions are not accessible for many olefin substrates due to competing pinacol coupling and/or reduction of ketones and aldehydes under these conditions, resulting in poor product selectivity.<sup>9, 13</sup>

Natural enzymes have provided a blueprint for tuning reaction selectivity by employing finely assembled pockets to specifically bind and activate substrates (**Figure 2-1a**).<sup>14-15</sup> A substrate selectively docks into the binding pocket, breaks and forms bonds, and is then released from the active site, thereby preventing unwanted side reactions. This substrate-binding strategy has been demonstrated in a few homogeneous catalysts for selective alkane oxidation and C-H functionalization but cannot be generalized to other organic reactions due to the difficulty of creating precise binding sites in molecular systems.<sup>16-17</sup>

In this chapter, we report a MOL, Hf-IrF-OTf, consisting of triflate (OTf)-capped Hf<sub>12</sub> SBUs and photosensitizing [Ir(DBB)(dF(CF<sub>3</sub>)ppy)<sub>2</sub>]<sup>+</sup> (IrF-PS; DBB = 4,4'-di(4-benzoato)-2,2'-bipyridine; dF(CF<sub>3</sub>)ppy = 2-(2,4-difluorophenyl)-5-(trifluoromethyl)-pyridine) ligands, as a selective catalyst for photoredox ECRC reactions. The triflated Hf<sub>12</sub> clusters bind olefinic substrates via Lewis acid-base interaction to accelerate addition of the ketyl radical generated by IrF-PS to the substrate (**Figure 2-1b**). By depleting the ketyl radical, Hf-IrF-OTf minimizes ketyl dimerization and reduction reactions and increases the reductive coupling product yield by an order of magnitude over the homogeneous counterpart.

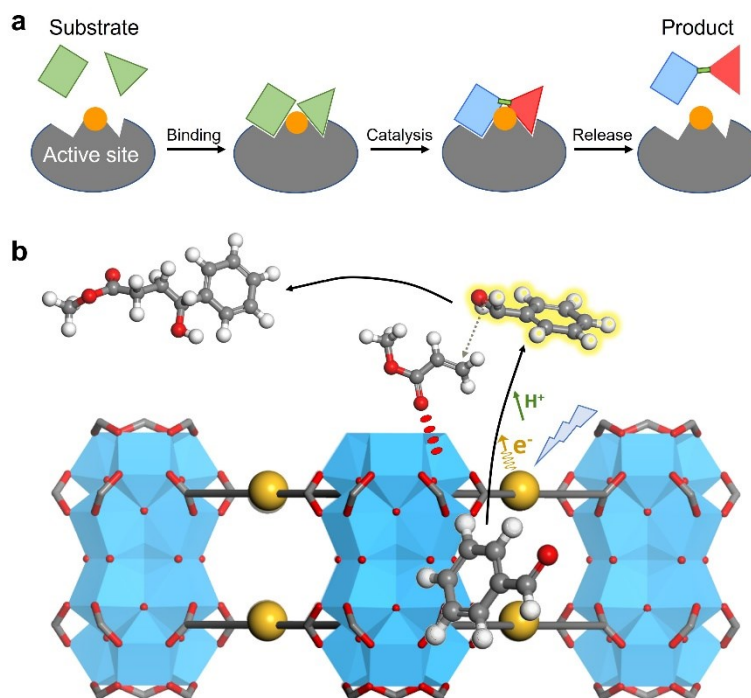
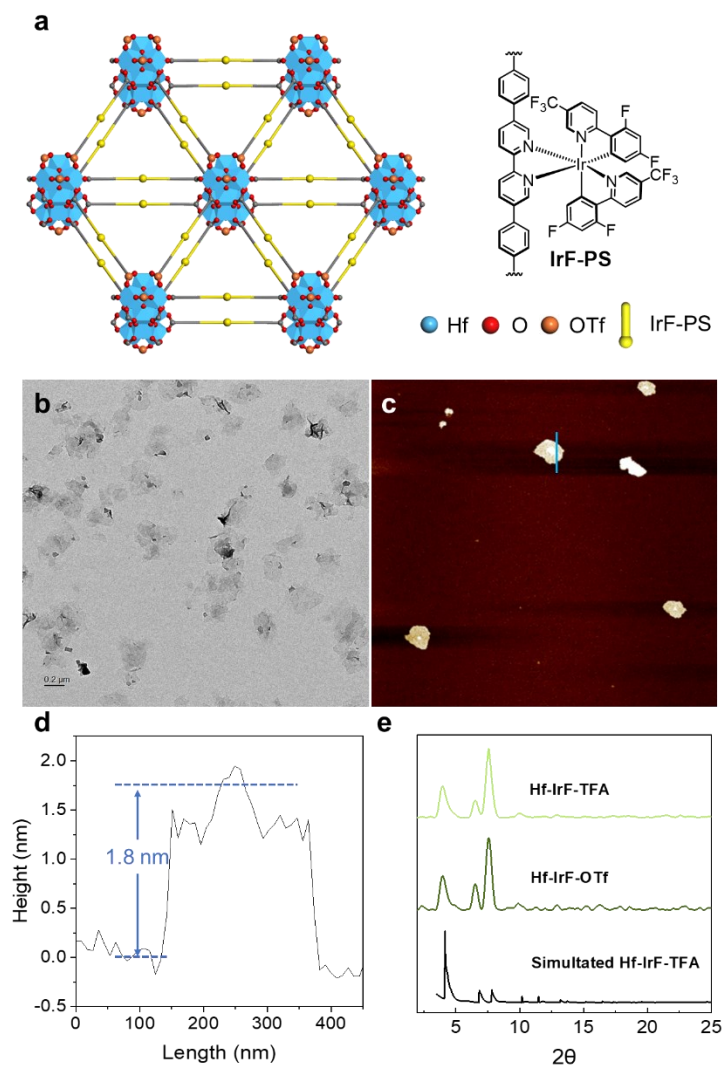


**Figure 2-1.** Substrate-binding strategy.(a) Schematic showing substrate binding in enzyme catalysis. (b) Schematic showing Hf-IrF-OTf catalyzed photoredox ECRC reactions. Gray, C; white, H; blue, Hf; red, O; yellow, IrF-PS.

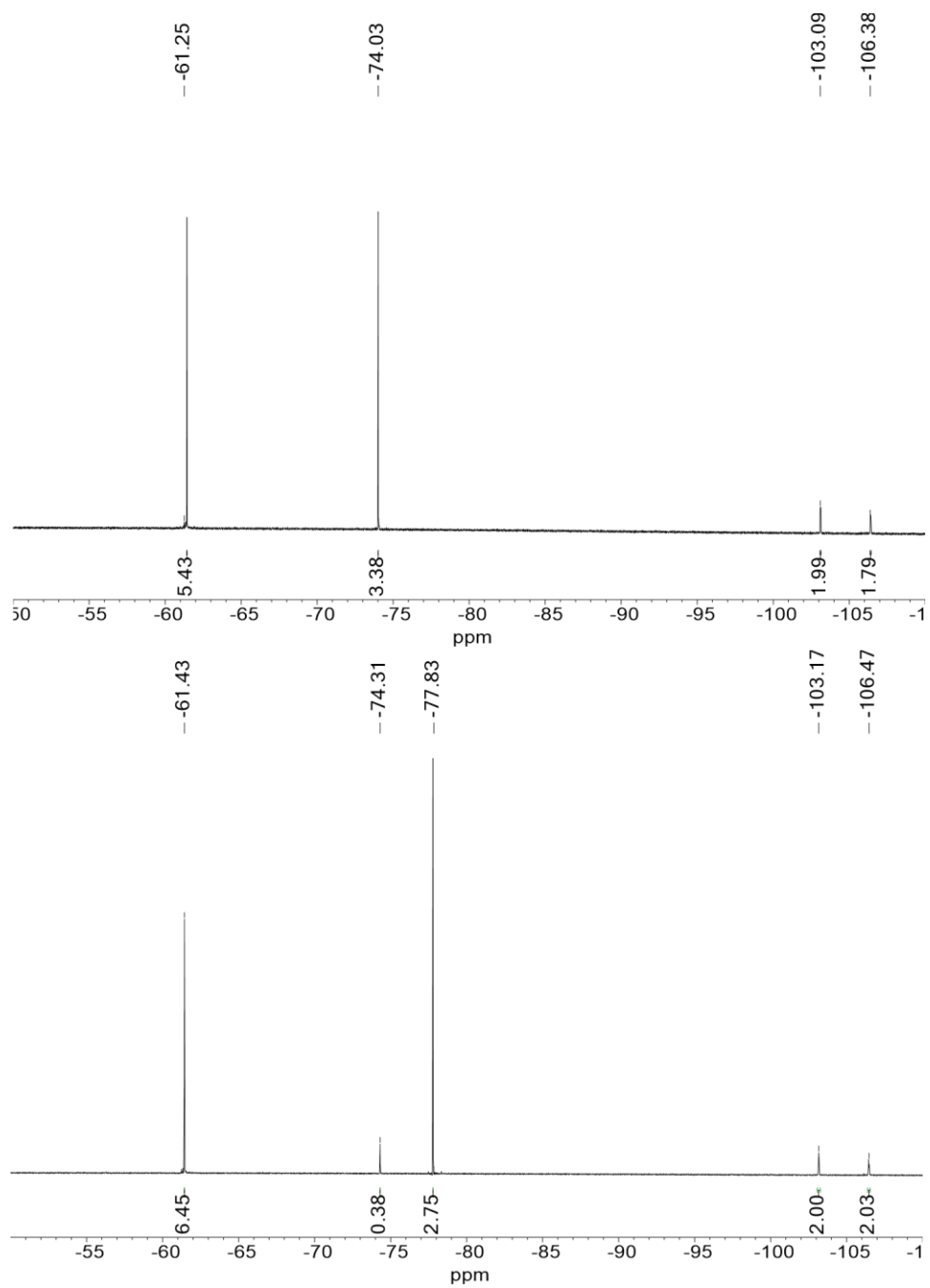
## 2.2 Results and Discussion

### 2.2.1 Synthesis and Characterization of Hf-IrF-OTf

The self-supporting MOL of the formula  $\text{Hf}_{12}(\mu_3\text{-O})_8(\mu_3\text{-OH})_8(\mu_2\text{-OH})_6(\text{IrF-PS})_6(\text{TFA})_6$  (Hf-IrF-TFA) was prepared by a solvothermal reaction between  $\text{HfCl}_4$  and IrF-PS in *N,N*-dimethylformamide (DMF) with water and trifluoroacetic acid (TFA) as modulators at 80 °C for 24 h.<sup>18</sup> TFA capping groups were replaced with OTf group via acid exchange in benzene to produce  $\text{Hf}_{12}(\mu_3\text{-O})_8(\mu_3\text{-OH})_8(\mu_2\text{-OH})_6(\text{IrF-PS})_6(\text{OTf})_6$  (Hf-IrF-OTf). PXRD results showed that Hf-IrF-OTf retained the structure of Hf-IrF-TFA (**Figure 2-2e**). TEM and AFM revealed a monolayer hexagonal nanoplate morphology of Hf-IrF-OTf, with a diameter of approximately 200 nm and a thickness of 1.8 nm (**Figure 2-2, b-d**). ICP-MS confirmed a Hf to Ir ratio of 2:1 in both Hf-IrF-TFA and Hf-IrF-OTf, whereas NMR spectra of digested MOLs supported the replacement of TFA by OTf after exchange reactions (**Figure 2-3**). In the structure of Hf-IrF-OTf,  $\text{Hf}_{12}$  clusters are laterally connected by IrF-PS ligands and vertically capped by OTf groups to afford highly Lewis acidic Hf sites (**Figure 2-2a**).



**Figure 2-2.** Structural model and characterization of Hf-IrF-OTf.(a) Schematic showing connectivity of Hf-IrF-OTf. (b–d) TEM image (b), AFM image (c), and height profile (d) of Hf-IrF-OTf. (e) PXRD patterns of Hf-IrF-TFA and Hf-IrF-OTf along with the simulated PXRD pattern of Hf-IrF-TFA.

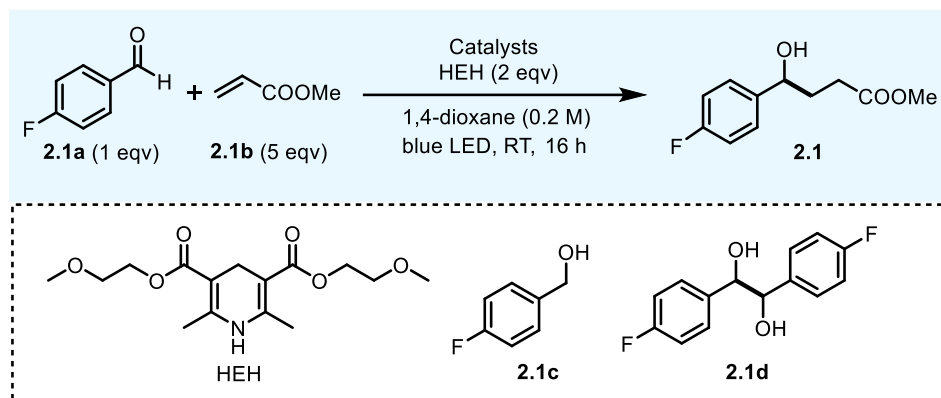


**Figure 2-3.**  $^{19}\text{F}$  NMR of digested Hf-IrF-TFA (top) and Hf-IrF-OTf (bottom). TFA ( $\delta$  -74.03) was replaced with OTf ( $\delta$  -77.83) after acid exchange.

### 2.2.2 ECRC Reactions and Mechanistic Studies

Hf-IrF-OTf was examined as a photoredox catalyst for the coupling between 4-fluorobenzaldehyde (**2.1a**) and methyl acrylate (**2.1b**) (Table 2-1). At 0.05 mol% loading of Hf-IrF-OTf under blue LED irradiation, the ECRC product **2.1** was obtained in 91% yield with bis(2-methoxyethyl) 2,6-dimethyl-1,4-dihydropyridine-3,5-dicarboxylate (HEH) as reductant and 1,4-dioxane as solvent. In contrast, the reaction yielded alcohol (**2.1c**) only when 0.25 mol% IrF-PS methyl ester and 30 mol% Sc(OTf)<sub>3</sub> were used under otherwise identical conditions. When the loadings of both IrF-PS and Sc(OTf)<sub>3</sub> were reduced to 0.05 mol%, the yield of **2.1** increased to 52% but the dimerization byproduct **2.1d** was obtained in 48% yield. Combination of IrF-PS with other Lewis acids in different solvents did not give better results. Control reaction using Hf-IrF-OTf without light irradiation showed no product formation, indicating the photocatalytic nature of the coupling reaction.

To investigate the origin of product selectivity in Hf-IrF-OTf catalyzed reaction, we examined the catalytic activity of Hf-IrF MOLs modified with Brønsted acids of varying pK<sub>a</sub> values: HOTf (-14.2),<sup>19</sup> ClSO<sub>3</sub>H (-6.0),<sup>20</sup> TFA (-0.3), and AcOH (4.8).<sup>21</sup> Hf-IrF-OSO<sub>2</sub>Cl and Hf-IrF-OAc were prepared from Hf-IrF-TFA by acid exchange and retained the structure and morphology of Hf-IrF-TFA. ICP-MS and NMR indicated a complete exchange of TFA to OSO<sub>2</sub>Cl and OAc capping groups, respectively, in Hf-IrF-OSO<sub>2</sub>Cl and Hf-IrF-OAc. At 0.25 mol% catalyst loading, four Hf-IrF MOLs with different capping groups showed an increasing selectivity of **2.1** over **2.1d** as the pK<sub>a</sub> of the capping acid decreased, suggesting that the ECRC reaction product selectivity increases as the binding of **2.1b** to the Lewis acidic Hf site becomes stronger.<sup>22-23</sup>

**Table 2-1.** Photoredox ECRC reactions catalyzed by Hf-IrF-OTf and homogeneous controls.

Entry	Catalyst(s)	Yield ( <b>2.1</b> ) <sup>a</sup>	Yield ( <b>2.1c</b> ) <sup>a</sup>	Yield ( <b>2.1d</b> ) <sup>a</sup>
1	0.05 mol% Hf-IrF-OTf	91%	0	9%
2	0.25 mol% IrF-PS, 30 mol% Sc(OTf) <sub>3</sub>	0	>99%	0
3	0.05 mol% IrF-PS, 0.05 mol% Sc(OTf) <sub>3</sub>	52%	0	48%
4	0.05 mol% Hf-IrF-OTf <sup>b</sup>	0	0	0

<sup>a</sup>Based on <sup>1</sup>H NMR. <sup>b</sup>Without blue LED irradiation.

Luminescence quenching studies imply that the photoredox ECRC reaction starts with quenching of photoexcited IrF-PS by HEH radical to generate highly reducing Ir(II) species. According to previous report,<sup>9, 11</sup> Ir(II) subsequently transfers one electron to **2.1a** to afford a ketyl radical, which rapidly adds to **2.1b** bound to adjacent Hf site to yield the coupling product **2.1**. However, the ketyl radicals dimerize concurrently to yield the pinacol coupling product **2.1d**.<sup>13</sup> The product selectivity thus depends on competition between ketyl radical addition and dimerization. It is assumed that the Lewis acidic Hf sites in Hf-IrF MOLs can bind and activate **2.1b** to accelerate the addition reaction.



To support this hypothesis, we measured the initial rates of the ECRC reaction catalyzed by Hf-IrF MOLs with different acidities, and with Hf-IrF-OTf at different loadings (**Figure 2-4, a-b**). The selectivity **2.1/2.1d** was inversely correlated to  $pK_a$  values of capping acids, suggesting that the Hf sites with stronger acidity bind and activate **2.1b** more efficiently to accelerate the radical addition. The selectivity **2.1/2.1d** was also inversely correlated to Hf-IrF-OTf loadings, matching the reaction order difference of ketyl radical addition (1st order) and dimerization (2nd order). A higher loading of PSs promotes ketyl radical generation to favor the undesired bimolecular reaction.

The interaction between Hf-IrF-OTf and olefinic substrates was further examined by IR spectroscopy. Mixtures of Hf-IrF-OTf with different amounts of butyl acrylate (0, 0.2, 0.4, 0.6, 0.8 and 1.0 eqv) (**Figure 2-4c**) exhibited four characteristic rising IR peaks at 1715, 1638, 1617 and 1594  $\text{cm}^{-1}$  (**Figure 2-4d**), which were assigned to stretching vibrations of carbonyl, *trans*- and *cis*-C=C double bonds and activated carbonyl in butyl acrylate, respectively.<sup>24-25</sup> A red shift of carbonyl IR peak from 1715  $\text{cm}^{-1}$  to 1594  $\text{cm}^{-1}$  indicated a strong activation of butyl acrylate by Hf-IrF-OTf.

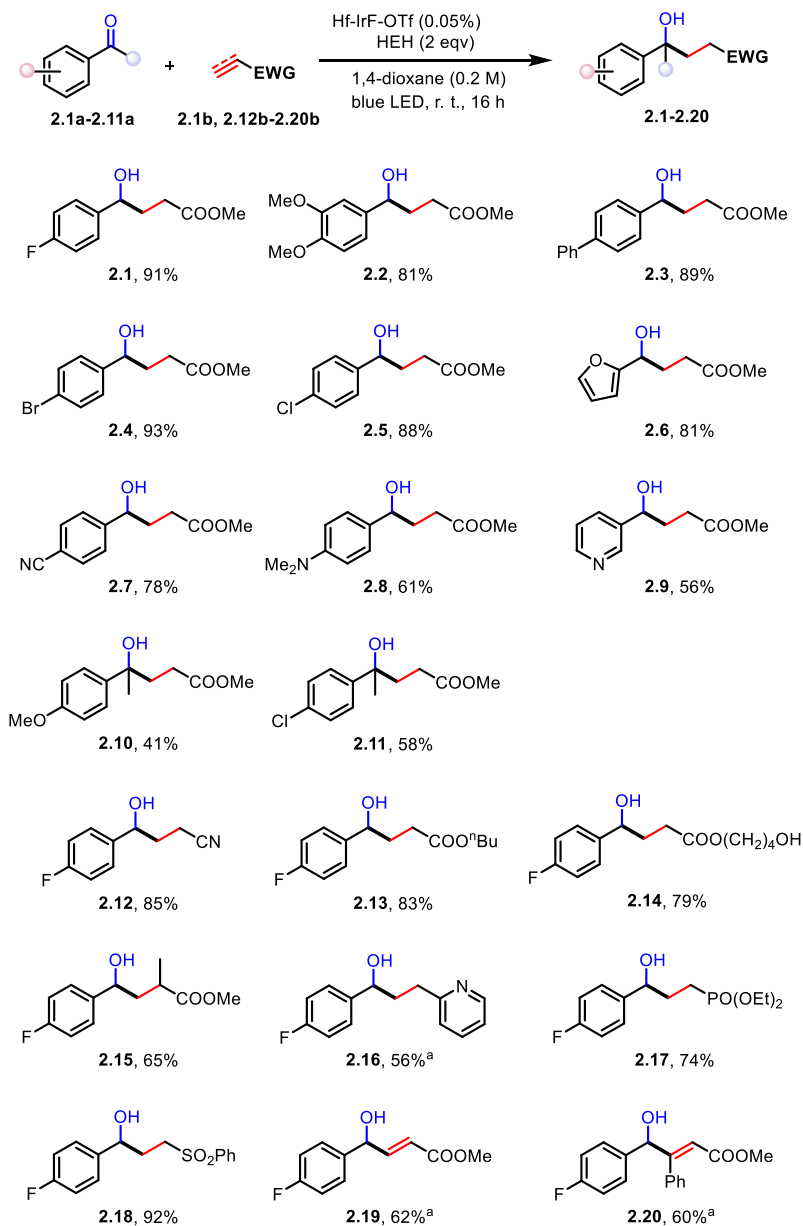
Based on the experimental results and literature precedents, we propose the following mechanism for Hf-IrF-OTf catalyzed photoredox ECRC reactions (**Figure 2-4e**). The reaction starts with a photoredox cycle that reduces aromatic aldehyde to a ketyl radical. The radical preferably adds to the C=C double bond in **2.1b**, which is bound to adjacent Hf sites via acid-base interaction of polar substituents. The resultant  $\alpha$ -carbonyl radical then abstracts a hydrogen atom from HEH, yielding the ECRC reaction product. Meanwhile, two undesired pathways including dimerization and direct reduction are suppressed due to the accelerated consumption of ketyl radical in the productive pathway.



### 2.2.3 Substrate Scope

The substrate scope of Hf-IrF-OTf catalyzed ECRC reaction was investigated (**Table 2-2**). Halo-substituted aromatic aldehydes (**2.1a**, **2.4a**, **2.5a**), an aryl-substituted benzaldehyde (**2.3a**), and a cyano-substituted aromatic aldehyde (**2.7a**) all smoothly underwent reactions to afford desired products **2.1**, **2.3**, **2.4**, **2.5**, and **2.7** in 78-93% yields. Aromatic aldehydes with electron-donating methoxy and dimethylamino groups (**2.2a**, **2.8a**) underwent the reaction to afford **2.2** and **2.8** in slightly lower yields of 81% and 61%. Extending the reaction time from 16 h to 48 h increased the yield for **2.8** from 61% to 82%. Reactions with pyridine and furan-substituted aldehydes **2.6a** and **2.9a** afforded the corresponding coupling products in 81% and 56% yields. Ketones **2.10a** and **2.11a** also reacted with **2.1b** to afford tertiary alcohols **2.10** and **2.11** in 41% and 58% yields, respectively. The lower reactivity of ketones is attributed to their resistance to reduction to ketyl radicals. Olefinic substrates with electron-withdrawing groups, including cyano, ester, pyridine, phosphate, and sulfonate groups coupled with **2.1a** to afford ECRC product **2.12-2.14**, **2.16-2.18** in 56-92% yields. Reaction between **2.1a** and  $\alpha$ -substituted acrylate **2.15b** afforded diastereomers mixture **2.15** in 65% yield. Finally, terminal and internal alkynes with ester groups reacted with **2.1a** to generate di-substituted or tri-substituted olefins **2.19** and **2.20** in ~60% yields. The broad scopes of the coupling reactions showcase the generality of the substrate-binding strategy, complementing current methods for ECRC reactions. Additionally, the Hf-IrF-OTf could be recovered and reused without loss of reactivity in five consecutive cycles (**Figure 2-5**).

**Table 2-2.** Substrate scope of Hf-Ir-OTf catalyzed photoredox ECRC reaction.



<sup>a</sup>Reactions were performed in dichloromethane.

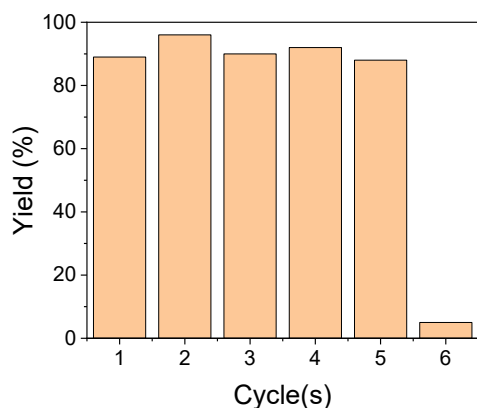


**Figure 2-5.** Catalyst reuse experiments. In the sixth cycle, Hf-IrF-OTf was removed from the reaction mixture for a filtration test.

### 2.3 Conclusion

In this chapter, we developed a MOL, Hf-IrF-OTf, as a photoredox catalyst for selective ene-carbonyl reductive coupling reactions. Hf-IrF-OTf increased the selectivity for the ECRC reaction by an order of magnitude over the homogeneous counterpart. Spectroscopic and kinetic studies revealed that Lewis acidic sites in Hf-IrF-OTf bind and activate olefinic substrates to facilitate addition of photo-generated ketyl radicals. The reaction has good functional group tolerance and accommodates various acrylate-type substrates and aromatic carbonyl compounds. Hierarchical integration of both Lewis acids and photosensitizers in the MOL thus achieves a unique synergistic effect, promising to serve as an excellent platform for developing new generation of multifunctional materials with biomimetic catalytic activities.

## 2.4 Methods

### 2.4.1 Material synthesis

**Synthesis of IrF-PS.** IrF-PS was synthesized according to the literature report.<sup>26</sup> <sup>1</sup>H NMR (500 MHz, DMSO-*d*<sub>6</sub>):  $\delta$  9.11 (d, 2H), 8.77 (dd, 2H), 8.48 (d, 2H), 8.43 (d, 2H), 8.15 (s, 2H), 8.04 (d, 4H), 7.81 (s, 2H), 7.67 (d, 4H), 7.11 (m, 2H), 5.89 (dd, 2H).

**Synthesis of Hf-IrF-TFA.** Hf-IrF-TFA was synthesized according to a previously reported procedure in the literature.<sup>18</sup> 0.5 mL of HfCl<sub>4</sub> solution [2.0 mg/mL in DMF], 0.5 mL of IrF-PS solution (4.0mg/mL in DMF), 2  $\mu$ L of TFA, and 5 $\mu$ L of water were mixed in a 4.6 mL vial. The resultant reaction mixture was placed in an 80 °C oven for 24 hours. The yellow precipitate was isolated in 52% yield by centrifugation and washed with DMF and ethanol. The isolated yield was determined by UV-vis analysis of digested Hf-IrF-TFA solution. UV-vis digestion method: 10  $\mu$ L of MOL dispersion was added to the mixture of 940  $\mu$ L DMF and 50  $\mu$ L H<sub>3</sub>PO<sub>4</sub>. The resultant solution was sonicated for 5 min before a UV-vis spectrum was recorded. The amount of IrF-PS was determined by a standard curve based on absorption at 354 nm.

**Synthesis of Hf-IrF-OTf.** Hf-IrF-OTf was synthesized according to a previously reported procedure in the literature.<sup>18</sup> To a 10 mL suspension of Hf-Ir-TFA (2.0  $\mu$ mol/mL in dry benzene) was added trimethylsilyl(TMS)-OTf (44.5 mg, 0.2 mmol, 10 equiv). The resultant mixture was stirred at room temperature for 12 hours. Hf-Ir-OTf was isolated in 93% yield as a yellow precipitate by centrifugation and washing with 10 mL benzene three times and 10 mL MeCN twice.

**Synthesis of Hf-IrF-OSO<sub>2</sub>Cl.** To a 10 mL suspension of Hf-IrF-TFA (2.0  $\mu$ mol/mL in dry benzene) was added TMS-OSO<sub>2</sub>Cl (37.7 mg, 0.2 mmol, 10 equiv). The resultant mixture was stirred at room temperature for 12 hours. Hf-IrF-OSO<sub>2</sub>Cl was isolated in a quantitative yield as a

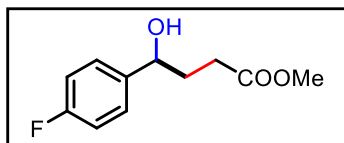
yellow precipitate by centrifugation and washing with 10 mL benzene three times and 10 mL MeCN twice.

**Synthesis of Hf-IrF-OAc.** To a 10 mL suspension of Hf-IrF-TFA (2.0  $\mu\text{mol/mL}$  in ethanol) was added KOAc (2.0 mg, 40  $\mu\text{mol}$ , 2 equiv). The resultant mixture was stirred at room temperature for 12 hours. Hf-IrF-OAc was isolated in 90% yield as a yellow precipitate by centrifugation and washing with 10 mL ethanol three times.

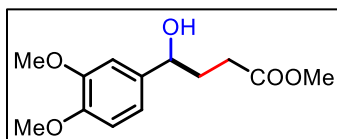
**NMR composition analysis of MOLs.** 1.0 mg of each Hf-IrF MOL was dried under vacuum and then digested in mixture of 500  $\mu\text{L}$  DMSO- $d_6$ , 10  $\mu\text{L}$   $\text{D}_3\text{PO}_4$ , and 50  $\mu\text{L}$   $\text{D}_2\text{O}$  via 10-min sonication. The solution was analyzed by  $^1\text{H}$  NMR and  $^{19}\text{F}$  NMR.  $^1\text{H}$  NMR spectra of digested Hf-IrF-OTf, Hf-IrF-OSO $_2$ Cl, and Hf-IrF-TFA showed peaks from IrF-PS, whereas  $^1\text{H}$  NMR spectra of digested Hf-Ir-OAc showed peaks from both IrF-PS and AcOH. The ratio of IrF-PS to AcOH was determined to be 1:0.96.  $^{19}\text{F}$  NMR spectra of digested Hf-IrF-TFA showed peaks from IrF-PS and TFA with a molar ratio of 1:1, whereas  $^{19}\text{F}$  NMR spectra of digested Hf-IrF-OTf showed peaks from IrF-PS and HOTf in a 1:0.92 molar ratio along with a peak from trace amount of TFA.

#### 2.4.2 Catalytic Reactions

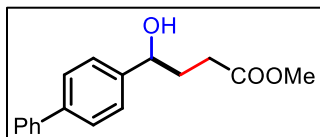
**General procedure for photoredox ECRC reactions.** To a 4 mL vial was added aldehyde (0.10 mmol), olefin (0.50 mmol, 5 equiv), HEH (0.20 mmol, 2 equiv), Hf-Ir-OTf (0.05  $\mu\text{mol}$  based on Ir, 0.05%) and 0.5 mL dioxane (or dichloromethane if mentioned) in an  $\text{N}_2$  atmosphere. The vial was sealed, and the resulting mixture was stirred under blue LED irradiation at room temperature for 16 hours. After the reaction, the solvent was removed under vacuum. The residue was purified by column chromatography on silica gel using n-hexane and ethyl acetate as eluent to give product **2.1** through **2.20**.



**2.1:** Yellowish oil. Yield: 91%. **<sup>1</sup>H NMR** (400 MHz, CDCl<sub>3</sub>) δ 7.33 – 7.30 (m, 2H), 7.05 – 7.00 (m, 2H), 4.75 (t, *J* = 6.4 Hz, 1H), 3.67 (s, 3H), 2.43 (t, *J* = 7.2 Hz, 2H), 2.04 (q, *J* = 6.8 Hz, 2H). **<sup>13</sup>C NMR** (101 MHz, CDCl<sub>3</sub>) δ 174.43, 163.57, 161.13, 139.96, 127.57, 127.49, 115.57, 115.36, 73.04, 51.91, 34.03, 30.47. **<sup>19</sup>F NMR** (400 MHz, CDCl<sub>3</sub>) δ 114.983. **HRMS** (ESI-TOF): calc'd for C<sub>13</sub>H<sub>18</sub>FO<sub>3</sub> [M+H-H<sub>2</sub>O]<sup>+</sup>: 195.0821, found 195.0893. **IR** (ATR, cm<sup>-1</sup>): 3450, 2950, 1766, 1732, 1604, 1509, 1220, 1156, 1014, 940, 836. Characterization data matched that reported in literature.<sup>27</sup>



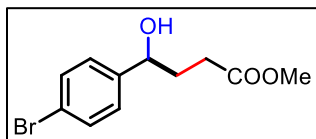
**2.2:** Yellowish oil. Yield: 81%. **<sup>1</sup>H NMR** (400 MHz, CDCl<sub>3</sub>) δ 6.84 (s, 1H), 6.81 – 6.73 (m, 2H), 4.63 (t, *J* = 5.5 Hz, 1H), 3.82 (d, *J* = 7.8 Hz, 7H), 3.61 (s, 3H), 2.37 (t, *J* = 7.2 Hz, 2H), 2.00 (dt, *J* = 14.3, 7.2 Hz, 2H). **<sup>13</sup>C NMR** (101 MHz, CDCl<sub>3</sub>) δ 174.31, 163.34, 148.53, 136.69, 118.01, 110.99, 108.82, 73.44, 55.96, 51.72, 33.80, 30.50. **HRMS** (ESI-TOF): calc'd for C<sub>13</sub>H<sub>18</sub>O<sub>5</sub> [M+H-H<sub>2</sub>O]<sup>+</sup>: 237.1127, found 237.1087. **IR** (ATR, cm<sup>-1</sup>): 3516, 2924, 1768, 1730, 1607, 1594, 1517, 1440, 1370, 1321, 1259, 1235, 1201, 1139, 1063, 1025, 911, 858, 811, 763.



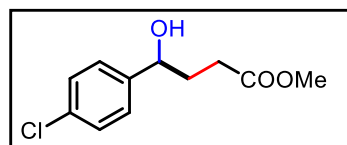
**2.3:** Yellowish oil. Yield 89% **<sup>1</sup>H NMR** (400 MHz, CDCl<sub>3</sub>) δ 7.33 – 7.3 (m, 4H), 7.05-7.00 (m, 5H), 4.75 (t, *J* = 6.4 Hz, 1H), 3.67 (s, 3H), 2.43 (t, *J* = 7.2 Hz, 2H), 2.04 (q, *J* = 6.8 Hz, 2H). **<sup>13</sup>C NMR** (101 MHz, CDCl<sub>3</sub>) δ 174.43, 163.57, 161.13, 139.96, 127.57, 127.49, 115.57, 115.36, 73.04, 51.91, 34.03, 30.47. **HRMS** (ESI-TOF): calc'd for C<sub>17</sub>H<sub>18</sub>O<sub>3</sub> [M+H-H<sub>2</sub>O]<sup>+</sup>: 253.1229, found



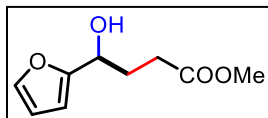
253.1190. **IR** (ATR,  $\text{cm}^{-1}$ ), 3527, 2923, 1772, 1594, 1491, 1456, 1414, 1326, 1296, 1214, 1173, 1140, 1070, 1027, 1010, 938, 889, 836, 806.



**2.4:** Colorless oil. Yield 93% **<sup>1</sup>H NMR** (400 MHz, CDCl<sub>3</sub>)  $\delta$  7.51 – 7.44 (m, 2H), 7.23 (d,  $J$  = 8.3 Hz, 2H), 4.75 (t,  $J$  = 6.3 Hz, 1H), 3.68 (s, 3H), 2.44 (td,  $J$  = 7.1, 2.1 Hz, 2H), 2.04 (q,  $J$  = 7.2 Hz, 2H). **<sup>13</sup>C NMR** (101 MHz, CDCl<sub>3</sub>)  $\delta$  174.31, 143.07, 131.61, 127.49, 121.42, 72.91, 51.81, 33.75, 30.24. **HRMS** (ESI-TOF): calc'd for C<sub>11</sub>H<sub>13</sub>BrO<sub>3</sub> [M+H-H<sub>2</sub>O]<sup>+</sup>: 255.0021, found 254.9980. **IR** (ATR,  $\text{cm}^{-1}$ ), 3461, 2924, 1777, 1734, 1593, 1488, 1438, 1415, 1366, 1328, 1297, 1255, 1214, 1174, 1071, 938, 824. Characterization data matched that reported in literature.<sup>27</sup>

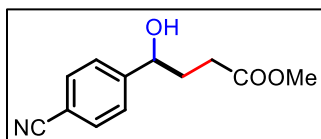


**2.5:** Colorless oil. Yield 88% **<sup>1</sup>H NMR** (400 MHz, CDCl<sub>3</sub>)  $\delta$  7.51 – 7.43 (m, 2H), 7.27 – 7.19 (m, 2H), 4.74 (t,  $J$  = 6.3 Hz, 1H), 3.68 (s, 3H), 2.44 (td,  $J$  = 7.1, 2.2 Hz, 2H), 2.11 – 1.97 (m, 2H). **<sup>13</sup>C NMR** (101 MHz, CDCl<sub>3</sub>)  $\delta$  174.31, 143.07, 131.96, 131.61, 127.50, 126.95, 121.41, 72.89, 51.81, 33.76, 30.24. **IR** (ATR,  $\text{cm}^{-1}$ ), 3463, 2924, 1777, 1734, 1593, 1489, 1456, 1438, 1416, 1365, 1328, 1297, 1260, 1214, 1174, 1144, 1071, 1010, 938, 823. Characterization data matched that reported in literature.<sup>27</sup>

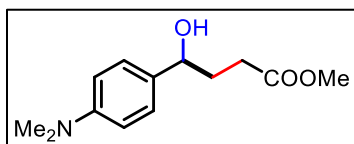


**2.6:** Yellowish oil. Yield 81% **<sup>1</sup>H NMR** (400 MHz, CDCl<sub>3</sub>)  $\delta$  7.37 (d,  $J$  = 1.0 Hz, 1H), 6.33 (dd,  $J$  = 3.2, 1.8 Hz, 1H), 6.26 (d,  $J$  = 3.2 Hz, 1H), 4.83 – 4.68 (m, 1H), 3.68 (s, 3H), 2.48 (t,  $J$  = 7.2

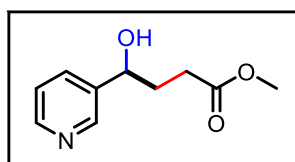
Hz, 2H), 2.22 – 2.14 (m, 2H). **<sup>13</sup>C NMR** (101 MHz, CDCl<sub>3</sub>) δ 174.12, 156.01, 142.08, 110.18, 106.07, 67.03, 51.77, 30.43. **HRMS** (ESI-TOF): calc'd for C<sub>9</sub>H<sub>12</sub>O<sub>4</sub> [M+H-H<sub>2</sub>O]<sup>+</sup>: 167.0708, found 167.0707. **IR** (ATR, cm<sup>-1</sup>), 3454, 2944, 1769, 1730, 1439, 1419, 1330, 1261, 1215, 1175, 1011, 916, 749.



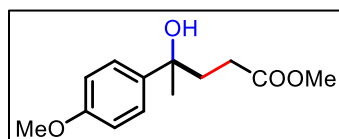
**2.7:** Yellowish oil. Yield 78% **<sup>1</sup>H NMR** (400 MHz, CDCl<sub>3</sub>) δ 7.65 (d, *J* = 8.2 Hz, 2H), 7.48 (d, *J* = 8.1 Hz, 2H), 4.89 – 4.83 (m, 1H), 3.69 (s, 2H), 2.56 – 2.38 (m, 2H), 2.16 – 1.94 (m, 2H). **<sup>13</sup>C NMR** (101 MHz, CDCl<sub>3</sub>) δ 174.35, 149.47, 132.37, 126.42, 118.78, 111.38, 72.78, 51.94, 33.72, 30.12. **HRMS** (ESI-TOF): calc'd for C<sub>12</sub>H<sub>13</sub>NO<sub>3</sub> [M+Na]<sup>+</sup>: 242.0793, found 242.0812. **IR** (ATR, cm<sup>-1</sup>), 3488, 2925, 2229, 1732, 1609, 1504, 1439, 1416, 1376, 1298, 1260, 1173, 1077, 1019, 990, 941, 888, 846, 567.



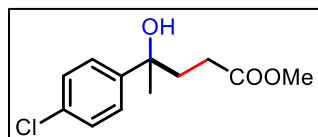
**2.8:** Colorless oil. Yield 61% **<sup>1</sup>H NMR** (400 MHz, CDCl<sub>3</sub>) δ 7.26 – 7.18 (m, 2H), 6.73 (d, *J* = 8.2 Hz, 2H), 4.68 – 4.60 (m, 1H), 3.66 (s, 3H), 2.94 (s, 6H), 2.50 – 2.33 (m, 2H), 2.19 – 1.96 (m, 2H). **<sup>13</sup>C NMR** (101 MHz, CDCl<sub>3</sub>) δ 174.33, 150.26, 127.23, 126.84, 112.64, 73.42, 51.64, 40.72, 33.59, 30.66. **HRMS** (ESI-TOF): calc'd for C<sub>13</sub>H<sub>19</sub>NO<sub>3</sub> [M+H-H<sub>2</sub>O]<sup>+</sup>: 220.1338, found 220.1330. **IR** (ATR, cm<sup>-1</sup>), 3461, 2924, 1777, 1734, 1593, 1488, 1455, 1438, 1415, 1365, 1328, 1297, 1255, 1214, 1174, 1146, 1071, 1010, 938, 824.



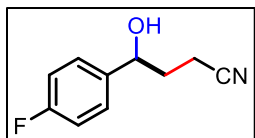
**2.9:** Yellowish oil. Yield 56%  $^1\text{H NMR}$  (500 MHz,  $\text{CDCl}_3$ )  $\delta$  8.84 (s, 1H), 8.62 (d,  $J = 3.3$  Hz, 1H), 8.57 (d,  $J = 4.5$  Hz, 1H), 8.19 (d,  $J = 7.8$  Hz, 1H), 5.01 (dd,  $J = 8.6, 4.0$  Hz, 1H), 3.69 (s, 3H), 2.75 – 2.67 (m, 1H), 2.60 – 2.53 (m, 1H), 2.19 – 2.01 (m, 2H).  $^{13}\text{C NMR}$  (101 MHz,  $\text{CDCl}_3$ )  $\delta$  174.18, 146.49, 145.83, 141.14, 135.70, 124.17, 70.74, 51.87, 33.72, 30.17. **HRMS** (ESI-TOF): calc'd for  $\text{C}_{13}\text{H}_{18}\text{O}_4$   $[\text{M}+\text{H}]^+$ : 196.0974, found 196.0962. **IR** (ATR,  $\text{cm}^{-1}$ ), 3351, 2950, 2924, 2852, 1777, 1731, 1581, 1435, 1378, 1328, 1255, 1200, 1173, 1175, 1026, 941, 890, 813, 715



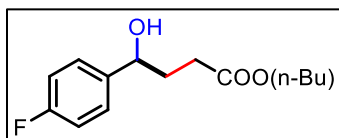
**2.10:** Yellowish oil. Yield 41%  $^1\text{H NMR}$  (400 MHz,  $\text{CDCl}_3$ )  $\delta$  7.38 – 7.26 (m, 2H), 6.93 – 6.83 (m, 2H), 3.80 (s, 3H), 3.62 (s, 3H), 2.41 – 2.16 (m, 2H), 2.16 – 2.07 (m, 2H), 1.56 (s, 3H).  $^{13}\text{C NMR}$  (101 MHz,  $\text{CDCl}_3$ )  $\delta$  174.94, 158.36, 139.08, 125.99, 113.57, 73.75, 55.27, 51.72, 38.61, 30.83, 29.25. **HRMS** (ESI-TOF): calc'd for  $\text{C}_{13}\text{H}_{18}\text{O}_4$   $[\text{M}+\text{H}-\text{H}_2\text{O}]^+$ : 221.1178, found 221.1190. **IR** (ATR,  $\text{cm}^{-1}$ ), 3515, 2926, 1772, 1738, 1613, 1583, 1514, 1462, 1418, 1378, 1303, 1252, 1214, 1182, 1134, 1077, 1031, 943, 834, 804.



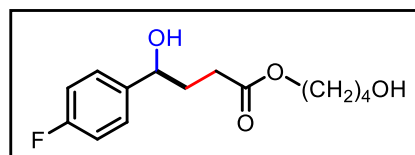
**2.11:** Yellowish oil. Yield 58%  $^1\text{H NMR}$  (400 MHz,  $\text{CDCl}_3$ )  $\delta$  7.38 – 7.33 (m, 2H), 7.33 – 7.27 (m, 2H), 3.63 (s, 3H), 2.36 – 2.27 (m, 1H), 2.27 – 2.21 (m, 1H), 2.17 – 2.09 (m, 2H), 1.56 (s, 3H).  $^{13}\text{C NMR}$  (101 MHz,  $\text{CDCl}_3$ )  $\delta$  174.91, 145.47, 128.36, 126.40, 73.78, 51.83, 38.39, 30.94, 29.09. **HRMS** (ESI-TOF): calc'd for  $\text{C}_{12}\text{H}_{15}\text{ClO}_3$   $[\text{M}+\text{Na}]^+$ : 265.0608, found 265.0560. **IR** (ATR,  $\text{cm}^{-1}$ ), 3522, 2925, 1778, 1492, 1456, 1421, 1402, 1378, 1294, 1261, 1241, 1213, 1167, 1133, 1094, 1075, 1013, 973, 943, 920, 831.



**2.12:** Yellowish oil. Yield 85%  $^1\text{H NMR}$  (400 MHz,  $\text{CDCl}_3$ )  $\delta$  7.51 – 7.44 (m, 2H), 7.23 (d,  $J$  = 8.2 Hz, 2H), 4.75 (t,  $J$  = 6.3 Hz, 1H), 3.68 (s, 3H), 2.44 (td,  $J$  = 7.1, 2.1 Hz, 2H), 2.04 (q,  $J$  = 7.2 Hz, 2H).  $^{13}\text{C NMR}$  (101 MHz,  $\text{CDCl}_3$ )  $\delta$  174.31, 143.07, 131.61, 127.49, 121.42, 72.91, 51.81, 33.75, 30.24. **IR** (ATR,  $\text{cm}^{-1}$ ), 3434, 2925, 2854, 2247, 1722, 1604, 1510, 1443, 1424, 1373, 1288, 1222, 1158, 1108, 1074, 1050, 1014, 941, 837, 774. Characterization data matched that reported in literature.<sup>6</sup>

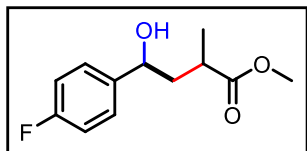


**2.13:** Yellowish oil. Yield 83%  $^1\text{H NMR}$  (400 MHz,  $\text{CDCl}_3$ )  $\delta$  7.32 (ddd,  $J$  = 10.2, 5.4, 2.8 Hz, 2H), 7.03 (ddt,  $J$  = 8.8, 7.1, 2.2 Hz, 2H), 4.75 (t,  $J$  = 6.4 Hz, 1H), 4.07 (t,  $J$  = 6.7 Hz, 2H), 2.46 – 2.23 (m, 2H), 2.11 – 1.78 (m, 2H), 1.69 – 1.53 (m, 3H), 1.37 (dq,  $J$  = 14.6, 7.3 Hz, 1H), 0.93 (td,  $J$  = 7.4, 2.9 Hz, 3H).  $^{13}\text{C NMR}$  (101 MHz,  $\text{CDCl}_3$ )  $\delta$  174.17, 163.62, 162.26, 140.03, 127.54, 127.45, 115.61, 115.40, 73.16, 64.75, 34.12, 30.82, 30.79, 19.35, 13.88.  $^{19}\text{F NMR}$  (377 MHz,  $\text{CDCl}_3$ )  $\delta$  -115.10. **HRMS** (ESI-TOF): calc'd for  $\text{C}_{14}\text{H}_{19}\text{FO}_3$   $[\text{M}+\text{H}-\text{H}_2\text{O}]^+$ : 237.1291, found 237.1221. **IR** (ATR,  $\text{cm}^{-1}$ ), 3504, 2933, 1776, 1731, 1605, 1511, 1457, 1394, 1224, 1175, 1158, 1068, 1015, 942, 837.

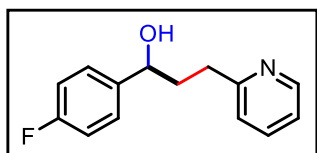


**2.14:** Yellowish oil. Yield 79%  $^1\text{H NMR}$  (400 MHz,  $\text{CDCl}_3$ )  $\delta$  7.29 – 7.22 (m, 2H), 7.00 – 6.92 (m, 2H), 4.69 (t,  $J$  = 6.4 Hz, 1H), 4.05 (t,  $J$  = 6.5 Hz, 2H), 3.61 (t,  $J$  = 6.3 Hz, 2H), 2.39 – 2.32 (m,

2H), 2.01 – 1.94 (m, 2H), 1.70 – 1.61 (m, 2H), 1.60 – 1.53 (m, 2H).  $^{13}\text{C}$  NMR (101 MHz,  $\text{CDCl}_3$ )  $\delta$  173.93, 163.45, 161.01, 130.82, 127.44, 127.36, 115.45, 115.24, 72.95, 64.46, 62.37, 33.93, 30.61, 29.11, 25.10.  $^{19}\text{F}$  NMR (377 MHz,  $\text{CDCl}_3$ )  $\delta$  -115.04. **HRMS** (ESI-TOF): calc'd for  $\text{C}_{14}\text{H}_{19}\text{FO}_3$   $[\text{M}+\text{H}-\text{H}_2\text{O}]^+$ : 253.1240, found 253.1238. **IR** (ATR,  $\text{cm}^{-1}$ ), 3396, 2924, 2852, 1770, 1607, 1513, 1458, 1419, 1328, 1288, 1226, 1177, 1158, 1046, 1014, 988, 940, 891, 837, 809, 782.

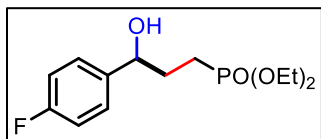


**2.15:** Yellowish oil. Yield 65%, diastereomers  $^1\text{H}$  NMR (400 MHz,  $\text{CDCl}_3$ )  $\delta$  7.25 (d,  $J = 5.6$  Hz, 2H), 6.96 (d,  $J = 1.3$  Hz, 2H), 4.71 – 4.62 (m, 1H), 3.62 (s, 3H), 2.71 – 2.49 (m, 1H), 2.20 – 2.09 (m, 1H), 1.99 (dd,  $J = 9.5, 4.1$  Hz, 1H), 1.74 – 1.62 (m, 1H), 1.14 (d,  $J = 7.1$  Hz, 3H).  $^{13}\text{C}$  NMR (101 MHz,  $\text{CDCl}_3$ )  $\delta$  177.34, 177.22, 163.49, 163.40, 161.04, 160.96, 140.16, 140.13, 140.09, 140.06, 127.52, 127.44, 127.37, 127.29, 115.46, 115.41, 115.25, 115.19, 72.24, 71.62, 51.83, 51.81, 42.97, 36.98, 36.20, 29.71, 17.84, 17.54.  $^{19}\text{F}$  NMR (377 MHz,  $\text{CDCl}_3$ )  $\delta$  -115.04. **HRMS** (ESI-TOF): calc'd for  $\text{C}_{14}\text{H}_{19}\text{FO}_3$   $[\text{M}+\text{H}-\text{H}_2\text{O}]^+$ : 209.0978.1240, found 209.0977. **IR** (ATR,  $\text{cm}^{-1}$ ), 3483, 2923, 2851, 1774, 1733, 1606, 1511, 1458, 1437, 1378, 1226, 1158, 1079, 1013, 930, 837.

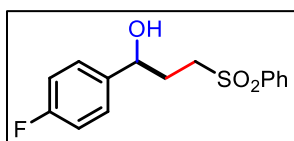


**2.16:** Yellowish oil. Yield 56%  $^1\text{H}$  NMR (400 MHz,  $\text{CDCl}_3$ )  $\delta$  8.51 (d,  $J = 5.0$  Hz, 1H), 7.62 (td,  $J = 7.7, 1.9$  Hz, 1H), 7.36 (dd,  $J = 8.9, 5.5$  Hz, 2H), 7.20 – 7.13 (m, 2H), 7.01 (t,  $J = 8.8$  Hz, 2H), 4.81 (dd,  $J = 8.1, 4.2$  Hz, 1H), 2.98 (t,  $J = 6.6$  Hz, 2H), 2.22 – 2.08 (m, 2H).  $^{13}\text{C}$  NMR (101 MHz,  $\text{CDCl}_3$ )  $\delta$  163.13, 161.18, 160.79, 148.51, 141.05, 137.01, 127.42, 127.34, 123.34, 121.31, 115.11, 114.90, 73.14, 37.91, 34.42.  $^{19}\text{F}$  NMR (377 MHz,  $\text{CDCl}_3$ )  $\delta$  -116.19. **HRMS** (ESI-TOF): calc'd

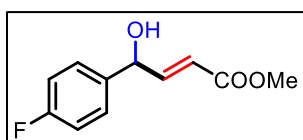
for C<sub>14</sub>H<sub>19</sub>FO<sub>3</sub> [M+H]<sup>+</sup>: 232.1137, found 232.1135. **IR** (ATR, cm<sup>-1</sup>), 3348, 2923, 2854, 1739, 1602, 1509, 1478, 1437, 1378, 1220, 1156, 1071, 1005, 837, 769, 752.



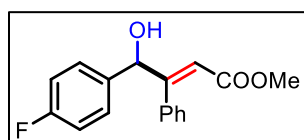
**2.17:** Yellowish oil. Yield 74% **<sup>1</sup>H NMR** (400 MHz, CDCl<sub>3</sub>) δ 7.40 – 7.28 (m, 2H), 7.09 – 6.95 (m, 2H), 4.77 (t, *J* = 5.2 Hz, 1H), 4.22 – 3.96 (m, 4H), 2.99 (d, *J* = 2.4 Hz, 1H), 2.09 – 1.95 (m, 2H), 1.89 – 1.72 (m, 2H), 1.31 (t, *J* = 7.1 Hz, 6H). **<sup>13</sup>C NMR** (101 MHz, CDCl<sub>3</sub>) δ 161.10, 139.81, 127.59, 127.50, 115.55, 115.34, 73.25, 61.90, 22.84, 21.43, 16.63. **<sup>19</sup>F NMR** (377 MHz, CDCl<sub>3</sub>) δ -115.08. **<sup>31</sup>P NMR** (162 MHz, CDCl<sub>3</sub>) δ 32.81. **HRMS** (ESI-TOF): calc'd for C<sub>13</sub>H<sub>20</sub>FO<sub>4</sub>P [M+H-H<sub>2</sub>O]<sup>+</sup>: 273.1056, found 273.1039. **IR** (ATR, cm<sup>-1</sup>), 3359, 2927, 1726, 1668, 1604, 1509, 1443, 1392, 1369, 1221, 1160, 1097, 1054, 1024, 964, 902, 863, 836, 792, 534.



**2.18:** White solid (mp 118.9-119.7 °C). Yield 92% **<sup>1</sup>H NMR** (400 MHz, CDCl<sub>3</sub>) δ 7.93 – 7.86 (m, 2H), 7.69 – 7.63 (m, 1H), 7.60 – 7.53 (m, 2H), 7.30 – 7.26 (m, 2H), 7.07 – 6.99 (m, 2H), 4.88 – 4.80 (m, 1H), 3.26 – 3.18 (m, 2H), 2.16 – 2.10 (m, 2H). **<sup>13</sup>C NMR** (101 MHz, CDCl<sub>3</sub>) δ 139.02, 138.78, 133.80, 129.36, 128.01, 127.34, 127.26, 115.71, 115.49, 71.62, 52.80, 31.85. **<sup>19</sup>F NMR** (377 MHz, CDCl<sub>3</sub>) δ -114.29. **HRMS** (ESI-TOF): calc'd for C<sub>15</sub>H<sub>15</sub>FO<sub>3</sub>S [M+H-H<sub>2</sub>O]<sup>+</sup>: 277.0699, found 277.0607. **IR** (ATR, cm<sup>-1</sup>), 3481, 3019, 2926, 1604, 1509, 1479, 1445, 1406, 1304, 1277, 1215, 1146, 1084, 1062, 912, 850, 828, 753, 738, 687, 668, 607, 570, 528, 494.



**2.19:** Yellowish oil. Reaction solvent was changed to dichloromethane (DCM). Yield 62%  $^1\text{H}$  NMR (400 MHz,  $\text{CDCl}_3$ )  $\delta$  7.38 – 7.28 (m, 1H), 7.10 – 6.99 (m, 2H), 6.17 (dd,  $J = 15.6, 1.7$  Hz, 1H), 5.37 (d,  $J = 4.9$  Hz, 1H), 3.75 (s, 2H).  $^{13}\text{C}$  NMR (101 MHz,  $\text{CDCl}_3$ )  $\delta$  166.75, 163.91, 161.45, 148.38, 136.63, 128.43, 128.35, 120.10, 115.91, 115.69, 72.88, 51.74.  $^{19}\text{F}$  NMR (377 MHz,  $\text{CDCl}_3$ )  $\delta$  -113.50. HRMS (ESI-TOF): calc'd for  $\text{C}_{11}\text{H}_{11}\text{FO}_3$   $[\text{M}+\text{H}-\text{H}_2\text{O}]^+$ : 193.0665, 193.0663. IR (ATR,  $\text{cm}^{-1}$ ), 3463, 3069, 2925, 1725, 1658, 1603, 1509, 1456, 1437, 1412, 1386, 1309, 1275, 1224, 1197, 1169, 1159, 1090, 1038, 1016, 984, 840.



**2.20:** Yellowish oil. Reaction solvent was changed to DCM. Yield 60%  $^1\text{H}$  NMR (400 MHz,  $\text{CDCl}_3$ )  $\delta$  7.47 – 7.38 (m, 2H), 7.36 – 7.29 (m, 3H), 7.28 – 7.24 (m, 2H), 7.11 – 7.00 (m, 2H), 6.94 (d,  $J = 1.2$  Hz, 1H), 5.59 (s, 1H), 3.55 (s, 3H).  $^{13}\text{C}$  NMR (101 MHz,  $\text{CDCl}_3$ )  $\delta$  169.02, 163.71, 161.26, 136.75, 136.72, 135.41, 135.15, 135.11, 128.52, 128.42, 128.37, 128.29, 128.26, 115.53, 115.32, 75.12, 51.77.  $^{19}\text{F}$  NMR (377 MHz,  $\text{CDCl}_3$ )  $\delta$  -114.36. HRMS (ESI-TOF): calc'd for  $\text{C}_{17}\text{H}_{15}\text{FO}_3$   $[\text{M}+\text{H}-\text{H}_2\text{O}]^+$ : 269.0978, found 269.0943. IR (ATR,  $\text{cm}^{-1}$ ), 3491, 3062, 2925, 1719, 1604, 1509, 1447, 1437, 1411, 1377, 1304, 1223, 1150, 1087, 1071, 1037, 839, 755, 738, 690, 546.

## 2.5 References

1. Romero, N. A.; Nicewicz, D. A., Organic Photoredox Catalysis. *Chem. Rev.* **2016**, *116* (17), 10075-10166.
2. Twilton, J.; Le, C.; Zhang, P.; Shaw, M. H.; Evans, R. W.; MacMillan, D. W. C., The merger of transition metal and photocatalysis. *Nature Reviews Chemistry* **2017**, *1* (7), 0052.
3. Matsui, J. K.; Lang, S. B.; Heitz, D. R.; Molander, G. A., Photoredox-Mediated Routes to Radicals: The Value of Catalytic Radical Generation in Synthetic Methods Development. *ACS Catal.* **2017**, *7* (4), 2563-2575.

4. Fukuzawa, S.-i.; Nakanishi, A.; Fujinami, T.; Sakai, S., Reductive coupling of ketones or aldehydes with electron-deficient alkenes promoted by samarium di-iodide. *J. Chem. Soc., Chem. Commun.* **1986**, (8), 624-625.
5. Pons, J.-M.; Santelli, M., Conjugate addition of the dianion of diaryl ketones to  $\alpha$ ,  $\beta$ -ethylenic ketones promoted by  $\text{TiCl}_4$ -Mg. *Tetrahedron* **1990**, *46* (2), 513-522.
6. Yeh, C.-H.; Korivi, R. P.; Cheng, C.-H., Ene-Carbonyl Reductive Coupling Mediated by Zinc and Ammonia for the Synthesis of  $\gamma$ -Hydroxybutyric Acid Derivatives. *Adv. Synth. Catal.* **2013**, *355* (7), 1338-1344.
7. Tarantino, K. T.; Liu, P.; Knowles, R. R., Catalytic Ketyl-Olefin Cyclizations Enabled by Proton-Coupled Electron Transfer. *J. Am. Chem. Soc.* **2013**, *135* (27), 10022-10025.
8. Rono, L. J.; Yayla, H. G.; Wang, D. Y.; Armstrong, M. F.; Knowles, R. R., Enantioselective Photoredox Catalysis Enabled by Proton-Coupled Electron Transfer: Development of an Asymmetric Aza-Pinacol Cyclization. *J. Am. Chem. Soc.* **2013**, *135* (47), 17735-17738.
9. Lee, K. N.; Lei, Z.; Ngai, M.-Y.,  $\beta$ -Selective Reductive Coupling of Alkenylpyridines with Aldehydes and Imines via Synergistic Lewis Acid/Photoredox Catalysis. *J. Am. Chem. Soc.* **2017**, *139* (14), 5003-5006.
10. Cao, K.; Tan, S. M.; Lee, R.; Yang, S.; Jia, H.; Zhao, X.; Qiao, B.; Jiang, Z., Catalytic Enantioselective Addition of Prochiral Radicals to Vinylpyridines. *J. Am. Chem. Soc.* **2019**, *141* (13), 5437-5443.
11. Qi, L.; Chen, Y., Polarity-Reversed Allylations of Aldehydes, Ketones, and Imines Enabled by Hantzsch Ester in Photoredox Catalysis. *Angew. Chem. Int. Ed.* **2016**, *55* (42), 13312-13315.
12. Seo, H.; Jamison, T. F., Catalytic Generation and Use of Ketyl Radical from Unactivated Aliphatic Carbonyl Compounds. *Org. Lett.* **2019**, *21* (24), 10159-10163.
13. Nakajima, M.; Fava, E.; Loescher, S.; Jiang, Z.; Rueping, M., Photoredox-Catalyzed Reductive Coupling of Aldehydes, Ketones, and Imines with Visible Light. *Angew. Chem. Int. Ed.* **2015**, *54* (30), 8828-8832.
14. Koshland, D. E., Application of a Theory of Enzyme Specificity to Protein Synthesis\*. *Proceedings of the National Academy of Sciences* **1958**, *44* (2), 98-104.
15. Sullivan, S. M.; Holyoak, T., Enzymes with lid-gated active sites must operate by an induced fit mechanism instead of conformational selection. *Proceedings of the National Academy of Sciences* **2008**, *105* (37), 13829-13834.
16. Das, S.; Incarvito, C. D.; Crabtree, R. H.; Brudvig, G. W., Molecular Recognition in the Selective Oxygenation of Saturated C-H Bonds by a Dimanganese Catalyst. *Science* **2006**, *312* (5782), 1941-1943.
17. Engle, K. M.; Mei, T.-S.; Wasa, M.; Yu, J.-Q., Weak Coordination as a Powerful Means for Developing Broadly Useful C-H Functionalization Reactions. *Acc. Chem. Res.* **2012**, *45* (6), 788-802.
18. Quan, Y.; Lan, G.; Fan, Y.; Shi, W.; You, E.; Lin, W., Metal-Organic Layers for Synergistic Lewis Acid and Photoredox Catalysis. *J. Am. Chem. Soc.* **2020**, *142* (4), 1746-1751.
19. Trummel, A.; Lipping, L.; Kaljurand, I.; Koppel, I. A.; Leito, I., Acidity of Strong Acids in Water and Dimethyl Sulfoxide. *The Journal of Physical Chemistry A* **2016**, *120* (20), 3663-3669.
20. Guthrie, J. P., Hydrolysis of esters of oxy acids: pKa values for strong acids; Brønsted relationship for attack of water at methyl; free energies of hydrolysis of esters of oxy acids; and a



linear relationship between free energy of hydrolysis and pKa holding over a range of 20 pK units. *Can. J. Chem.* **1978**, *56* (17), 2342-2354.

21. American Chemistry Society, Division of Organic Chemistry. A pKa values in DMSO compilation (by Reich and Bordwell). American Chemical Society, 2021 [https://organicchemistrydata.org/hansreich/resources/pka/pka\\_data/pka-compilation-reich-bordwell.pdf](https://organicchemistrydata.org/hansreich/resources/pka/pka_data/pka-compilation-reich-bordwell.pdf) (accessed 2021-06-02).

22. Ji, P.; Drake, T.; Murakami, A.; Oliveres, P.; Skone, J. H.; Lin, W., Tuning Lewis Acidity of Metal–Organic Frameworks via Perfluorination of Bridging Ligands: Spectroscopic, Theoretical, and Catalytic Studies. *J. Am. Chem. Soc.* **2018**, *140* (33), 10553-10561.

23. Vermoortele, F.; Vandichel, M.; Van de Voorde, B.; Ameloot, R.; Waroquier, M.; Van Speybroeck, V.; De Vos, D. E., Electronic Effects of Linker Substitution on Lewis Acid Catalysis with Metal–Organic Frameworks. *Angew. Chem. Int. Ed.* **2012**, *51* (20), 4887-4890.

24. Coblenz Society, Inc., ‘Evaluated Infrared Reference Spectra’ in NIST Chemistry Webbook, NIST Standard Reference Database Number 69; National Institute of Standards and Technology, <https://webbook.nist.gov/cgi/cbook.cgi?ID=C141322&Type=IR-SPEC&Index=1#IR-SPEC> (retrieved June 8, 2021).

25. Hanson, C. S.; Psaltakis, M. C.; Cortes, J. J.; Siddiqi, S. S.; Devery, J. J., III, Investigation of Lewis Acid-Carbonyl Solution Interactions via Infrared-Monitored Titration. *J. Org. Chem.* **2020**, *85* (2), 820-832.

26. Zhu, Y.-Y.; Lan, G.; Fan, Y.; Veroneau, S. S.; Song, Y.; Micheroni, D.; Lin, W., Merging Photoredox and Organometallic Catalysts in a Metal–Organic Framework Significantly Boosts Photocatalytic Activities. *Angew. Chem. Int. Ed.* **2018**, *57* (43), 14090-14094.

27. Borowiecki, P.; Telatycka, N.; Tataruch, M.; Źądło-Dobrowolska, A.; Reiter, T.; Schühle, K.; Heider, J.; Szaleniec, M.; Kroutil, W., Biocatalytic Asymmetric Reduction of  $\gamma$ -Keto Esters to Access Optically Active  $\gamma$ -Aryl- $\gamma$ -butyrolactones. *Advanced Synthesis & Catalysis* **2020**, *362* (10), 2012-2029.

# Chapter 3. Site Isolation in Metal-Organic Layers Enhances Photoredox Gold Catalysis

## 3.1 Introduction

Gold catalysts are widely used in various transformations of C-C multiple bonds, including hydrofunctionalization and difunctionalization of alkenes, alkynes, and allenes.<sup>1-3</sup> In these reactions, Au complexes serve as soft  $\pi$ -Lewis acids to activate unsaturated C-C bonds for nucleophilic additions. Au complexes can also catalyze cross-coupling reactions in the presence of strong oxidants.<sup>4</sup> In 2013, Glorius and coworkers merged photoredox catalysis with Au catalysis to mediate the Au(I)/Au(III) cycle for oxy- and aminoarylation of alkenes.<sup>5</sup> Photoredox Au catalysis has provided powerful methods for the difunctionalization of  $\pi$ -systems.<sup>6-9</sup>

Despite their synthetic utility, homogeneous Au-catalyzed reactions typically require high catalyst loadings (1-10 mol%) due to relatively low reactivity of Au complexes and rapid catalyst deactivation.<sup>10-11</sup> Hammond, Xu, and coworkers proposed the deactivation of Au catalysts via a ligand redistribution to form bis(phosphine)-Au(I) and non-coordinated Au(I) compounds, followed by disproportionation of non-coordinated Au(I) compounds to Au(III) species and catalytically-inactive Au(0) nanoparticles.<sup>11, 12</sup> The (aryl)(phosphine)gold intermediate can also undergo aryl-phosphine reductive elimination to deactivate gold catalysts.<sup>13</sup> While there are many applications of Au catalysis in the fields of total synthesis<sup>14-15</sup> and materials science,<sup>16-18</sup> these catalyst deactivation pathways present a hurdle to its application in industry.

MOFs have provided a versatile platform for studying single-site catalysis.<sup>19-27</sup> Incorporation of metal catalysts into MOFs creates site-isolated metal centers that periodically decorate MOF ligands or SBUs, which prevents catalyst deactivation via disproportionation

pathways.<sup>28</sup> Au(I) centers were previously incorporated into a phosphine-containing MOF for the hydroaddition of 4-pentyn-1-ol.<sup>21</sup>

Although MOFs can be functionalized to afford single-site catalysts,<sup>19,29-31</sup> it is challenging to hierarchically incorporate multiple distinct active sites into MOFs.<sup>32-38</sup> The development of two-dimensional MOLs allows incorporation of multiple active sites for tandem and photoredox catalysis.<sup>39-42</sup> Unlike MOFs, MOLs have completely accessible and modifiable ligands and SBUs to allow hierarchical integration of distinct active sites. The proximity between different active sites in MOLs further enhances their catalytic efficiency. We hypothesized that MOLs could hierarchically integrate photosensitizers and Au catalysts to not only prevent Au catalyst deactivation but also enhance photoredox catalytic activities with proximately placed photosensitizers and Au(I) complexes (**Figure 3-1**).

In this chapter, we synthesized a new Hf-Ru-Au MOL containing Ru((BPY)(bpy)<sub>2</sub>)<sup>2+</sup> (BPY = 4',6'-dibenzoato-[2,2'-bipyridine]-4-carboxylate, bpy = bipyridine) photosensitizers (Ru-PSs) and (phosphine)-AuCl complexes for photoredox catalysis. Hf-BPY MOL was first built from Hf<sub>6</sub> SBUs and BPY bridging ligands. Postsynthetic modification of Hf<sub>6</sub>-BPY allowed the installation of Ru-PSs on BPY ligands and (4-(diphenylphosphino)phenyl acetic acid)-Au(I) chloride (**P**-AuCl) on Hf<sub>6</sub> SBUs to afford Hf-Ru-Au, which showed 14- to 200-fold higher catalytic activities over homogeneous controls in cross-coupling reactions of allenates, alkenes, or alkynes with aryldiazonium salts to afford furanone, tetrahydrofuran, or aryl alkyne derivatives, respectively.

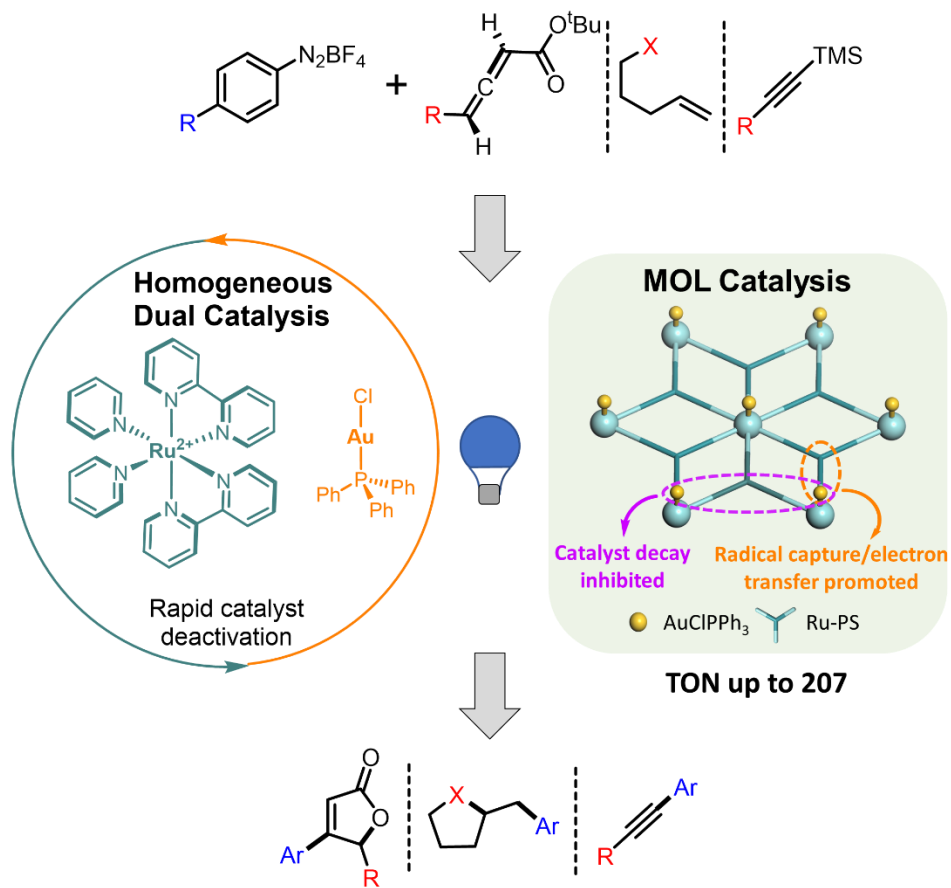


**Figure 3-1.** Dual photoredox and gold-catalyzed cross-coupling reactions.

## 3.2 Results and Discussion

### 3.2.1 Synthesis and Characterization of Hf-Ru-Au

The synthesis of Hf-Ru-Au started from a solvothermal reaction of HfCl<sub>4</sub> and H<sub>3</sub>BPY in dimethylformamide with formic acid and water at 120 °C to afford the known Hf-BPY MOL with a formula of Hf<sub>6</sub>(μ<sub>3</sub>-O)<sub>4</sub>(μ<sub>3</sub>-OH)<sub>4</sub>(BPY)<sub>2</sub>(HCO<sub>2</sub>)<sub>6</sub> (**Figure 3-2**).<sup>43</sup> Hf-BPY was treated with Ru(bpy)<sub>2</sub>Cl<sub>2</sub> at 80 °C for two days to yield Hf-Ru MOL by partially metalating bipyridine sites in Hf-BPY. Subsequent reaction of Hf-Ru with **P**-AuCl in acetonitrile at 60 °C afforded Hf-Ru-Au by partially replacing formate capping groups on Hf<sub>6</sub> SBU in Hf-Ru with **P**-AuCl (**Figure 3-2**).

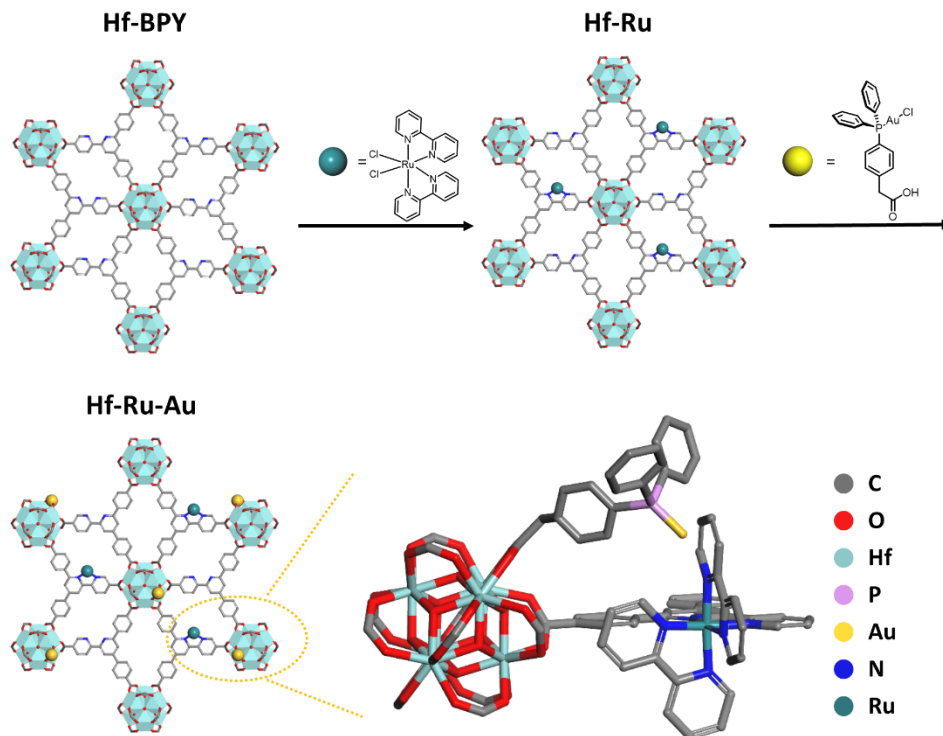


**Figure 3-2.** Schematic showing the synthesis of Hf-Ru-Au.

ICP-MS measurements showed a Hf:Ru:Au molar ratio of 6 : 0.32 : 0.50 for Hf-Ru-Au. Extended X-ray absorption fine structure (EXAFS) analysis revealed that Hf-Ru-Au had a similar Au(I) coordination environment to  $(\text{PPh}_3)\text{AuCl}$  with Au-P and Au-Cl distances of 2.31 and 2.22 Å, respectively (**Figure 3-3**). The UV-vis spectrum of Hf-Ru-Au showed additional peaks at 350 nm and 460 nm over Hf-BPY (**Figure 3-3**), confirming the installation of Ru-PSs.  $^1\text{H}$  and  $^{31}\text{P}$  NMR spectra of digested Hf-Ru-Au showed signals of BPY, Ru-PS, and P-AuCl (**Figure 3-4, 3-5**). These results support the successful integration of Ru-PSs and Au catalysts into Hf-Ru-Au with an empirical formula of  $\text{Hf}_6(\mu_3\text{-O})_4(\mu_3\text{-OH})_4(\text{BPY})_{1.68}(\text{Ru}(\text{bpy})_2\text{BPY})_{0.32}(\text{HCO}_2)_{5.5}(\text{P-AuCl})_{0.5}$ .

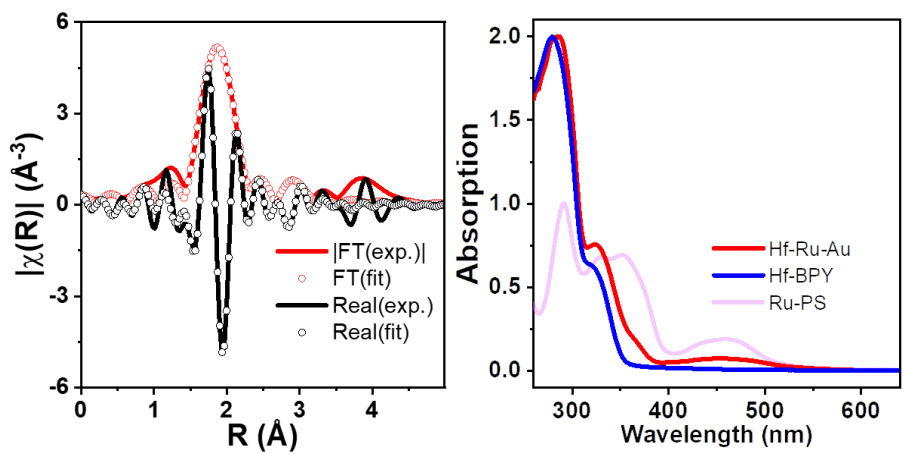


**Figure 3-3.** EXAFS fitting (left) and UV-vis analysis (right) of Hf-Ru-Au.

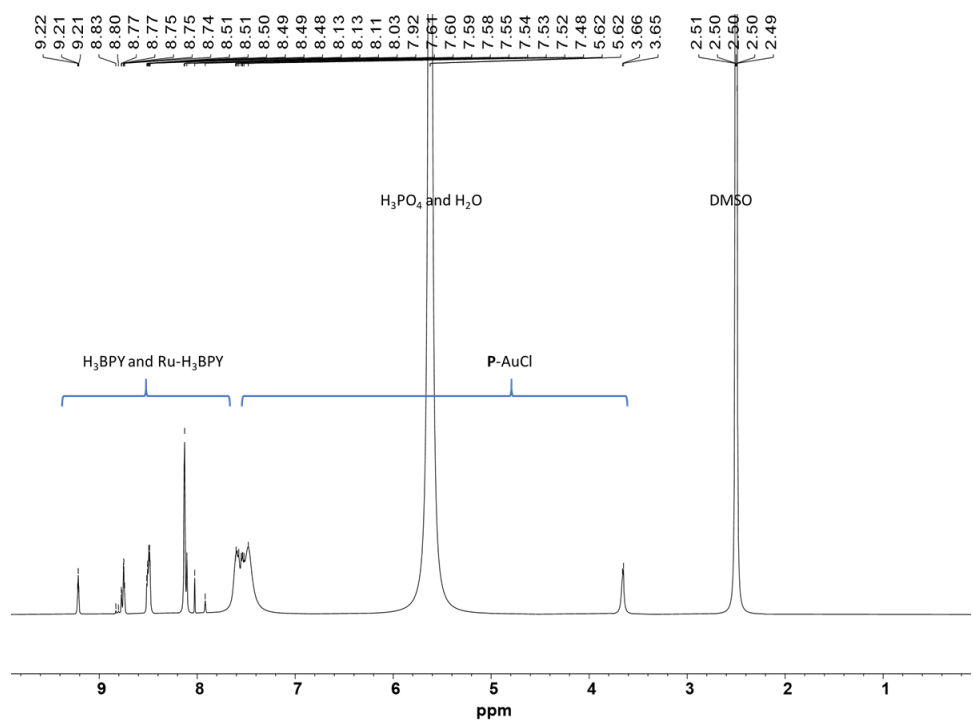


**Figure 3-4.**  $^1\text{H}$  NMR spectrum of digested Hf-Ru-Au in  $\text{DMSO-d}_6$ .

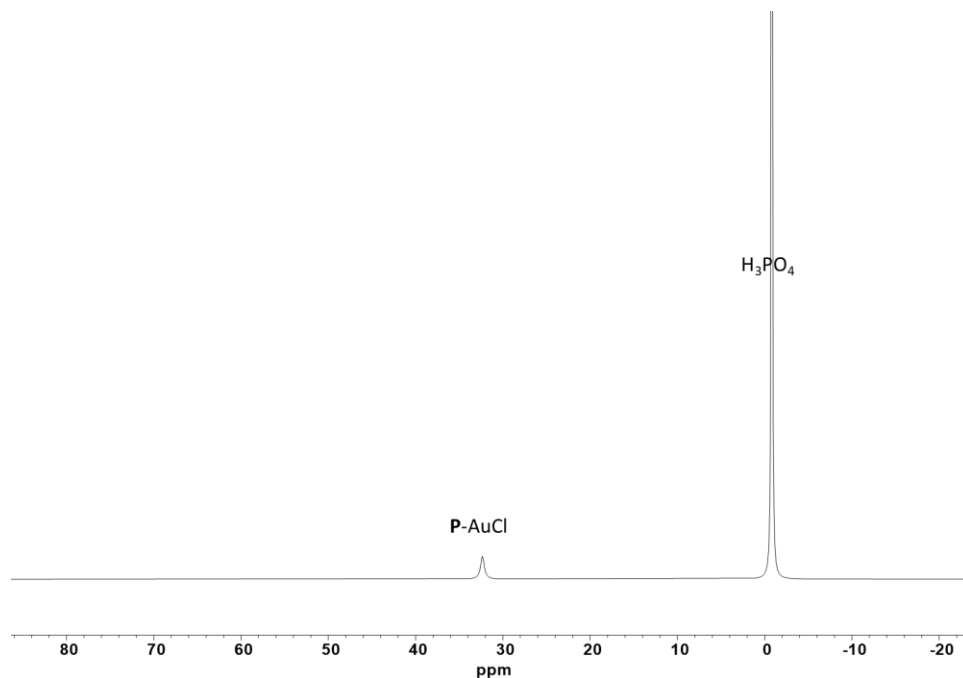


**Figure 3-5.**  $^{31}\text{P}$  NMR spectrum of digested Hf-Ru-Au in  $\text{DMSO-}d_6$ .

TEM showed a similar ruffled nanosheet morphology for Hf-BPY, Hf-Ru, and Hf-Ru-Au (**Figure 3-6a**). High-resolution TEM (HRTEM) image of Hf-Ru-Au revealed a regular lattice structure with its fast Fourier Transform (FFT) showing a hexagonal symmetry corresponding to the 2D MOL structure (**Figure 3-6b**). The thickness of Hf-Ru-Au nanosheets was measured to be 1.5 nm by AFM, corresponding to the height of a modified Hf<sub>6</sub> cluster (**Figure 3-6c**).<sup>42</sup> Hf-BPY, Hf-Ru, and Hf-Ru-Au showed similar PXRD patterns that matched the simulated pattern of Hf-BPY (**Figure 3-6d**). These results indicated that Hf-Ru-Au retained the structure of Hf-BPY after post-synthetic modifications. In Hf-Ru-Au, 8% of formate groups were replaced by P-AuCl and 16% of BPY ligands were metalated with Ru(bpy)<sub>2</sub>Cl<sub>2</sub>.

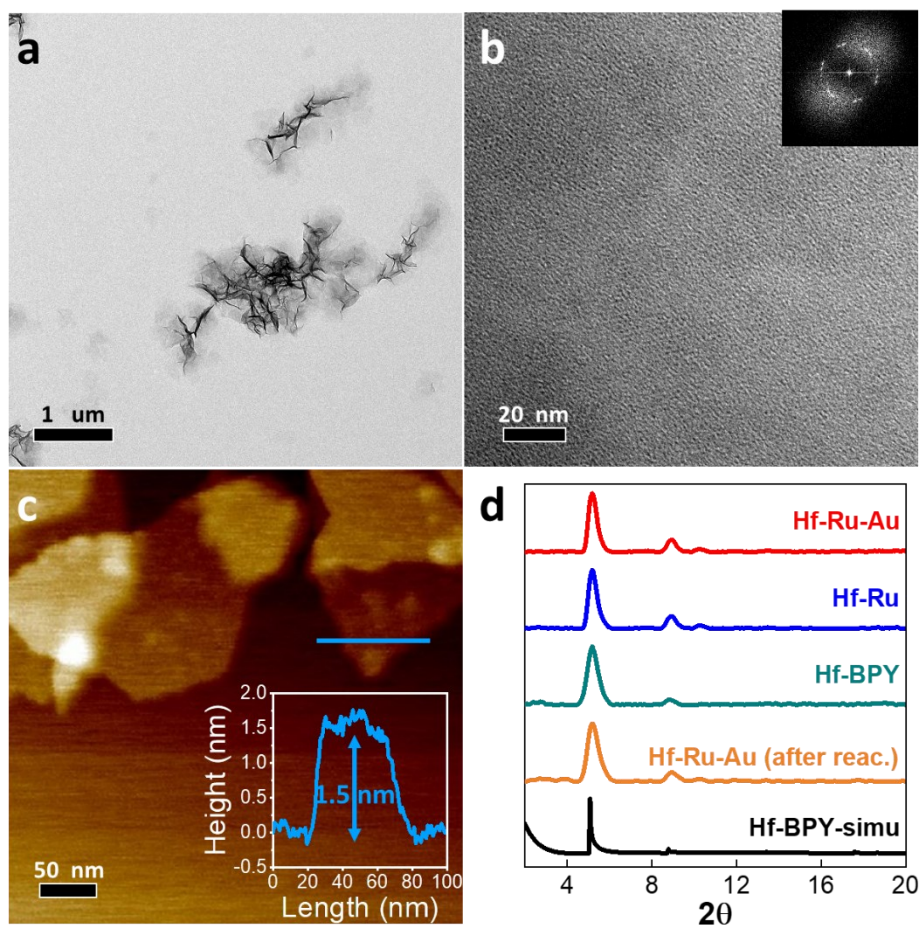


**Figure 3-6.** Morphology and structure of Hf-Ru-Au. (a) TEM image, (b) HRTEM image (FFT pattern in the inset), (c) AFM image (height profile in the inset) of Hf-Ru-Au. (d) PXRD patterns of Hf-Ru-Au, Hf-Ru, Hf-BPY, Hf-Ru-Au after a catalytic reaction, and simulated PXRD pattern of Hf-BPY.

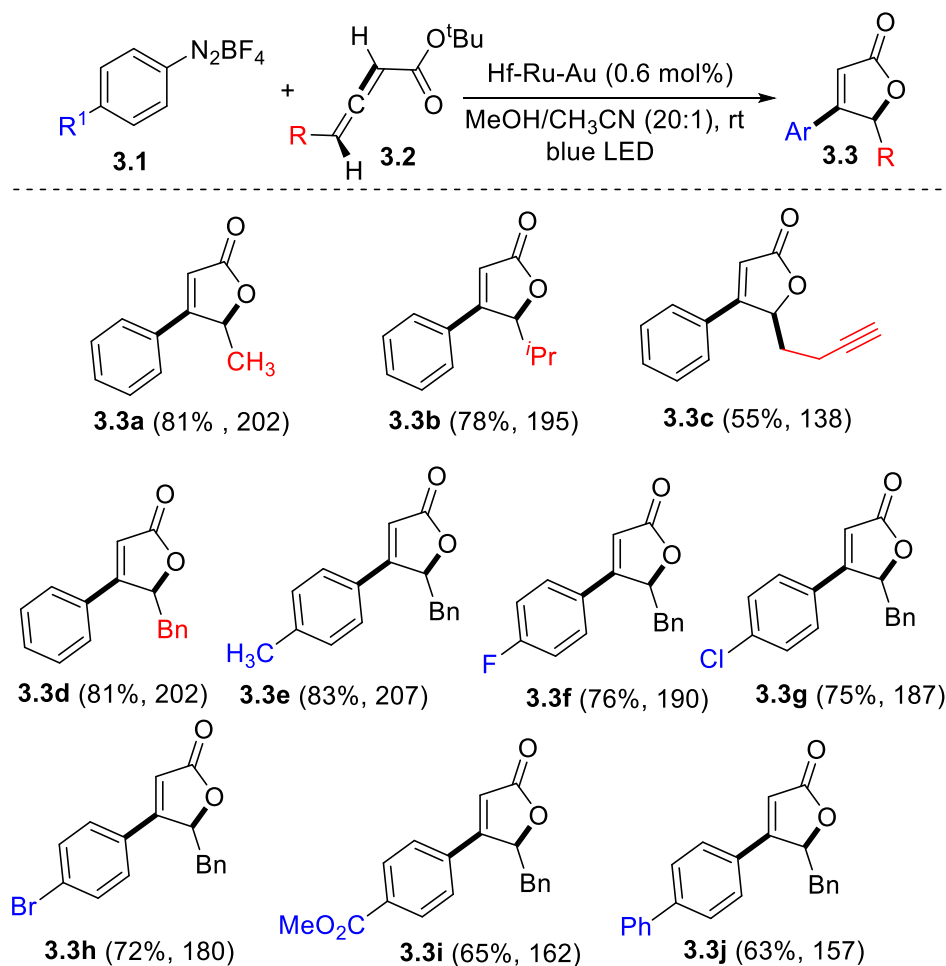
### 3.2.2 Cross-Coupling Reactions of Unsaturated Carbon-Carbon Bonds

With installed Ru-PSs and Au catalysts, Hf-Ru-Au competently mediated dual photoredox and Au catalysis. The photocatalytic performance of Hf-Ru-Au was evaluated in three important cross-coupling reactions, including cross-coupling of allenates, alkenes, and alkynes with aryldiazonium salts under mild conditions (visible light and room temperature).<sup>3-4,7-8, 44-45</sup>



As shown in **Table 3-1**, 0.6 mol% Hf-Ru-Au efficiently catalyzed the cross-coupling of allenates with aryldiazonium salts to afford furanone derivatives. Substituents on allenates (**2**), such as methyl (**3.2a**), isopropyl (**3.2b**), and benzyl (**3.2d**) groups were tolerated in the reactions to furnish the corresponding products **3.3a**, **3.3b**, and **3.3d** in 78-81% yields. Homopropargyl allenate (**3.2c**) also reacted with phenyldiazonium salt (**3.1a**) to afford **3.3c** in 55% yield. Both electron-donating (**3.1b**) and electron-withdrawing (**3.1c-3.1f**) substituents on aryldiazonium salts were tolerated in these reactions to form **3.3e-3.3h** in 65-83% yields.

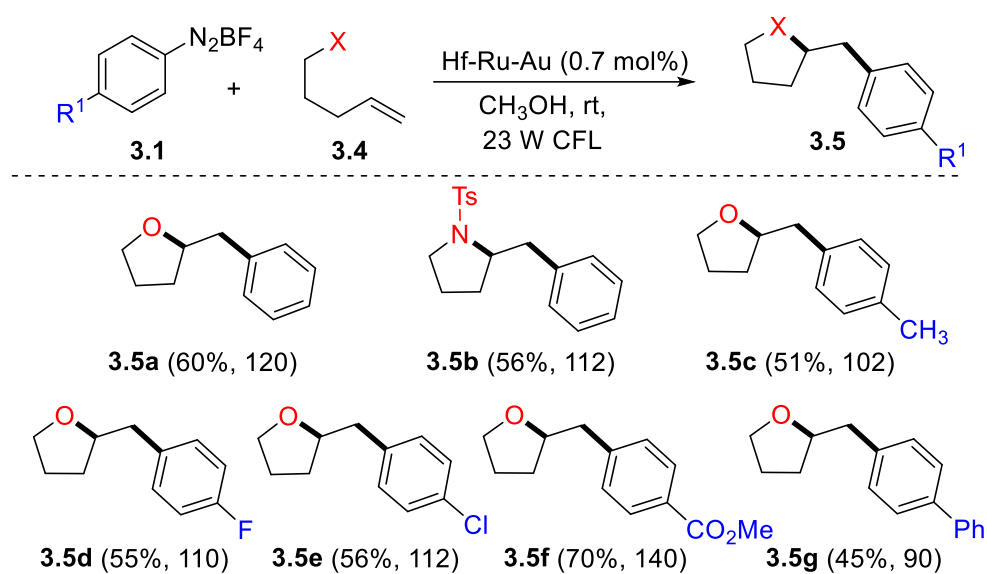
**Table 3-1.** Hf-Ru-Au-catalyzed cross-coupling of allenates with aryldiazonium salts.



Standard condition: **3.2** (0.2 mmol), **3.1** (0.8 mmol), and Hf-Ru-Au (0.6 mol %) in CH<sub>3</sub>OH/CH<sub>3</sub>CN.

Hf-Ru-Au at a 0.7 mol% catalyst loading catalyzed intermolecular oxy- and aminoarylation of alkenes and aryldiazonium salts to produce tetrahydrofuran and pyrrolidine derivatives (**Table 3-2**). Homoallylic alcohol (**3.4a**) and sulfonamide (**3.4b**) reacted with **3.1a** to afford tetrahydrofuran product **3.5a** and pyrrolidine product **3.5b** in 60% and 55% yields, respectively. The oxyarylation process worked with a diverse range of substituted aryldiazonium salts **3.1b-3.1g** to yield the corresponding tetrahydrofuran derivatives **3.5c-3.5g** in 45%-70% isolated yields. Aryldiazonium salts bearing electron-withdrawing substituents (**3.1c-3.1e**) had higher yields than those with electron-donating groups (**3.1b** and **3.1f**).

**Table 3-2.** Hf-Ru-Au-catalyzed cross-coupling of alkenes with aryldiazonium salts.

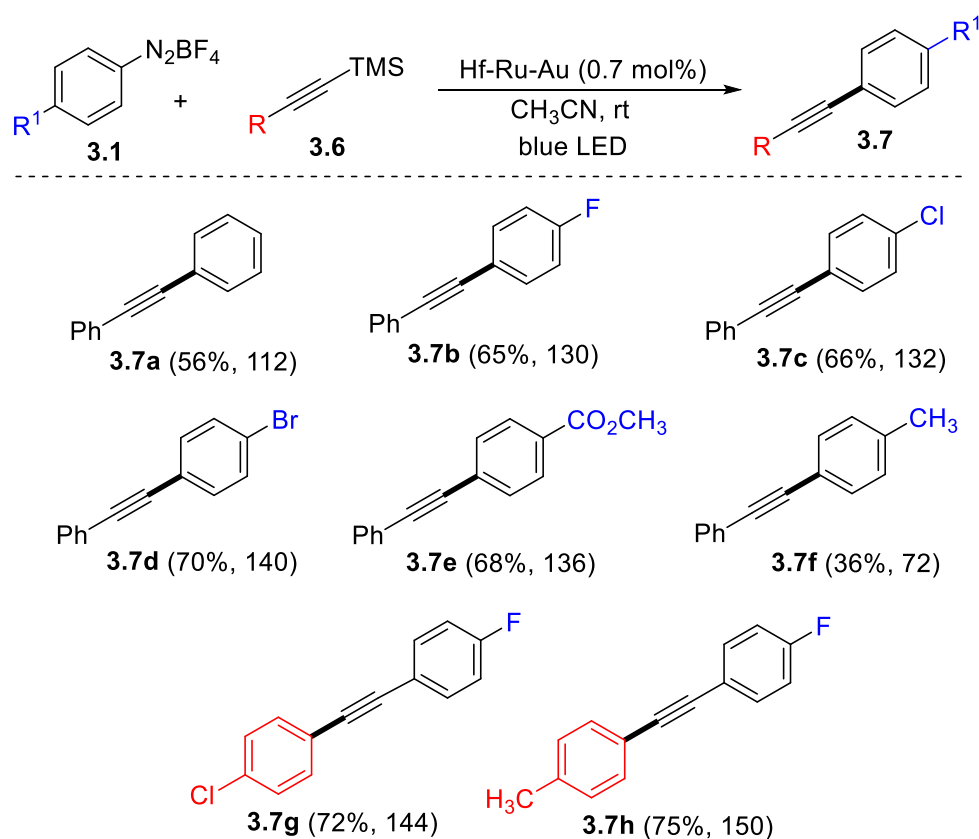


Standard condition: **3.4** (0.2 mmol), **3.1** (0.8 mmol), and Hf-Ru-Au (0.7 mol %) in CH<sub>3</sub>OH.

Hf-Ru-Au at a 0.7 mol % catalyst loading also catalyzed cross-coupling of aryldiazonium salts (**3.1**) and arylethynylsilanes (**3.6**, **Table 3-3**). Aryldiazonium salts with various substituents (**3.1a-3.1f**) reacted with **3.6a** to furnish aryl alkynes **3.7a-3.7f** in 36-70% yields. Electron-rich aryldiazonium **3.1b** gave a lower yield than electron-poor aryldiazoniums **3.1c-3.1f**, likely due to

the competitive generation of aryl cations through loss of dinitrogen in **3.1b**. Arylethynylsilanes with both electron-withdrawing 4-chloro (**3.6b**) and electron-donating 4-methyl (**3.6c**) substituents reacted with **3.1c** to afford **3.7g** and **3.7h** in 72% and 75% yields, respectively. It is worth noting that the coupling reaction tolerates aryldiazonium salts and arylethynylsilanes with halogen substituents which allow for further functionalization.

**Table 3-3.** Hf-Ru-Au-catalyzed cross-coupling of alkynes with aryldiazonium salts.



Standard condition: **3.6** (0.2 mmol), **3.1** (0.4 mmol) and Hf-Ru-Au (0.7 mol%) in CH<sub>3</sub>CN.

### 3.2.3 Mechanistic Studies

We performed several control reactions to reveal the mechanism of Hf-Ru-Au catalyzed cross-coupling reactions. With alkyne **3.6a** as substrate, a homogeneous mixture of Ru-PS and P-AuCl in a 1:1.5 molar ratio afforded cross-coupled products in low yields (**Table 3-4**, entry 2).

Seven-fold higher **P**-AuCl and 2-fold higher Ru-PS were needed to afford the cross-coupled product in a comparable yield as Hf-Ru-Au (**Table 3-4**, entry 3), suggesting that Hf-Ru-Au is approximately 14 times more active than the homogeneous control. When allenolate **3.2d** or alkene **3.4a** was used as substrate, Hf-Ru-Au showed 200- or 140-fold higher activity, respectively, than the corresponding homogeneous control. MOLs loaded with Ru-PS only (Hf-Ru) or **P**-AuCl only (Hf-Au) afforded the cross-coupling product **3.7b** in trace or 14% yields (**Table 3-4**, entry 4 and 5), which could come from a radical chain process.<sup>46</sup> Hf-Ru-Au failed to catalyze the reaction in the absence of light irradiation (**Table 3-4**, entry 6). These results indicate the photoredox nature of the reaction and its dependence on the cooperativity between Ru-PS and **P**-AuCl.

**Table 3-4.** Control experiments for Hf-Ru-Au catalyzed cross-coupling reactions.

Entry	Catalyst(s) <sup>b</sup>	Yield ( <b>3.7b</b> )
1	0.7 mol% Hf-Ru-Au	65%
2	0.5 mol% Ru-PS, 0.7 mol% <b>P</b> -AuCl	8%
3	1 mol% Ru-PS, 5 mol% <b>P</b> -AuCl	68%
4 <sup>b</sup>	0.5 mol% Hf-Ru	0
5	1 mol% Hf-Au	14
6 <sup>c</sup>	0.7 mol% Hf-Ru-Au	0

<sup>a</sup>Reactions were performed with **3.6a** (0.2 mmol), **3.1c** (0.4 mmol) and the catalyst loadings were based on Au. <sup>b</sup>Catalyst loading was based on Ru. <sup>c</sup>Without blue LED irradiation.

Hf-Ru-Au catalyzed all three cross-coupling reactions with very low catalyst loadings of 0.6-0.7 mol %. In contrast, homogeneous methods typically required 5-10 mol% Au catalysts.<sup>3-4,7-8, 44-45</sup> We attributed this large difference in catalytic activity to two factors: the proximity between

Ru-PSs and Au catalysts (with the shortest distance of 0.7 nm, **Figure 3-2**) which facilitates the transfer of electron and radical intermediates<sup>39</sup>, and the isolation of Au catalysts which prevent their deactivation via ligand redistribution, Au(I) disproportionation, and aryl-phosphine reductive elimination.

To understand the effect of Au(I) site isolation on the catalytic reactions, we examined the reaction mixtures of **3.1c** and **3.6a** with Hf-Ru-Au or homogeneous catalysts at 12 h by <sup>31</sup>P NMR. The <sup>31</sup>P NMR spectra of **P**-AuCl and digested Hf-Ru-Au (0 h) were collected for comparison (**Figure 3-7**). The **P**-AuCl complex in Hf-Ru-Au remained unchanged with a peak at  $\delta$ 32.6 throughout the photocatalytic reaction. PXRD studies demonstrated the structural stability of Hf-Ru-Au MOL during the reaction (**Figure 3-6**). When higher loadings of homogeneous catalysts were used to afford cross-coupled products in reasonable yields, we observed complete disappearance of **P**-AuCl and the formation of the phenyl-phosphonium salt with a <sup>31</sup>P NMR peak at  $\delta$  22.9 and a characteristic high-resolution MS peak for [**P**<sub>2</sub>-Au]<sup>+</sup>. We believe that the phenyl-phosphonium salt likely results from reductive elimination from the putative **P**<sub>2</sub>-Au-aryl intermediate (**Figure 3-8**).<sup>10, 47-48</sup>

In support of this hypothesis, a mixture of Ru-PS and **P**<sub>2</sub>-AuCl competently catalyzed cross-coupling of **3.1c** and **3.6a** to afford **3.7b** in a comparable yield to the reaction catalyzed by Ru-PS and **P**-AuCl. Neither **P**<sub>2</sub>-Au complex nor phenyl-phosphonium salt was observed during the Hf-Ru-Au catalyzed reactions. We believe that the isolation of Au(I) sites in Hf-Ru-Au shuts down the ligand redistribution and Au(I) disproportionation pathway as well as preventing the formation of the **P**<sub>2</sub>-Au-aryl intermediate and hence the phenyl-phosphonium byproduct (**Figure 3-8**). Consequently, the catalytic activity of Hf-Ru-Au was maintained throughout the reactions, which was further demonstrated by recovery and reuse of Hf-Ru-Au in three runs of cross-coupling

between **3.1c** and **3.6a**, with no decrease in catalytic activity. Leaching of Hf, Ru, and Au in the first cycle was determined by ICP-MS to be <0.5%, <0.5% and <1.6%, respectively.

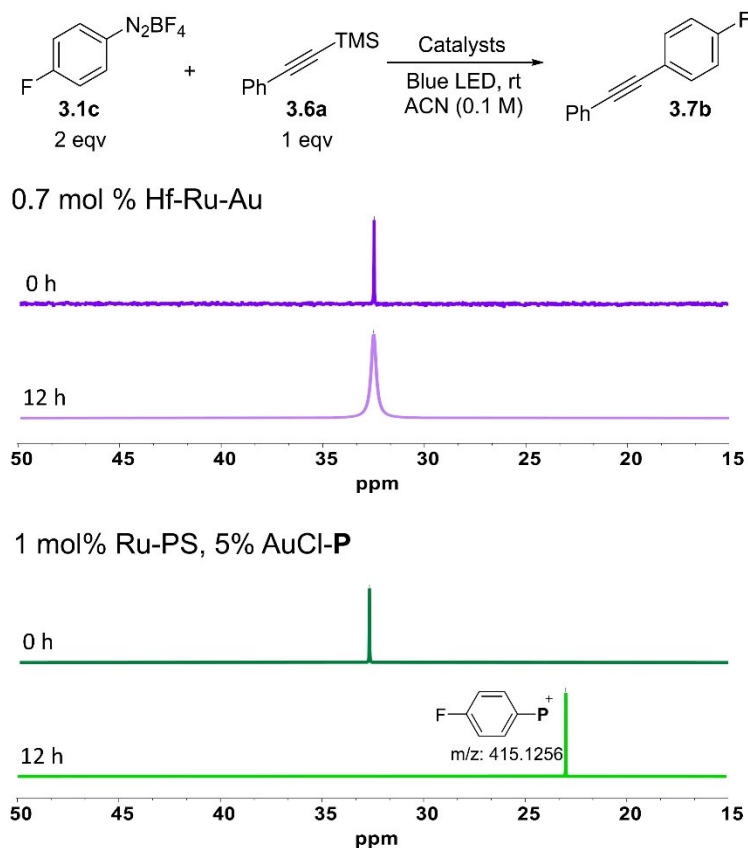


**Figure 3-7.** <sup>31</sup>P NMR study of cross-coupling reaction between **3.1c** and **3.6a**.

Based on these results and literature precedents,<sup>6, 10, 49-53</sup> we propose a plausible mechanism for Hf-Ru-Au catalyzed cross-coupling in **Figure 3-8**. Aryldiazonium salt **3.1c** is reduced by excited Ru-PS or partially initiated by a visible light-mediated radical chain process to generate an aryl radical, which adds to **P**-AuCl and forms an Au(II)-aryl complex. The Au(II) complex is oxidized by [Ru-PS]<sup>+</sup> to Au(III). After coordination of Au(III) with alkyne **3.6a** and tetrafluoroborate-assisted desilylation, reductive elimination of the Au(III)-(aryl)(alkynyl) intermediate afforded product **3.7b** and regenerated the **P**-AuCl catalyst. Due to site isolation of

**P-AuCl** species and synergistic effect between Ru-PS and **P-AuCl**, Hf-Ru-Au effectively shuts down the side reaction pathway and enhances catalytic activity by 14-200 times.

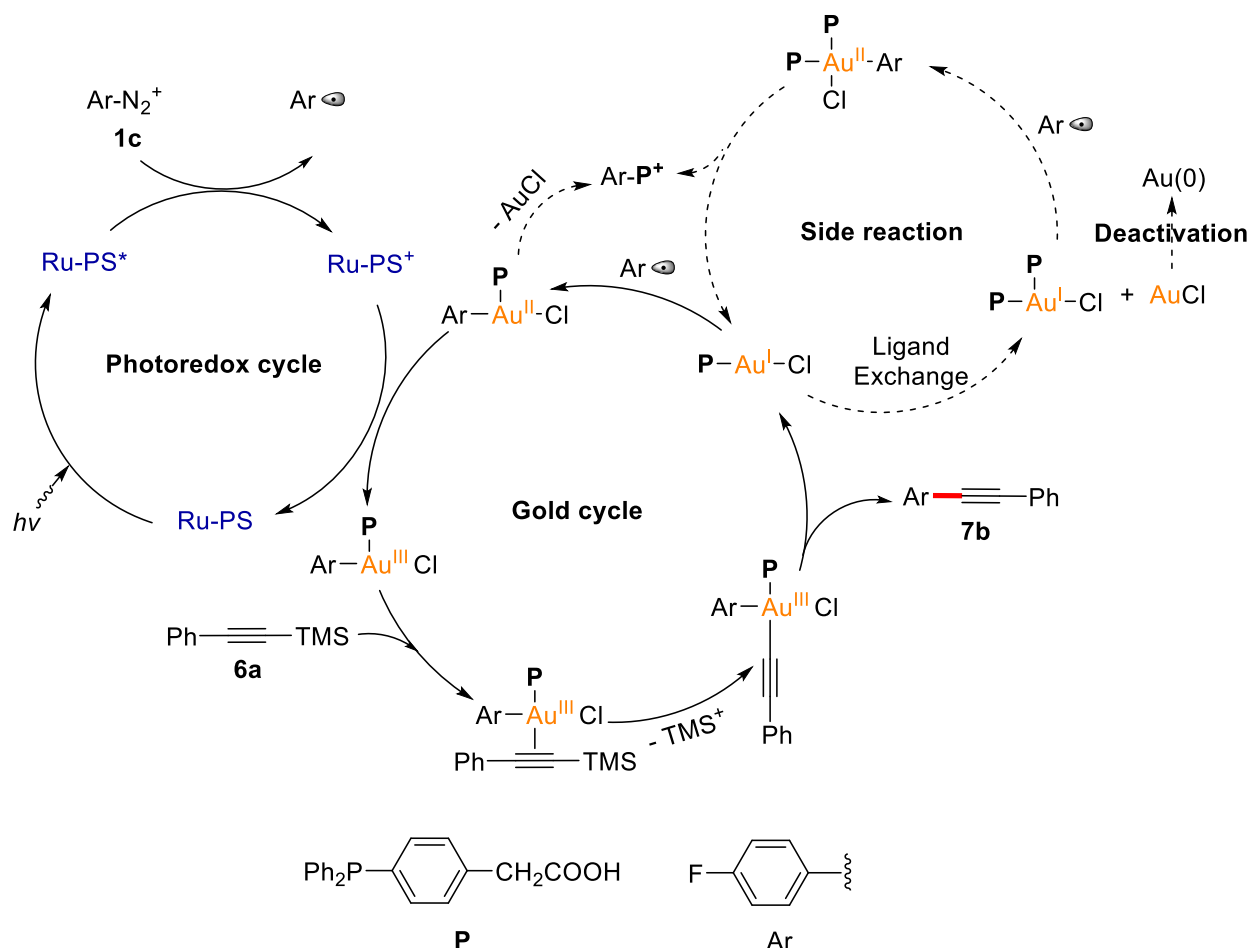


**Figure 3-8.** Proposed mechanism for Hf-Ru-Au catalyzed cross-coupling reaction.

### 3.3. Conclusion

In this chapter, we designed a new bifunctional MOL, Hf-Ru-Au, containing Ru(bpy)<sub>3</sub><sup>2+</sup>-type photosensitizer and **P-AuCl** catalyst. Hf-Ru-Au effectively catalyzed photoredox cross-coupling reactions alkenes, allenates, or alkynes with aryldiazonium salts to afford furanone, tetrahydrofuran, and aryl alkyne derivatives with turnover numbers of up to 207. Hf-Ru-Au

outperformed homogeneous controls by 14-200 times owing to site isolation of Au(I) and the proximity of Ru-PS and the Au catalyst. This work highlights the potential of MOLs as an excellent platform for developing synergistic photoredox catalysts with enhanced activities.

### 3.4. Methods

#### 3.4.1 Material synthesis

**Synthesis of 4-(Diphenylphosphino)phenylacetic acid (P).** **P** was synthesized according to the modified procedure.<sup>54</sup> 4-Iodophenylacetic acid (2.62g, 10 mmol, 1.0 equiv.), diphenylphosphine (1.86 g, 10 mmol, 1.0 equiv.), triethylamine (2.8 ml, 20 mol, 2.0 equiv.) and palladium(II) acetate (112 mg, 0.5 mol, 5 mol%) were dissolved in acetonitrile (50 ml) under argon, and heated to reflux for 4 h. The volatiles were evaporated under reduced pressure. The solid residue was purified by flash chromatography (hexane/ethyl acetate = 2/1) to give the desired product as a white solid. Yield: 82%. <sup>1</sup>H NMR (400 MHz, DMSO-*d*<sub>6</sub>): δ 12.40 (s, 1H), 7.43 – 7.36 (comp, 6H), 7.32 – 7.19 (comp, 8H), 3.60 (s, 2H); <sup>13</sup>C NMR (101 MHz, DMSO-*d*<sub>6</sub>): δ 172.9, 137.3, 137.2, 136.5, 135.1, 135.0, 133.9, 133.7, 133.7, 133.5, 130.4, 130.3, 129.4, 129.2, 129.2; <sup>31</sup>P{<sup>1</sup>H} NMR (162 MHz, DMSO-*d*<sub>6</sub>): δ -7.38. Characterization data matched that reported in the literature.

**Synthesis of 4-(Diphenylphosphino)phenylacetic Acid-Gold(I) Complex (P-AuCl).** A 25 mL round-bottomed flask was equipped with a magnetic stirring bar, and charged with **P** (320 mg, 1 mol, 1.0 equiv.) and chloro(dimethylsulfide)gold (295 mg, 1.00 mmol, 1.0 equiv). Dichloromethane (5 mL) was added via a syringe. The resulting colorless solution was stirred at room temperature for 10 min. The volatiles were removed by rotatory evaporation and dried under high vacuum for 24 h to afford **P-AuCl** (615 mg) as a white solid in a quantitative yield. <sup>1</sup>H NMR



(400 MHz, chloroform-*d*):  $\delta$  7.55 – 7.29 (comp, 14H), 3.64 (s, 2H);  $^{13}\text{C}$  NMR (101 MHz, chloroform-*d*):  $\delta$  174.42, 137.54, 137.52, 134.50, 134.36, 134.21, 134.08, 132.07, 132.05, 130.35, 130.23, 129.34, 129.22, 128.89, 128.27, 40.35;  $^{31}\text{P}\{^1\text{H}\}$  NMR (162 MHz, chloroform-*d*):  $\delta$  32.75; HRMS (ESI-TOF): calculated for  $[\text{M}+\text{NH}_4]^+$ ,  $\text{C}_{20}\text{H}_{21}\text{AuClNO}_2\text{P}$ ,  $m/z$ : 570.0664, observed: 570.0667.

**Synthesis of 4',6'-dibenzoato-[2,2'-bipyridine]-4-carboxylic acid (H<sub>3</sub>BPY).** H<sub>3</sub>BPY was synthesized according to the literature report.<sup>43</sup>  $^1\text{H}$  NMR (500 MHz, DMSO-*d*<sub>6</sub>):  $\delta$  12.23 (br, 3H), 9.24 (s, 1H), 8.79-8.76 (comp, 2H), 8.53-8.49 (comp, 4H), 8.18 - 8.11 (comp, 6H).

**Synthesis of Hf-BPY.**<sup>43</sup> To a 20 mL glass vial was added 2.5 mL of HfCl<sub>4</sub> solution (5.60 mg/mL in DMF) 2.5 mL of the H<sub>3</sub>BPY solution (5 mg/mL in DMF), 0.5 mL of formic acid, and 0.75 mL of water. The reaction mixture was kept in a 120 °C oven for 24 hours. The white precipitate was collected by centrifugation and washed with DMF and ethanol.

**Synthesis of Hf-Ru.** To a 7.5 mL dimethylformamide suspension of Hf-BPY MOL (48 mg) was added 55 mg Ru(bpy)<sub>2</sub>Cl<sub>2</sub>. The reaction mixture was stirred at 80 °C for 2 days. The red precipitate was collected by centrifugation and washed with DMF and ethanol.

**Synthesis of Hf-Ru-Au.** To a 3 mL acetonitrile suspension of Hf-BPY MOL (20 mg) was added 120 mg P-AuCl. The reaction mixture was stirred at 60 °C overnight. The red precipitate was collected by centrifugation and washed with acetonitrile and ethanol.

**ICP-MS analysis of Hf-Ru-Au.** To a mixture of 200  $\mu\text{L}$  HNO<sub>3</sub>, 200  $\mu\text{L}$  HCl, and 200  $\mu\text{L}$  HF was added 20  $\mu\text{L}$  Hf-Ru-Au dispersion (2 mM based on Hf). The mixture was sonicated for 10 mins and kept at room temperature overnight before subjecting to ICP-MS analysis. Based on ICP-MS results, the loadings of Ru and Au on the MOL were determined as 16 mol% based on BPY

and 50 mol% based on Hf<sub>6</sub> cluster. Hf-Ru-Au MOL was formulated as Hf<sub>6</sub>(μ<sub>3</sub>-O)<sub>4</sub>(μ<sub>3</sub>-OH)<sub>4</sub>(BPY)<sub>1.68</sub>(Ru(bpy)<sub>2</sub>BPY)<sub>0.32</sub>(HCO<sub>2</sub>)<sub>5.5</sub>(P-AuCl)<sub>0.5</sub>.

**NMR analysis of Hf-Ru-Au.** To 2 mg Hf-Ru-Au were added 600 μL DMSO-*d*<sub>6</sub>, 60 μL D<sub>3</sub>PO<sub>4</sub> and 60 μL D<sub>2</sub>O. The mixture was sonicated for 10 mins to obtain a clear solution and analyzed by <sup>1</sup>H NMR and <sup>31</sup>P NMR. <sup>1</sup>H NMR spectrum of the digested Hf-Ru-Au showed signals corresponding to H<sub>3</sub>BPY, Ru-PS and P-AuCl (**Figure 3-4**). <sup>31</sup>P NMR spectrum showed signals corresponding to P-AuCl (**Figure 3-5**).

**UV analysis of Hf-Ru-Au.** 10 μL of Hf-Ru-Au (or Hf-BPY, 2 mM based on Hf) was added to a mixture of 940 μL DMSO and 50 μL H<sub>3</sub>PO<sub>4</sub>. After sonicating for 10 min, a clear solution was obtained and subjected to UV analysis. The UV spectrum of Ru-PS was recorded from its solution in DMSO. The rise of peak at around 460 nm in UV of Hf-Ru-Au compared to Hf-BPY indicated the presence of the Ru(BPY)(bpy)<sub>2</sub> species in Hf-Ru-Au (**Figure 3-3**).

### 3.4.2 Catalytic Reactions

#### **General procedure for cross-coupling reactions between diazonium salts and allenes.**

Diazonium salt (0.8 mmol, 4.0 equiv.), allene (0.2 mmol, 1.0 equiv.), and Hf-Ru-Au (1.2 μmol based on Au, 0.6 mol%) were mixed in dry CH<sub>3</sub>OH/CH<sub>3</sub>CN (v/v = 20:1, 2 mL). The resulting solution was stirred under blue LED irradiation at room temperature in an N<sub>2</sub> atmosphere 12 h. After the reaction, the solvent was removed under vacuum. The residue was then subjected to column chromatography on silica gel using n-hexane and ethyl acetate as eluent to give the cross-coupling products **3.3a-3.3j**.

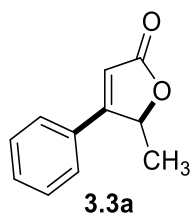
#### **General procedure for cross-coupling reactions between diazonium salts and alkenes.**

Diazonium salt (0.8 mmol, 4.0 equiv.), alkene (0.2 mmol, 1.0 equiv.), and Hf-Ru-Au (1.4 μmol based on Au, 0.7 mol%) were mixed in dry CH<sub>3</sub>OH (2 mL). The resulting solution was stirred

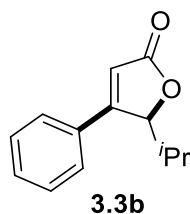
under CFL light irradiation at room temperature in an N<sub>2</sub> atmosphere 12 h. After the reaction, the solvent was removed under vacuum. The residue was then subjected to column chromatography on silica gel using n-hexane and ethyl acetate or DCM as eluent to give the cross-coupling products **3.5a-3.5g**.

**General procedure for cross-coupling reactions between diazonium salts and alkynes.**

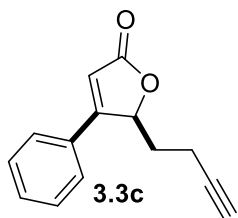
Diazonium salt (0.4 mmol, 2.0 equiv.), alkyne (0.2 mmol, 1.0 equiv.), and Hf-Ru-Au (1.4 μmol based on Au, 0.7 mol%) were mixed in dry CH<sub>3</sub>CN (2 mL). The resulting solution was stirred under blue LED irradiation at room temperature in an N<sub>2</sub> atmosphere 12 h. After the reaction, the solvent was removed under vacuum. The residue was then subjected to column chromatography on silica gel using n-hexane as eluent to give the cross-coupling products **3.7a-3.7h**.



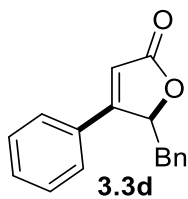
Colorless oil, 81% yield. <sup>1</sup>H NMR (400 MHz, chloroform-*d*): δ 7.50-7.46 (comp, 5H), 6.28 (s, 1H), 5.57 (q, *J* = 6.4 Hz, 1H), 1.54 (d, *J* = 6.4 Hz, 3H); <sup>13</sup>C NMR (101 MHz, chloroform-*d*): δ 172.6, 168.9, 131.3, 130.0, 129.2, 127.2, 113.8, 78.6, 19.8; Characterization data matched that reported in the literature.<sup>44</sup>



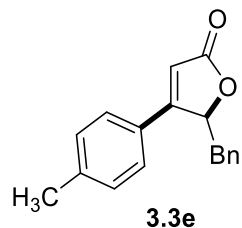
Colorless oil, 78% yield.  $^1\text{H NMR}$  (400 MHz, chloroform-*d*):  $\delta$  7.49-7.44 (comp, 5H), 6.27 (d,  $J$  = 1.6 Hz, 1H), 5.43 (t,  $J$  = 2.0 Hz, 1H), 2.22-2.12 (m, 1H), 1.23 (d,  $J$  = 6.8 Hz, 3H), 0.63 (d,  $J$  = 6.8 Hz, 3H);  $^{13}\text{C NMR}$  (101 MHz, chloroform-*d*):  $\delta$  173.2, 167.3, 131.2, 130.5, 129.2, 127.1, 115.1, 86.3, 30.7, 20.2, 13.4; **HRMS** (ESI-TOF): calculated  $m/z$  for  $[\text{M}+\text{H}]^+$  ( $\text{C}_{13}\text{H}_{15}\text{O}_2$ ), 203.1072; observed, 203.1069.



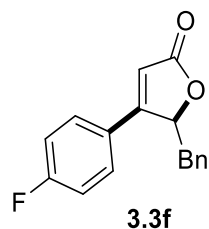
Colorless oil, 55% yield.  $^1\text{H NMR}$  (400 MHz, chloroform-*d*):  $\delta$  7.55-7.48 (comp, 5H), 6.32 (d,  $J$  = 1.6 Hz, 1H), 5.70 (d,  $J$  = 9.2 Hz, 1H), 2.58-2.49 (m, 1H), 2.46-2.36 (m, 1H), 2.28-2.20 (m, 1H), 2.01 (t,  $J$  = 3.0 Hz, 1H), 1.79-1.70 (m, 1H);  $^{13}\text{C NMR}$  (101 MHz, chloroform-*d*):  $\delta$  172.5, 167.3, 131.5, 129.8, 129.3, 127.2, 114.4, 82.5, 80.5, 70.0, 33.0, 15.0; **HRMS** (ESI-TOF): calculated  $m/z$  for  $[\text{M}+\text{H}]^+$  ( $\text{C}_{14}\text{H}_{13}\text{O}_2$ ), 213.0915; observed, 213.0911.



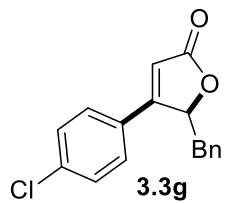
Colorless oil, 81% yield.  $^1\text{H NMR}$  (400 MHz, chloroform-*d*):  $\delta$  7.55-7.44 (comp, 5H), 7.23-7.19 (comp, 3H), 7.03-7.01 (m, 2H), 6.15 (s, 1H), 5.73-5.72 (m, 1H), 3.35 (dd,  $J$  = 14.8, 3.6 Hz, 1H), 2.95 (dd,  $J$  = 14.8, 6.4 Hz, 1H);  $^{13}\text{C NMR}$  (101 MHz, chloroform-*d*):  $\delta$  172.4, 166.7, 134.6, 131.4, 130.3, 129.6, 129.4, 128.3, 127.2, 127.1, 115.3, 82.0, 39.2; **HRMS** (ESI-TOF): calculated  $m/z$  for  $[\text{M}+\text{H}]^+$  ( $\text{C}_{17}\text{H}_{15}\text{O}_2$ ), 251.1072; observed, 251.1066.



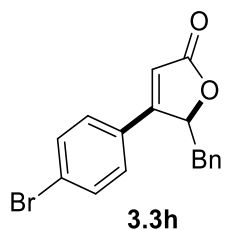
Colorless oil, 83% yield. **<sup>1</sup>H NMR** (400 MHz, chloroform-*d*):  $\delta$  7.36 (d,  $J = 8.0$  Hz, 2H), 7.31 (d,  $J = 8.0$  Hz, 2H), 7.23-7.17 (comp, 3H), 7.04-7.02 (comp, 2H), 6.10 (s, 1H), 5.72-5.09 (m, 1H), 3.35 (dd,  $J = 14.4, 3.6$  Hz, 1H), 2.94 (dd,  $J = 14.4, 6.4$  Hz, 1H), 2.44 (s, 3H); **<sup>13</sup>C NMR** (101 MHz, chloroform-*d*):  $\delta$  172.6, 166.6, 142.0, 134.7, 130.1, 129.6, 128.3, 127.5, 127.2, 127.1, 114.2, 81.9, 39.4, 21.6; **HRMS** (ESI-TOF): calculated  $m/z$  for  $[M+H]^+$  ( $C_{18}H_{17}O_2$ ), 265.1228; observed, 295.1225.



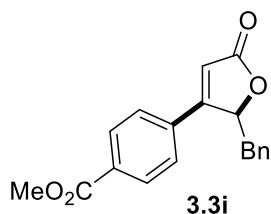
Colorless oil, 76% yield. **<sup>1</sup>H NMR** (400 MHz, chloroform-*d*):  $\delta$  7.48 – 7.38 (comp, 2H), 7.24 – 7.14 (comp, 5H), 7.03– 6.99 (comp, 2H), 6.10 (s, 1H), 5.71– 5.68 (m, 1H), 3.33 (dd,  $J = 14.4, 4.0$  Hz, 1H), 2.95 (dd,  $J = 14.4, 6.0$  Hz, 1H); **<sup>13</sup>C NMR** (101 MHz, chloroform-*d*):  $\delta$  172.15, 165.41, 164.34 (d,  $J = 254.4$  Hz, 1C), 134.34, 129.58, 129.34, 129.25, 128.34, 127.20, 126.59 (d,  $J = 3.5$  Hz, 1C), 116.77, 116.55, 115.14 (d,  $J = 21$  Hz, 1C), 81.82, 39.21; **<sup>19</sup>F NMR** (377 MHz, chloroform-*d*):  $\delta$  -107.37; **HRMS** (ESI-TOF): calculated  $m/z$  for  $[M+H]^+$  ( $C_{17}H_{14}FO_2$ ), 269.0977; observed, 269.0969.



Colorless oil, 75% yield. **<sup>1</sup>H NMR** (400 MHz, chloroform-*d*):  $\delta$  7.48 (d,  $J = 8.4$  Hz, 2H), 7.38 (d,  $J = 8.4$  Hz, 2H), 7.23-7.18 (comp, 3H), 7.02-6.97 (comp, 2H), 6.13 (s, 1H), 5.71-5.68 (m, 1H), 3.33 (dd,  $J = 14.4, 3.6$  Hz, 1H), 2.95 (dd,  $J = 14.4, 6.0$  Hz, 1H); **<sup>13</sup>C NMR** (101 MHz, chloroform-*d*):  $\delta$  172.0, 165.3, 137.5, 134.2, 129.7, 129.6, 128.8, 128.4, 128.4, 127.2, 115.8, 81.7, 39.1; **HRMS** (ESI-TOF): calculated  $m/z$  for  $[M+H]^+$  ( $C_{17}H_{14}ClO_2$ ), 285.0682; observed, 285.0673.

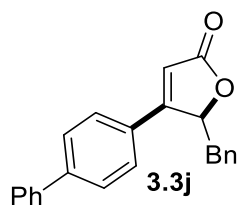


White solid, 72% yield. **<sup>1</sup>H NMR** (400 MHz, chloroform-*d*):  $\delta$  7.64 (d,  $J = 8.4$  Hz, 2H), 7.31 (d,  $J = 8.4$  Hz, 2H), 7.23-7.19 (comp, 3H), 7.02-6.98 (comp, 2H), 6.14 (s, 1H), 5.71-5.68 (m, 1H), 3.33 (dd,  $J = 14.4, 3.6$  Hz, 1H), 2.95 (dd,  $J = 14.4, 6.0$  Hz, 1H); **<sup>13</sup>C NMR** (101 MHz, chloroform-*d*):  $\delta$  172.0, 165.3, 134.2, 132.7, 129.6, 129.2, 128.6, 128.4, 127.2, 125.9, 115.9, 81.7, 39.1; **HRMS** (ESI-TOF): calculated  $m/z$  for  $[M+H]^+$  ( $C_{17}H_{14}BrO_2$ ), 329.0177; observed, 329.0165.

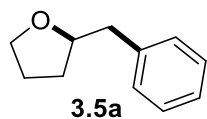


Colorless oil, 65% yield. **<sup>1</sup>H NMR** (400 MHz, chloroform-*d*):  $\delta$  8.18 (d,  $J = 8.4$  Hz, 2H), 7.53 (d,  $J = 8.4$  Hz, 2H), 7.26 – 7.16 (com, 3H), 7.01-6.99 (comp, 2H), 6.25 (s, 1H), 5.80-5.77 (m, 1H),

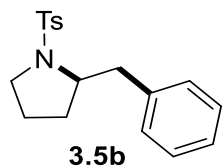
4.00 (s, 3H), 3.37 (dd,  $J = 14.4, 3.6$  Hz, 1H), 2.99 (dd,  $J = 14.4, 6.0$  Hz, 1H);  $^{13}\text{C}$  NMR (101 MHz, chloroform- $d$ ):  $\delta$  171.8, 166.0, 165.3, 134.3, 134.1, 132.4, 130.5, 129.6, 128.4, 127.3, 127.2, 117.3, 81.9, 52.5, 39.0; HRMS (ESI-TOF): calculated  $m/z$  for  $[\text{M}+\text{H}]^+$  ( $\text{C}_{19}\text{H}_{17}\text{O}_4$ ), 309.11226; observed, 309.1123.



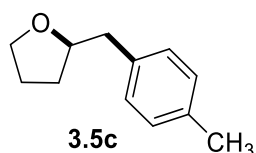
Colorless oil, 63% yield.  $^1\text{H}$  NMR (400 MHz, chloroform- $d$ ):  $\delta$  7.74 (d,  $J = 8.4$  Hz, 2H), 7.66 (d,  $J = 7.2$  Hz, 2H), 7.57 – 7.48 (comp, 4H), 7.46 – 7.41 (m, 1H), 7.24-7.21 (comp, 3H), 7.11 – 7.04 (comp, 2H), 6.19 (s, 1H), 5.77-5.75 (m, 1H), 3.40 (dd,  $J = 14.4, 3.6$  Hz, 1H), 3.01 (dd,  $J = 14.4, 6.0$  Hz, 1H);  $^{13}\text{C}$  NMR (101 MHz, chloroform- $d$ ):  $\delta$  172.4, 166.2, 144.1, 139.6, 134.6, 129.7, 129.1, 129.1, 128.3, 128.3, 127.9, 127.7, 127.1, 127.1, 115.0, 82.0, 39.4; HRMS (ESI-TOF): calculated  $m/z$  for  $[\text{M}+\text{H}]^+$  ( $\text{C}_{19}\text{H}_{17}\text{O}_4$ ), 309.11226; observed, 309.1123.



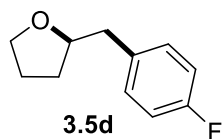
Colorless oil, 60% yield.  $^1\text{H}$  NMR (400 MHz, chloroform- $d$ ):  $\delta$  7.34 – 7.23 (comp, 5H), 4.16 – 4.07 (m, 1H), 3.97 – 3.91 (m, 1H), 3.81 – 3.74 (m, 1H), 2.96 (dd,  $J = 13.6, 6.4$  Hz, 1H), 2.78 (dd,  $J = 13.6, 6.4$  Hz, 1H), 2.02 – 1.82 (m, 3H), 1.65 – 1.53 (m, 1H);  $^{13}\text{C}$  NMR (101 MHz, chloroform- $d$ ):  $\delta$  139.0, 129.2, 128.3, 126.2, 80.1, 67.9, 41.9, 31.0, 25.6; Characterization data matched that reported in literature.<sup>5</sup>



Colorless oil, 56% yield.  $^1\text{H NMR}$  (400 MHz, chloroform-*d*):  $\delta$  7.68 (d,  $J = 8.4$  Hz, 2H), 7.24 (d,  $J = 8.4$  Hz, 2H), 7.23 – 7.12 (comp, 5H), 3.78 – 3.72 (m, 1H), 3.36 – 3.28 (m, 1H), 3.17 (dd,  $J = 13.2, 3.6$  Hz, 1H), 3.09 – 3.02 (m, 1H), 2.68 (dd,  $J = 13.2, 9.6$  Hz, 1H), 2.35 (s, 3H), 1.61 – 1.51 (m, 2H), 1.42 – 1.29 (m, 2H);  $^{13}\text{C NMR}$  (101 MHz, chloroform-*d*):  $\delta$  143.3, 138.5, 134.7, 129.7, 129.6, 128.4, 127.5, 126.4, 61.6, 49.3, 42.7, 29.9, 23.8, 21.5. Characterization data matched that reported in literature.<sup>55</sup>



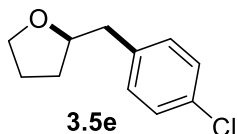
Colorless oil, 51% yield.  $^1\text{H NMR}$  (400 MHz, chloroform-*d*):  $\delta$  7.17 – 7.04 (comp, 4H), 4.10 – 3.98 (m, 1H), 3.92-3.86 (m, 1H), 3.75-3.70 (m, 1H), 2.89 (dd,  $J = 13.6, 6.4$  Hz, 1H), 2.70 (dd,  $J = 13.6, 6.4$  Hz, 1H), 2.32 (s, 3H), 1.97 – 1.78 (m, 3H), 1.62 – 1.49 (m, 1H);  $^{13}\text{C NMR}$  (101 MHz, chloroform-*d*):  $\delta$  135.9, 135.6, 129.1, 129.0, 80.2, 67.9, 41.5, 31.0, 25.6, 21.0; Characterization data matched that reported in literature.<sup>5</sup>



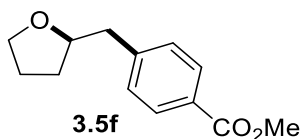
Colorless oil, 55% yield.  $^1\text{H NMR}$  (400 MHz, chloroform-*d*):  $\delta$  7.22 – 7.14 (comp, 2H), 7.01 – 6.92 (comp, 2H), 4.12 (q,  $J = 7.2$  Hz, 1H), 4.06 – 3.96 (m, 1H), 3.90-3.85 (m, 1H), 3.79 – 3.67 (m, 1H), 2.86 (dd,  $J = 13.6, 6.4$  Hz, 1H), 2.73 (dd,  $J = 13.6, 6.4$  Hz, 1H), 1.96 – 1.80 (m, 3H), 1.60 –



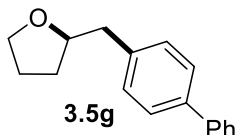
1.48 (m, 1H);  $^{13}\text{C}$  NMR (101 MHz, chloroform-*d*):  $\delta$  161.52 (d,  $J = 254$  Hz, 1C), 134.67, 134.64, 130.61, 130.53, 115.14, 114.93, 79.91, 67.96, 41.03, 30.95, 25.62;  $^{19}\text{F}$  NMR (377 MHz, chloroform-*d*):  $\delta$  -117.38; Characterization data matched that reported in literature.<sup>5</sup>



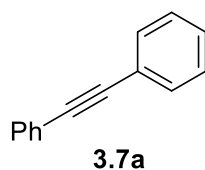
Colorless oil, 56% yield.  $^1\text{H}$  NMR (400 MHz, chloroform-*d*):  $\delta$  7.19-7.15 (comp, 2H), 7.12 – 7.03 (comp, 2H), 4.02-3.92 (m, 1H), 3.84-3.78 (m, 1H), 3.70 – 3.61 (m, 1H), 2.78 (dd,  $J = 13.6, 6.8$  Hz, 1H), 2.67 (dd,  $J = 13.6, 6.8$  Hz, 1H), 1.91 – 1.68 (m, 3H), 1.50 – 1.44 (m, 1H);  $^{13}\text{C}$  NMR (101 MHz, chloroform-*d*):  $\delta$  137.5, 130.6, 128.4, 128.2, 79.7, 68.0, 41.2, 31.0, 25.6; Characterization data matched that reported in literature.<sup>5</sup>



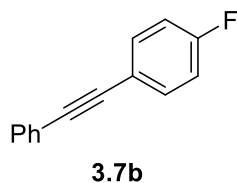
Colorless oil, 70% yield.  $^1\text{H}$  NMR (500 MHz, chloroform-*d*):  $\delta$  7.96 (d,  $J = 8.4$  Hz, 2H), 7.30 (d,  $J = 8.4$  Hz, 2H), 4.11-4.04 (m, 1H), 3.90 (s, 3H), 3.89 – 3.85 (m, 1H), 3.75-3.68 (m, 1H), 2.94 (dd,  $J = 13.6, 6.4$  Hz, 1H), 2.82 (dd,  $J = 13.6, 6.4$  Hz, 1H), 1.96-1.90 (m, 1H), 1.90 – 1.79 (m, 2H), 1.59 – 1.49 (m, 1H);  $^{13}\text{C}$  NMR (101 MHz, chloroform-*d*):  $\delta$  167.1, 144.5, 129.6, 129.3, 128.1, 79.5, 68.0, 52.0, 41.9, 31.0, 25.6; Characterization data matched that reported in literature.<sup>5</sup>



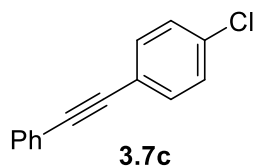
Colorless oil, 45% yield.  $^1\text{H NMR}$  (400 MHz, chloroform-*d*):  $\delta$  7.59 (d,  $J = 8.0$  Hz, 2H), 7.53 (d,  $J = 8.0$  Hz, 2H), 7.43 (t,  $J = 7.5$  Hz, 2H), 7.35-7.30 (comp, 3H), 4.15-4.08 (m, 1H), 3.95-3.90 (m, 1H), 3.84 – 3.71 (m, 1H), 2.96 (dd,  $J = 13.6, 6.8$  Hz, 1H), 2.81 (dd,  $J = 13.6, 6.8$  Hz, 1H), 2.02 – 1.79 (m, 3H), 1.64-1.53 (m, 1H);  $^{13}\text{C NMR}$  (101 MHz, chloroform-*d*):  $\delta$  141.1, 139.1, 138.2, 129.6, 128.7, 127.1, 127.0, 80.0, 68.0, 41.6, 31.1, 25.7; Characterization data matched that reported in literature.<sup>5</sup>



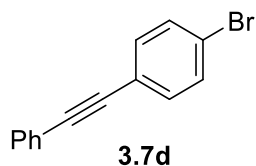
White solid, 56% yield.  $^1\text{H NMR}$  (400 MHz, chloroform-*d*):  $\delta$  7.62 – 7.52 (comp, 4H), 7.42 – 7.32 (comp, 6H);  $^{13}\text{C NMR}$  (101 MHz, chloroform-*d*):  $\delta$  131.6, 128.4, 128.3, 123.3, 89.4; Characterization data matched that reported in literature.<sup>45, 56</sup>



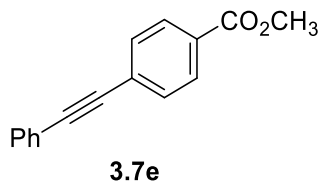
White solid, 65% yield.  $^1\text{H NMR}$  (400 MHz, chloroform-*d*):  $\delta$  7.39-7.35 (comp, 4H), 7.23-7.21 (comp, 3H), 6.92-6.88 (comp, 2H);  $^{13}\text{C NMR}$  (101 MHz, chloroform-*d*):  $\delta$  162.50 (d,  $J = 254$  Hz, 1C), 133.52, 133.44, 131.56, 128.38, 128.34, 123.10, 115.75, 115.53, 89.05, 88.29;  $^{19}\text{F NMR}$  (377 MHz, chloroform-*d*):  $\delta$  -110.99; Characterization data matched that reported in literature.<sup>45, 56</sup>



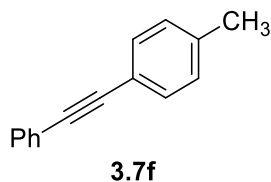
White solid, 66% yield.  $^1\text{H NMR}$  (400 MHz, chloroform-*d*):  $\delta$  7.56 – 7.50 (comp, 2H), 7.49 – 7.43 (comp, 2H), 7.34-7.26 (comp, 5H);  $^{13}\text{C NMR}$  (101 MHz, chloroform-*d*):  $\delta$  134.3, 132.8, 131.6, 129.0, 128.7, 128.5, 128.4, 128.2, 122.9, 121.8, 90.3, 88.2. Characterization data matched that reported in literature.<sup>45, 56</sup>



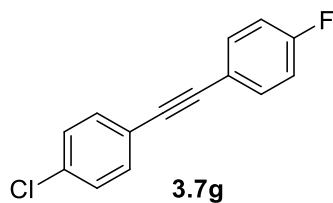
White solid, 70% yield.  $^1\text{H NMR}$  (400 MHz, chloroform-*d*):  $\delta$  7.56 – 7.51 (comp, 2H), 7.51 – 7.46 (comp, 2H), 7.42 – 7.37 (comp, 2H), 7.36-7.33 (comp, 3H);  $^{13}\text{C NMR}$  (101 MHz, chloroform-*d*):  $\delta$  133.0, 131.6, 131.6, 128.4, 122.9, 122.5, 122.3, 90.5, 88.3; Characterization data matched that reported in literature.<sup>45, 56</sup>



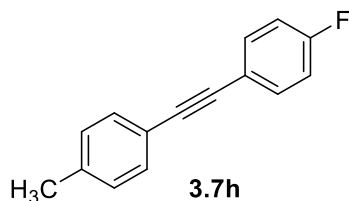
White solid, 68% yield.  $^1\text{H NMR}$  (400 MHz, chloroform-*d*):  $\delta$  8.02 (d,  $J$  = 8.4 Hz, 2H), 7.59 (d,  $J$  = 8.4 Hz, 2H), 7.57 – 7.52 (comp, 2H), 7.37-7.35 (comp, 3H), 3.93 (s, 3H);  $^{13}\text{C NMR}$  (101 MHz, chloroform-*d*):  $\delta$  166.6, 131.7, 131.5, 129.52, 129.48, 128.8, 128.4, 128.0, 122.7, 92.4, 88.6, 52.2; Characterization data matched that reported in literature.<sup>45, 56</sup>



White solid, 36% yield. **<sup>1</sup>H NMR** (400 MHz, Chloroform-*d*):  $\delta$  7.55 – 7.49 (comp, 2H), 7.46 – 7.38 (comp, 2H), 7.35 – 7.32 (comp, 3H), 7.16-7.14 (comp, 2H), 2.37 (s, 3H); **<sup>13</sup>C NMR** (101 MHz, chloroform-*d*):  $\delta$  138.4, 131.5, 131.5, 129.1, 128.3, 123.5, 120.2, 89.6, 88.7, 21.5. Characterization data matched that reported in literature.<sup>45, 56</sup>



White solid, 72% yield. **<sup>1</sup>H NMR** (400 MHz, chloroform-*d*):  $\delta$  7.55 – 7.47 (comp, 2H), 7.47 – 7.42 (comp, 2H), 7.34 – 7.30 (comp, 2H), 7.08 – 7.01 (comp, 2H); **<sup>13</sup>C NMR** (101 MHz, chloroform-*d*):  $\delta$  162.39 (d,  $J$  = 254 Hz, 1C), 134.3, 133.5, 133.5, 132.7, 128.7, 121.6, 119.0, 115.8, 115.6, 89.2, 87.9. **<sup>19</sup>F NMR** (377 MHz, chloroform-*d*):  $\delta$  -110.53; Characterization data matched that reported in literature.<sup>45, 56</sup>



White solid, 75% yield. **<sup>1</sup>H NMR** (400 MHz, chloroform-*d*):  $\delta$  7.45 – 7.39 (comp, 2H), 7.34 (d,  $J$  = 8.0 Hz, 2H), 7.08 (d,  $J$  = 8.0 Hz, 2H), 7.00 – 6.92 (comp, 2H), 2.29 (s, 3H); **<sup>13</sup>C NMR** (101 MHz, chloroform-*d*):  $\delta$  162.39 (d,  $J$  = 254 Hz, 1C), 138.48, 133.43, 133.35, 131.44, 129.14, 120.00, 119.80 (d,  $J$  = 3.5 Hz, 1C), 115.70, 115.48, 89.21, 87.63, 21.52; **<sup>19</sup>F NMR** (377 MHz, chloroform-*d*):  $\delta$  -111.31; Characterization data matched that reported in literature.<sup>45, 56</sup>

### 3.5 References

1. Hashmi, A. S. K., Gold-Catalyzed Organic Reactions. *Chem. Rev.* **2007**, *107* (7), 3180-3211.
2. Zheng, Z.; Ma, X.; Cheng, X.; Zhao, K.; Gutman, K.; Li, T.; Zhang, L., Homogeneous Gold-Catalyzed Oxidation Reactions. *Chem. Rev.* **2021**, *121* (14), 8979-9038.
3. Michelet, V.; Toste, F. D., *Gold catalysis : an homogeneous approach / edited by F. Dean Toste, Veronique Michelet*. Imperial College Press: London, England, 2014.
4. Zhang, G.; Cui, L.; Wang, Y.; Zhang, L., Homogeneous Gold-Catalyzed Oxidative Carboheterofunctionalization of Alkenes. *J. Am. Chem. Soc.* **2010**, *132* (5), 1474-1475.
5. Sahoo, B.; Hopkinson, M. N.; Glorius, F., Combining Gold and Photoredox Catalysis: Visible Light-Mediated Oxy- and Aminoarylation of Alkenes. *J. Am. Chem. Soc.* **2013**, *135* (15), 5505-5508.
6. Hopkinson, M. N.; Tlahuext-Aca, A.; Glorius, F., Merging Visible Light Photoredox and Gold Catalysis. *Acc. Chem. Res.* **2016**, *49* (10), 2261-2272.
7. Tlahuext-Aca, A.; Hopkinson, M. N.; Sahoo, B.; Glorius, F., Dual gold/photoredox-catalyzed C(sp)<sup>3</sup>-H arylation of terminal alkynes with diazonium salts. *Chem. Sci.* **2016**, *7* (1), 89-93.
8. He, Y.; Wu, H.; Toste, F. D., A dual catalytic strategy for carbon-phosphorus cross-coupling via gold and photoredox catalysis. *Chem. Sci.* **2015**, *6* (2), 1194-1198.
9. Witzel, S.; Hashmi, A. S. K.; Xie, J., Light in Gold Catalysis. *Chem. Rev.* **2021**, *121* (14), 8868-8925.
10. Cai, R.; Lu, M.; Aguilera, E. Y.; Xi, Y.; Akhmedov, N. G.; Petersen, J. L.; Chen, H.; Shi, X., Ligand-Assisted Gold-Catalyzed Cross-Coupling with Aryldiazonium Salts: Redox Gold Catalysis without an External Oxidant. *Angew. Chem. Int. Ed.* **2015**, *54* (30), 8772-8776.
11. Lu, Z.; Hammond, G. B.; Xu, B., Improving Homogeneous Cationic Gold Catalysis through a Mechanism-Based Approach. *Acc. Chem. Res.* **2019**, *52* (5), 1275-1288.
12. Sinha, P.; Wilson, A. K.; Omary, M. A., Beyond a T-Shape. *J. Am. Chem. Soc.* **2005**, *127* (36), 12488-12489.
13. Kawai, H.; Wolf, W. J.; DiPasquale, A. G.; Winston, M. S.; Toste, F. D., Phosphonium Formation by Facile Carbon-Phosphorus Reductive Elimination from Gold(III). *J. Am. Chem. Soc.* **2016**, *138* (2), 587-593.
14. Pflästerer, D.; Hashmi, A. S. K., Gold catalysis in total synthesis – recent achievements. *Chem. Soc. Rev.* **2016**, *45* (5), 1331-1367.
15. Rudolph, M.; Hashmi, A. S. K., Gold catalysis in total synthesis—an update. *Chem. Soc. Rev.* **2012**, *41* (6), 2448-2462.
16. Hendrich, C. M.; Sekine, K.; Koshikawa, T.; Tanaka, K.; Hashmi, A. S. K., Homogeneous and Heterogeneous Gold Catalysis for Materials Science. *Chem. Rev.* **2021**, *121* (14), 9113-9163.
17. Stuck, F.; Dietl, M. C.; Meißner, M.; Sebastian, F.; Rudolph, M.; Rominger, F.; Krämer, P.; Hashmi, A. S. K., Modular Two-Step Access to  $\pi$ -Extended Naphthyridine Systems—Potent Building Blocks for Organic Electronics. *Angew. Chem. Int. Ed.* **2022**, *61* (4), e202114277.
18. Heckershoff, R.; Schnitzer, T.; Diederich, T.; Eberle, L.; Krämer, P.; Rominger, F.; Rudolph, M.; Hashmi, A. S. K., Efficient Synthesis of Dipyrrolobenzenes and Dipyrrolopyrazines via Bidirectional Gold Catalysis: a Combined Synthetic and Photophysical Study. *J. Am. Chem. Soc.* **2022**, *144* (18), 8306-8316.

19. Drake, T.; Ji, P.; Lin, W., Site Isolation in Metal–Organic Frameworks Enables Novel Transition Metal Catalysis. *Acc. Chem. Res.* **2018**, *51* (9), 2129-2138.
20. Sun, C.; Skorupskii, G.; Dou, J.-H.; Wright, A. M.; Dincă, M., Reversible Metalation and Catalysis with a Scorpionate-like Metallo-ligand in a Metal–Organic Framework. *J. Am. Chem. Soc.* **2018**, *140* (50), 17394-17398.
21. Dunning, S. G.; Nandra, G.; Conn, A. D.; Chai, W.; Sikma, R. E.; Lee, J. S.; Kunal, P.; Reynolds Iii, J. E.; Chang, J.-S.; Steiner, A.; Henkelman, G.; Humphrey, S. M., A Metal–Organic Framework with Cooperative Phosphines That Permit Post-Synthetic Installation of Open Metal Sites. *Angew. Chem. Int. Ed.* **2018**, *57* (30), 9295-9299.
22. Mon, M.; Ferrando-Soria, J.; Grancha, T.; Fortea-Pérez, F. R.; Gascon, J.; Leyva-Pérez, A.; Armentano, D.; Pardo, E., Selective Gold Recovery and Catalysis in a Highly Flexible Methionine-Decorated Metal–Organic Framework. *J. Am. Chem. Soc.* **2016**, *138* (25), 7864-7867.
23. Lee, J. S.; Kapustin, E. A.; Pei, X.; Llopis, S.; Yaghi, O. M.; Toste, F. D., Architectural Stabilization of a Gold(III) Catalyst in Metal–Organic Frameworks. *Chem* **2020**, *6* (1), 142-152.
24. Furukawa, H.; Cordova, K. E.; O'Keeffe, M.; Yaghi, O. M., The Chemistry and Applications of Metal–Organic Frameworks. *Science* **2013**, *341* (6149), 974-974.
25. Liang, J.; Chen, R.-P.; Wang, X.-Y.; Liu, T.-T.; Wang, X.-S.; Huang, Y.-B.; Cao, R., Postsynthetic ionization of an imidazole-containing metal–organic framework for the cycloaddition of carbon dioxide and epoxides. *Chem. Sci.* **2017**, *8* (2), 1570-1575.
26. Zhao, M.; Ou, S.; Wu, C.-D., Porous Metal–Organic Frameworks for Heterogeneous Biomimetic Catalysis. *Acc. Chem. Res.* **2014**, *47* (4), 1199-1207.
27. Li, B.; Wen, H.-M.; Cui, Y.; Zhou, W.; Qian, G.; Chen, B., Emerging Multifunctional Metal–Organic Framework Materials. *Adv. Mater.* **2016**, *28* (40), 8819-8860.
28. Islamoglu, T.; Goswami, S.; Li, Z.; Howarth, A. J.; Farha, O. K.; Hupp, J. T., Postsynthetic Tuning of Metal–Organic Frameworks for Targeted Applications. *Acc. Chem. Res.* **2017**, *50* (4), 805-813.
29. Feng, X.; Song, Y.; Li, Z.; Kaufmann, M.; Pi, Y.; Chen, J. S.; Xu, Z.; Li, Z.; Wang, C.; Lin, W., Metal–Organic Framework Stabilizes a Low-Coordinate Iridium Complex for Catalytic Methane Borylation. *J. Am. Chem. Soc.* **2019**, *141* (28), 11196-11203.
30. Sawano, T.; Lin, Z.; Boures, D.; An, B.; Wang, C.; Lin, W., Metal–Organic Frameworks Stabilize Mono(phosphine)–Metal Complexes for Broad-Scope Catalytic Reactions. *J. Am. Chem. Soc.* **2016**, *138* (31), 9783-9786.
31. Lv, X.-L.; Wang, K.; Wang, B.; Su, J.; Zou, X.; Xie, Y.; Li, J.-R.; Zhou, H.-C., A Base-Resistant Metalloporphyrin Metal–Organic Framework for C–H Bond Halogenation. *J. Am. Chem. Soc.* **2017**, *139* (1), 211-217.
32. Cao, C.-C.; Chen, C.-X.; Wei, Z.-W.; Qiu, Q.-F.; Zhu, N.-X.; Xiong, Y.-Y.; Jiang, J.-J.; Wang, D.; Su, C.-Y., Catalysis through Dynamic Spacer Installation of Multivariate Functionalities in Metal–Organic Frameworks. *J. Am. Chem. Soc.* **2019**, *141* (6), 2589-2593.
33. Chen, C.-X.; Wei, Z.-W.; Pham, T.; Lan, P. C.; Zhang, L.; Forrest, K. A.; Chen, S.; Al-Enizi, A. M.; Nafady, A.; Su, C.-Y.; Ma, S., Nanospace Engineering of Metal–Organic Frameworks through Dynamic Spacer Installation of Multifunctionalities for Efficient Separation of Ethane from Ethane/Ethylene Mixtures. *Angew. Chem. Int. Ed.* **2021**, *60* (17), 9680-9685.
34. Hwang, Y. K.; Hong, D.-Y.; Chang, J.-S.; Jhung, S. H.; Seo, Y.-K.; Kim, J.; Vimont, A.; Daturi, M.; Serre, C.; Férey, G., Amine Grafting on Coordinatively Unsaturated Metal Centers of MOFs: Consequences for Catalysis and Metal Encapsulation. *Angew. Chem. Int. Ed.* **2008**, *47* (22), 4144-4148.

35. Yuan, S.; Chen, Y.-P.; Qin, J.-S.; Lu, W.; Zou, L.; Zhang, Q.; Wang, X.; Sun, X.; Zhou, H.-C., Linker Installation: Engineering Pore Environment with Precisely Placed Functionalities in Zirconium MOFs. *J. Am. Chem. Soc.* **2016**, *138* (28), 8912-8919.
36. Chang, G.-G.; Ma, X.-C.; Zhang, Y.-X.; Wang, L.-Y.; Tian, G.; Liu, J.-W.; Wu, J.; Hu, Z.-Y.; Yang, X.-Y.; Chen, B., Construction of Hierarchical Metal–Organic Frameworks by Competitive Coordination Strategy for Highly Efficient CO<sub>2</sub> Conversion. *Adv. Mater.* **2019**, *31* (52), 1904969.
37. Zhou, W.; Huang, D.-D.; Wu, Y.-P.; Zhao, J.; Wu, T.; Zhang, J.; Li, D.-S.; Sun, C.; Feng, P.; Bu, X., Stable Hierarchical Bimetal–Organic Nanostructures as High-Performance Electrocatalysts for the Oxygen Evolution Reaction. *Angew. Chem. Int. Ed.* **2019**, *58* (13), 4227-4231.
38. Wang, Y.; Jia, X.; Yang, H.; Wang, Y.; Chen, X.; Hong, A. N.; Li, J.; Bu, X.; Feng, P., A Strategy for Constructing Pore-Space-Partitioned MOFs with High Uptake Capacity for C<sub>2</sub> Hydrocarbons and CO<sub>2</sub>. *Angew. Chem. Int. Ed.* **2020**, *59* (43), 19027-19030.
39. Lan, G.; Quan, Y.; Wang, M.; Nash, G. T.; You, E.; Song, Y.; Veroneau, S. S.; Jiang, X.; Lin, W., Metal–Organic Layers as Multifunctional Two-Dimensional Nanomaterials for Enhanced Photoredox Catalysis. *J. Am. Chem. Soc.* **2019**, *141* (40), 15767-15772.
40. Shi, W.; Quan, Y.; Lan, G.; Ni, K.; Song, Y.; Jiang, X.; Wang, C.; Lin, W., Bifunctional Metal–Organic Layers for Tandem Catalytic Transformations Using Molecular Oxygen and Carbon Dioxide. *J. Am. Chem. Soc.* **2021**, *143* (40), 16718-16724.
41. Fan, Y.; You, E.; Xu, Z.; Lin, W., A Substrate-Binding Metal–Organic Layer Selectively Catalyzes Photoredox Ene-Carbonyl Reductive Coupling Reactions. *J. Am. Chem. Soc.* **2021**, *143* (45), 18871-18876.
42. Cao, L.; Lin, Z.; Peng, F.; Wang, W.; Huang, R.; Wang, C.; Yan, J.; Liang, J.; Zhang, Z.; Zhang, T.; Long, L.; Sun, J.; Lin, W., Self-Supporting Metal–Organic Layers as Single-Site Solid Catalysts. *Angew. Chem. Int. Ed.* **2016**, *55* (16), 4962-4966.
43. Lan, G.; Ni, K.; Xu, R.; Lu, K.; Lin, Z.; Chan, C.; Lin, W., Nanoscale Metal–Organic Layers for Deeply Penetrating X-ray-Induced Photodynamic Therapy. *Angew. Chem. Int. Ed.* **2017**, *56* (40), 12102-12106.
44. Patil, D. V.; Yun, H.; Shin, S., Catalytic Cross-Coupling of Vinyl Golds with Diazonium Salts under Photoredox and Thermal Conditions. *Adv. Synth. Catal.* **2015**, *357* (12), 2622-2628.
45. Kim, S.; Rojas-Martin, J.; Toste, F. D., Visible light-mediated gold-catalysed carbon(sp<sup>2</sup>)–carbon(sp) cross-coupling. *Chem. Sci.* **2016**, *7* (1), 85-88.
46. Huang, L.; Rudolph, M.; Rominger, F.; Hashmi, A. S. K., Photosensitizer-Free Visible-Light-Mediated Gold-Catalyzed 1,2-Difunctionalization of Alkynes. *Angew. Chem. Int. Ed.* **2016**, *55* (15), 4808-4813.
47. Marcoux, D.; Charette, A. B., Nickel-Catalyzed Synthesis of Phosphonium Salts from Aryl Halides and Triphenylphosphine. *Adv. Synth. Catal.* **2008**, *350* (18), 2967-2974.
48. Shu, X.-z.; Zhang, M.; He, Y.; Frei, H.; Toste, F. D., Dual Visible Light Photoredox and Gold-Catalyzed Arylative Ring Expansion. *J. Am. Chem. Soc.* **2014**, *136* (16), 5844-5847.
49. Huang, L.; Rominger, F.; Rudolph, M.; Hashmi, A. S. K., A general access to organogold(III) complexes by oxidative addition of diazonium salts. *Chem. Commun.* **2016**, *52* (38), 6435-6438.
50. Asomoza-Solís, E. O.; Rojas-Ocampo, J.; Toscano, R. A.; Porcel, S., Arenediazonium salts as electrophiles for the oxidative addition of gold(I). *Chem. Commun.* **2016**, *52* (45), 7295-7298.

51. Witzel, S.; Hoffmann, M.; Rudolph, M.; Rominger, F.; Dreuw, A.; Hashmi, A. S. K., A Radical Chain: Mononuclear “Gold Only” Photocatalysis. *Adv. Synth. Catal.* **2022**, *364* (3), 581-592.
52. Hashmi, A. S. K., Homogeneous Gold Catalysis Beyond Assumptions and Proposals—Characterized Intermediates. *Angew. Chem. Int. Ed.* **2010**, *49* (31), 5232-5241.
53. Lauterbach, T.; Asiri, A. M.; Hashmi, A. S. K., Chapter Five - Organometallic Intermediates of Gold Catalysis. In *Adv. Organomet. Chem.*, Pérez, P. J., Ed. Academic Press: 2014; Vol. 62, pp 261-297.
54. Dydio, P.; Detz, R. J.; de Bruin, B.; Reek, J. N. H., Beyond Classical Reactivity Patterns: Hydroformylation of Vinyl and Allyl Arenes to Valuable  $\beta$ - and  $\gamma$ -Aldehyde Intermediates Using Supramolecular Catalysis. *J. Am. Chem. Soc.* **2014**, *136* (23), 8418-8429.
55. Nikolaienko, P.; Jentsch, M.; Kale, A. P.; Cai, Y.; Rueping, M., Electrochemical and Scalable Dehydrogenative C(sp<sup>3</sup>)-H Amination via Remote Hydrogen Atom Transfer in Batch and Continuous Flow. *Chemistry – A European Journal* **2019**, *25* (29), 7177-7184.
56. Wu, C.; Li, Q.-H., Highly efficient synthesis of 1,2-disubstituted acetylenes derivatives from the cross-coupling reactions of 1-bromoalkynes with organotitanium reagents. *Tetrahedron* **2021**, *96*, 132370.



## Chapter 4. Sequential Modifications of Metal-Organic Layer Nodes for Highly Efficient Photocatalyzed Hydrogen Atom Transfer

### 4.1 Introduction

Directed photocatalyzed hydrogen atom transfer (HAT) is widely used in the transformation of aliphatic C–H bonds into C–C, C–N, C–O, C–F, and C–S bonds. In these reactions, a photocatalyst uses the energy of a photon to trigger the homolytic cleavage of C–H bonds in organic compounds to generate open-shell R $\cdot$  species for further transformations (**Figure 4-1a**).<sup>1-4</sup> The ability of aromatic ketones to abstract a hydrogen atom has been known since the birth of photochemistry and these carbonyl derivatives have gained much attention as HAT catalysts in the recent renaissance of photochemistry and photocatalysis.<sup>4-9</sup> Upon irradiation, the long-lived triplet state of the carbonyl compound can abstract hydrogen from aliphatic C–H compounds to initiate radical-based coupling reactions.<sup>10-13</sup> For example, HAT catalysts and Lewis acids can be synergistically combined to mediate hydrofunctionalization of electron-deficient alkenes.<sup>14-16</sup> Lewis acids activate alkenes for the addition of radicals which are generated from a photo-induced HAT process.

The catalytic efficiency of hydrofunctionalization reactions is, however, limited by deactivation of photocatalysts via radical dimerization or radical trapping. A high catalyst loading (above 10 mol%) is typically needed to generate hydrofunctionalization products in moderate yields.<sup>17-18</sup> It is highly desirable to develop bifunctional catalytic systems that synergize Lewis acids and photocatalysts for efficient hydrofunctionalization of olefins.<sup>19</sup>

MOFs have provided a versatile platform for studying single-site catalysis and the synergy between multiple functionalities.<sup>20-23</sup> MOFs isolate catalytic centers to prevent catalyst

deactivation via multi-molecular decomposition processes. Recently, Duan and coworkers encapsulated anthraquinone into MOFs to obtain a site-isolated HAT photocatalyst, which accelerates reverse HAT and prevents catalyst decomposition via dimerization.<sup>24</sup> However, the 3D structures of MOFs are not amenable to the hierarchical installation of multiple active sites.<sup>25-32</sup> We have developed MOLs via proximal installation of multiple functionalities to promote synergistic and tandem photoredox catalysis.<sup>33-38</sup> We hypothesized that a bifunctional HAT photocatalyst could be synthesized by installing Lewis acids and HAT photocatalysts through sequential modifications of SBUs (**Figure 4-1b**).<sup>39</sup> We further posited that the proximally placed Lewis acids and HAT catalysts could synergistically activate olefinic substrates for the addition of HAT-generated radicals to not only accelerate reaction rates but also improve selectivity for hydrofunctionalization products.

In this chapter, we synthesized a Zr-OTf-EY MOL containing highly Lewis acidic triflate-modified Zr<sub>6</sub>-based SBUs and Eosin-Y (EY) photosensitizers for photocatalyzed HAT reactions. The Zr<sub>6</sub> SBUs of the Zr-BTB MOL (BTB represents 4-[3,5-bis(4-carboxyphenyl)phenyl]benzoate) underwent sequential modifications to generate Zr-triflate and install EY. The resultant Zr-OTf-EY efficiently catalyzed HAT cross-coupling reactions of electron-deficient alkenes and azodicarboxylate with C-H compounds, with a turnover number (TON) of up to 1980 TON and a 400-fold higher activity over homogeneous controls.

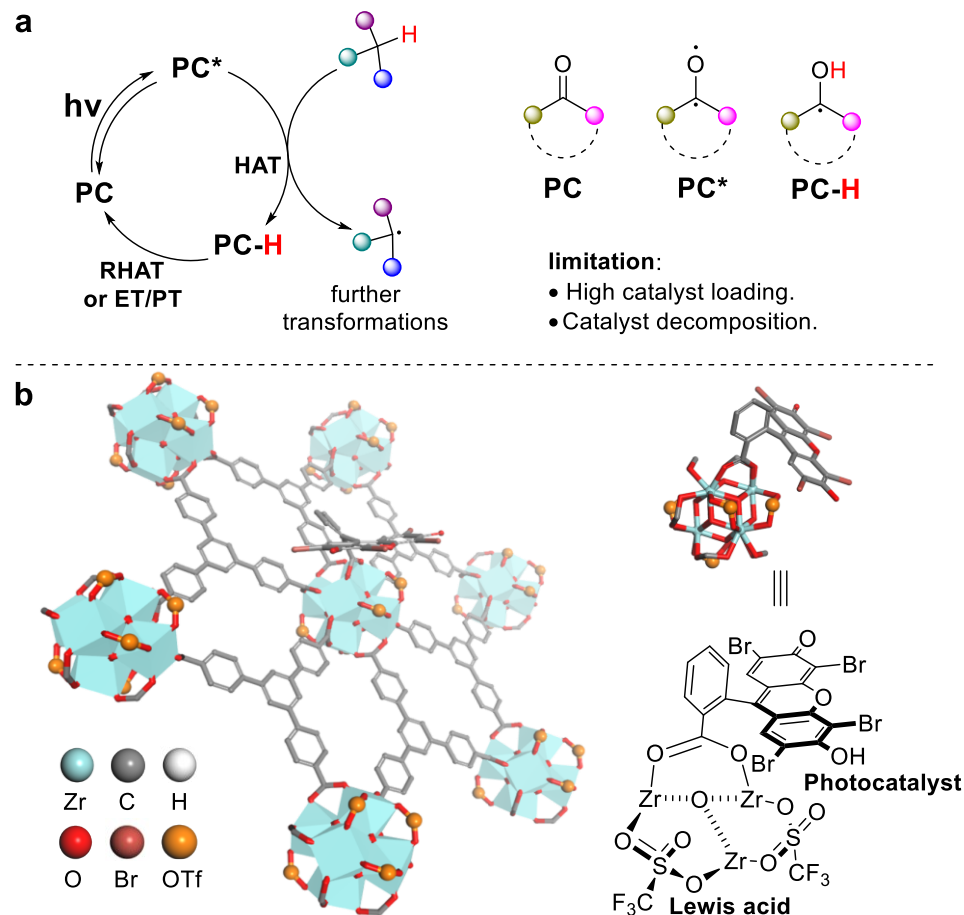


**Figure 4-1.** Direct HAT reactions. (a) Direct HAT by carbonyl-based photocatalysts. (b) Schematic showing the design of bifunctional HAT photo-catalyst based on MOL.

## 4.2 Results and Discussion

### 4.2.1 Synthesis and Characterization of Zr-OTf-EY

A solvothermal reaction between  $\text{ZrCl}_4$  and  $\text{H}_3\text{BTB}$  in DMF with formic acid and water at  $120\text{ }^\circ\text{C}$  afforded the known Zr-BTB MOL with a formula of  $\text{Zr}_6(\mu_3\text{-O})_4(\mu_3\text{-OH})_4(\text{BTB})_2(\text{HCO}_2)_6$  (**Figure 4-2**).<sup>40-42</sup> In Zr-BTB, the  $\text{Zr}_6$  SBUs are laterally bridged by BTB ligands and vertically terminated by formate groups to afford an infinite 2D network. Zr-BTB was then treated with 1 M

HCl to transform the terminating  $Zr_2$ -formate into  $Zr_2$ -OH/OH<sub>2</sub>.<sup>37, 43</sup> Subsequent triflation by trimethylsilyl triflate produced strongly Lewis acidic  $Zr_2$ -OTf sites on the SBUs.<sup>37</sup> Reaction of Zr-BTB-OTf with EY in acetonitrile at 60 °C yielded Zr-OTf-EY by partially replacing OTf capping groups with the carboxylates in EY (**Figure 4-2**). <sup>1</sup>H NMR analysis of the digested Zr-OTf-EY gave an EY to BTB molar ratio of 0.1:1 (**Figure 4-3**). Another HAT photocatalyst, 4-(9,10-dioxo-9,10-dihydroanthracen-2-yl)benzoic acid (AQ), was similarly loaded on Zr-BTB-OTf to afford Zr-OTf-AQ HAT photocatalyst.

Zr-BTB, Zr-BTB-OTf, Zr-OTf-AQ, and Zr-OTf-EY showed similar PXRD patterns that matched the simulated pattern for Zr-BTB (**Figure 4-4a**), demonstrating the preservation of 2D network structure throughout the SBU modification processes. UV-vis spectrum of digested Zr-OTf-EY showed contributions from both BTB ligand and EY (**Figure 4-4b**). TEM showed the ruffled nanosheet morphologies for Zr-BTB-OTf and Zr-OTf-EY (**Figure 4-4c, 4-4d**),

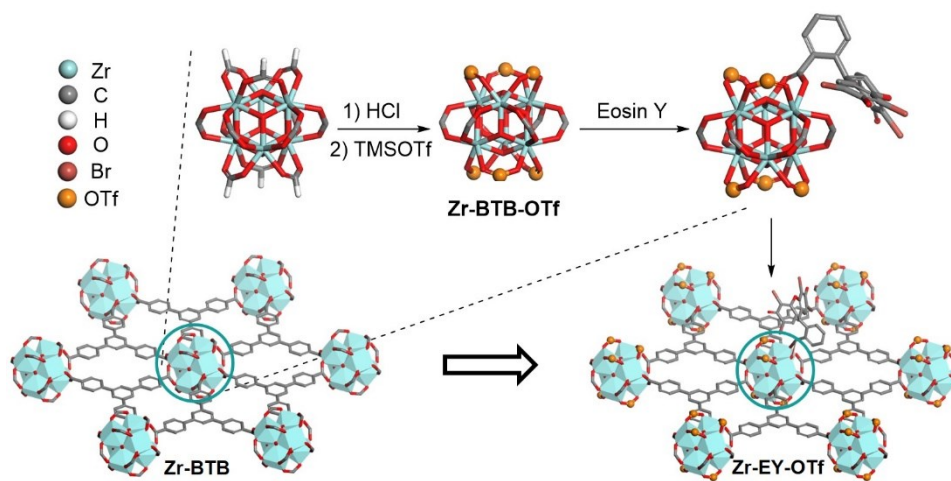


**Figure 4-2.** Schematic showing the synthesis of Zr-OTf-EY.

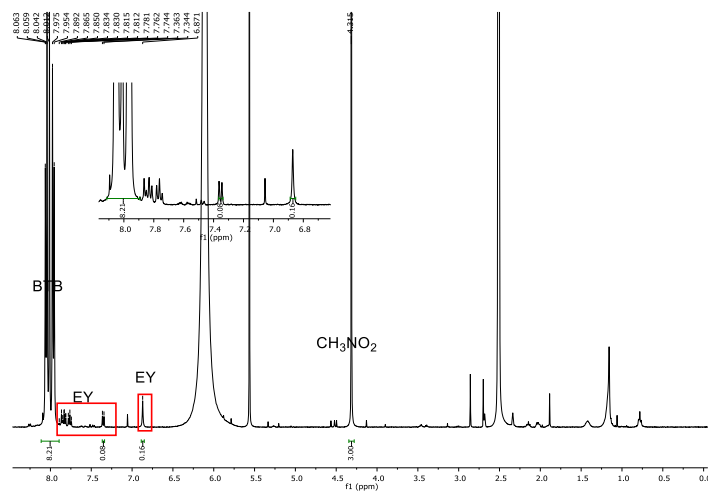


**Figure 4-3.**  $^1\text{H}$  NMR spectrum of digested Zr-OTf-EY in  $\text{DMSO-}d_6$ .

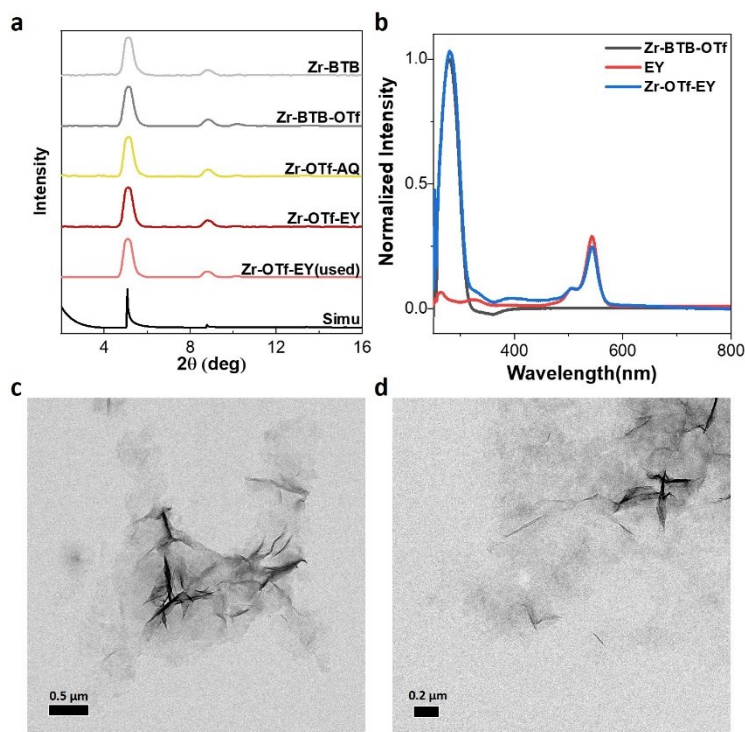
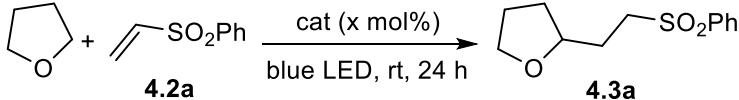


**Figure 4-4.** Characterization of Zr-OTf-EY. (a) PXRD patterns of Zr-BTB, Zr-BTB-OTf, Zr-OTf-AQ, and Zr-OTf-EY before and after a catalytic reaction, along with the simulated PXRD pattern for Zr-BTB. (b) UV-vis spectra of digested Zr-BTB-OTf, EY, and digested Zr-BTB-EY. (c-d) TEM images of Zr-BTB-OTf and Zr-OTf-EY.

## 4.2.2 HAT Reactions and Mechanistic Studies

Zr-OTf-EY was examined as a bifunctional HAT photocatalyst for the cross-coupling reaction between tetrahydrofuran (THF) and phenyl vinyl sulfone (**4.2a**). At 0.05 mol% loading of Zr-OTf-EY, the addition product **4.3a** was obtained in 98% yield with a TON of 1960 under blue LED irradiation (**Table 4-1**, entry 1). In comparison, a mixture of 0.05 mol% EY and 0.5 mol% Zr-BTB-OTf produced **4.3a** in 29% yield (**Table 4-1**, entry 2). The yield of **4.3a** further decreased to 16% in the presence of 0.05 mol% EY (**Table 4-1**, entry 3), indicating an important role of Lewis acid in the reaction. Approximately 20-fold higher loadings of both Zr-BTB-OTf and EY were needed to afford **4.3a** in a yield comparable to that of Zr-OTf-EY (**Table 4-1**, entry 4), suggesting approximately 400-fold higher activity for Zr-OTf-EY over the homogeneous control. Zr-OTf-AQ MOL showed lower activity and afforded **4.3a** in 30% yield (**Table 4-1**, entry 5).

**Table 4-1.** HAT reactions and control groups.



Entry <sup>a</sup>	Condition variation	Yield <sup>b</sup> (%)
1	<b>Zr-OTf-EY</b> (0.05 mol%)	98
2	<b>EY</b> (0.05 mol%)	16
3	<b>Zr-BTB-OTf</b> (0.5 mol%) + <b>EY</b> (0.05 mol%)	29
4	<b>Zr-BTB-OTf</b> (10 mol%) + <b>EY</b> (1 mol%)	95
5	<b>Zr-OTf-AQ</b> (0.05 mol%)	30

<sup>a</sup>Reactions were performed with **4.2a** (0.2 mmol), catalyst (x mol%) in THF (2 mL) at rt under blue LED light for 24 h; <sup>b</sup>Isolated yield.

Additionally, in the cross-coupling between THF and **4.2a**, Zr-OTf-EY exhibited orders of magnitude higher TONs than other commonly used HAT catalysts, including 9-fluorenone, thioxanthone and, tetrabutylammonium decatungstate (TBADT) (**Figure 4-5a**).<sup>44-47</sup> Time-

dependent experiments were also performed for coupling reactions between THF and **4.2a**, using 0.05 mol% Zr-OTf-EY or 0.05 mol% EY and 0.5 mol% Zr-BTB-OTf as catalysts under identical conditions (**Figure 4-5b**). Zr-OTf-ET catalyzed the reaction about three times faster than the homogeneous control. These results suggest a better synergy between HAT photocatalyst and Lewis acid in Zr-OTf-EY than that in the homogeneous control, which can be attributed to the proximity between catalytic sites on the MOL.<sup>35, 38</sup>

Zr-OTf-EY remained stable under photocatalytic conditions, as evidenced by the retention of PXRD pattern and UV-vis spectrum for the catalysts recovered from the reaction (**Figure 4-4b, 4-5c**). However, UV-vis spectrum revealed the decomposition of EY under photocatalytic conditions in the homogeneously catalyzed reaction (**Figure 4-5c**). After 24-hour irradiation, the characteristic peak of EY at 543 nm completely disappeared and new peaks arose below 300 nm. Zr-OTf-EY was also recovered and reused in four runs of cross-coupling reactions between THF and **4.2a** without a significant decrease in catalytic activity (**Figure 4-5d**).

The Lewis acidity of Zr-OTf-EY was quantified using *N*-methylacridone (NMA) as a fluorescence probe.<sup>48</sup> The emission peak maxima of NMA shifts to longer wavelength when bound to Lewis acids. The differences are used to qualitatively compare the Lewis acidity of different acids. Zr-OTf-EY and TiCl<sub>4</sub> shifted NMA emission peak maxima from 413 nm to 472 nm and 474 nm, respectively, suggesting their similar Lewis acidities (**Figure 4-6b**). The activation of **4.2a** by TiCl<sub>4</sub> was further confirmed by <sup>1</sup>H NMR (**Figure 4-6c**). Proton signals of **4.2a** all shifted to lower field upon addition of TiCl<sub>4</sub> to a solution of **4.2a**. The proton at the anti-position to the sulfone group shifted the most, from 6.04 ppm to 6.31 ppm, indicating binding of the sulfone to TiCl<sub>4</sub>. Presumably, **4.2a** should also be activated by Zr-OTf-EY, with a Lewis acidity as strong as TiCl<sub>4</sub>, under catalytic conditions.

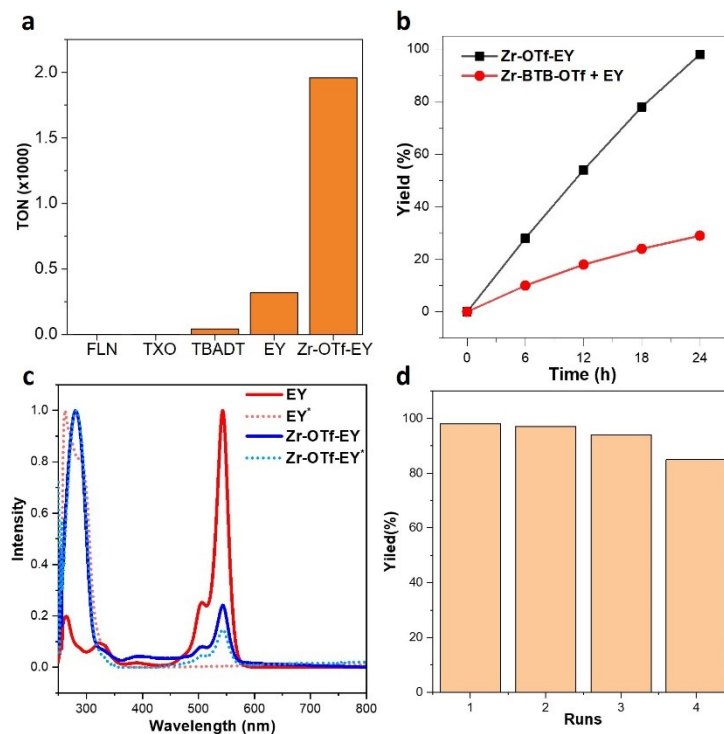


**Figure 4-5.** Reactivity and stability of Zr-OTf-EY. (a) TONs of Zr-OTf-EY and other common HAT catalysts. (b) Time-dependent experiments for reactions catalyzed by 0.05 mol% Zr-OTf-EY or 0.05 mol% EY and 0.5 mol% Zr-BTB-OTf. (c) UV-vis spectra of EY and Zr-OTf-EY before and after the coupling reaction. (d) Yields of **4.3a** in four consecutive runs of Zr-OTf-EY-catalyzed coupling reactions.



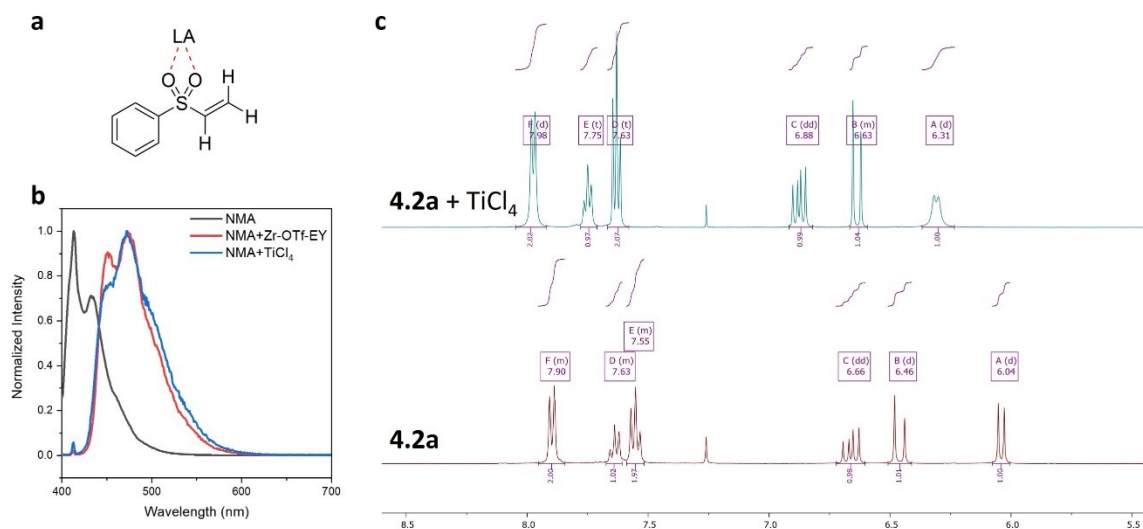


**Figure 4-6.** Activation of **4.2a** with Zr-OTf-EY. (a) Interaction between **4.2a** and Lewis acids. (b) Determination of Lewis acidity of Zr-OTf-EY by fluorescence probe. (c) <sup>1</sup>H NMR shift of **4.2a** with Lewis acid activation.

Based on these experimental results and literature precedents,<sup>14, 16</sup> we propose a plausible reaction mechanism for Zr-OTf-EY catalyzed cross-coupling of THF and **4.2a** (**Figure 4-7**). Strongly Lewis acidic site, Zr<sub>2</sub>-OTf, in the MOL binds **4.2a** to enhance its electron-deficiency and to increase its local concentration near the EY photocatalyst sites. In the meantime, EY is excited with blue light to form the diradical intermediate **I**, which undergoes a direct HAT with THF to afford a carbon radical intermediate **II**. **II** is subsequently trapped by the activated **4.2a** to form a radical adduct **III**. A reverse HAT process between **III** and EY radical affords the product **4.3a** and regenerates EY. In this mechanistic scenario, isolation of EY photocatalysts on SBUs improves the catalyst stability, which explains the durability of MOL catalysts in the recycle and reuse experiments. Additionally, the proximity between photocatalysts and Lewis acids facilitates the reaction between carbon radical **II** and activated **4.2a**, enhancing the catalytic efficiency activity by 400 times over the homogeneous control.

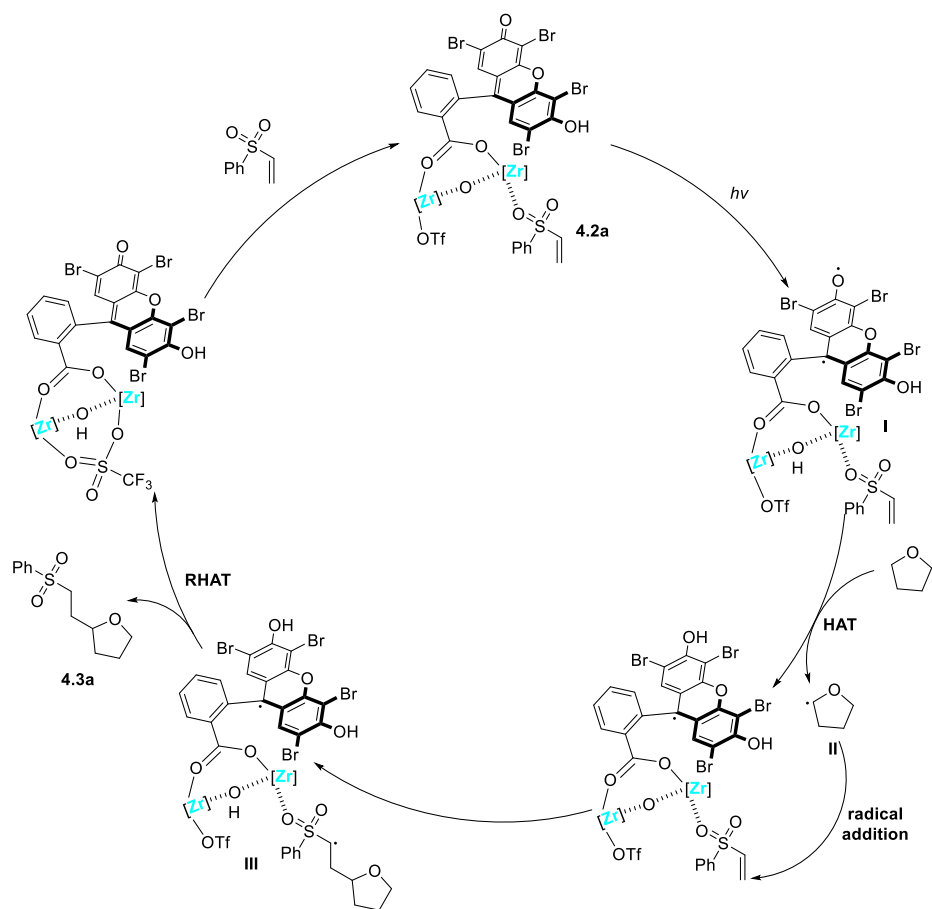


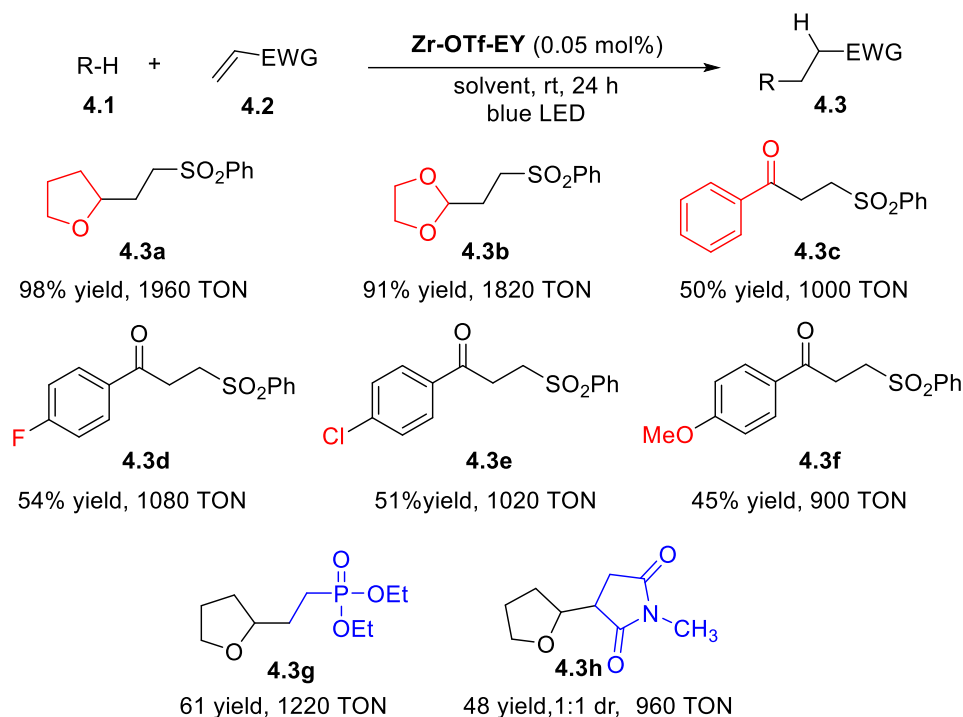
**Figure 4-7.** Proposed mechanism for Zr-OTf-EY-catalyzed HAT coupling reaction.

### 4.2.3 Substrate Scope

We next examined the generality of the MOL-based photoinduced HAT method. As shown in **Table 4-2**, 0.05 mol % Zr-OTf-EY efficiently catalyzed the cross-coupling of various C-H compounds with electron-deficient alkenes to afford addition products **4.3**. C-H partner 1,3-dioxolane (**4.1b**) reacted with **4.2a**, producing Giese adduct **4.3b** in 91% yield with a TON of 1820. Substituents on the benzaldehyde, including hydrogen (**4.1c**), fluorine (**4.1d**), chlorine (**4.1e**), and methoxy group (**4.1f**), were tolerated in the reactions to furnish the corresponding products **4.3c-4.3f** in 45-54% yields. Other electron-deficient alkenes, diethyl vinylphosphonate (**4.2b**) and 1-

methyl-1*H*-pyrrole-2,5-dione (**4.2c**), coupled with THF to afford alkylation products **4.3g** and **4.3h** in 61% and 48% yield, respectively.

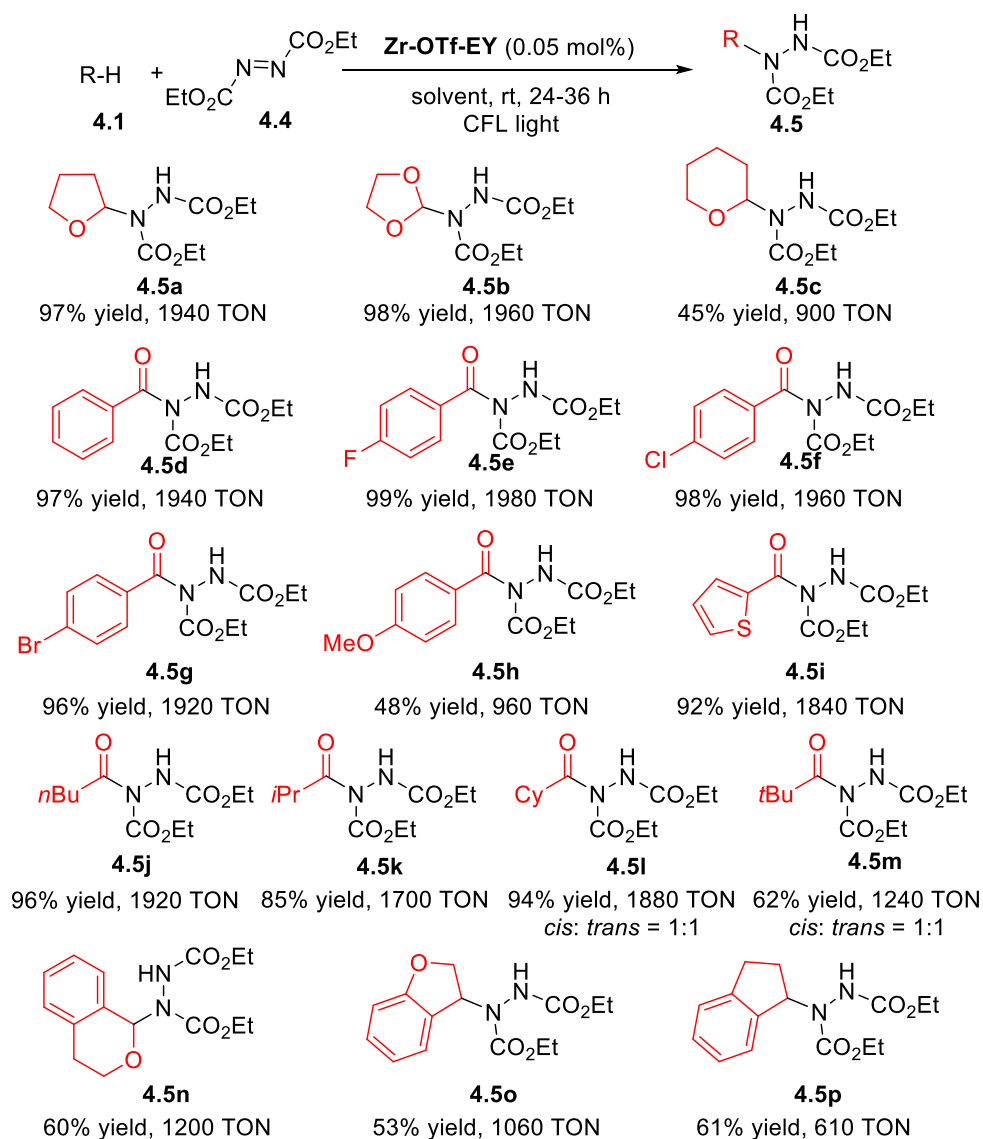
**Table 4-2.** Zr-OTf-EY-catalyzed HAT C-C coupling reactions.



The formation of C–N bonds is one of the most important transformations in organic chemistry and has wide applications in the synthesis of natural and unnatural biologically active molecules.<sup>49-51</sup> We chose the cross-coupling reactions of diethyl azodicarboxylate (**4.4**) with C-H derivatives as a model reaction to evaluate the catalytic performance of Zr-OTf-EY in C-N bond formation reactions.<sup>52-53</sup> Under CFL light irradiation at room temperature, Zr-OTf-EY (0.05–0.1 mol % based on EY) competently catalyzed the coupling reactions of various C-H derivatives with **4.4** in good to excellent yields with TONs of up to 1980 (**Table 4-3**). Ethers including tetrahydropyran, 1,3-dioxane, and tetrahydro-2*H*-pyran afforded the adducts **4.5a-4.5c** in 45-98% yields. Aryl-substituted aldehydes with both electron-withdrawing and -donating groups were

tolerated to afford the corresponding products **4.5d-4.5h** in 48-99% isolated yields. Thiophene-2-carbaldehyde also reacted with **4.4** to afford **4.5i** in 92% yield. The reactions with primary, secondary, and tertiary alkyl aldehydes proceeded smoothly to yield products **4.5j-4.5m** in good to excellent yields. It is worth noting that *cis*-/*trans*- isomers were detected for products **4.5i** and **4.5m**, which contain steric bulky cyclohexyl and *tert*-butyl groups. The cross-coupling reactions with benzylic substrates (**4.1n-4.1p**) also proceeded smoothly to afford **4.5n-4.5p** in 53-61% yields.

**Table 4-3.** Zr-OTf-EY-catalyzed HAT C-N coupling reactions.



### 4.3. Conclusion

In this chapter, we sequentially installed strongly Lewis acidic sites and HAT photocatalysts on the SBUs of Zr-BTB MOL to afford the bifunctional Zr-OTf-EY MOL for photocatalytic hydrofunctionalization reactions. Zr-OTf-EY effectively catalyzed cross-coupling reactions of electron-deficient alkenes or azodicarboxylate with various C-H compounds through photo-induced HAT to afford C-C and C-N bond formation products with TONs of up to 1980. Zr-OTf-EY outperformed homogeneous controls by 400 times because of higher photocatalytic stability, increased local concentration of Lewis acid-activated alkene and azo substrates, and enhanced alkyl radical transfer from photocatalysts to activated substrates. The MOL catalyst was readily recovered and reused in photocatalytic hydrofunctionalization reactions. This work highlights the potential of MOL node modifications as an effective strategy for developing synergistic catalysts for sustainable catalysis.

### 4.4. Methods

#### 4.4.1 Material synthesis

**Synthesis of Zr-BTB-OTf.**<sup>37</sup> To a 20 mL glass vial was added 2.5 mL of ZrCl<sub>4</sub> solution (43.7 μmol in DMF), 2.5 mL of H<sub>3</sub>BTB solution (28.5 μmol in DMF), followed by the addition of 0.15 mL H<sub>2</sub>O and 0.85 mL HCOOH (99%). The mixture was sonicated for 5 min and kept in a 120 °C oven for 2 days. The white precipitate was collected by centrifugation and washed with DMF three times. Zr-BTB with a formula of Zr<sub>6</sub>O<sub>4</sub>(OH)<sub>4</sub>(BTB)<sub>2</sub>(HCOO)<sub>6</sub> was obtained in 62% yield and dispersed in DMF for further use. Zr-BTB (5.0 μmol) was first treated with 5 mL of HCl (1 M) at 100 °C under stirring for 24 h to exchange the capping formate with water and hydroxide to afford Zr<sub>6</sub>O<sub>4</sub>(OH)<sub>4</sub>(BTB)<sub>2</sub>(OH)<sub>6</sub>(OH<sub>2</sub>)<sub>6</sub>. The resultant white solid was centrifugated and washed

with DMF three times. In an N<sub>2</sub>-filled glovebox, the above MOL (5.0 μmol) was suspended in 3 mL of toluene. TMSOTf (54.0 μL, 0.3 mmol) was then added slowly to the suspension to transform the Zr-OH/OH<sub>2</sub> sites into strongly Lewis acidic Zr-OTf sites. The mixture was stirred at room temperature for 12 h. The suspension was then washed with dry toluene 3 times to remove the soluble species to quantitatively afford Zr-BTB-OTf with a formula of Zr<sub>6</sub>O<sub>4</sub>(OH)<sub>4</sub>(BTB)<sub>2</sub>(OTf)<sub>6</sub>.

**Synthesis of Zr-OTf-EY.** Zr-BTB-OTf (5.0 μmol) and neutral Eosin Y (30 μmol) were dissolved in 20 mL dry CH<sub>3</sub>CN the mixture was stirred at 60 °C for 24 h. The red precipitate was collected by centrifugation and washed with CH<sub>3</sub>CN.

**NMR analysis of Zr-OTf-EY.** To 2 mg Hf-Ru-Au were added 600 μL DMSO-*d*<sub>6</sub>, 60 μL D<sub>3</sub>PO<sub>4</sub> and 60 μL D<sub>2</sub>O. The mixture was sonicated for 10 mins to obtain a clear solution and analyzed by <sup>1</sup>H NMR and <sup>31</sup>P NMR. <sup>1</sup>H NMR spectrum of the digested Hf-Ru-Au showed signals corresponding to EY and BTB (**Figure 4-3**).

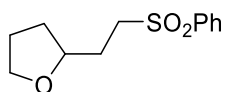
**UV-vis analysis of Zr-OTf-EY.** 10 μL of Zr-OTf-EY (or Zr-BTB-OTf, 2 mM based on Zr) was added to a mixture of 940 μL DMSO and 50 μL H<sub>3</sub>PO<sub>4</sub>. After sonicating for 10 min, a clear solution was obtained and subjected to UV analysis. The rise of an additional peak at around 540 nm in UV-vis spectrum of Zr-OTf-EY over Zr-BTB-OTf indicated the successful integration of EY into Zr-OTf-EY (**Figure 4-4b**).

#### 4.4.2 Catalytic Reactions

**General procedure for cross-coupling reactions between aliphatic C–H and electron-deficient olefins.** Electron-deficient olefin (0.2 mmol), and Zr-OTf-EY (0.1 μmol based on EY sites, 0.05 mol%) were mixed in dry THF or 1,3-dioxalane (2 mL). The resulting solution was stirred under blue LED irradiation at room temperature in an N<sub>2</sub> atmosphere for 24 h. Reactions with aldehyde substrates use 1.0 mmol aldehyde in 2 mL dry DCM. After the reaction, the solvent

was removed under vacuum. The residue was then subjected to column chromatography on silica gel using n-hexane and ethyl acetate as eluent to give the cross-coupling products.

**General procedure for cross-coupling reactions between aliphatic C–H and diethyl (*E*)-diazene-1,2-dicarboxylate.** Diethyl (*E*)-diazene-1,2-dicarboxylate (0.2 mmol) and Zr-OTf-EY (0.1  $\mu$ mol based on EY sites, 0.05 mol%) were mixed in dry THF, 1,3-dioxalane, or tetrahydro-2*H*-pyran (2 mL). Reactions with other C-H partners use 2.0 mmol substrates in 2 mL dry DCM. The resulting solution was stirred under CFL light irradiation at room temperature in an N<sub>2</sub> atmosphere for 24 h. After the reaction, the solvent was removed under vacuum. The residue was then subjected to column chromatography on silica gel using n-hexane and ethyl acetate as eluent to give the cross-coupling products.

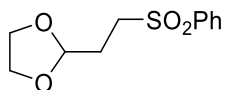


Colorless oil, 98% yield.

**<sup>1</sup>H NMR** (400 MHz, chloroform-*d*)  $\delta$  7.96 – 7.85 (comp, 2H), 7.68 – 7.60 (m, 1H), 7.57 – 7.53 (comp, 2H), 3.86 – 3.79 (m, 1H), 3.78 – 3.74 (m, 1H), 3.68 – 3.63 (m, 1H), 3.32 – 3.24 (m, 1H), 3.16 – 3.08 (m, 1H), 2.02 – 1.90 (m, 2H), 1.88 – 1.78 (comp, 3H), 1.50 – 1.39 (m, 1H);

**<sup>13</sup>C {<sup>1</sup>H} NMR** (101 MHz, chloroform-*d*)  $\delta$  139.2, 133.7, 129.3, 128.0, 67.8, 53.6, 31.2, 28.5, 25.6;

**HRMS** (ESI) scaled for [M+Na]<sup>+</sup>: C<sub>12</sub>H<sub>16</sub>O<sub>3</sub>SNa, 263.0717, observed: 263.0714. Characterization data matched that reported in literature.<sup>54</sup>

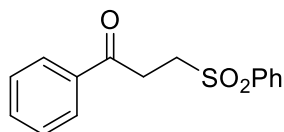


Colorless oil, 91% yield.

**<sup>1</sup>H NMR** (400 MHz, chloroform-*d*) δ 7.93 – 7.87 (comp, 2H), 7.68 – 7.62 (m, 1H), 7.60 – 7.51 (comp, 2H), 4.94 (t, *J* = 4.0 Hz, 1H), 3.94 – 3.77 (comp, 4H), 3.28 – 3.17 (m, 2H), 2.09 – 2.04 (m, 2H);

**<sup>13</sup>C {<sup>1</sup>H} NMR** (101 MHz, chloroform-*d*) δ 138.9, 133.8, 129.4, 129.3, 128.1, 128.0, 101.7, 65.2, 50.7, 27.1;

**HRMS** (ESI) scaled for [M+Na]<sup>+</sup>: C<sub>11</sub>H<sub>14</sub>O<sub>4</sub>SNa, 265.0510, observed: 265.0507.

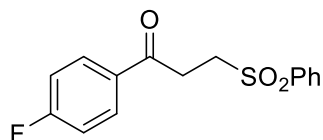


Colorless oil, 50% yield.

**<sup>1</sup>H NMR** (500 MHz, chloroform-*d*) δ 7.98 – 7.93 (comp, 2H), 7.93 – 7.88 (comp, 2H), 7.69 – 7.64 (m, 1H), 7.61 – 7.54 (comp, 3H), 7.47 – 7.44 (comp, 2H), 3.57 – 3.54 (comp, 2H), 3.50 – 3.47 (m, 2H);

**<sup>13</sup>C {<sup>1</sup>H} NMR** (101 MHz, chloroform-*d*) δ 195.4, 139.1, 135.8, 134.0, 133.8, 129.4, 128.8, 128.1, 128.0, 51.0, 31.4;

**HRMS** (ESI) scaled for [M+H]<sup>+</sup>: C<sub>15</sub>H<sub>15</sub>O<sub>3</sub>S, 275.0741, observed: 275.0721. Characterization data matched that reported in literature.<sup>24</sup>



Colorless oil, 54% yield.

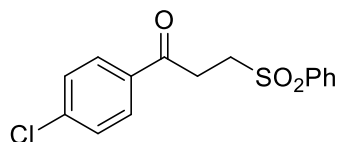
**<sup>1</sup>H NMR** (400 MHz, chloroform-*d*) δ 7.98 – 7.90 (comp, 4H), 7.70 – 7.62 (m, 1H), 7.58 – 7.53 (comp, 2H), 7.15 – 7.10 (comp, 2H), 3.56 – 3.52 (m, 2H), 3.47 – 3.43 (m, 2H);



$^{13}\text{C}$   $\{^1\text{H}\}$  NMR (101 MHz, chloroform-*d*)  $\delta$  193.85, 166.08 (d,  $J = 254$  Hz, 1C), 139.02, 133.99, 132.27 (d,  $J = 3.0$  Hz, 1C), 130.83, 130.78 (d,  $J = 9.5$  Hz, 1C), 129.25, 128.19, 127.98, 115.97 (d,  $J = 21.9$  Hz, 1C), 50.96, 31.28;

$^{19}\text{F}$   $\{^1\text{H}\}$  NMR (377 MHz, chloroform-*d*)  $\delta$  -103.74;

HRMS (ESI) scaled for  $[\text{M}+\text{H}]^+$ :  $\text{C}_{15}\text{H}_{14}\text{O}_3\text{SF}$ , 293.0647, observed: 293.0648.

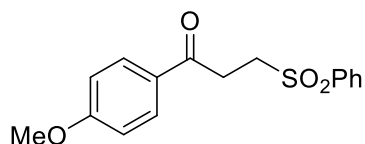


Colorless oil, 51% yield.

$^1\text{H}$  NMR (400 MHz, chloroform-*d*)  $\delta$  7.98 – 7.91 (comp, 2H), 7.88 – 7.83 (comp, 2H), 7.70 – 7.64 (m, 1H), 7.61 – 7.55 (comp, 2H), 7.47 – 7.41 (comp, 2H), 3.56 – 3.52 (m, 2H), 3.48 – 3.44 (m, 2H);

$^{13}\text{C}$   $\{^1\text{H}\}$  NMR (101 MHz, chloroform-*d*)  $\delta$  194.3, 140.3, 139.0, 134.1, 134.0, 129.5, 129.3, 128.0, 50.9, 31.3;

HRMS (ESI) scaled for  $[\text{M}+\text{Na}]^+$ :  $\text{C}_{15}\text{H}_{13}\text{O}_3\text{SNaCl}$ , 331.0171, observed: 331.0158.

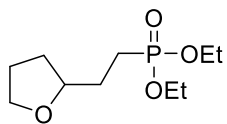


Colorless oil, 45% yield.

$^1\text{H}$  NMR (400 MHz, chloroform-*d*)  $\delta$  7.97 – 7.94 (comp, 2H), 7.92 – 7.89 (comp, 2H), 7.70 – 7.64 (m, 1H), 7.60 – 7.56 (comp, 2H), 6.96 – 6.90 (comp, 2H), 3.88 (s, 3H), 3.58 – 3.52 (m, 2H), 3.48 – 3.43 (m, 2H);

$^{13}\text{C}$   $\{^1\text{H}\}$  NMR (101 MHz, chloroform-*d*)  $\delta$  193.9, 164.0, 133.1, 130.4, 129.4, 128.0, 114.0, 55.6, 51.2, 30.9;

**HRMS** (ESI) scaled for  $[M+H]^+$ :  $C_{16}H_{17}O_4S$ , 305.0847, observed: 305.0841.

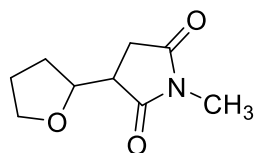


Colorless oil, 61% yield.

**$^1H$  NMR** (400 MHz, chloroform-*d*)  $\delta$  4.26 – 4.07 (comp, 4H), 3.92 – 3.81 (m, 2H), 3.75 – 3.69 (m, 1H), 2.05 – 1.94 (m, 1H), 1.92 – 1.77 (comp, 4H), 1.68 – 1.55 (m, 2H), 1.48 (s, 1H), 1.34 (s, 6H);

**$^{13}C$  { $^1H$ } NMR** (101 MHz, chloroform-*d*)  $\delta$  79.0, 67.9, 62.0, 31.1, 29.7, 28.7, 25.8, 16.6;

**HRMS** (ESI) scaled for  $[M+H]^+$ :  $C_{10}H_{22}O_4P$ , 237.1255, observed: 237.1251.

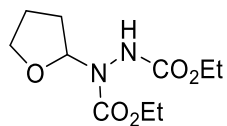


Colorless oil, 48% yield.

Report as 1:1 mixture.  **$^1H$  NMR** (400 MHz, chloroform-*d*)  $\delta$  4.32 – 4.28 (m, 1H), 4.16 – 4.12 (m, 1H), 3.86 – 3.79 (m, 4H), 3.76 – 3.69 (m, 4H), 3.14 – 3.09 (m, 1H), 2.97 (s, 3H), 2.96 (s, 3H), 2.94 – 2.89 (m, 1H), 2.81 – 2.75 (m, 1H), 2.71 – 2.57 (comp, 3H), 2.11 – 2.05 (m, 1H), 1.97 – 1.84 (comp, 6H), 1.64 – 1.57 (m, 1H);

**$^{13}C$  { $^1H$ } NMR** (101 MHz, chloroform-*d*)  $\delta$  178.22, 177.49, 176.84, 176.71, 78.56, 68.74, 68.72, 44.48, 43.35, 32.22, 29.76, 29.55, 27.59, 25.91, 25.85, 24.88, 24.76;

**HRMS** (ESI) scaled for  $[M+H]^+$ :  $C_9H_{14}O_3N$ , 184.0973, observed: 184.0970.

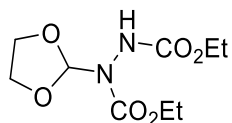


Colorless oil, 97% yield.

**<sup>1</sup>H NMR** (400 MHz, chloroform-*d*) δ 6.60 (s, 1H), 6.00 (s, 1H), 4.25 – 4.16 (comp, 4H), 4.06 – 3.95 (m, 1H), 3.79 – 3.73 (m, 1H), 2.10 – 1.95 (comp, 3H), 1.91 – 1.95 (m, 1H), 1.30 – 1.25 (comp, 6H);

**<sup>13</sup>C {<sup>1</sup>H} NMR** (101 MHz, chloroform-*d*) δ 156.7, 155.5, 87.6, 68.7, 62.8, 62.1, 28.2, 25.3, 14.4, 14.4;

**HRMS** (ESI) scaled for [M+Na]<sup>+</sup>: C<sub>10</sub>H<sub>18</sub>N<sub>2</sub>O<sub>5</sub>Na, 269.1113, observed: 269.1100.

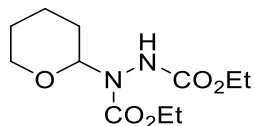


Colorless oil, 98% yield.

**<sup>1</sup>H {<sup>1</sup>H} NMR** (400 MHz, chloroform-*d*) δ 6.68 (s, 1H), 6.52 (s, 1H), 4.25 – 4.18 (comp, 4H), 4.13 – 4.11 (m, 2H), 4.0 – 3.95 (m, 2H), 1.30 – 1.25 (comp, 6H);

**<sup>13</sup>C {<sup>1</sup>H} NMR** (101 MHz, chloroform-*d*) δ 161.1, 154.4, 104.7, 65.4, 62.9, 62.2, 14.4, 14.3;

**HRMS** (ESI) scaled for [M+Na]<sup>+</sup>: C<sub>9</sub>H<sub>16</sub>N<sub>2</sub>O<sub>6</sub>Na, 271.0906, observed: 271.0903.

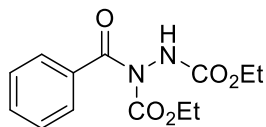


Colorless oil, 45% yield.

**<sup>1</sup>H NMR** (400 MHz, chloroform-*d*) δ 6.77 (s, 1H), 5.25 (s, 1H), 4.21 – 4.13 (comp, 4H), 3.99 (d, *J* = 11.6 Hz, 1H), 3.56 (t, *J* = 11.6 Hz, 1H), 1.92 – 1.42 (comp, 6H), 1.29 – 1.16 (comp, 6H);

**<sup>13</sup>C {<sup>1</sup>H} NMR** (101 MHz, chloroform-*d*) δ 156.7, 155.4, 84.8, 68.1, 62.8, 61.9, 29.7, 27.8, 25.0, 22.9, 14.5, 14.4;

**HRMS** (ESI) scaled for [M+Na]<sup>+</sup>: C<sub>11</sub>H<sub>21</sub>N<sub>2</sub>O<sub>5</sub>Na, 283.1269, observed: 283.1234.

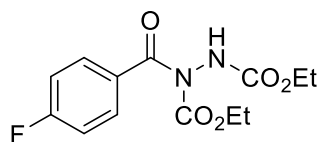


Colorless oil, 97% yield.

**<sup>1</sup>H NMR** (400 MHz, chloroform-*d*)  $\delta$  7.70 – 7.60 (comp, 2H), 7.49 (t,  $J = 7.6$  Hz, 1H), 7.39 (t,  $J = 7.6$  Hz, 2H), 4.22 (q,  $J = 7.2$  Hz, 2H), 4.12 (q,  $J = 7.2$  Hz, 2H), 1.26 (t,  $J = 7.2$  Hz, 3H), 1.04 (t,  $J = 7.2$  Hz, 3H);

**<sup>13</sup>C {<sup>1</sup>H} NMR** (101 MHz, chloroform-*d*)  $\delta$  171.1, 155.7, 153.5, 134.8, 132.0, 128.2, 128.1, 64.0, 62.7, 14.4, 13.7;

**HRMS** (ESI) scaled for  $[M+H]^+$ : C<sub>13</sub>H<sub>17</sub>N<sub>2</sub>O<sub>5</sub>, 281.1137, observed: 281.1134. Characterization data matched that reported in literature.<sup>52</sup>



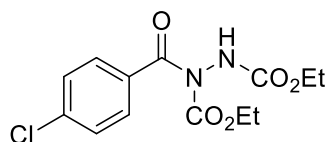
Colorless oil, 99% yield.

**<sup>1</sup>H NMR** (400 MHz, chloroform-*d*)  $\delta$  7.76 – 7.72 (comp, 2H), 7.27 (s, 1H), 7.11 (t,  $J = 8.0$  Hz, 2H), 4.27 – 4.15 (comp, 4H), 1.30 (t,  $J = 6.8$  Hz, 3H), 1.13 (t,  $J = 6.8$  Hz, 3H);

**<sup>13</sup>C {<sup>1</sup>H} NMR** (101 MHz, chloroform-*d*)  $\delta$  170.01, 165.04 (d,  $J = 254$  Hz, 1C), 155.67, 153.42, 130.95 (d,  $J = 8.9$  Hz, 1C), 115.38 (d,  $J = 22.0$  Hz, 1C), 64.12, 62.75, 14.36, 13.84;

**<sup>19</sup>F {<sup>1</sup>H} NMR** (377 MHz, chloroform-*d*)  $\delta$  -106.16.

**HRMS** (ESI) scaled for  $[M+Na]^+$ : C<sub>13</sub>H<sub>15</sub>N<sub>2</sub>O<sub>5</sub>NaF, 321.0862, observed: 321.0861.

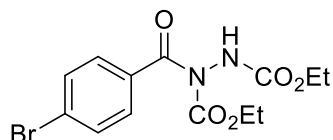


Colorless oil, 98% yield.

**<sup>1</sup>H NMR** (400 MHz, chloroform-*d*) δ 7.70 – 7.55 (comp, 2H), 7.40 (d, *J* = 7.6 Hz, 2H), 7.30 – 7.16 (m, 1H), 4.27 – 4.15 (comp, 4H), 1.30 (t, *J* = 6.8 Hz, 3H), 1.14 (t, *J* = 6.8 Hz, 3H);

**<sup>13</sup>C {<sup>1</sup>H} NMR** (101 MHz, chloroform-*d*) δ 170.1, 155.6, 153.3, 138.4, 133.1, 129.7, 128.5, 64.2, 62.8, 14.4, 13.8;

**HRMS** (ESI) scaled for [M+H]<sup>+</sup>: C<sub>13</sub>H<sub>15</sub>N<sub>2</sub>O<sub>5</sub>Cl, 315.0747, observed: 315.0747.

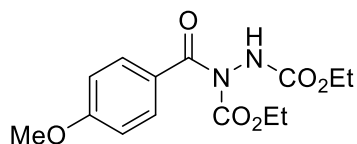


Colorless oil, 96% yield.

**<sup>1</sup>H NMR** (400 MHz, chloroform-*d*) δ 7.62 – 7.50 (comp, 4H), 7.33 – 7.20 (m, 1H), 4.27 – 4.15 (comp, 4H), 1.30 (t, *J* = 6.8 Hz, 3H), 1.14 (t, *J* = 6.8 Hz, 3H);

**<sup>13</sup>C {<sup>1</sup>H} NMR** (101 MHz, chloroform-*d*) δ 170.2, 155.6, 153.3, 133.6, 131.5, 129.8, 126.8, 64.2, 62.8, 14.4, 13.9;

**HRMS** (ESI) scaled for [M+Na]<sup>+</sup>: C<sub>13</sub>H<sub>15</sub>N<sub>2</sub>O<sub>5</sub>NaBr, 381.0061, observed: 381.0049.

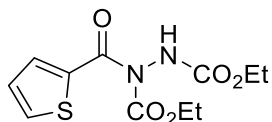


Colorless oil, 48% yield.

**<sup>1</sup>H NMR** (400 MHz, chloroform-*d*) δ 7.71 (d, *J* = 8.4 Hz, 2H), 7.10 (s, 1H), 6.90 (d, *J* = 8.4 Hz, 2H), 4.26 – 4.15 (comp, 4H), 3.85 (s, 3H), 1.27 (d, *J* = 6.8 Hz, 3H), 1.13 (t, *J* = 6.8 Hz, 3H);

**<sup>13</sup>C {<sup>1</sup>H} NMR** (101 MHz, chloroform-*d*) δ 170.4, 163.1, 155.7, 153.8, 131.1, 126.5, 113.5, 63.9, 62.6, 55.5, 14.4, 13.9;

**HRMS** (ESI) scaled for [M+Na]<sup>+</sup>: C<sub>14</sub>H<sub>18</sub>N<sub>2</sub>O<sub>6</sub>Na, 333.1062, observed: 333.1055.

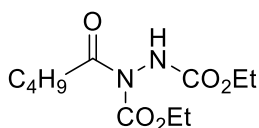


Colorless oil, 92% yield.

**$^1\text{H}$  NMR** (400 MHz, chloroform-*d*)  $\delta$  7.82 (d,  $J$  = 3.6 Hz, 1H), 7.54 (d,  $J$  = 4.8 Hz, 1H), 7.21 (d,  $J$  = 4.8 Hz, 1H), 7.02 (t,  $J$  = 4.8 Hz, 1H), 4.30 – 4.08 (comp, 4H), 1.26 – 1.15 (comp, 6H);

**$^{13}\text{C}$  { $^1\text{H}$ } NMR** (101 MHz, Chloroform-*d*)  $\delta$  162.6, 155.8, 153.4, 135.8, 134.7, 133.9, 127.3, 64.4, 62.9, 14.4, 14.1;

**HRMS** (ESI) scaled for  $[\text{M}+\text{Na}]^+$ :  $\text{C}_{11}\text{H}_{14}\text{N}_2\text{O}_5\text{SNa}$ , 309.0521, observed: 309.0513.

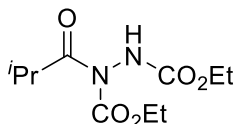


Colorless oil, 96% yield.

**$^1\text{H}$  NMR** (400 MHz, chloroform-*d*)  $\delta$  6.88 (s, 1H), 4.29 – 4.15 (comp, 4H), 2.91 – 2.77 (m, 2H), 1.65 – 1.58 (m, 2H), 1.39 – 1.22 (comp, 8H), 0.89 (t,  $J$  = 7.2 Hz, 3H);

**$^{13}\text{C}$  { $^1\text{H}$ } NMR** (101 MHz, chloroform-*d*)  $\delta$  173.9, 155.6, 153.2, 63.8, 62.5, 36.7, 26.6, 22.2, 14.3, 14.1, 13.8;

**HRMS** (ESI) scaled for  $[\text{M}+\text{H}]^+$ :  $\text{C}_{11}\text{H}_{21}\text{N}_2\text{O}_5$ , 261.1450, observed: 261.1450.

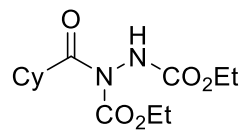


Colorless oil, 85% yield.

**$^1\text{H}$  NMR** (400 MHz, chloroform-*d*)  $\delta$  6.83 (s, 1H), 4.34 – 4.15 (comp, 4H), 3.68 – 3.61 (m, 1H), 1.36 – 1.26 (comp, 6H), 1.21 – 1.19 (comp, 6H);

**$^{13}\text{C}$  { $^1\text{H}$ } NMR** (101 MHz, chloroform-*d*)  $\delta$  178.2, 155.6, 153.1, 63.8, 62.5, 34.3, 19.2, 14.4, 14.1.

**HRMS** (ESI) scaled for  $[M+H]^+$ :  $C_{10}H_{19}N_2O_5$ , 247.1294, observed: 261.1292.

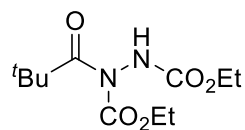


Colorless oil, 94% yield.

**$^1H$  NMR** (400 MHz, chloroform-*d*)  $\delta$  6.88 (s, 1H), 4.30 – 4.15 (comp, 4H), 3.39 – 3.32 (m, 1H), 1.95 – 1.85 (m, 2H), 1.79 – 1.74 (m, 2H), 1.68 – 1.61 (m, 1H), 1.48 – 1.39 (m, 2H), 1.34 – 1.22 (comp, 9H);

**$^{13}C$   $\{^1H\}$  NMR** (101 MHz, chloroform-*d*)  $\delta$  181.0, 177.1, 155.7, 153.2, 63.8, 62.5, 44.0, 42.8, 29.4, 28.8, 25.8, 25.7, 25.6, 25.3, 14.3, 14.1;

**HRMS** (ESI) scaled for  $[M+H]^+$ :  $C_{13}H_{22}N_2O_5$ , 287.1607, observed: 287.1614.

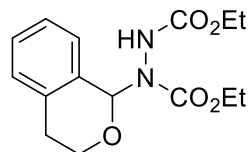


Colorless oil, 62% yield.

**$^1H$  NMR** (400 MHz, chloroform-*d*)  $\delta$  6.78 (s, 1H), 4.32 – 4.19 (comp, 4H), 1.32 (comp, 15H);

**$^{13}C$   $\{^1H\}$  NMR** (101 MHz, chloroform-*d*)  $\delta$  179.7, 156.1, 154.0, 64.1, 62.7, 42.1, 27.4, 14.4, 14.2;

**HRMS** (ESI) scaled for  $[M+Na]^+$ :  $C_{11}H_{20}N_2O_5Na$ , 283.1269, observed: 283.1233.

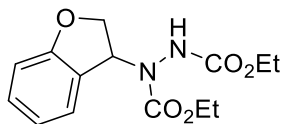


Colorless oil, 60% yield.

**$^1H$  NMR** (400 MHz, chloroform-*d*)  $\delta$  7.39 (s, 1H), 7.26 – 7.20 (comp, 2H), 7.11 – 7.10 (m, 1H), 6.60 (s, 1H), 6.43 (s, 1H), 4.29 – 4.20 (m, 2H), 4.18 – 3.85 (comp, 4H), 3.03 – 2.82 (m, 1H), 2.73 (d,  $J = 16.8$  Hz, 1H), 1.29 (t,  $J = 7.2$  Hz, 3H), 1.15 (t,  $J = 7.2$  Hz, 3H);

$^{13}\text{C}$   $\{^1\text{H}\}$  NMR (101 MHz, chloroform-*d*)  $\delta$  156.2, 135.5, 131.7, 128.4, 126.9, 126.4, 83.9, 63.1, 61.9, 29.7, 28.3, 14.4, 14.3;

HRMS (ESI) scaled for  $[\text{M}+\text{Na}]^+$ :  $\text{C}_{15}\text{H}_{20}\text{N}_2\text{O}_5\text{Na}$ , 331.1269, observed: 331.1242.

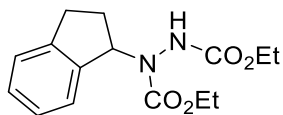


Colorless oil, 53% yield.

$^1\text{H}$  NMR (400 MHz, chloroform-*d*)  $\delta$  7.55 – 7.42 (m, 1H), 7.37 – 7.28 (comp, 2H), 7.23 (d,  $J$  = 7.6 Hz, 1H), 7.19 – 7.07 (m, 1H), 6.45 (s, 1H), 5.22 (d,  $J$  = 12.4 Hz, 1H), 5.04 (d,  $J$  = 12.4 Hz, 1H), 4.28 (q,  $J$  = 7.2 Hz, 2H), 4.02 (s, 2H), 1.31 (t,  $J$  = 7.2 Hz, 3H), 1.20 – 1.00 (m, 3H);

$^{13}\text{C}$   $\{^1\text{H}\}$  NMR (101 MHz, chloroform-*d*)  $\delta$  155.6, 139.8, 134.5, 129.0, 127.5, 123.8, 120.8, 73.0, 63.0, 61.8, 14.4, 14.3;

HRMS (ESI) scaled for  $[\text{M}+\text{H}]^+$ :  $\text{C}_{14}\text{H}_{19}\text{N}_2\text{O}_5$ , 295.1294, observed: 295.1259.



Colorless oil, 61% yield.

$^1\text{H}$  NMR (400 MHz, chloroform-*d*)  $\delta$  7.34 – 7.15 (comp, 4H), 6.19 (s, 1H), 5.87 (s, 1H), 4.30 – 4.13 (comp, 4H), 3.04 – 2.97 (m, 1H), 2.88 – 2.80 (m, 1H), 2.45 – 2.39 (m, 1H), 2.29 – 2.12 (m, 1H), 1.42 – 1.20 (comp, 6H);

$^{13}\text{C}$   $\{^1\text{H}\}$  NMR (101 MHz, chloroform-*d*)  $\delta$  156.2, 144.1, 140.5, 128.1, 126.6, 125.0, 62.7, 61.0, 30.4, 14.5, 14.4;

HRMS (ESI) scaled for  $[\text{M}+\text{Na}]^+$ :  $\text{C}_{15}\text{H}_{20}\text{N}_2\text{O}_4\text{Na}$ , 315.1320, observed: 315.1313.



## 4.5 References

1. Capaldo, L.; Ravelli, D.; Fagnoni, M., Direct Photocatalyzed Hydrogen Atom Transfer (HAT) for Aliphatic C–H Bonds Elaboration. *Chem. Rev.* **2022**, *122* (2), 1875-1924.
2. Cao, H.; Tang, X.; Tang, H.; Yuan, Y.; Wu, J., Photoinduced intermolecular hydrogen atom transfer reactions in organic synthesis. *Chem Catalysis* **2021**, *1* (3), 523-598.
3. Mayer, J. M., Understanding Hydrogen Atom Transfer: From Bond Strengths to Marcus Theory. *Acc. Chem. Res.* **2011**, *44* (1), 36-46.
4. Capaldo, L.; Ravelli, D., Hydrogen Atom Transfer (HAT): A Versatile Strategy for Substrate Activation in Photocatalyzed Organic Synthesis. *Eur. J. Org. Chem.* **2017**, *2017* (15), 2056-2071.
5. Wagner, P. J.; Hammond, G. S., Properties and Reactions of Organic Molecules in their Triplet States. In *Advances in Photochemistry*, 1968; pp 21-156.
6. Formosinho, S. J., Photochemical hydrogen abstractions as radiationless transitions. Part 2.—Thioketones, quinones, aza-aromatics, olefins and azobenzenes. *Journal of the Chemical Society, Faraday Transactions 2: Molecular and Chemical Physics* **1976**, *72* (0), 1332-1339.
7. Walling, C.; Gibian, M. J., Hydrogen Abstraction Reactions by the Triplet States of Ketones I. *J. Am. Chem. Soc.* **1965**, *87* (15), 3361-3364.
8. Burrows, H. D.; Formosinho, S. J., Photochemical hydrogen abstractions as radiationless transitions. Part 3.—Theoretical analysis of hydrogen abstraction by excited uranyl (UO) ion. *Journal of the Chemical Society, Faraday Transactions 2: Molecular and Chemical Physics* **1977**, *73* (2), 201-208.
9. Masakazu, A.; Yutaka, K., Reactivity of Excited Triplet Alkyl Ketones in Solution. I. Quenching and Hydrogen Abstraction of Triplet Acetone. *Bull. Chem. Soc. Jpn.* **1977**, *50* (8), 1913-1916.
10. Wu, Y.; Kim, D.; Teets, T. S., Photophysical Properties and Redox Potentials of Photosensitizers for Organic Photoredox Transformations. *Synlett* **2021**, *33* (12), 1154-1179.
11. Wagner, P. J.; Truman, R. J.; Scaiano, J. C., Substituent effects on hydrogen abstraction by phenyl ketone triplets. *J. Am. Chem. Soc.* **1985**, *107* (24), 7093-7097.
12. Chandra, A. K., The perturbational treatment of the process of hydrogen abstraction by ketones. *Journal of Photochemistry* **1979**, *11* (5), 347-360.
13. Péter, Á.; Agasti, S.; Knowles, O.; Pye, E.; Procter, D. J., Recent advances in the chemistry of ketyl radicals. *Chem. Soc. Rev.* **2021**, *50* (9), 5349-5365.
14. Luo, Y.; Wei, Q.; Yang, L.; Zhou, Y.; Cao, W.; Su, Z.; Liu, X.; Feng, X., Enantioselective Radical Hydroacylation of  $\alpha,\beta$ -Unsaturated Carbonyl Compounds with Aldehydes by Triplet Excited Anthraquinone. *ACS Catal.* **2022**, *12* (20), 12984-12992.
15. Dai, Z.-Y.; Nong, Z.-S.; Wang, P.-S., Light-Mediated Asymmetric Aliphatic C–H Alkylation with Hydrogen Atom Transfer Catalyst and Chiral Phosphoric Acid. *ACS Catal.* **2020**, *10* (8), 4786-4790.
16. Kuang, Y.; Wang, K.; Shi, X.; Huang, X.; Meggers, E.; Wu, J., Asymmetric Synthesis of 1,4-Dicarbonyl Compounds from Aldehydes by Hydrogen Atom Transfer Photocatalysis and Chiral Lewis Acid Catalysis. *Angew. Chem. Int. Ed.* **2019**, *58* (47), 16859-16863.
17. Cardarelli, A. M.; Fagnoni, M.; Mella, M.; Albini, A., Hydrocarbon Activation. Synthesis of  $\beta$ -Cycloalkyl (Di)nitriles through Photosensitized Conjugate Radical Addition. *J. Org. Chem.* **2001**, *66* (22), 7320-7327.

18. Zhou, M.-J.; Zhang, L.; Liu, G.; Xu, C.; Huang, Z., Site-Selective Acceptorless Dehydrogenation of Aliphatics Enabled by Organophotoredox/Cobalt Dual Catalysis. *J. Am. Chem. Soc.* **2021**, *143* (40), 16470-16485.
19. Huo, H.; Shen, X.; Wang, C.; Zhang, L.; Röse, P.; Chen, L.-A.; Harms, K.; Marsch, M.; Hilt, G.; Meggers, E., Asymmetric photoredox transition-metal catalysis activated by visible light. *Nature* **2014**, *515* (7525), 100-103.
20. Drake, T.; Ji, P.; Lin, W., Site Isolation in Metal–Organic Frameworks Enables Novel Transition Metal Catalysis. *Acc. Chem. Res.* **2018**, *51* (9), 2129-2138.
21. Feng, X.; Song, Y.; Li, Z.; Kaufmann, M.; Pi, Y.; Chen, J. S.; Xu, Z.; Li, Z.; Wang, C.; Lin, W., Metal–Organic Framework Stabilizes a Low-Coordinate Iridium Complex for Catalytic Methane Borylation. *J. Am. Chem. Soc.* **2019**, *141* (28), 11196-11203.
22. Sawano, T.; Lin, Z.; Boures, D.; An, B.; Wang, C.; Lin, W., Metal–Organic Frameworks Stabilize Mono(phosphine)–Metal Complexes for Broad-Scope Catalytic Reactions. *J. Am. Chem. Soc.* **2016**, *138* (31), 9783-9786.
23. Lv, X.-L.; Wang, K.; Wang, B.; Su, J.; Zou, X.; Xie, Y.; Li, J.-R.; Zhou, H.-C., A Base-Resistant Metalloporphyrin Metal–Organic Framework for C–H Bond Halogenation. *J. Am. Chem. Soc.* **2017**, *139* (1), 211-217.
24. Wang, Z.; Zeng, L.; He, C.; Duan, C., Metal–Organic Framework-Encapsulated Anthraquinone for Efficient Photocatalytic Hydrogen Atom Transfer. *ACS Applied Materials & Interfaces* **2022**, *14* (6), 7980-7989.
25. Cao, C.-C.; Chen, C.-X.; Wei, Z.-W.; Qiu, Q.-F.; Zhu, N.-X.; Xiong, Y.-Y.; Jiang, J.-J.; Wang, D.; Su, C.-Y., Catalysis through Dynamic Spacer Installation of Multivariate Functionalities in Metal–Organic Frameworks. *J. Am. Chem. Soc.* **2019**, *141* (6), 2589-2593.
26. Hwang, Y. K.; Hong, D.-Y.; Chang, J.-S.; Jhung, S. H.; Seo, Y.-K.; Kim, J.; Vimont, A.; Daturi, M.; Serre, C.; Férey, G., Amine Grafting on Coordinatively Unsaturated Metal Centers of MOFs: Consequences for Catalysis and Metal Encapsulation. *Angew. Chem. Int. Ed.* **2008**, *47* (22), 4144-4148.
27. Yuan, S.; Chen, Y.-P.; Qin, J.-S.; Lu, W.; Zou, L.; Zhang, Q.; Wang, X.; Sun, X.; Zhou, H.-C., Linker Installation: Engineering Pore Environment with Precisely Placed Functionalities in Zirconium MOFs. *J. Am. Chem. Soc.* **2016**, *138* (28), 8912-8919.
28. Chang, G.-G.; Ma, X.-C.; Zhang, Y.-X.; Wang, L.-Y.; Tian, G.; Liu, J.-W.; Wu, J.; Hu, Z.-Y.; Yang, X.-Y.; Chen, B., Construction of Hierarchical Metal–Organic Frameworks by Competitive Coordination Strategy for Highly Efficient CO<sub>2</sub> Conversion. *Adv. Mater.* **2019**, *31* (52), 1904969.
29. Zhou, W.; Huang, D.-D.; Wu, Y.-P.; Zhao, J.; Wu, T.; Zhang, J.; Li, D.-S.; Sun, C.; Feng, P.; Bu, X., Stable Hierarchical Bimetal–Organic Nanostructures as HighPerformance Electrocatalysts for the Oxygen Evolution Reaction. *Angew. Chem. Int. Ed.* **2019**, *58* (13), 4227-4231.
30. Wang, Y.; Jia, X.; Yang, H.; Wang, Y.; Chen, X.; Hong, A. N.; Li, J.; Bu, X.; Feng, P., A Strategy for Constructing Pore-Space-Partitioned MOFs with High Uptake Capacity for C<sub>2</sub> Hydrocarbons and CO<sub>2</sub>. *Angew. Chem. Int. Ed.* **2020**, *59* (43), 19027-19030.
31. Niu, Z.; Zhang, W.; Lan, P. C.; Aguila, B.; Ma, S., Promoting Frustrated Lewis Pairs for Heterogeneous Chemoselective Hydrogenation via the Tailored Pore Environment within Metal–Organic Frameworks. *Angew. Chem. Int. Ed.* **2019**, *58* (22), 7420-7424.
32. Chen, C.-X.; Wei, Z.-W.; Pham, T.; Lan, P. C.; Zhang, L.; Forrest, K. A.; Chen, S.; Al-Enizi, A. M.; Nafady, A.; Su, C.-Y.; Ma, S., Nanospace Engineering of Metal–Organic

Frameworks through Dynamic Spacer Installation of Multifunctionalities for Efficient Separation of Ethane from Ethane/Ethylene Mixtures. *Angew. Chem. Int. Ed.* **2021**, *60* (17), 9680-9685.

33. Lan, G.; Fan, Y.; Shi, W.; You, E.; Veroneau, S. S.; Lin, W., Biomimetic active sites on monolayered metal–organic frameworks for artificial photosynthesis. *Nat. Catal.* **2022**, *5* (11), 1006-1018.

34. Zheng, H.; Fan, Y.; Song, Y.; Chen, J. S.; You, E.; Labalme, S.; Lin, W., Site Isolation in Metal–Organic Layers Enhances Photoredox Gold Catalysis. *J. Am. Chem. Soc.* **2022**, *144* (24), 10694-10699.

35. Fan, Y.; You, E.; Xu, Z.; Lin, W., A Substrate-Binding Metal–Organic Layer Selectively Catalyzes Photoredox Ene-Carbonyl Reductive Coupling Reactions. *J. Am. Chem. Soc.* **2021**, *143* (45), 18871-18876.

36. Quan, Y.; Shi, W.; Song, Y.; Jiang, X.; Wang, C.; Lin, W., Bifunctional Metal–Organic Layer with Organic Dyes and Iron Centers for Synergistic Photoredox Catalysis. *J. Am. Chem. Soc.* **2021**, *143* (8), 3075-3080.

37. Feng, X.; Song, Y.; Lin, W., Dimensional Reduction of Lewis Acidic Metal–Organic Frameworks for Multicomponent Reactions. *J. Am. Chem. Soc.* **2021**, *143* (21), 8184-8192.

38. Quan, Y.; Lan, G.; Fan, Y.; Shi, W.; You, E.; Lin, W., Metal–Organic Layers for Synergistic Lewis Acid and Photoredox Catalysis. *J. Am. Chem. Soc.* **2020**, *142* (4), 1746-1751.

39. Feng, X.; Song, Y.; Lin, W., Transforming Hydroxide-Containing Metal–Organic Framework Nodes for Transition Metal Catalysis. *Trends in Chemistry* **2020**, *2* (11), 965-979.

40. Wang, R.; Wang, Z.; Xu, Y.; Dai, F.; Zhang, L.; Sun, D., Porous Zirconium Metal–Organic Framework Constructed from 2D → 3D Interpenetration Based on a 3,6-Connected kgd Net. *Inorg. Chem.* **2014**, *53* (14), 7086-7088.

41. Tao, Z.-R.; Wu, J.-X.; Zhao, Y.-J.; Xu, M.; Tang, W.-Q.; Zhang, Q.-H.; Gu, L.; Liu, D.-H.; Gu, Z.-Y., Untwisted restacking of two-dimensional metal-organic framework nanosheets for highly selective isomer separations. *Nat. Commun.* **2019**, *10* (1), 2911.

42. Qiao, G.-Y.; Yuan, S.; Pang, J.; Rao, H.; Lollar, C. T.; Dang, D.; Qin, J.-S.; Zhou, H.-C.; Yu, J., Functionalization of Zirconium-Based Metal–Organic Layers with Tailored Pore Environments for Heterogeneous Catalysis. *Angew. Chem. Int. Ed.* **2020**, *59* (41), 18224-18228.

43. Feng, L.; Qiu, Y.; Guo, Q.-H.; Chen, Z.; Seale, J. S. W.; He, K.; Wu, H.; Feng, Y.; Farha, O. K.; Astumian, R. D.; Stoddart, J. F., Active mechanisorption driven by pumping cassettes. *Science* **2021**, *374* (6572), 1215-1221.

44. Raviola, C.; Ravelli, D., Efficiency and Selectivity Aspects in the C–H Functionalization of Aliphatic Oxygen Heterocycles by Photocatalytic Hydrogen Atom Transfer. *Synlett* **2019**, *30* (07), 803-808.

45. Zhang, Y.; Yang, X.; Wu, J.; Huang, D., Aerobic C–H Functionalization Using Pyrenedione as the Photocatalyst. *Synthesis* **2020**, *52* (17), 2512-2520.

46. Kamijo, S.; Takao, G.; Kamijo, K.; Tsuno, T.; Ishiguro, K.; Murafuji, T., Alkylation of Nonacidic C(sp<sup>3</sup>)–H Bonds by Photoinduced Catalytic Michael-Type Radical Addition. *Org. Lett.* **2016**, *18* (19), 4912-4915.

47. Fan, X.-Z.; Rong, J.-W.; Wu, H.-L.; Zhou, Q.; Deng, H.-P.; Tan, J. D.; Xue, C.-W.; Wu, L.-Z.; Tao, H.-R.; Wu, J., Eosin Y as a Direct Hydrogen-Atom Transfer Photocatalyst for the Functionalization of C–H Bonds. *Angew. Chem. Int. Ed.* **2018**, *57* (28), 8514-8518.

48. Ji, P.; Drake, T.; Murakami, A.; Oliveres, P.; Skone, J. H.; Lin, W., Tuning Lewis Acidity of Metal–Organic Frameworks via Perfluorination of Bridging Ligands: Spectroscopic, Theoretical, and Catalytic Studies. *J. Am. Chem. Soc.* **2018**, *140* (33), 10553-10561.

49. Bariwal, J.; Van der Eycken, E., C–N bond forming cross-coupling reactions: an overview. *Chem. Soc. Rev.* **2013**, *42* (24), 9283-9303.
50. Song, G.; Wang, F.; Li, X., C–C, C–O and C–N bond formation via rhodium(iii)-catalyzed oxidative C–H activation. *Chem. Soc. Rev.* **2012**, *41* (9), 3651-3678.
51. Lundgren, R. J.; Wilsily, A.; Marion, N.; Ma, C.; Chung, Y. K.; Fu, G. C., Catalytic Asymmetric C-N Bond Formation: Phosphine-Catalyzed Intra- and Intermolecular  $\gamma$ -Addition of Nitrogen Nucleophiles to Allenates and Alkynoates. *Angew. Chem. Int. Ed.* **2013**, *52* (9), 2525-2528.
52. Zhang, H.-B.; Wang, Y.; Gu, Y.; Xu, P.-F., Lewis- and Brønsted-acid cooperative catalytic radical coupling of aldehydes and azodicarboxylate. *RSC Advances* **2014**, *4* (53), 27796-27799.
53. Papadopoulos, G. N.; Kokotos, C. G., Photoorganocatalytic One-Pot Synthesis of Hydroxamic Acids from Aldehydes. *Chem. Eur. J.* **2016**, *22* (20), 6964-6967.
54. Fan, X.-Z.; Rong, J.-W.; Wu, H.-L.; Zhou, Q.; Deng, H.-P.; Tan, J. D.; Xue, C.-W.; Wu, L.-Z.; Tao, H.-R.; Wu, J., Eosin Y as a Direct Hydrogen-Atom Transfer Photocatalyst for the Functionalization of C–H Bonds. **2018**, *57* (28), 8514-8518.

## Chapter 5. Metal-Organic Layers with Photosensitizer and Pyridine Pairs Activate Alkyl Halides for Photocatalytic Heck-type Coupling with Olefins

### 5.1 Introduction

Radical chemistry involving single-electron processes has been widely explored in the recent renaissance of photo- and electro-catalysis for chemical synthesis.<sup>1-2</sup> However, radical generation from most substrates requires strong energy input from ultraviolet light or a powerful photo-reductant, which compromises reaction selectivity.<sup>3</sup> These substrates can be pre-functionalized to enhance their photoredox activity. For example, carboxylic acids can be converted to redox-active esters which react with photo-reductants to form decarboxylated radicals.<sup>4</sup> Aldehydes can be converted  $\alpha$ -acetoxy iodides which are easier to reduce.<sup>5</sup> Haloalkanes can be activated via a halogen atom transfer process, wherein heteroatom-based radicals are generated (from silanes, amines, etc.) and used for halogen atom abstraction and alkyl radical generation,<sup>6-7</sup> or an  $S_N2$ -based strategy, wherein alkyl dithiocarbamates are converted to alkyl radicals via photoinduced C-S bond cleavage (**Figure 5-1**).<sup>8</sup>

Nitrogen-based nucleophiles have shown potential in  $S_N2$ -based activation of haloalkanes.<sup>9-10</sup> In particular, Katritzky (pyridinium) salts, originally accessed from primary amines and 2,4,6-triphenylpyrylium tetrafluoroborate, have served as radical precursors in deaminative Suzuki-Miyaura and Heck-type coupling reactions (**Figure 5-1**).<sup>11-14</sup> The reactivity of pyridinium salts is highly sensitive to their steric properties.<sup>15-18</sup> Pyridinium salts with large *ortho* substituents are readily reduced to generate radicals, but difficult to access via  $S_N2$  reactions between pyridines and haloalkanes. The opposite steric requirements on pyridinium salts limit the

use of pyridines as nucleophiles in photocatalytic activation of haloalkanes. We hypothesized that PS and pyridine pairs could be installed on MOLs to address this issue.

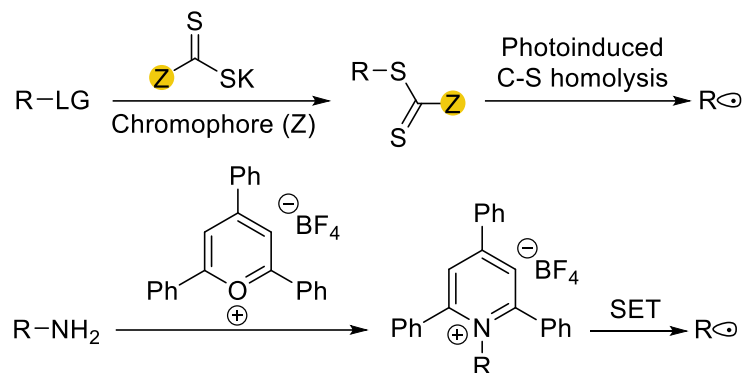


**Figure 5-1.** Radical generation from dithiocarbamates (top) and pyridinium salts (bottom).

We have demonstrated hierarchical modifications of MOLs for photocatalytic reactions by bringing PSs and catalytic sites in proximity to improve reaction kinetics.<sup>19-20</sup> We recently designed biomimetic MOL catalysts comprising heme, amino acids, and PSs for artificial photosynthesis (**Figure 5-2**).<sup>21</sup> These precedents prompted us to design PS and pyridine pairs on MOLs for cooperative photochemical alkyl radical generation from haloalkanes (**Figure 5-2**). We hypothesized that the proximity of PSs and pyridines could promote electron transfer to and radical dissociation from unsubstituted pyridinium salts which could be readily accessed via S<sub>N</sub>2 reactions of pyridines and haloalkanes.

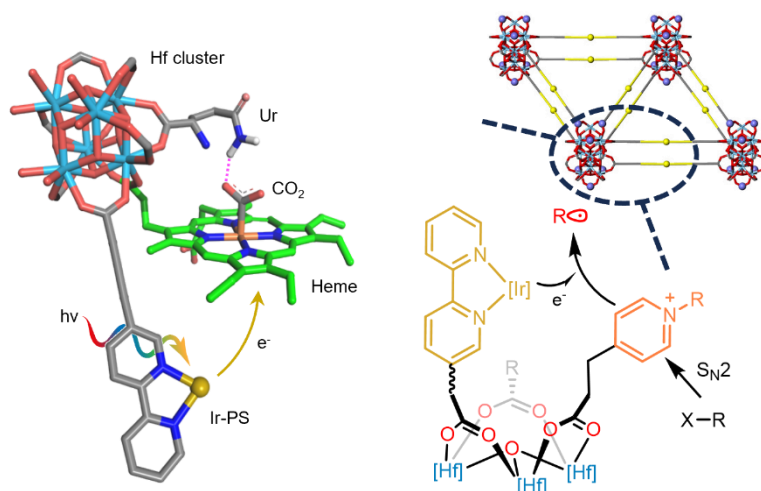


**Figure 5-2.** MOL design for biomimetic CO<sub>2</sub> reduction (left) and haloalkane activation (right).

In this chapter, we report the design of Hf<sub>12</sub> MOLs with iridium-based photosensitizing bridging ligands and SBU-supported pyridines for photocatalytic radical generation from haloalkanes. SBU-supported pyridines reacted with haloalkanes to form pyridinium salts which were reduced by nearby photoexcited Ir-based PSs to generate alkyl radicals for Heck-type coupling with alkenes. The MOL catalyst showed 4.6 times higher catalytic efficiency than the homogeneous counterpart and was used in 5 consecutive cycles without loss of activities.

## 5.2 Results and Discussion

### 5.2.1 Synthesis and Characterization of Hf-IrF-PPA

The **Hf-IrF** MOL was synthesized via a solvothermal reaction between HfCl<sub>4</sub> and **IrF** [Ir(DBB)(dF(CF<sub>3</sub>)ppy)]<sup>+</sup> in DMF with TFA as modulator at 80 °C.<sup>22</sup> **Hf-IrF** was modified with 4-pyridinepropionic acid (PPA) via a carboxylate exchange reaction to afford **Hf-IrF-PPA**. TEM imaging revealed nanoplates of **Hf-IrF** and **Hf-IrF-PPA** with diameters of 100-300 nm (**Figure 5-3a, 5-3d**), whereas AFM gave thicknesses of 1.5 and 2 nm for **Hf-IrF** and **Hf-IrF-PPA**,

respectively (Figure 5-3b, 5-3c, 5-3e, 5-3f). These thicknesses matched the heights of Hf<sub>12</sub> clusters and PPA-modified Hf<sub>12</sub> SBUs. Hf-IrF and Hf-IrF-PPA showed similar PXRD patterns to the simulated one based on the hexagonal structure of Hf-IrF (Figure 5-4). <sup>1</sup>H NMR spectrum of digested Hf-IrF-PPA indicated complete replacement of TFA by PPA with a PPA to IrF ratio of 1:1 (Figure 5-5), leading to a formula of Hf<sub>12</sub>(μ<sub>3</sub>-O)<sub>8</sub>(μ<sub>3</sub>-OH)<sub>8</sub>(μ<sub>2</sub>-OH)<sub>6</sub>(IrF)<sub>6</sub>(PPA)<sub>6</sub>.

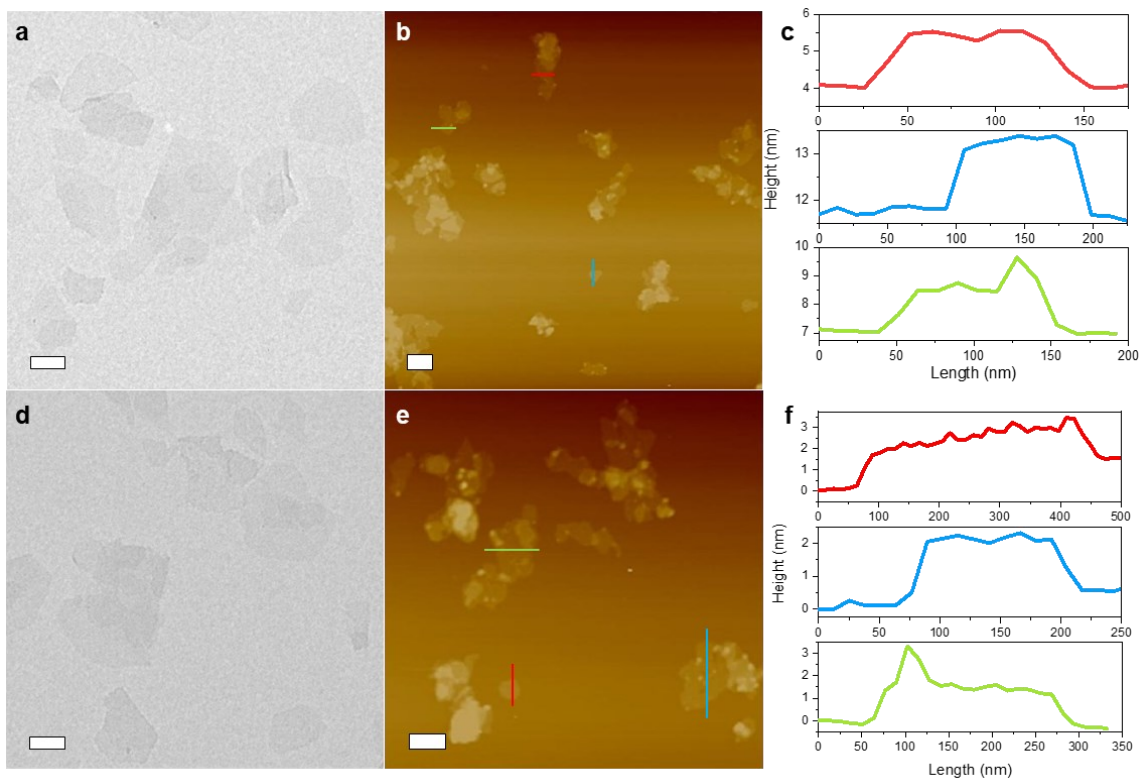


**Figure 5-3.** Morphologies of Hf-IrF and Hf-IrF-PPA. TEM images (a, d), AFM images (b, e) and height profile (c, f) of Hf-IrF and Hf-IrF-PPA. The colored height profiles in c and f correspond to the colored dashed lines in b and e, respectively.



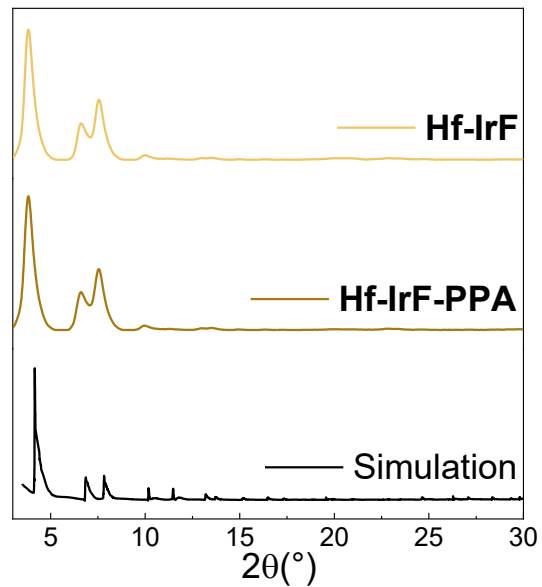


Figure 5-4. PXRD patterns of **Hf-IrF** and **Hf-IrF-PPA**.

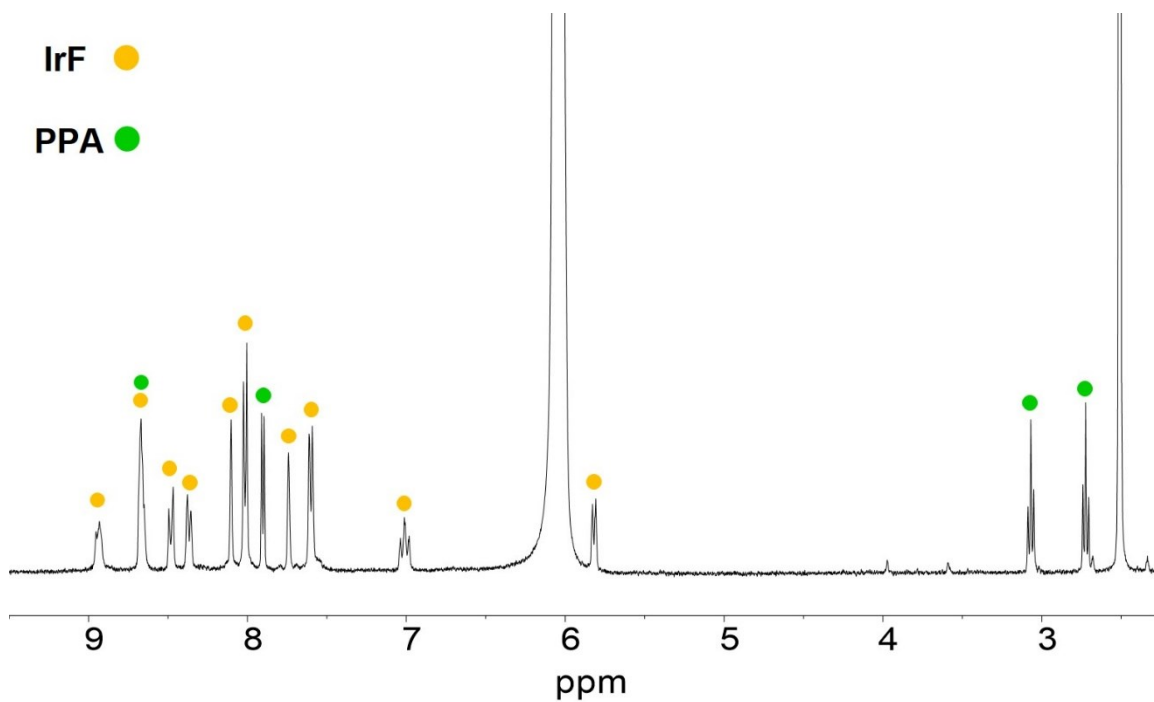
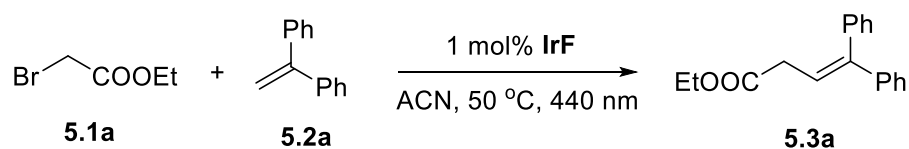


Figure 5-5.  $^1\text{H}$  NMR spectrum of digested **Hf-IrF-PPA**.

## 5.2.2 Heck-Type Coupling Reactions

We tested cross-coupling of ethyl bromoacetate (**5.1a**), an activated haloalkane, with 1,1-diphenylethylene (**5.2a**) using IrF and substituted pyridines as catalysts. The reaction conditions with pyridine, *N,N*-dimethylamino pyridine (DMAP), and 4-phenylpyridine produced ethyl 4,4-diphenylbut-3-enoate (**5.3a**) in low yields. With 120 mol% 2,4,6-collidine, the reaction proceeded smoothly in acetonitrile at 50 °C under 440 nm irradiation to give **5.3a** in 84% yield (**Table 5-1**). Thus, *ortho* substituents are essential for pyridinium reduction and alkyl radical generation.<sup>15</sup> However, with the optimized condition, sterically hindered ethyl 2-bromo propionate (**5.1c**) and un-activated 1-bromo-3-phenylpropane (**5.1j**) reacted with **5.2a** to afford **5.3j** and **5.3q** in only 49%, and 0%, respectively.

**Table 5-1.** Nucleophile screening for homogenously catalyzed reactions.



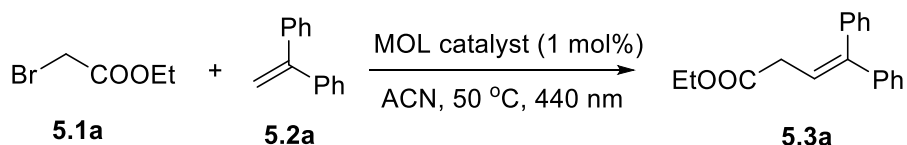
Reaction scheme showing the Heck-type coupling of ethyl bromoacetate (**5.1a**) and 1,1-diphenylethylene (**5.2a**) to form ethyl 4,4-diphenylbut-3-enoate (**5.3a**). The reaction is catalyzed by 1 mol% IrF in ACN at 50 °C under 440 nm irradiation.

Entry	Additive	Yield of <b>5.3a</b> (%)
1	20 mol% pyridine	39
2	20 mol% DMAP	23
3	20 mol% 4-phenylpyridine	55
4	20 mol% 2,4,6-collidine	69
5	120 mol% 2,4,6-collidine	84

**Hf-IrF-PPA** catalyzed photocatalytic coupling of **5.1a** and **5.2a** to afford **5.3a** in 82% yield in the presence of stoichiometric amounts of 1,8-bis(dimethylamino)naphthalene (proton sponge) and NaI. The proton sponge served as a base to neutralize the acid generated from the cross-coupling whereas NaI likely transformed **5.1a** into ethyl iodoacetate to enhance the S<sub>N</sub>2 reaction between **5.1a** and PPA.<sup>23</sup> Interestingly, although 4-phenyl pyridine and 2,4,6-collidine outperformed pyridine in homogeneous reactions, they were outperformed by PPA in MOL-

catalyzed reactions (**Table 5-2**). This result suggests enhanced alkyl radical generation from pyridinium salts on the MOL due to the proximity between the **IrF** and PPA pair.

**Table 5-2.** Nucleophile, additive and solvent screening for MOL-catalyzed reactions.

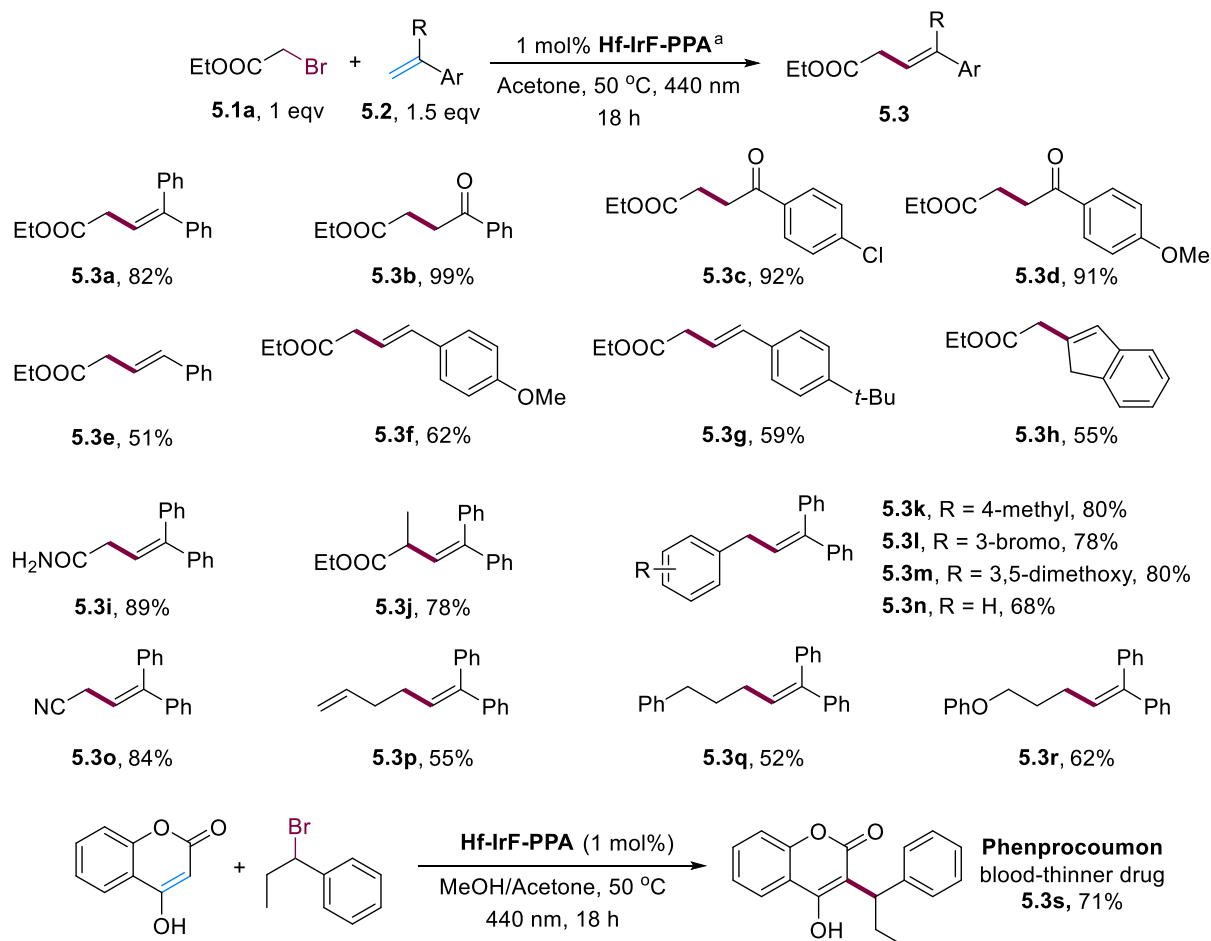


Entry	Catalyst	Additive	Yield of <b>5.3a</b> (%)
1	Hf-IrF-PPA		25
2	Hf-IrF-PhPy		20
3	Hf-IrF-PhLut		19
4	Hf-IrF-PPA	Proton sponge (1.2 eqv)	31
5	Hf-IrF-PPA	DIPEA (1.2 eqv)	11
6	Hf-IrF-PPA	DABCO (1.2 eqv)	8
7	Hf-IrF-PPA	Proton sponge (1.2 eqv) + NaI (1 eqv)	69
8 <sup>a</sup>	Hf-IrF-PPA	Proton sponge (1.2 eqv) + NaI (1 eqv)	82
9 <sup>a</sup>	Hf-IrF-PhPy	Proton sponge (1.2 eqv) + NaI (1 eqv)	79
10 <sup>a</sup>	Hf-IrF-PhLut	Proton sponge (1.2 eqv) + NaI (1 eqv)	67

<sup>a</sup>Reaction was run in 2 mL Acetone.

We next investigated the substrate scope of Heck-type coupling reactions. As shown in **Table 5-3**, **5.1a** reacted with silyl enol ethers **5.2b**, **5.2c**, and **5.2d** to give **5.3b**, **5.3c**, and **5.3d** in >90% yields. Styrene derivatives **5.2e**, **5.2f**, and **5.2g** also coupled with **5.1a** to afford **5.3e**, **5.3f**, and **5.3g** as *E* isomers in 51-62% yields. Indene (**5.2h**) reacted with **5.1a** to give **5.3h** in 55% yield. Electron-donating and aromatic substituents in the olefins were generally favored in the reactions, suggesting a cationic intermediate for double bond formation. Other activated haloalkanes, including 2-bromo acetamide (**5.1b**) and ethyl 2-bromo propionate (**5.1c**), smoothly reacted with **5.2a** to give **5.3i** and **5.3j** in 89% and 78% yields, respectively. Substituted benzyl bromides **5.1d**, **5.1e**, and **5.1f** reacted with **5.2a** to afford **5.3k**, **5.3l**, and **5.3m** in approximately 80% yields. Alkyl chlorides, including benzyl chloride (**5.1g**) and 2-chloro acetonitrile (**5.1h**), also reacted with **5.2a** to afford **5.3n** and **5.3o** in 68% and 84% yields, respectively.

**Table 5-3.** Substrate scope for MOL-catalyzed Heck-type radical coupling reactions.



<sup>a</sup>Reactions were performed with 0.2 mmol **5.1**, 0.3 mmol **5.2**, 0.2 mmol NaI, 0.24 mmol proton sponge, and 1 mol% **Hf-IrF-PPA** in 4 mL acetone at 50 °C under LED irradiation (440 nm) for 18 hrs. <sup>b</sup>Reactions were performed with **Hf-Ir(C<sup>^</sup>N)<sub>3</sub>-PPA**.

**Hf-IrF-PPA** did not catalyze cross-coupling reactions between non-activated primary alkyl bromides and **5.2a**, likely due to the limited reduction potential of **IrF**. We synthesized a new MOL, **Hf-Ir(C<sup>^</sup>N)<sub>3</sub>**, with a more reducing photosensitizing ligand, **Ir(C<sup>^</sup>N)<sub>3</sub>** {with one 4'- (5-(4-carboxyphenyl)pyridin-2-yl)-[1,1'-biphenyl]-4-carboxylate and two 2-phenylpyridine ligands}. **Hf-Ir(C<sup>^</sup>N)<sub>3</sub>** showed an ultrathin nanoplate morphology with 3-4 layers of Hf<sub>12</sub> hexagonal networks and was modified with PPA to afford **Hf-Ir(C<sup>^</sup>N)<sub>3</sub>-PPA**. **Hf-Ir(C<sup>^</sup>N)<sub>3</sub>-PPA**

successfully catalyzed cross-coupling of 4-bromo-1-butene (**5.1i**), **5.1j**, and 3-bromophenoxypropane (**5.1k**) with **5.2a** to give **5.3p**, **5.3q**, and **5.3r** in 55%, 52% and 62% yields, respectively. Under identical conditions, the homogeneous catalyst produced **5.3p**, **5.3q**, and **5.3r** in 10%, 7%, and 17% yields, respectively.

**Hf-IrF-PPA** catalyzed the cross-coupling between 4-hydroxycoumarin and 1-bromo-1-phenylpropane to produce Phenprocoumon, a blood-thinner drug, in 71% yield (**Table 5-3**). **Hf-IrF-PPA** was recycled by centrifugation and used in five cycles of cross-coupling between **5.1a** and **5.2a** without loss of catalytic activity (**Figure 5-6d**). The recovered **Hf-IrF-PPA** remained crystalline. In the sixth cycle, **Hf-IrF-PPA** was removed by centrifugation, and the yield of **5.3a** dropped to 3% with <1% Hf leaching into the solution. This experiment demonstrated the heterogeneity of MOL-catalyzed reactions.

### 5.2.3 Mechanistic Studies

We performed several control experiments to gain insights into the MOL catalysts (**Table 5-4**). A mixture of 1 mol% **IrF** and 1 mol% pyridine catalyzed the coupling between **5.1a** and **5.2a** to give **5.3a** in 18% yield. Thus, the MOL catalyst outperformed the homogeneous control by 4.6-fold. **IrF** alone or pyridine alone afforded **5.3a** in 10% and 0%, respectively. Without LED irradiation, **Hf-IrF-PPA** did not catalyze the reaction. The addition of 2,2,6,6-tetramethyl-1-piperidinyloxy (TEMPO) to the **Hf-IrF-PPA**-catalyzed reaction decreased the yield of **5.3a** from 82% to 11%. A reaction at room temperature afforded **5.3a** in 68% yield. These results indicate a strong synergy between **IrF** and PPA on the MOL and the radical nature of the cross-coupling reaction.



control, demonstrating a faster electron transfer from the photoexcited **Hf-IrF** to the PPA<sup>+</sup> on the MOL and the superiority of the MOL catalyst over the homogeneous control.

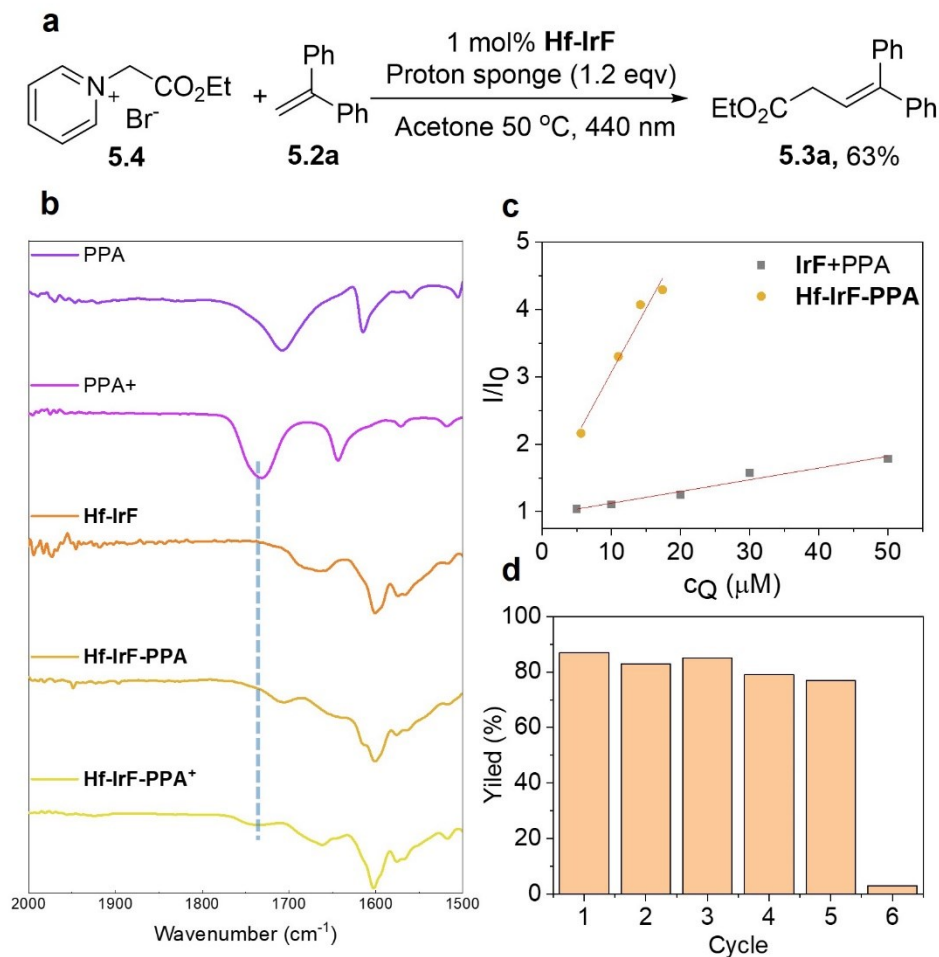


**Figure 5-6.** Mechanistic studies. (a) **Hf-IrF**-catalyzed cross-coupling between **5.4** and **5.2a**. (b) IR spectra of PPA, PPA<sup>+</sup>, **Hf-IrF**, **Hf-IrF-PPA**, and **Hf-IrF-PPA<sup>+</sup>**. (c) Photoluminescence quenching of **IrF** by PPA<sup>+</sup> in homogeneous solutions and in **Hf-IrF-PPA<sup>+</sup>**. (d) Yield of **5.3a** in 5 consecutive reactions between **5.1a** and **5.2a**.

Based on these results, we propose a reaction mechanism for **Hf-IrF-PPA**-catalyzed Heck-type coupling reactions in **Figure 5-7**. The installation of **IrF** and PPA on the MOL creates the catalyst pair in proximity (with a separation of ~11 Å). At elevated temperatures, the pyridine

undergoes a  $S_N2$  reaction with haloalkane to form a pyridinium salt, which is promptly reduced by adjacent **IrF** under light irradiation to generate an alkyl radical. The acceleration of this step by the proximity between PSs and pyridines allows the use of more nucleophilic pyridines without 2,6-substituents. The alkyl radical then adds to an olefin quickly. The adduct is oxidized by  $[\text{IrF}]^+$  to generate a carbocation intermediate which undergoes E1-type elimination to afford the cross-coupled product.<sup>26-27</sup> This mechanism explains a decrease in the reaction yield with sterically hindered or non-activated haloalkanes due to the slower pyridinium formation via the  $S_N2$  reaction. Furthermore, electron-poor olefin acceptors did not work in the reactions due to the formation of a high-energy carbocation intermediate.

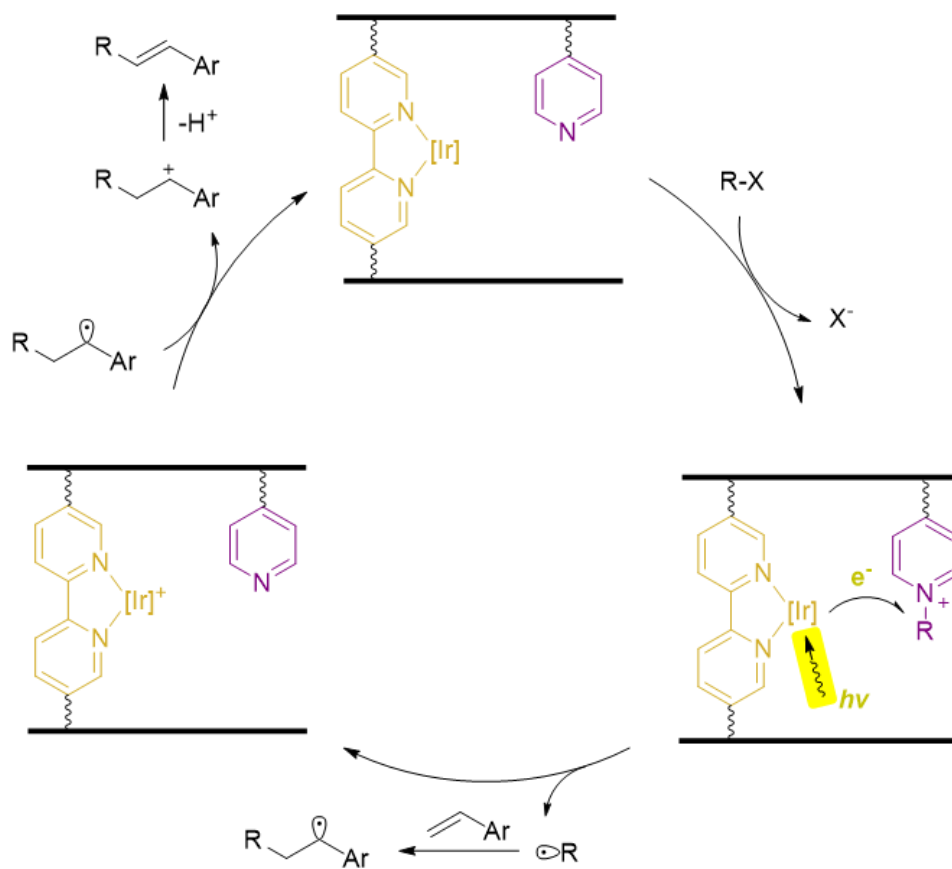


**Figure 5-7.** Proposed mechanism for Hf-IrF-PPA-catalyzed Heck-type coupling reactions.



### 5.3. Conclusion

In this chapter, we designed MOL catalysts with photosensitizer and pyridine pairs for Heck-type cross-coupling reactions between haloalkanes and olefins. The proximity of photosensitizers and pyridines on the MOL allows facile access to the pyridinium salts from S<sub>N</sub>2 reactions between haloalkanes and pyridines and enhances electron transfer from excited PSs to non-*ortho*-substituted pyridinium salts to facilitate alkyl radical generation. Consequently, the MOLs efficiently catalyze Heck-type cross-coupling reactions between haloalkanes and olefinic substrates to generate functionalized alkenes. The MOL catalyst shows 4.6 times higher catalytic efficiency than the homogeneous counterpart and is used in 5 consecutive cycles without loss of catalytic activities. This work establishes MOLs as a unique molecular material platform to discover synergistic catalysts for challenging organic transformations.

### 5.4. Methods

#### 5.4.1 Material synthesis

**Synthesis of Ir-1.** *Fac*-bis(2-phenylpyridine-C<sup>2</sup>,N')[2-(*p*-bromophenyl)-5-bromopyridine-C<sup>2</sup>,N']iridium (**Ir-1**) was synthesized according to the literature report.<sup>28</sup> Ir<sub>2</sub>(ppy)<sub>4</sub>Cl<sub>2</sub> (0.32 mmol, 343 mg), silver triflate (165 mg, 0.32 mmol), and 2-(4'-bromophenyl)-5-bromopyridine (0.6 g, 1.9 mmol) were mixed in 5 mL of degassed 2-ethoxyethanol and heated to 120 °C for 18 h. After cooling to room temperature, a yellow precipitate was collected by filtration and washed successively with water, methanol, and hexane. The crude product was purified via column chromatography with methylene chloride as eluent to afford **Ir-1** as a yellow powder (395 mg, 76%). <sup>1</sup>H NMR (400 MHz, chloroform-*d*) δ 7.90 (dd, J = 8.1, 4.6 Hz, 2H), 7.75 – 7.59 (m, 6H), 7.54 – 7.43 (m, 4H), 7.04 (dd, J = 8.3, 2.1 Hz, 1H), 6.97 – 6.79 (m, 8H), 6.78 – 6.72 (m, 1H).

**Synthesis of  $\text{Me}_2\text{Ir}(\text{C}^{\wedge}\text{N})_3$ . Ir-1** (0.15 mmol, 125 mg), 4-(methoxycarbonyl)phenylboronic acid (0.9 mmol, 163 mg),  $\text{Cs}_2\text{CO}_3$  (0.9 mmol, 296 mg), and 22 mg  $\text{PdCl}_2(\text{dppf})$  (dppf is 1,1'-bis(diphenylphosphino)ferrocene) were added to mixture of 8 mL 1,4-dioxane and 2 mL water in a 15 mL thick-walled Pyrex vessel. The mixture was heated under 80 °C under nitrogen for 2 days to afford an orange precipitate, which was purified by column chromatography to yield  $\text{Me}_2\text{Ir}(\text{C}^{\wedge}\text{N})_3$  (94 mg, 68%) as an orange solid.  **$^1\text{H NMR}$**  (500 MHz, chloroform-*d*)  $\delta$  8.00 (d, *J* = 7.6 Hz, 2H), 7.96 (d, *J* = 7.6 Hz, 2H), 7.92 (d, *J* = 8.2 Hz, 2H), 7.89 (d, *J* = 8.2 Hz, 1H), 7.79 (d, *J* = 8.5 Hz, 1H), 7.74 (d, *J* = 5.8 Hz, 2H), 7.69 – 7.66 (m, 2H), 7.59 (dd, *J* = 9.9, 5.3 Hz, 4H), 7.46 (d, *J* = 7.6 Hz, 2H), 7.28 (d, *J* = 7.7 Hz, 2H), 7.24 – 7.17 (m, 2H), 6.93 (m, *J* = 15.6, 8.8 Hz, 8H), 3.92 (s, 3H), 3.89 (s, 3H). **HRMS(ESI)** *m/z* Calcd. for  $[\text{C}_{49}\text{H}_{36}\text{IrN}_3\text{O}_4+\text{H}]^+$  924.2413, found 924.2414.

**Synthesis of  $\text{Ir}(\text{C}^{\wedge}\text{N})_3$ .**  $\text{Me}_2\text{Ir}(\text{C}^{\wedge}\text{N})_3$  (92 mg, 0.1 mmol), THF (5 mL), EtOH (5 mL), NaOH (150 mg), and  $\text{H}_2\text{O}$  (2 mL) were added to a 50 mL round bottom flask. The solution was stirred under reflux overnight. The solution was then acidified with concentrated HCl until the pH was 1. THF and MeOH were removed under reduced pressure to afford an orange precipitate. The solid was collected by centrifugation, washed with water and finally dried under vacuum to afford  $\text{Ir}(\text{C}^{\wedge}\text{N})_3$  (79 mg, 88%) as an orange solid.  **$^1\text{H NMR}$**  (400 MHz, DMSO-*d*<sub>6</sub>):  $\delta$  8.32 (d, *J* = 8.5 Hz, 1H), 8.24 – 8.13 (m, 3H), 7.98 – 7.92 (m, 3H), 7.91 – 7.84 (m, 3H), 7.84 – 7.76 (m, 3H), 7.69 (m, 2H), 7.63 (d, *J* = 5.6 Hz, 1H), 7.45 (d, *J* = 8.0 Hz, 2H), 7.39 (d, *J* = 8.4 Hz, 2H), 7.24 – 7.13 (m, 3H), 7.01 (d, *J* = 1.7 Hz, 1H), 6.90 – 6.80 (m, 2H), 6.76 (m, 4H). **HRMS(ESI):** *m/z* Calcd. for  $[\text{C}_{49}\text{H}_{36}\text{IrN}_3\text{O}_4+\text{H}]^+$  896.2100, found 896.2096.

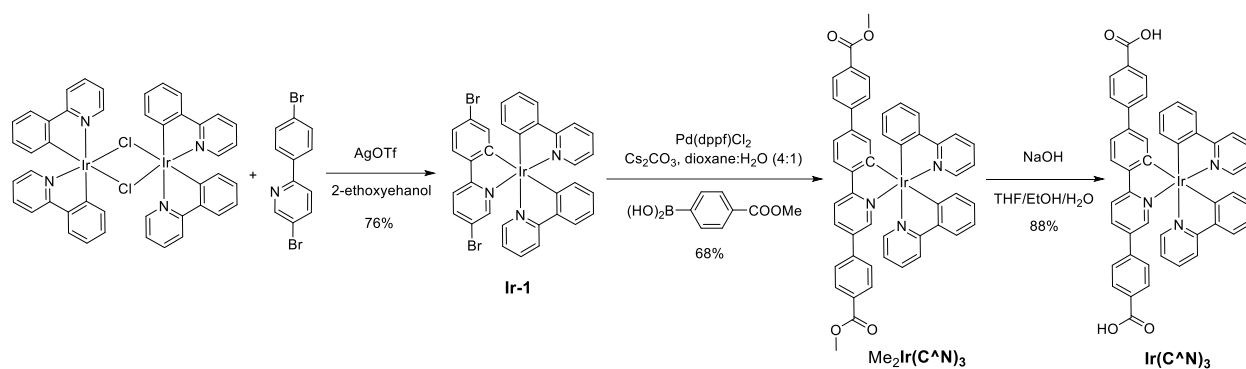


**Figure 5-8.** Synthetic scheme of  $\text{Ir}(\text{C}^{\wedge}\text{N})_3$ .

**Synthesis of Hf-IrF MOL.** Hf-IrF MOL was synthesized according to the literature report.<sup>20</sup> To a 4 mL glass vial was added 0.5 mL of  $\text{HfCl}_4$  solution (2.0 mg/mL in DMF), 0.5 mL of **IrF** solution (4.0 mg/mL in DMF), 2  $\mu\text{L}$  of TFA, and 5  $\mu\text{L}$  of  $\text{H}_2\text{O}$ . The reaction mixture was kept in an 80 °C oven for 24 hours. The yellow precipitate was collected by centrifugation and washed with DMF and ethanol. Yield: 48% based on Hf.

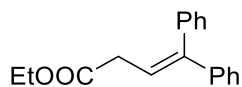
**Synthesis of Hf-Ir( $\text{C}^{\wedge}\text{N}$ )<sub>3</sub> MOL.** To a 4 mL glass vial was added 0.5 mL of  $\text{HfCl}_4$  solution (2.0 mg/mL DMF), 0.5 mL of **Ir( $\text{C}^{\wedge}\text{N}$ )<sub>3</sub>** solution (2.8 mg/mL in DMF), 1.5  $\mu\text{L}$  of DCA, and 5  $\mu\text{L}$  of  $\text{H}_2\text{O}$ . The reaction mixture was kept in a 70 °C oven for 24 hours. The orange precipitate was collected by centrifugation and washed with DMF and ethanol. Yield: 82% based on Hf. The morphology of **Hf-Ir( $\text{C}^{\wedge}\text{N}$ )<sub>3</sub>** MOL was revealed by TEM and AFM to be nanoplates of around 10 nm in height. The nanoplates contain 3~4  $\text{Hf}_{12}$  layers according to the  $\text{Hf}_{12}$  MOF structural model.

**General procedure for post-modification of MOLs with pyridines.** To 10 mL 1 mM MOL dispersion in acetonitrile (concentration based on Ir) was added 60  $\mu\text{mol}$  PPA (9.1 mg). The mixture was stirred at 60 °C for 24 h. The precipitate was then collected by centrifugation and washed with acetonitrile to afford pyridine-modified MOLs in quantitative yields.

**General procedure for NMR characterization of MOLs.** The solvent was removed from 2 mL MOL dispersion by centrifugation. The precipitate was dried under vacuum. To the resulting solid was added 500  $\mu\text{L}$   $\text{DMSO-}d_6$ , 50  $\mu\text{L}$   $\text{D}_3\text{PO}_4$ , and 50  $\mu\text{L}$   $\text{D}_2\text{O}$ . The mixture was sonicated for 10 mins to obtain a clear solution, which was analyzed by  $^1\text{H}$  NMR (**Figure 5-5**).

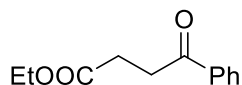
#### 5.4.2 Catalytic Reactions

**General procedure for coupling reactions between alkyl bromides and olefins.** Alkyl bromide (0.2 mmol, 1 equiv.), alkene (0.3 mmol, 1.5 equiv), **Hf-IrF-PPA** (1 mol% based on Ir, stored in acetone), NaI (30 mg, 1 equiv.), and proton sponge (51 mg, 1.2 equiv.) were mixed in 4 mL acetone in a 2-dram vial under nitrogen atmosphere. The vial was placed 10 cm away from a blue LED (emission at 440 nm). The mixture was stirred for 18 hours. After the reaction was complete, acetone was removed under reduced pressure and the product was purified by column chromatography with hexane and ethyl acetate as eluent.



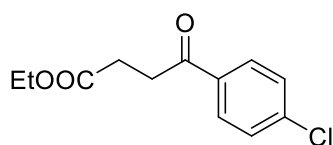
**5.3a**, yellowish solid, 82% yield.

$^1\text{H}$  NMR (400 MHz, Chloroform-*d*):  $\delta$  7.33 – 7.26 (m, 3H), 7.20 – 7.09 (m, 7H), 6.19 (t,  $J = 7.4$  Hz, 1H), 4.08 (q,  $J = 7.1$  Hz, 2H), 3.08 (d,  $J = 7.4$  Hz, 2H), 1.19 (t,  $J = 7.1$  Hz, 3H).  $^{13}\text{C}\{^1\text{H}\}$  NMR (101 MHz, chloroform-*d*):  $\delta$  171.89, 144.66, 142.01, 139.30, 129.81, 128.37, 128.15, 127.46, 127.39, 120.54, 114.30, 60.72, 35.53, 14.23. **HRMS** (ESI) calcd for  $[\text{M}+\text{H}]^+$ :  $\text{C}_{18}\text{H}_{19}\text{O}_2$ , 267.1385, observed: 267.1384.



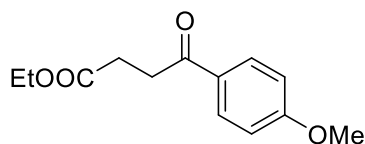
**5.3b**, yellowish liquid, 99% yield.

**<sup>1</sup>H NMR** (400 MHz, CDCl<sub>3</sub>): δ 7.98 (d, *J* = 7.2 Hz, 2H), 7.57 (t, *J* = 7.4 Hz, 1H), 7.46 (t, *J* = 7.6 Hz, 2H), 4.16 (q, *J* = 7.1 Hz, 2H), 3.31 (t, *J* = 6.7 Hz, 2H), 2.76 (t, *J* = 6.7 Hz, 2H), 1.27 (t, *J* = 7.1 Hz, 3H). **<sup>13</sup>C NMR** (101 MHz, CDCl<sub>3</sub>): δ 198.15, 172.92, 136.61, 133.21, 128.62, 128.05, 60.67, 33.41, 28.31, 14.21. **HRMS** (ESI) calcd for [M+H]<sup>+</sup>: C<sub>12</sub>H<sub>15</sub>O<sub>3</sub>, 207.1021, observed: 207.1021.



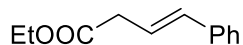
**5.3c**, white solid, 92% yield.

**<sup>1</sup>H NMR** (400 MHz, CDCl<sub>3</sub>): δ 7.91 (d, *J* = 8.3 Hz, 2H), 7.43 (d, *J* = 8.2 Hz, 2H), 4.15 (q, *J* = 7.0 Hz, 2H), 3.26 (t, *J* = 6.4 Hz, 2H), 2.74 (t, *J* = 6.3 Hz, 2H), 1.25 (t, *J* = 7.0 Hz, 3H). **<sup>13</sup>C NMR** (101 MHz, CDCl<sub>3</sub>): δ 196.97, 172.79, 139.66, 134.93, 129.48, 128.95, 60.75, 33.36, 28.23, 14.21. **HRMS** (ESI) calcd for [M+H]<sup>+</sup>: C<sub>12</sub>H<sub>14</sub>ClO<sub>3</sub>, 241.0361, observed: 241.0361.



**5.3d**, yellowish liquid, 91% yield.

**<sup>1</sup>H NMR** (400 MHz, CDCl<sub>3</sub>): δ 7.94 (d, *J* = 8.1 Hz, 2H), 6.91 (d, *J* = 8.1 Hz, 2H), 4.13 (q, *J* = 7.3 Hz, 2H), 3.84 (s, 3H), 3.24 (t, *J* = 5.8 Hz, 2H), 2.71 (t, *J* = 5.7 Hz, 2H), 1.24 (q, *J* = 6.2 Hz, 3H). **<sup>13</sup>C NMR** (101 MHz, CDCl<sub>3</sub>): δ 196.66, 173.06, 163.55, 130.30, 129.72, 113.74, 60.61, 55.48, 33.03, 28.42, 14.21. **HRMS** (ESI) calcd for [M+H]<sup>+</sup>: C<sub>13</sub>H<sub>17</sub>O<sub>4</sub>, 237.1127, observed: 237.1129.

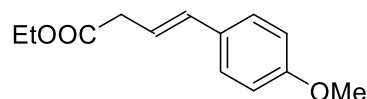


**5.3e**, yellowish liquid, 51% yield.

**<sup>1</sup>H NMR** (400 MHz, CDCl<sub>3</sub>): δ 7.38 – 7.29 (m, 5H), 6.50 (d, *J* = 15.9 Hz, 1H), 6.35 – 6.26 (m, 1H), 4.18 (q, *J* = 7.1 Hz, 2H), 3.24 (d, *J* = 7.1 Hz, 2H), 1.28 (t, *J* = 7.2 Hz, 3H). **<sup>13</sup>C NMR** (101

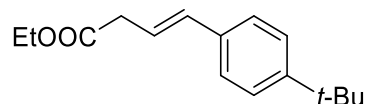
MHz, CDCl<sub>3</sub>):  $\delta$  171.62, 136.90, 133.37, 128.55, 127.55, 126.31, 121.89, 60.81, 38.52, 14.24.

**HRMS** (ESI) calcd for [M+H]<sup>+</sup>: C<sub>12</sub>H<sub>15</sub>O<sub>2</sub>, 191.1072, observed: 191.1069.



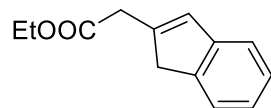
**5.3f**, white solid, 62% yield.

**<sup>1</sup>H NMR** (400 MHz, CDCl<sub>3</sub>):  $\delta$  7.28 (d,  $J$  = 8.8 Hz, 2H), 6.82 (d,  $J$  = 8.8 Hz, 2H), 6.41 (m,  $J$  = 15.7 Hz, 1H), 6.13 (dt,  $J$  = 15.8, 7.1 Hz, 1H), 4.14 (q,  $J$  = 7.1 Hz, 2H), 3.78 (s, 3H), 3.19 (dd,  $J$  = 7.1, 1.4 Hz, 2H), 1.26 (t,  $J$  = 7.2 Hz, 3H). **<sup>13</sup>C NMR** (101 MHz, CDCl<sub>3</sub>):  $\delta$  171.83, 159.16, 132.76, 129.74, 119.62, 113.95, 60.75, 55.30, 38.51, 14.24. **HRMS** (ESI) calcd for [M+H]<sup>+</sup>: C<sub>13</sub>H<sub>16</sub>O<sub>3</sub>, 221.1178, observed: 221.1179.



**5.3g**, colorless liquid, 59% yield.

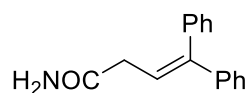
**<sup>1</sup>H NMR** (400 MHz, CDCl<sub>3</sub>):  $\delta$  7.27 – 7.22 (m, 4H), 6.39 (d,  $J$  = 15.9 Hz, 1H), 6.23 – 6.15 (m, 1H), 4.09 (d,  $J$  = 7.1 Hz, 2H), 3.15 (d,  $J$  = 6.9 Hz, 2H), 1.27-1.15 (m, 12H). **<sup>13</sup>C NMR** (101 MHz, CDCl<sub>3</sub>):  $\delta$  170.66, 149.57, 133.12, 132.05, 127.42, 124.97, 124.42, 59.70, 37.53, 33.52, 30.26, 13.20. **HRMS** (ESI) calcd for [M+H]<sup>+</sup>: C<sub>16</sub>H<sub>22</sub>O<sub>2</sub>, 247.1698, observed: 247.1698.



**5.3h**, yellowish liquid, 55% yield.

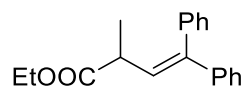
**<sup>1</sup>H NMR** (400 MHz, CDCl<sub>3</sub>):  $\delta$  7.33 (d,  $J$  = 7.3 Hz, 1H), 7.24 (d,  $J$  = 7.4 Hz, 1H), 7.15 (m, 1H), 7.07 (t,  $J$  = 7.3 Hz, 1H), 6.63 (s, 1H), 4.10 (q,  $J$  = 7.1 Hz, 2H), 3.45 (s, 2H), 3.38 (s, 2H), 1.21 (t,  $J$  = 7.1 Hz, 3H). **<sup>13</sup>C NMR** (101 MHz, CDCl<sub>3</sub>):  $\delta$  171.02, 144.78, 143.47, 141.14, 130.03, 126.33,

124.37, 123.51, 120.56, 60.90, 41.34, 37.17, 14.24. **HRMS** (ESI) calcd for  $[M+H]^+$ :  $C_{13}H_{14}O_2$ , 203.1072, observed: 203.1071.



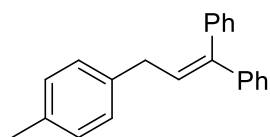
**5.3i**, brownish solid, 89% yield.

**$^1H$  NMR** (500 MHz,  $CDCl_3$ ):  $\delta$  7.43 – 7.34 (m, 4H), 7.31 – 7.28 (m, 3H), 7.22 – 7.19 (m, 3H), 6.30 (t,  $J = 7.7$  Hz, 1H), 3.09 (d,  $J = 7.7$  Hz, 2H).  **$^{13}C$  NMR** (101 MHz,  $CDCl_3$ ):  $\delta$  173.59, 145.58, 141.66, 139.10, 129.66, 128.53, 128.22, 127.61, 127.58, 127.40, 120.80, 77.39, 77.08, 76.76, 37.06. **HRMS** (ESI) calcd for  $[M+H]^+$ :  $C_{16}H_{15}NO$ , 238.1231, observed: 238.1236.



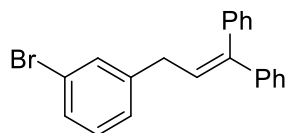
**5.3j**, colorless liquid, 78% yield.

**$^1H$  NMR** (400 MHz,  $CDCl_3$ ):  $\delta$  7.43 – 7.33 (m, 5H), 7.25 – 7.20 (m, 5H), 6.14 (d,  $J = 10.2$  Hz, 1H), 4.15 (q,  $J = 7.1$  Hz, 2H), 3.31 – 3.26 (m, 1H), 1.29 (m, 6H).  **$^{13}C$  NMR** (101 MHz,  $CDCl_3$ ):  $\delta$  175.20, 143.28, 142.21, 139.71, 130.05, 128.63, 128.56, 128.43, 128.21, 127.66, 127.63, 60.90, 40.73, 18.79, 14.51. **HRMS** (ESI) calcd for  $[M+H]^+$ :  $C_{19}H_{21}O_2$ , 281.1541, observed: 281.1542.



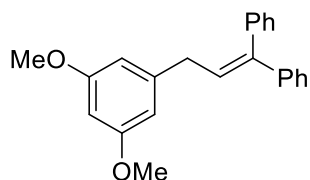
**5.3k**, yellowish solid, 80% yield.

**$^1H$  NMR** (400 MHz,  $CDCl_3$ ):  $\delta$  7.44 – 7.26 (m, 10H), 7.12 (m, 4H), 6.28 (t,  $J = 7.6$  Hz, 1H), 3.46 (d,  $J = 7.6$  Hz, 2H), 2.35 (s, 3H).  **$^{13}C$  NMR** (101 MHz,  $CDCl_3$ ):  $\delta$  142.52, 142.26, 139.89, 137.88, 135.49, 129.98, 129.19, 128.30, 128.12, 127.36, 127.12, 127.03, 35.53, 21.04. **HRMS** (ESI) calcd for  $[M-H]^+$ :  $C_{22}H_{19}$ , 283.1487, observed: 283.1489.



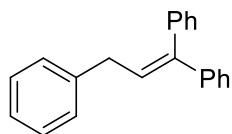
**5.3l**, colorless solid, 78% yield.

**<sup>1</sup>H NMR** (400 MHz, CDCl<sub>3</sub>): δ 7.44 (t, *J* = 7.2 Hz, 2H), 7.40 – 7.35 (m, 5H), 7.28 – 7.25 (m, 4H), 7.23 – 7.12 (m, 3H), 6.26 (t, *J* = 7.6 Hz, 1H), 3.48 (d, *J* = 7.6 Hz, 2H). **<sup>13</sup>C NMR** (101 MHz, CDCl<sub>3</sub>): δ 143.34, 143.23, 142.17, 139.59, 131.45, 130.05, 129.86, 129.18, 128.41, 128.20, 127.37, 127.32, 127.28, 127.09, 126.62, 122.60, 35.58. **HRMS** (ESI) calcd for [M-H]<sup>+</sup>: C<sub>21</sub>H<sub>16</sub>Br, 347.0431, observed: 347.0431.



**5.3m**, brown solid, 80% yield.

**<sup>1</sup>H NMR** (400 MHz, CDCl<sub>3</sub>): δ 7.42 – 7.32 (m, 4H), 7.23 (m, 6H), 6.39 – 6.31 (m, 3H), 6.26 (t, *J* = 7.6 Hz, 1H), 3.78 (s, 6H), 3.41 (d, *J* = 7.6 Hz, 2H). **<sup>13</sup>C NMR** (101 MHz, CDCl<sub>3</sub>): δ 160.86, 143.40, 142.66, 142.41, 139.79, 129.95, 128.31, 128.18, 128.13, 127.38, 127.17, 127.10, 106.51, 97.89, 36.14. **HRMS** (ESI) calcd for [M+H]<sup>+</sup>: C<sub>23</sub>H<sub>23</sub>O<sub>2</sub>, 331.1698, observed: 331.1701.

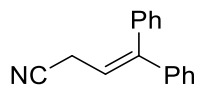


**5.3n**, colorless solid, 68% yield.

**<sup>1</sup>H NMR** (400 MHz, CDCl<sub>3</sub>): δ 7.43 – 7.16 (m, 15H), 6.29 (t, *J* = 7.6 Hz, 1H), 3.49 (d, *J* = 7.6 Hz, 2H). **<sup>13</sup>C NMR** (101 MHz, CDCl<sub>3</sub>): δ 141.43, 141.40, 139.92, 138.78, 128.90, 127.45, 127.38,

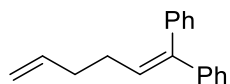


127.26, 127.08, 126.73, 126.30, 126.10, 126.02, 124.96, 34.89. **HRMS** (ESI) calcd for  $[M-H]^+$ :  $C_{21}H_{17}$ , 269.1330, observed: 269.1329.



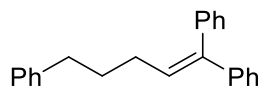
**5.3o**, dark red solid, 84% yield.

**$^1H$  NMR** (400 MHz,  $CDCl_3$ ):  $\delta$  7.48 – 7.36 (m, 3H), 7.33 – 7.27 (m, 3H), 7.23 (m, 2H), 7.20 – 7.16 (m, 2H), 6.05 (t,  $J = 7.4$  Hz, 1H), 3.15 (d,  $J = 7.4$  Hz, 2H).  **$^{13}C$  NMR** (101 MHz,  $CDCl_3$ ):  $\delta$  147.58, 140.71, 138.01, 129.40, 128.82, 128.38, 128.22, 128.16, 127.46, 118.16, 115.49, 29.73. **HRMS** (ESI) calcd for  $[M+H]^+$ :  $C_{16}H_{14}N$ , 220.1126, observed: 220.1119.



**5.3p**, colorless solid, 55% yield.

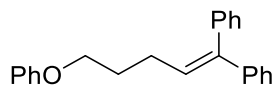
**$^1H$  NMR** (400 MHz,  $CDCl_3$ ):  $\delta$  7.42 – 7.28 (m, 8H), 7.24 – 7.19 (m, 2H), 6.12 (t,  $J = 7.0$  Hz, 1H), 5.84 (ddd,  $J = 16.9, 10.3, 6.2$  Hz, 1H), 5.10 – 4.97 (m, 2H), 2.31 – 2.18 (m, 4H).  **$^{13}C$  NMR** (101 MHz,  $CDCl_3$ ):  $\delta$  142.79, 141.95, 141.51, 140.20, 138.13, 129.92, 129.20, 128.28, 128.17, 128.08, 127.72, 127.26, 126.91, 126.86, 114.94, 114.31, 34.05, 29.14. **HRMS** (ESI) calcd for  $[M+H]^+$ :  $C_{18}H_{19}$ , 235.1481, observed: 235.1480.



**5.3q**, yellowish solid, 52% yield.

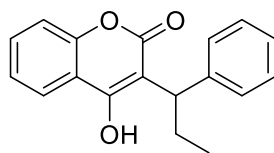
**$^1H$  NMR** (400 MHz,  $CDCl_3$ ):  $\delta$  7.30 – 7.23 (m, 3H), 7.17 – 7.13 (m, 7H), 7.10 – 7.04 (m, 5H), 6.03 (t,  $J = 7.5$  Hz, 1H), 2.57 – 2.49 (t,  $J = 7.8$  Hz, 2H), 2.10 (q,  $J = 7.4$  Hz, 2H), 1.70 (p,  $J = 7.6$  Hz, 2H).  **$^{13}C$  NMR** (101 MHz,  $CDCl_3$ ):  $\delta$  142.84, 142.38, 141.97, 140.21, 129.94, 129.66, 128.40,

128.27, 128.15, 128.09, 127.25, 126.88, 126.84, 125.68, 35.50, 31.73, 29.42. **HRMS** (ESI) calcd for  $[M+H]^+$ :  $C_{23}H_{23}$ , 299.1800, observed: 299.1794.



**5.3r**, white solid, 62% yield.

**$^1H$  NMR** (400 MHz,  $CDCl_3$ ):  $\delta$  7.32 (m, 3H), 7.24 (m, 7H), 7.16 (d,  $J = 6.8$  Hz, 2H), 6.92 (t,  $J = 7.3$  Hz, 1H), 6.85 (d,  $J = 8.1$  Hz, 2H), 6.12 (t,  $J = 7.5$  Hz, 1H), 3.94 (t,  $J = 6.4$  Hz, 2H), 2.31 (q,  $J = 7.4$  Hz, 2H), 1.93 (p,  $J = 6.7$  Hz, 2H).  **$^{13}C$  NMR** (101 MHz,  $CDCl_3$ ):  $\delta$  158.94, 142.63, 142.47, 140.04, 129.89, 129.42, 128.78, 128.22, 128.13, 127.23, 126.98, 126.96, 120.56, 114.49, 67.06, 29.55, 26.36. **HRMS** (ESI) calcd for  $[M+H]^+$ :  $C_{23}H_{23}O$ , 315.1749, observed: 315.1752.



**5.3s**, white solid, 71% yield. The solvent was changed to 1/1(v/v) methanol/acetone to dissolve starting materials.

**$^1H$  NMR** (400 MHz,  $CDCl_3$ ):  $\delta$  7.70 (dd,  $J = 7.9, 1.2$  Hz, 1H), 7.54 – 7.46 (m, 3H), 7.40 (t,  $J = 7.6$  Hz, 2H), 7.30 (t,  $J = 7.4$  Hz, 2H), 7.22 (t,  $J = 7.9$  Hz, 1H), 4.53 (t,  $J = 7.7$  Hz, 1H), 2.32 – 2.06 (m, 2H), 1.07 (t,  $J = 7.3$  Hz, 3H).  **$^{13}C$  NMR** (101 MHz,  $CDCl_3$ ):  $\delta$  163.78, 159.96, 152.59, 141.21, 131.84, 129.61, 127.69, 127.61, 123.83, 122.84, 116.41, 116.04, 108.94, 41.71, 24.00, 12.35. **HRMS** (ESI) calcd for  $[M+H]^+$ :  $C_{18}H_{17}O_3$ , 281.1177, observed: 281.1177.

## 5.5 References

1. Yan, M.; Kawamata, Y.; Baran, P. S., Synthetic Organic Electrochemical Methods Since 2000: On the Verge of a Renaissance. *Chem. Rev.* **2017**, *117* (21), 13230-13319.

2. Shaw, M. H.; Twilton, J.; MacMillan, D. W. C., Photoredox Catalysis in Organic Chemistry. *J. Org. Chem.* **2016**, *81* (16), 6898-6926.
3. Studer, A.; Curran, D. P., Catalysis of Radical Reactions: A Radical Chemistry Perspective. *Angew. Chem. Int. Ed.* **2016**, *55* (1), 58-102.
4. Okada, K.; Okamoto, K.; Morita, N.; Okubo, K.; Oda, M., Photosensitized decarboxylative Michael addition through N-(acyloxy)phthalimides via an electron-transfer mechanism. *J. Am. Chem. Soc.* **1991**, *113* (24), 9401-9402.
5. Wang, L.; Lear, J. M.; Rafferty, S. M.; Fosu, S. C.; Nagib, D. A., Ketyl radical reactivity via atom transfer catalysis. *Science* **2018**, *362* (6411), 225-229.
6. Juliá, F.; Constantin, T.; Leonori, D., Applications of Halogen-Atom Transfer (XAT) for the Generation of Carbon Radicals in Synthetic Photochemistry and Photocatalysis. *Chem. Rev.* **2022**, *122* (2), 2292-2352.
7. Zhang, P.; Le, C. C.; MacMillan, D. W. C., Silyl Radical Activation of Alkyl Halides in Metallaphotoredox Catalysis: A Unique Pathway for Cross-Electrophile Coupling. *J. Am. Chem. Soc.* **2016**, *138* (26), 8084-8087.
8. Schweitzer-Chaput, B.; Horwitz, M. A.; de Pedro Beato, E.; Melchiorre, P., Photochemical generation of radicals from alkyl electrophiles using a nucleophilic organic catalyst. *Nat. Chem.* **2019**, *11* (2), 129-135.
9. Liu, Q.; Yi, H.; Liu, J.; Yang, Y.; Zhang, X.; Zeng, Z.; Lei, A., Visible-Light Photocatalytic Radical Alkenylation of  $\alpha$ -Carbonyl Alkyl Bromides and Benzyl Bromides. *Chem. Eur. J.* **2013**, *19* (16), 5120-5126.
10. Su, Y.; Zhang, L.; Jiao, N., Utilization of Natural Sunlight and Air in the Aerobic Oxidation of Benzyl Halides. *Org. Lett.* **2011**, *13* (9), 2168-2171.
11. Basch, C. H.; Liao, J.; Xu, J.; Pian, J. J.; Watson, M. P., Harnessing Alkyl Amines as Electrophiles for Nickel-Catalyzed Cross Couplings via C–N Bond Activation. *J. Am. Chem. Soc.* **2017**, *139* (15), 5313-5316.
12. Jiang, X.; Zhang, M.-M.; Xiong, W.; Lu, L.-Q.; Xiao, W.-J., Deaminative (Carbonylative) Alkyl-Heck-type Reactions Enabled by Photocatalytic C–N Bond Activation. *Angew. Chem. Int. Ed.* **2019**, *58* (8), 2402-2406.
13. Katritzky, A. R.; Manzo, R. H.; Lloyd, J. M.; Patel, R. C., Mechanism of the Pyrylium/Pyridinium Ring Interconversion. Mild Preparative Conditions for Conversion of Amines into Pyridinium Ions. *Angewandte Chemie International Edition in English* **1980**, *19* (4), 306-306.
14. Yang, Z.-K.; Xu, N.-X.; Wang, C.; Uchiyama, M., Photoinduced C(sp<sup>3</sup>)–N Bond Cleavage Leading to the Stereoselective Syntheses of Alkenes. *Chem. Eur. J.* **2019**, *25* (21), 5433-5439.
15. Tcyrulnikov, S.; Cai, Q.; Twitty, J. C.; Xu, J.; Atifi, A.; Bercher, O. P.; Yap, G. P. A.; Rosenthal, J.; Watson, M. P.; Kozlowski, M. C., Dissection of Alkylpyridinium Structures to Understand Deamination Reactions. *ACS Catal.* **2021**, *11* (14), 8456-8466.
16. He, F.-S.; Ye, S.; Wu, J., Recent Advances in Pyridinium Salts as Radical Reservoirs in Organic Synthesis. *ACS Catal.* **2019**, *9* (10), 8943-8960.
17. Grimshaw, J.; Moore, S.; Thompson, N.; Trocha-Grimshaw, J., Carbon–nitrogen bond cleavage in  $\pi$ -radicals derived by reduction of N-benzyl- and N-allyl-pyridinium salts. *J. Chem. Soc., Chem. Commun.* **1983**, (14), 783-784.
18. Fortage, J.; Peltier, C.; Perruchot, C.; Takemoto, Y.; Teki, Y.; Bedioui, F.; Marvaud, V.; Dupeyre, G.; Pospíšil, L.; Adamo, C.; Hromadová, M.; Ciofini, I.; Lainé, P. P., Single-Step versus

Stepwise Two-Electron Reduction of Polyarylpyridiniums: Insights from the Steric Switching of Redox Potential Compression. *J. Am. Chem. Soc.* **2012**, *134* (5), 2691-2705.

19. Fan, Y.; You, E.; Xu, Z.; Lin, W., A Substrate-Binding Metal–Organic Layer Selectively Catalyzes Photoredox Ene-Carbonyl Reductive Coupling Reactions. *J. Am. Chem. Soc.* **2021**, *143* (45), 18871-18876.

20. Fan, Y.; Zheng, H.; Labalme, S.; Lin, W., Molecular Engineering of Metal–Organic Layers for Sustainable Tandem and Synergistic Photocatalysis. *J. Am. Chem. Soc.* **2023**, *145* (7), 4158-4165.

21. Lan, G.; Fan, Y.; Shi, W.; You, E.; Veroneau, S. S.; Lin, W., Biomimetic active sites on monolayered metal–organic frameworks for artificial photosynthesis. *Nat. Catal.* **2022**, *5* (11), 1006-1018.

22. Lan, G.; Quan, Y.; Wang, M.; Nash, G. T.; You, E.; Song, Y.; Veroneau, S. S.; Jiang, X.; Lin, W., Metal–Organic Layers as Multifunctional Two-Dimensional Nanomaterials for Enhanced Photoredox Catalysis. *J. Am. Chem. Soc.* **2019**, *141* (40), 15767-15772.

23. Finkelstein, H., Darstellung organischer Jodide aus den entsprechenden Bromiden und Chloriden. *Berichte der deutschen chemischen Gesellschaft* **1910**, *43* (2), 1528-1532.

24. Wang, J.-X.; Wang, Y.-T.; Zhang, H.; Fu, M.-C., Visible-light-induced iodine-anion-catalyzed decarboxylative/deaminative C–H alkylation of enamides. *Organic Chemistry Frontiers* **2021**, *8* (16), 4466-4472.

25. Fu, M.-C.; Shang, R.; Zhao, B.; Wang, B.; Fu, Y., Photocatalytic decarboxylative alkylations mediated by triphenylphosphine and sodium iodide. *Science* **2019**, *363* (6434), 1429-1434.

26. Ishiguro, K.; Nakano, T.; Shibata, H.; Sawaki, Y., Redox Reaction of Benzyl Radicals with Aromatic Radical Ions Photogenerated. The Marcus Inverted Region and the Selective Formation of Carbocations or Carbanions. *J. Am. Chem. Soc.* **1996**, *118* (31), 7255-7264.

27. Lowry, M. S.; Goldsmith, J. I.; Slinker, J. D.; Rohl, R.; Pascal, R. A.; Malliaras, G. G.; Bernhard, S., Single-Layer Electroluminescent Devices and Photoinduced Hydrogen Production from an Ionic Iridium(III) Complex. *Chem. Mater.* **2005**, *17* (23), 5712-5719.

28. Langecker, J.; Karg, O.; Meusinger, R.; Rehahn, M., The synthesis of brominated heteroleptic tris-cyclometallated Ir(III)-complexes as photoactive building blocks on polyaryl backbones. *J. Organomet. Chem.* **2018**, *862*, 105-116.

# Chapter 6. Molecular Engineering of Metal-Organic Layers for Sustainable Photocatalysis

## 6.1 Introduction

In the chapters 2 through 5, we have discussed four examples utilizing material design of MOL to facilitate synergistic photoredox catalysis. These MOL catalysts can be readily recovered from reaction mixtures by simple centrifugation or filtration and exhibit enhanced stability over their homogeneous counterparts due to active site isolation which shuts down common multimolecular catalyst deactivation pathways.<sup>1-2</sup> The ease of recovery and the extended catalyst lifetime enable the efficient reuse of MOL catalysts to reduce the consumption of precious resources, the generation of hazardous waste materials, and the economic costs.<sup>3</sup>

Despite their great potential for sustainable catalysis, the difficulty in MOL synthesis and characterization presents a significant bottleneck for the further development of MOL catalysts. To date, only  $\text{Hf}_6$  and  $\text{Hf}_{12}$  SBUs have been combined with a limited number of bridging ligands to construct MOLs.<sup>4-6</sup> Although several 2D MOFs based on Zn, Cu, and Al SBUs have been reported,<sup>7-10</sup> they lack stability or cannot be post-synthetically modified for catalytic applications. In recent work, a porphyrinic  $\text{Hf}_{12}$ -MOL was successfully synthesized by screening a library of monocarboxylate modulators.<sup>6</sup> Tuning the modulator from acetic acid to propionic acid downsized the product from a 3D MOF to a 2D MOL. Further development of synthetic methods for multifunctional MOLs should allow the design of a new generation of sustainable catalysts.

In the renaissance of visible-light-mediated photoredox chemistry, recent efforts have been devoted to organic transformations that cannot be readily accessed in a single catalytic cycle.<sup>11-12</sup> As an Earth-abundant element, cobalt has attracted particular attention due to its ability to mediate

radical chemistry and catalyze dehydrogenative reactions.<sup>13-24</sup> Leonori and coworkers recently reported a tandem photochemical method for aniline synthesis from cyclohexanones and amines using cobaloximes as dehydrogenation catalysts.<sup>25</sup> With a wide substrate scope, this method can access and simplify the preparation of important pharmaceuticals. In another work, they discovered a halogen-atom transfer (XAT) mechanism for the activation of alkyl and aryl halides. By combining the XAT process and cobaloxime-mediated dehydrogenation, they realized synergistic Heck-type coupling reactions between alkyl iodides and aryl olefins.<sup>26</sup> Considering the synthetic utility of these methods, we set out to design multifunctional MOLs as sustainable catalysts to realize these transformations.

In this chapter, we report molecular engineering of MOLs for sustainable tandem and synergistic photoredox catalysis (**Figure 6-1**). Hierarchical assemblies of photosensitizers and cobaloximes in the MOLs afforded recyclable and reusable multifunctional catalysts for tandem dehydrogenative coupling reactions between amines and cyclohexanones as well as synergistic Heck-type coupling reactions between alkyl iodides and aryl olefins. A wide scope of aniline and alkene derivatives were obtained in good to excellent yields (up to 95%). The MOL catalysts were also applied to late-stage functionalization and synthesis of bioactive molecules. Gram-scale synthesis of vesnarinone, a cardiogenic agent, was achieved in 80% yield and with a TON of 400.

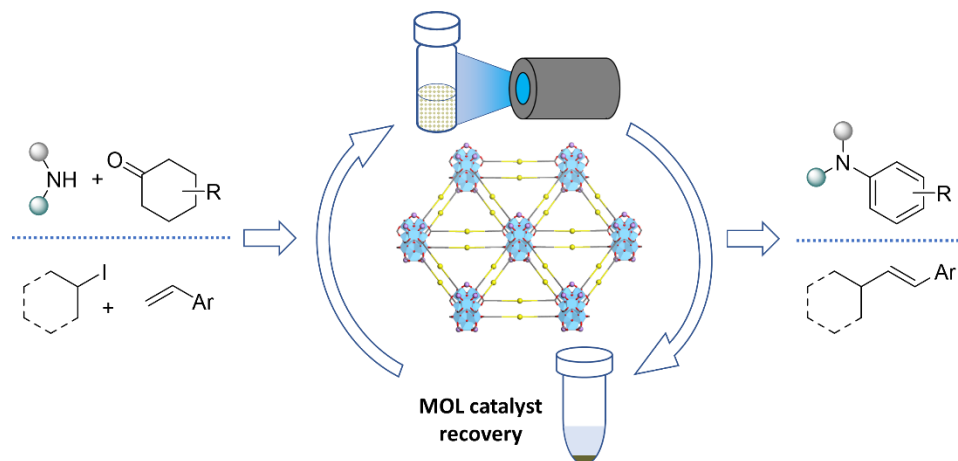


**Figure 6-1.** Dehydrogenative coupling reactions catalyzed by MOLs comprising photosensitizers and cobaloximes.

## 6.2 Results and Discussion

### 6.2.1 Synthesis and Characterization of MOLs

A new MOL, Hf-Ir, and two known MOLs, Hf-Ru and Hf-IrF, composed of Hf<sub>12</sub> SBUs and different PSs (Ir-PS, IrF-PS, Ru-PS), were synthesized via solvothermal synthesis in the presence of appropriate modulators (**Figure 6-2**). The modulators play an essential role in MOL synthesis to produce monolayered coordination networks by suppressing the coordination of the bridging dicarboxylate ligands to the SBUs along the vertical direction. The use of dichloroacetic acid (DCA) as modulator led to the successful synthesis of Hf-Ir MOL which was inaccessible by previous methods using TFA or acetic acid.<sup>27</sup> Hf-IrF and Hf-Ru were also successfully synthesized using TFA as modulator. In the proposed structural model of the MOLs, each Hf<sub>12</sub> SBU is laterally connected to 12 bidentate ligands to form a double-decker structure. The six remaining coordination sites on the top and bottom of each SBU are capped by monocarboxylate modulators. DCA and TFA modulators could be replaced by more basic carboxylates to install transition metal

catalysts. By using this post-synthetic modification strategy, Hf-Ir, Hf-IrF, and Hf-Ru were further modified with two carboxylate-modified cobaloxime catalysts, Co-PPA and Co-PAPA, to yield six MOLs, Hf-Ir-Co-PPA, Hf-Ir-Co-PAPA, Hf-IrF-Co-PPA, Hf-IrF-Co-PAPA, Hf-Ru-Co-PPA, and Hf-Ru-Co-PAPA (**Figure 6-2**).

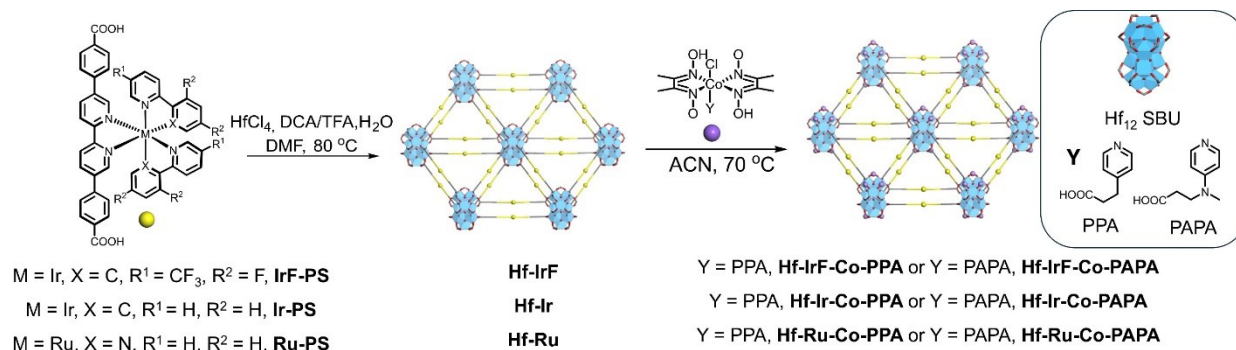


**Figure 6-2.** Synthetic schemes of MOLs.

TEM, HRTEM, and FFT of HRTEM images revealed Hf-Ir-Co-PPA as flat nanoplates with a diameter of approximately 200 nm and a periodic lattice structure of hexagonal symmetry (**Figure 6-3a, 6-3b**). The thickness of the nanoplates was measured by AFM to be approximately 2.2 nm (**Figure 6-3c**), slightly higher than the height of Hf<sub>12</sub> cluster (1.7 nm) in the proposed monolayer structure. The height difference was attributed to the SBU-bound cobaloxime complexes that were introduced by replacing the smaller DCA. Hf-Ir and Hf-Ir-Co-PPA showed similar PXRD patterns to the simulated one for Hf-Ir MOL (**Figure 6-3d**). EXAFS analysis of Hf-Ir-Co-PPA revealed that the coordination environments of Ir and Co in the MOL were identical to those of Ir(ppy)<sub>2</sub>(bpy) and chloro(pyridine)cobaloxime, respectively, indicating that the structures of the molecular PS ligand and cobaloxime catalyst remained intact during the assembly of the Hf-Ir-Co-PPA MOL (**Figure 6-3e, 6-3f**).



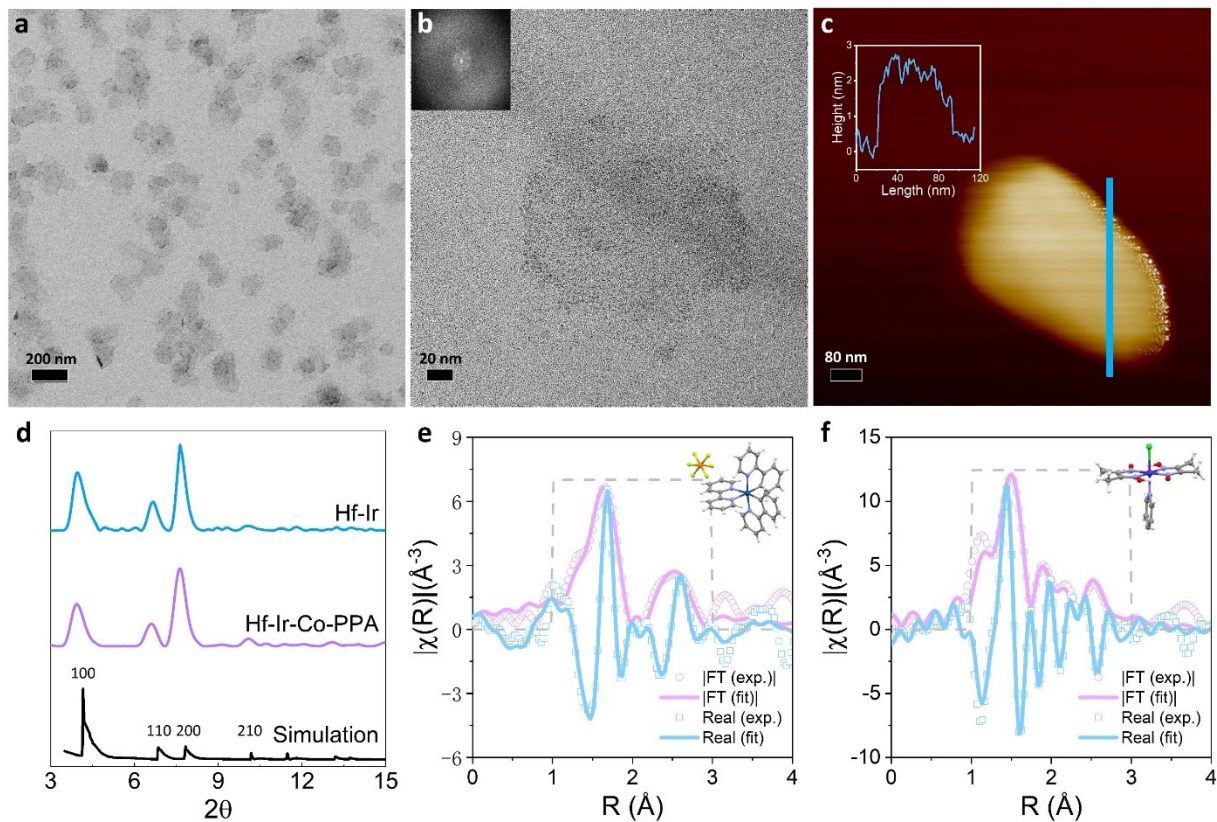


**Figure 6-3.** Characterization of Hf-Ir-Co-PPA. (a) TEM image of Hf-Ir-Co-PPA. (b) HRTEM image of Hf-Ir-Co-PPA. FFT pattern is shown in the inset. (c) AFM image of Hf-Ir-Co-PPA. The height profile is shown in the inset. (d) PXRD patterns of Hf-Ir, Hf-Ir-Co-PPA, and simulated PXRD pattern of Hf-Ir. Miller indices are shown for the corresponding peaks in the simulated PXRD pattern. (e) EXAFS analysis of Ir in Hf-Ir-Co-PPA. The structure of the fitting model, Ir(ppy)<sub>2</sub>(bpy), is shown in the inset. (f) EXAFS analysis of Co in Hf-Ir-Co-PPA. The structure of the fitting model, Co(dmgh)<sub>2</sub>(Py)Cl, is shown in the inset.

ICP-MS showed that Hf-Ir-Co-PPA had a Hf:Ir:Co molar ratio of 1:0.54:0.40, suggesting an empirical formula of Hf<sub>12</sub>(μ<sub>3</sub>-O)<sub>8</sub>(μ<sub>3</sub>-OH)<sub>8</sub>(μ<sub>2</sub>-OH)<sub>6</sub>(Ir-PS)<sub>6.5</sub>(Co-PPA)<sub>4.8</sub>(DCA)<sub>0.7</sub>. The slightly higher Ir-PS to Hf ratio of 6.5:12 than the theoretical ratio of 6:12 for the infinite 2D structure indicates terminating Ir-PS ligand on the edges of the MOL of 200 nm in dimensions. This

formulation was supported by  $^1\text{H}$  NMR analysis of the digested Hf-Ir-Co-PPA which showed Co-PPA to Ir-PS molar ratio of 0.76:1 (**Figure 6-4**).

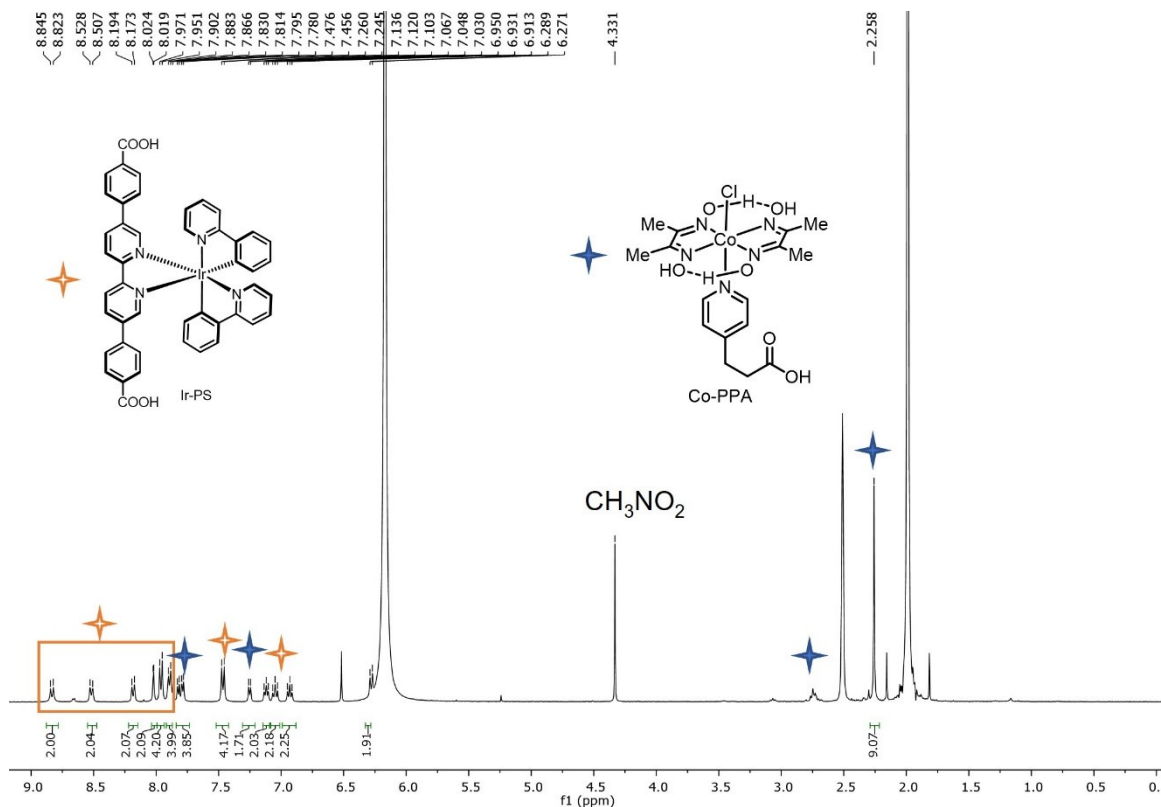


**Figure 6-4.**  $^1\text{H}$  NMR spectrum of digested Hf-Ir-Co-PPA in  $\text{DMSO-}d_6$ .

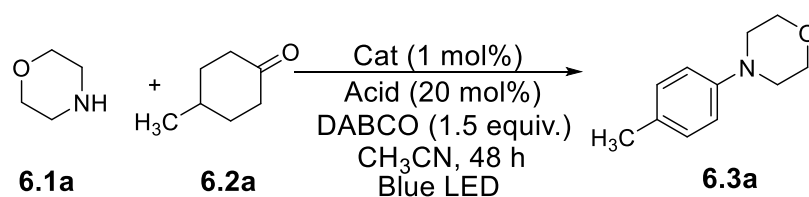
TEM, HRTEM, and AFM studies revealed that Hf-Ir-Co-PAPA, Hf-IrF-Co-PPA, Hf-IrF-Co-PAPA, Hf-Ru-Co-PPA, and Hf-Ru-Co-PAPA exhibited similar nanoplate morphologies to Hf-Ir-Co-PPA. As expected, the morphologies of these cobaloxime-modified MOLs were identical to the unmodified Hf-Ir, Hf-IrF, and Hf-Ru MOLs. ICP-MS and  $^1\text{H}$  NMR analyses of the digested MOLs showed similar compositions to Hf-Ir-Co-PPA with comparable loadings of PSs and cobaloximes. These results indicate that all six cobaloxime-modified MOLs exhibit hexagonal nanoplate morphologies based on the proposed  $\text{Hf}_{12}$  monolayer structure of kgd topology. The

structures of the MOLs remained intact after post-synthetic functionalization of cobaloximes with cobaloxime loadings ranging from 60% to 80 mol% relative to the amounts of PSs.

## 6.2.2 Reaction Optimization and Mechanistic Insights

Owing to the presence of both PSs and cobaloximes, the MOLs were evaluated as catalysts for dehydrogenative coupling reaction between morpholine **6.1a** and 4-methyl cyclohexanone **6.2a**. In the initial screening of reaction conditions,<sup>25</sup> the six MOLs showed different catalytic activities (**Table 6-1**). The MOLs containing Ru-PS did not catalyze the reaction. The MOLs containing Ir-PS and IrF-PS successfully catalyzed the reaction to give the aniline product **6.3a**. Among them, Hf-Ir-Co-PPA afforded the highest yield of 42%. Further optimization of Brønsted acids identified bistriflimidic acid (HNTf<sub>2</sub>)<sup>28</sup> as the best acid cocatalyst to afford **6.3a** in a 75% isolated yield. Hf-Ir-Co-PPA outperformed its homogeneous counterpart by 7.6 times.

**Table 6-1.** Reaction optimization for photochemical aniline synthesis.



entry <sup>a</sup>	variation reaction conditions	yield of <b>6.3a</b> <sup>b</sup> (%)
1	Hf-Ru-Co-PAPA, AcOH	trace
2	Hf-Ru-Co-PPA, AcOH	trace
3	Hf-IrF-Co-PAPA, AcOH	15
4	Hf-IrF-Co-PPA, AcOH	28
5	Hf-Ir-Co-PAPA, AcOH	30
6	Hf-Ir-Co-PPA, AcOH	42
7	Hf-Ir-Co-PPA, p-TsOH	42
8	Hf-Ir-Co-PPA, TFA	35
9	Hf-Ir-Co-PPA, TMSOTf	48
10	Hf-Ir-Co-PPA, HNTf <sub>2</sub>	75

<sup>a</sup>Reactions were performed with **6.1a** (0.2 mmol), catalyst (1 mol% based on cobalt), acid (20 mol%), DABCO (0.15 mmol) and **6.2a** (0.1 mmol) in CH<sub>3</sub>CN at 40 °C under blue LED for 48 h;

<sup>b</sup>Isolated yield.

According to the proposed mechanism in the literature (Figure 6-5),<sup>25</sup> amine **6.1a** and cyclohexanone **6.2a** first condensate to form an enamine. The enamine ( $E^{\circ} = 0.26$  V vs.  $\text{Fc}^+/\text{Fc}$ ) is then oxidized by excited PSs and deprotonates to generate a  $\beta$ -enamine radical, **rad**, which binds cobaloxime and undergoes a  $\beta$ -hydride elimination to afford the intermediate product, **int**, which proceeds through a tandem oxidation-dehydrogenation process to give the final aniline product. However, as Ir-PS, IrF-PS, and Ru-PS are strong photo-oxidants, they can competitively oxidize the amine **6.1a** ( $E^{\circ} = 0.75$  V vs.  $\text{Fc}^+/\text{Fc}$ ) to produce undesired byproducts.

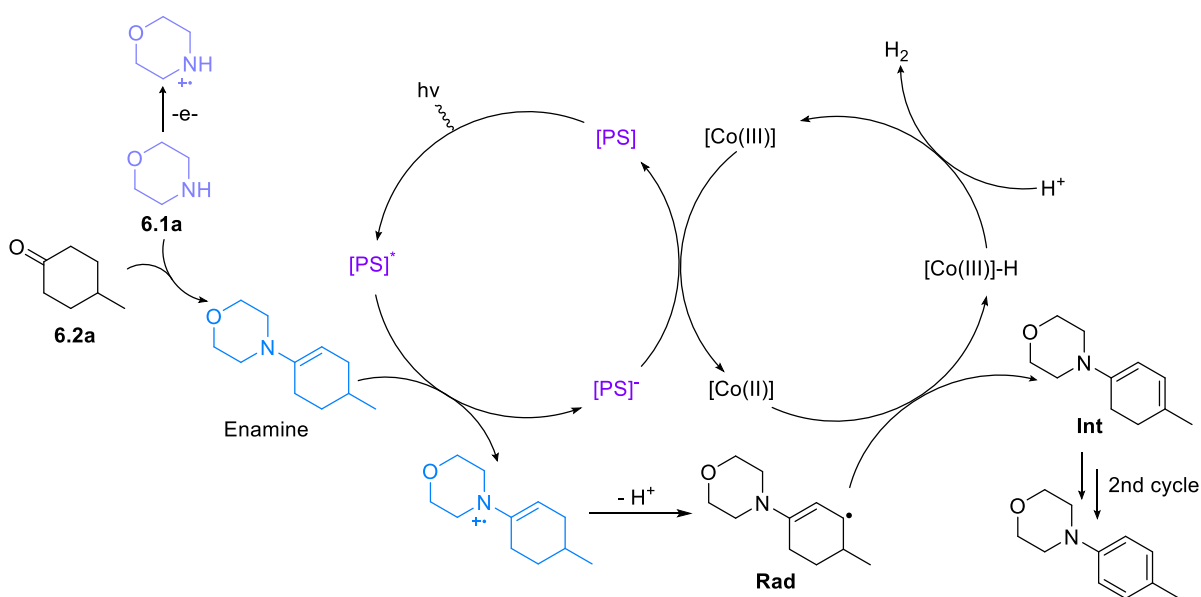


**Figure 6-5.** Proposed mechanistic cycles for photochemical aniline synthesis.

Cyclic voltammetry (CV) and luminescence studies indicated that the different catalytic activities of the MOLs in the dehydrogenative coupling reactions likely resulted from the different photoredox properties of the PSs. The reduction potentials of the triplet photoexcited PSs were calculated from their emission spectra and ground state reduction potentials to be 0.63 V, 0.99 V and 0.61 V versus  $\text{Fc}^+/\text{Fc}$  for  $[\text{Ir-PS}]^*$ ,  $[\text{IrF-PS}]^*$  and  $[\text{Ru-PS}]^*$ , respectively. Kinetic constants of photooxidation of the enamine and the amine were calculated based on the Stern-Völmer plots

from luminescence quenching experiments (**Figure 6-6**). [Ir-PS]\* had a mildly oxidizing triplet state that was selectively quenched by the enamine. [IrF-PS]\* had a triplet state with the strongest oxidation power and was rapidly quenched by both the enamine and the amine. Despite a low reduction potential, the triplet photoexcited [Ru-PS]\* could still be quenched by both the enamine and the amine. The selectivity of enamine photo-oxidation over amine photo-oxidation were determined as 1068, 23, and 35 for Ir-PS, IrF-PS and Ru-PS, respectively. Therefore, we propose that Hf-Ir-Co-PPA and Hf-Ir-Co-PAPA MOLs with Ir-PS can preferentially oxidize the enamine in the reactions to minimize side reactions and increase the product yield. The optimized strong acid catalyst, HNTf<sub>2</sub>, likely also improved the selectivity by accelerating the condensation between cyclohexanone and morpholine to increase the enamine concentration in solution. Furthermore, the counter anion NTf<sub>2</sub><sup>-</sup> is a weak nucleophile and does not deactivate the MOL through coordination to the SBU.

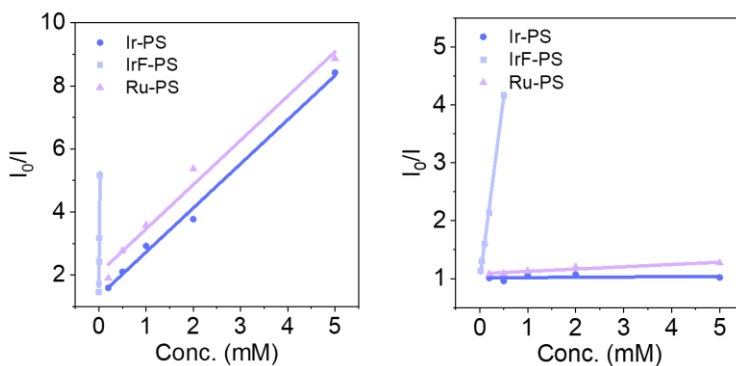
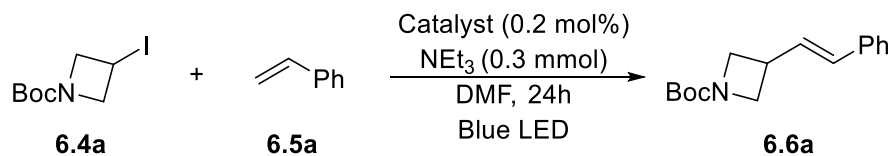


**Figure 6-6.** Stern-Völmer plots of PSs quenched by enamine (left) and amine (right).

The MOLs also competently catalyzed Heck-type coupling reactions between alkyl iodides and alkenes to afford the cross-coupling products. Catalyst screening studies identified Hf-Ir-Co-PPA as the best catalyst (**Table 6-2**). Further optimization of base and alkene equivalents improved the reaction yield to 92% (**Table 6-2**). 2 mol% Ir-PS and 5 mol% Co-PPA were required in

homogeneous conditions to yield **6.6a** in comparable yield 86%, suggesting a 178 times higher catalytic efficiency of Hf-Ir-Co-PPA.

**Table 6-2.** Reaction optimization for Heck-type coupling reactions.



entry <sup>a</sup>	variation reaction conditions	yield of <b>6.6a</b> <sup>b</sup> (%)
1	<b>Hf-IrF-Co-PPA</b>	15
2	<b>Hf-Ir-Co-PPA</b>	20
3 <sup>c</sup>	<b>Hf-Ir-Co-PPA</b>	52
4 <sup>d</sup>	<b>Hf-Ir-Co-PPA</b>	92
5 <sup>d,e</sup>	<b>Hf-Ir-Co-PPA</b>	52
6 <sup>d,f</sup>	<b>Hf-Ir-Co-PPA</b>	46

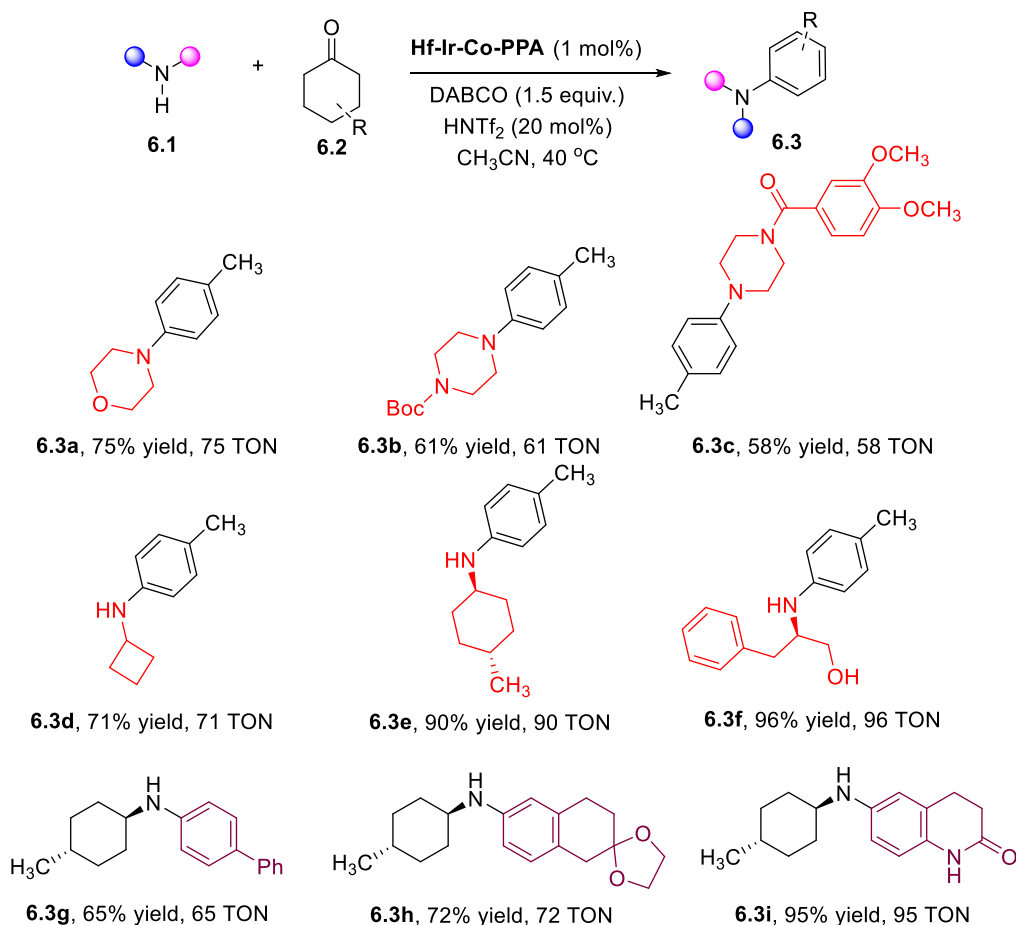
<sup>a</sup>Reactions were performed with **6.4a** (0.2 mmol), catalyst (0.2 mol% based on cobalt), Et<sub>3</sub>N (0.3 mmol) and **6.5a** (0.1 mmol) in DMF at rt under blue LED for 24 h; <sup>b</sup>Isolated yield. <sup>c</sup>**6.4a** (0.1 mmol) and **6.5a** (0.2 mmol) were used. <sup>d</sup>**6.4a** (0.1 mmol) and **6.5a** (0.3 mmol) were used. <sup>e</sup>Et<sub>3</sub>N (0.2 mmol). <sup>f</sup>Et<sub>3</sub>N (0.1 mmol).

### 6.2.3 Substrate Scope

We next investigated the substrate scopes of both amine and cyclohexanone partners in photocatalytic dehydrogenative coupling reactions under the optimized reaction conditions (**Table 6-3**). Secondary amines, including morpholine and protected piperidines, were suitable for these reactions, with the corresponding products **6.3a-6.3c** isolated in 58-75% yields. Primary amines, such as cyclobutyl amine, *trans*-4-methylcyclohexylamine, and (*S*)-(-)-2-Amino-3-phenyl-1-propanol, smoothly reacted with 4-methyl cyclohexanone to afford products **6.3d**, **6.3e** and **6.3f** in 71%, 90% and 95% isolated yields, respectively. Mono- and di-substituted ketones were synthesized and used as substrates in the reactions to afford the desired cross-coupling products **6.3g-6.3i** in 65-95% isolated yields.

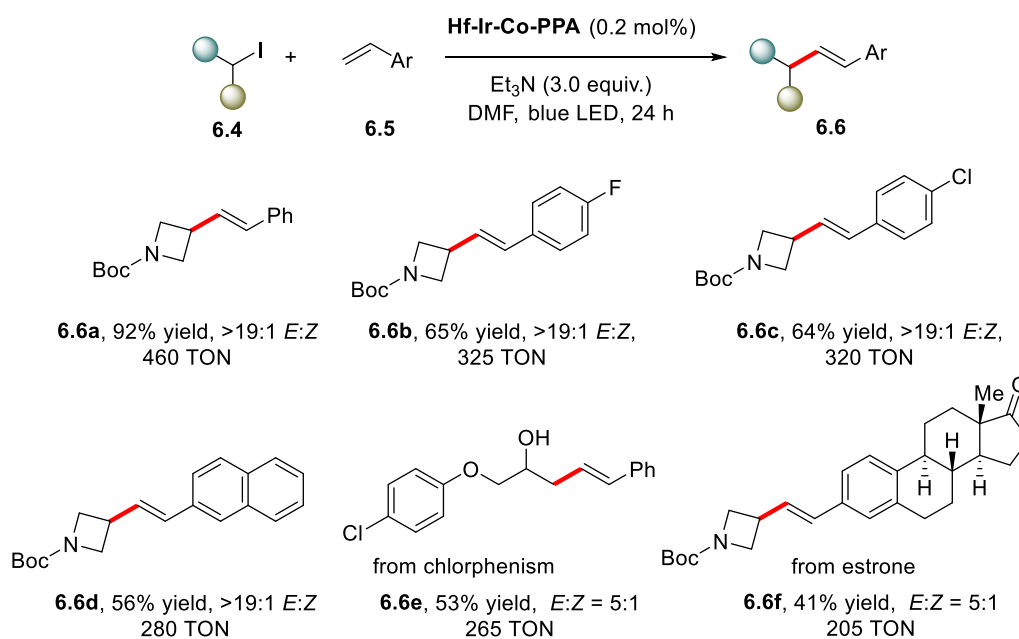
Hf-Ir-Co-PPA was also used for late-stage functionalization and synthesis of bioactive molecules. Improved substrate accessibility of 2D MOLs compared to 3D MOFs allows the use of large molecules as substrates in photocatalytic dehydrogenative coupling reactions. Estra-3,9-diene-3,17-dione, approximately 1.2 nm in size, efficiently underwent dehydrogenative cross-coupling reaction with *trans*-4-methylcyclohexylamine to produce the aniline product **6.3j** in 75% isolated yield. Vesnarinone **6.3k**, a cardiotonic agent of approximately 1.7 nm in size, was successfully synthesized in an 85% isolated yield by photocatalytic dehydrogenative coupling between 1,3,4,5,7,8-hexahydroquinoline-2,6-dione and (3,4-dimethoxyphenyl)(piperazin-1-yl)methanone.

**Table 6-3.** Substrate scope for photochemical aniline synthesis catalyzed by Hf-Ir-Co-PPA.



Hf-Ir-Co-PPA also efficiently catalyzed Heck-type coupling reactions between alkyl iodides **6.4** and aryl alkenes **6.5**, to produce the cross-coupling products **6.6a-6.6f** with TONs of up to 460 (Table 6-4). Aryl alkenes bearing electron-withdrawing or electron-donating groups underwent Heck-type coupling with *tert*-butyl 3-iodoazetidide-1-carboxylate **6.4a** smoothly to give corresponding products **6.6a-6.6d** in good to excellent isolated yields. The alkyl iodide derived from the natural product chlorphenesin underwent the coupling reaction with styrene to afford **6.6e** in 53% isolated yield with a 5:1 *E:Z* ratio. The alkene derivative from the natural product estrone was also tolerated in the Heck-type coupling reaction to give **6.6f** in 41% isolated yield with a 5:1 *E:Z* ratio.

**Table 6-4.** Substrate scope for Heck-type coupling reaction catalyzed by Hf-Ir-Co-PPA.



## 6.2.4 Gram-Scale Synthesis and Catalyst Recycle

Gram-scale synthesis of **6.3k** was performed to illustrate the synthetic utility of MOL catalysts (Figure 6-7). 4 mmol 1,3,4,5,7,8-hexahydroquinoline-2,6-dione and 6 mmol (3,4-dimethoxyphenyl)(piperazin-1-yl)methanone were subjected to the standard photocatalytic



dehydrogenative coupling reaction condition in the presence of 0.2 mol% Hf-Ir-Co-PPA. 1.26 g of the target product, vesnarinone, was isolated as a white crystalline solid in 80% yield in 48 h. The TON of the MOL catalyst reached 400 in this one-pot synthesis.

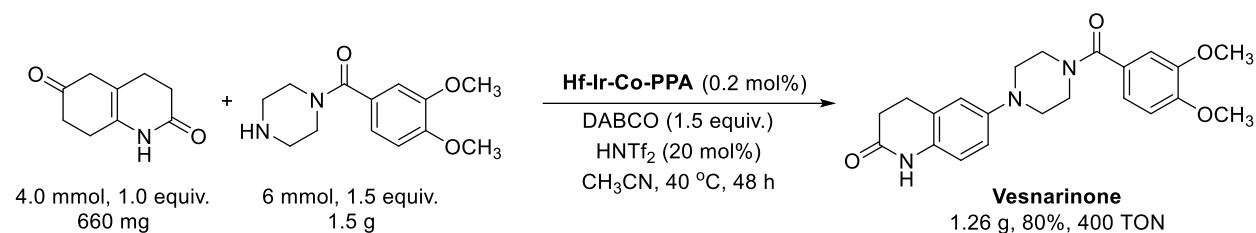


**Figure 6-7.** Gram-scale synthesis of vesnarinone.

To probe the stability of Hf-Ir-Co-PPA in the photocatalytic reaction, the catalyst was separated from the reaction mixture by centrifugation (**Figure 6-8a**). The recovered Hf-Ir-Co-PPA was washed with DMF and ethanol and examined by TEM and PXRD. TEM images showed that Hf-Ir-Co-PPA maintained the nanoplate morphology after the photocatalytic reaction (**Figure 6-8b**), whereas PXRD studies showed that the recovered Hf-Ir-Co-PPA retained the crystalline structure of as-synthesized Hf-Ir-Co-PPA (**Figure 6-8c**). These results indicate that the structure of Hf-Ir-Co-PPA remains intact during the 48-hour photocatalytic reaction.

The catalytic activity of the recovered Hf-Ir-Co-PPA was then reused to catalyze the photocatalytic dehydrogenative coupling reaction. Hf-Ir-Co-PPA-catalyzed synthesis of vesnarinone was performed in a 0.1 mmol scale in eight consecutive reaction cycles. After each cycle, the MOL was collected by centrifugation, washed with acetonitrile, and directly used in the next cycle. The reaction yields gradually decreased from 85% to 76% in seven consecutive 24-hour reaction cycles (**Figure 6-8d**), likely due to incomplete recovery of Hf-Ir-Co-PPA from the reaction mixture. By extending the reaction time to 36 hours, the product yield returned to 82% in the eighth run. A total turnover number of 651 was achieved in the eight reaction cycles. The

recyclability and stability of Hf-Ir-Co-PPA underscore the potential of MOL catalysts in sustainable photoredox catalysis.

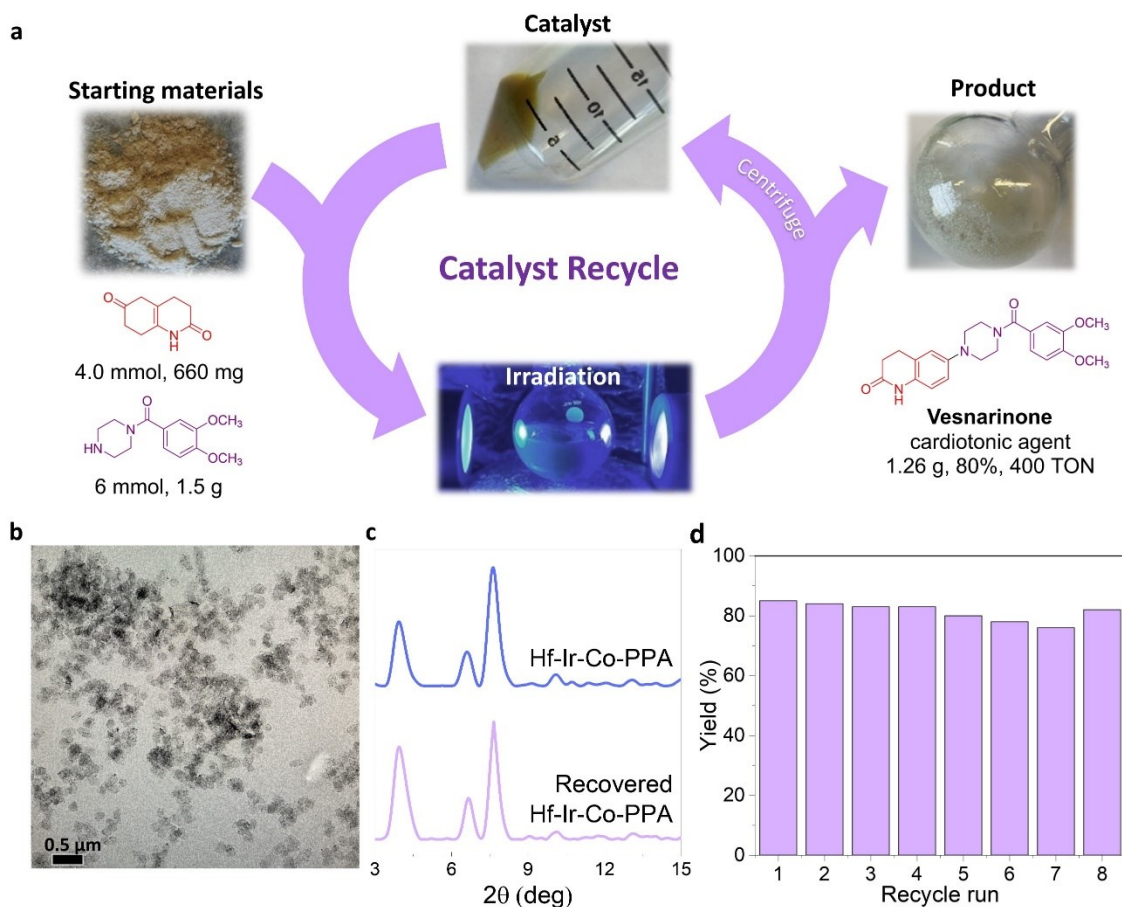


**Figure 6-8.** Catalyst recycle. (a) The protocol for catalyst recycle. (b) TEM image of recovered Hf-Ir-Co-PPA. (c) PXRD patterns of Hf-Ir-Co-PPA before and after the photocatalytic reaction. (d) Reaction yields in eight consecutive cycles of vesnarione synthesis.

### 6.3 Conclusion

We present in this chapter the molecular engineering of multifunctional MOLs of approximately 2 nm in thickness and 200 nm in width for sustainable photocatalysis. We

successfully synthesized three photosensitizing MOFs via judicious choices of monocarboxylic acid modulators and post-synthetically modified these MOFs with two cobaloxime catalysts to create a library of six MOFs for photoredox dual cobalt catalysis. Screening of these MOFs identified Hf-Ir-Co-PPA as the best catalyst for both photochemical aniline synthesis and Heck-type coupling reactions. Hf-Ir-Co-PPA efficiently catalyzed both cross-coupling reactions with broad substrate scopes. Owing to the hierarchical integration of both PSs and cobaloximes, the MOFs significantly outperformed their homogenous controls with up to 178 times higher efficiency. Furthermore, Hf-Ir-Co-PPA effectively catalyzed late-stage functionalization and synthesis of large bioactive molecules owing to facile substrate accessibility to the active sites in the MOF. The synthetic utility of the MOF catalyst was also demonstrated in a one-pot gram-scale synthesis of a cardioprotective agent, vesnarinone and in eight consecutive cycles of vesnarinone synthesis by recycled MOF without significant loss of activity. This work highlights the potential of MOFs as a unique 2D molecular material platform for the molecular engineering of recyclable and reusable multifunctional catalysts for synergistic photocatalysis.

## 6.4 Methods

### 6.4.1 Material synthesis

**Synthesis of 3-(Methyl-4-pyridylamino)propionic Acid.** 3-(methyl-4-pyridylamino)propionic acid (PAPA) was synthesized according to the literature report.<sup>29-30</sup> A mixture of methyl acrylate (5 mL, 55 mmol) and 4-(methylamino)pyridine (808 mg, 7.47 mmol) was refluxed for two days and cooled to room temperature. Excess methyl acrylate was removed under reduced pressure and the mixture was separated by column chromatography (CHCl<sub>3</sub>/MeOH=10/1) to afford 3-(methyl-4-pyridylamino)propionic acid methyl ester (MePAPA,

1.43 g, 99%).  $^1\text{H NMR}$  (400 MHz, chloroform-*d*)  $\delta$  8.11 (s, 2H), 6.42 (s, 2H), 3.60 – 3.56 (comp, 5H), 2.94 – 2.84 (m, 3H), 2.49 (q,  $J = 6.6$  Hz, 2H).  $^{13}\text{C}\{^1\text{H}\}$  NMR (101 MHz, chloroform-*d*)  $\delta$  171.9, 153.0, 149.4, 106.5, 51.7, 47.1, 37.4, 31.4.

To a solution of the resulting liquid (777 mg, 4.0 mmol) in 5 mL methanol was added 5 mL 2 M NaOH aqueous solution. After stirring overnight, the mixture was neutralized with 3 M HCl solution. The solvent was then removed under reduced pressure. Methanol was added to dissolve the crude product, and the insoluble salts were removed by filtration. The filtrate was evaporated to afford 3-(methyl-4-pyridylamino)propionic acid as a white solid (PAPA, 701 mg, 97%).  $^1\text{H NMR}$  (400 MHz, DMSO-*d*<sub>6</sub>)  $\delta$  8.06 (d,  $J = 6.8$  Hz, 2H), 6.55 (d,  $J = 6.8$  Hz, 2H), 3.60 – 3.46 (m, 2H), 2.89 (s, 3H), 2.29 – 2.18 (m, 2H).  $^{13}\text{C}\{^1\text{H}\}$  NMR (101 MHz, DMSO-*d*<sub>6</sub>)  $\delta$  174.1, 152.9, 149.2, 106.6, 48.1, 36.9, 33.7.

**Synthesis of pyridine-substituted cobaloxime complexes.** Pyridine-substituted cobaloxime complexes were synthesized according to the literature report.<sup>31</sup> A mixture of  $\text{CoCl}_2$  (1.3 g, 10 mmol, 1.0 equiv.), dimethylglyoxime (dmgh, 2.6 g, 22 mmol, 2.2 equiv.), and acetone (50 mL) was stirred and bubbled with air for 30 minutes. After cooling in ice water, the mixture was filtered and green crystals were collected. The crystals were then washed with cold acetone (5 mL) and further dried at room temperature under vacuum. To a mixture of the green solid (0.22 g) and methanol (10 mL) was added PPA (200 mg, 1.3 mmol) or PAPA (231 mg, 1.3 mmol). The resulting suspension was stirred until the green solid was converted to a brown crystalline solid, then water (10 mL) was added. After cooling in ice water, the mixture was filtered. Brown crystals were collected and washed with water/methanol 2:1 (v/v) followed by diethyl ether. The crystalline solid was then dried at room temperature under vacuum to afford  $\text{Co}(\text{dmgh})_2(\text{PPA})\text{Cl}$  (Co-PPA) in 70 % yield or  $\text{Co}(\text{dmgH})_2(\text{PAPA})\text{Cl}$  (Co-PAPA) in 58% yield. Co-PPA,  $^1\text{H NMR}$  (400 MHz,

DMSO- $d_6$ )  $\delta$  7.88 (d,  $J$  = 6.8 Hz, 2H), 7.35 (d,  $J$  = 4.8 Hz, 2H), 2.79 (t,  $J$  = 7.6 Hz, 2H), 2.56 – 2.51 (m, 2H), 2.31 (s, 12H).  $^{13}\text{C}\{^1\text{H}\}$  NMR (101 MHz, DMSO- $d_6$ )  $\delta$  173.2, 154.6, 152.4, 149.4, 126.3, 32.3, 28.9, 12.6. Co-PAPA,  $^1\text{H}$  NMR (400 MHz, DMSO- $d_6$ )  $\delta$  7.36 (d,  $J$  = 7.2 Hz, 2H), 6.62 (d,  $J$  = 7.2 Hz, 2H), 3.52 (t,  $J$  = 7.6 Hz, 2H), 2.88 (s, 3H), 2.41 (t,  $J$  = 7.6 Hz, 2H), 2.31 (s, 12H).  $^{13}\text{C}\{^1\text{H}\}$  NMR (101 MHz, DMSO- $d_6$ )  $\delta$  173.1, 154.2, 152.3, 148.3, 109.2, 47.2, 37.7, 31.6, 13.0.

**Synthesis of Ir, IrF and Ru photosensitizers.** Ir(ppy) $_2$ (H $_2$ DBB)Cl (Ir-PS), Ir[dF(CF $_3$ )ppy] $_2$ (H $_2$ DBB)Cl (IrF-PS) and Ru(bpy) $_2$ (H $_2$ DBB)Cl $_2$  (Ru-PS) were synthesized according to literature reports.<sup>27,32-33</sup>  $^1\text{H}$  NMR spectra of these complexes match literature reports. Ir-PS  $^1\text{H}$  NMR (400 MHz, DMSO- $d_6$ )  $\delta$  9.06 (d,  $J$  = 8.6 Hz, 2H), 8.67 (dd,  $J$  = 8.6, 2.2 Hz, 2H), 8.28 (d,  $J$  = 8.4 Hz, 2H), 8.08 (d,  $J$  = 2.0 Hz, 2H), 7.97 (dt,  $J$  = 16.0, 8.0 Hz, 8H), 7.88 (d,  $J$  = 5.6 Hz, 2H), 7.53 (d,  $J$  = 8.0 Hz, 4H), 7.17 (t,  $J$  = 6.4 Hz, 2H), 7.09 (t,  $J$  = 7.6 Hz, 2H), 6.98 (t,  $J$  = 7.2 Hz, 2H), 6.33 (d,  $J$  = 7.2 Hz, 2H). IrF-PS  $^1\text{H}$  NMR (400 MHz, DMSO- $d_6$ )  $\delta$  9.10 (d,  $J$  = 8.8 Hz, 2H), 8.77 (dd,  $J$  = 8.8, 2.0 Hz, 2H), 8.54 – 8.42 (comp, 4H), 8.16 (d,  $J$  = 2.0 Hz, 2H), 8.09 – 7.99 (comp, 4H), 7.82 (d,  $J$  = 2.0 Hz, 2H), 7.66 (d,  $J$  = 8.0 Hz, 4H), 7.14 – 7.08 (comp, 2H), 5.90 (dd,  $J$  = 8.4, 2.4 Hz, 2H). Ru-PS  $^1\text{H}$  NMR (400 MHz, DMSO- $d_6$ )  $\delta$  9.01 (d,  $J$  = 8.8 Hz, 2H), 8.86 (dd,  $J$  = 14.4, 8.0 Hz, 4H), 8.56 (dd,  $J$  = 8.4, 2.0 Hz, 2H), 8.25 – 8.15 (comp, 4H), 8.00 – 7.92 (comp, 6H), 7.86 (dd,  $J$  = 5.7, 1.6 Hz, 2H), 7.78 (d,  $J$  = 2.0 Hz, 2H), 7.62 – 7.54 (comp, 8H).

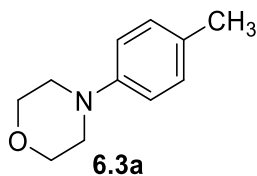
**Synthesis of Hf-Ir, Hf-IrF, and Hf-Ru MOLs.** Hf-IrF and Hf-Ru MOLs were synthesized according to literature reports.<sup>4-5</sup> To a 4 mL glass vial was added 0.5 mL of HfCl $_4$  solution (2.0 mg/mL in DMF), 0.5 mL of IrF-PS solution (4.0 mg/mL in DMF) or Ru-PS solution (4.0 mg/mL in DMF), 2  $\mu\text{L}$  of TFA, and 5  $\mu\text{L}$  of water. The reaction mixture was kept in an 80  $^\circ\text{C}$  oven for 24 hours. The yellow precipitate (Hf-IrF MOL) or red precipitate (Hf-Ru MOL) was collected by

centrifugation and washed with DMF and ethanol. Hf-Ir MOL was synthesized through solvothermal reactions. To a 4 mL glass vial was added 0.5 mL of HfCl<sub>4</sub> solution (2.0 mg/mL in DMF), 0.5 mL of Ir-PS solution (3.2 mg/mL in DMF), 1.5 μL of DCA, and 5 μL of water. The reaction mixture was kept in an 80 °C oven for 24 hours. The orange precipitate was collected by centrifugation and washed with DMF and ethanol.

**General procedure for post-modification of MOLs with cobaloxime complexes.** To 10 mL 1 mM MOL dispersion in acetonitrile (based on the photosensitizer) was added 60 μmol Co-PPA (28.5 mg) or Co-PAPA (30.2 mg). The mixture was stirred at 60 °C for 48 h. The brown precipitate was collected by centrifugation and washed with acetonitrile. The loading of Co-PPA or Co-PAPA was determined by ICP-MS and NMR.

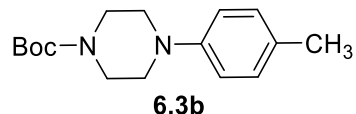
#### 6.4.2 Catalytic Reactions

**General procedure for photochemical aniline synthesis.** Cyclohexanone **6.2** (0.1 mmol, 1 equiv.), amine **6.1** (0.2 mmol, 2.0 equiv.), 1,4-diazabicyclo[2.2.2]octane (DABCO, 0.15 mmol, 1.5 equiv.), HNTf<sub>2</sub> (0.02 mmol, 0.2 equiv.) and Hf-Ir-Co-PPA (1 μmol based on Co, 1 mol%; 1.4 μmol based on Ir, 1.4 mol%) were mixed in dry CH<sub>3</sub>CN (2 mL). The resulting solution was stirred under blue LED irradiation at 40 °C in an N<sub>2</sub> atmosphere for 48 h. After the reaction, the solvent was removed under vacuum. The residue was purified by silica gel column chromatography using n-hexane and ethyl acetate as eluent to give the dehydrogenative cross-coupling products **6.3a-6.3k**. Turnover number (TON) of the catalytic reaction was calculated based on Co catalyst: TON = (product amount) / (catalyst amount) = (yield)/(1%).



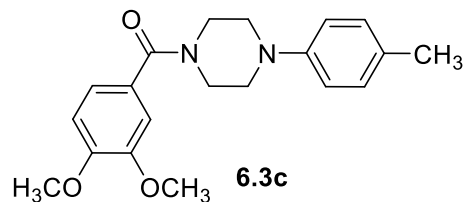
Colorless oil, 75% yield.

**<sup>1</sup>H NMR** (400 MHz, chloroform-*d*)  $\delta$  7.02 – 7.00 (comp, 2H), 6.76 – 6.74 (comp, 2H), 3.81 – 3.73 (comp, 4H), 3.07 – 3.00 (comp, 4H), 2.20 (s, 3H); **<sup>13</sup>C{<sup>1</sup>H} NMR** (101 MHz, chloroform-*d*)  $\delta$  149.2, 129.7, 116.1, 67.0, 50.0, 20.4; **HRMS** (ESI) scaled for [M+H]<sup>+</sup>: C<sub>11</sub>H<sub>16</sub>NO, 178.1231, observed: 178.1238.



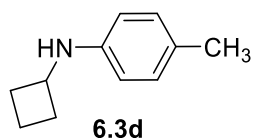
Colorless oil, 61% yield.

**<sup>1</sup>H NMR** (400 MHz, chloroform-*d*)  $\delta$  7.10 – 7.08 (comp, 2H), 6.87 – 6.85 (comp, 2H), 3.59 – 3.57 (comp, 4H), 3.08 – 3.06 (comp, 4H), 2.28 (s, 3H), 1.48 (s, 9H); **<sup>13</sup>C{<sup>1</sup>H} NMR** (101 MHz, chloroform-*d*)  $\delta$  154.7, 129.7, 117.1, 79.9, 50.1, 28.5, 20.5; **HRMS** (ESI) scaled for [M+H]<sup>+</sup>: C<sub>16</sub>H<sub>25</sub>N<sub>2</sub>O<sub>2</sub>, 277.1916, observed: 277.1916.



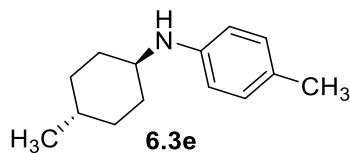
Colorless oil, 58% yield.

**<sup>1</sup>H NMR** (400 MHz, chloroform-*d*)  $\delta$  7.13 – 7.07 (comp, 2H), 7.05 – 6.98 (comp, 2H), 6.92 – 6.81 (comp, 3H), 3.91 (s, 3H), 3.90 (s, 3H), 3.86– 3.71 (comp, 4H), 3.20– 3.05 (comp, 4H), 2.28 (s, 3H); **<sup>13</sup>C{<sup>1</sup>H} NMR** (101 MHz, chloroform-*d*)  $\delta$  170.3, 150.4, 149.0, 129.8, 127.8, 120.2, 117.1, 111.0, 110.5, 56.0, 20.5; **HRMS** (ESI) scaled for [M+H]<sup>+</sup>: C<sub>20</sub>H<sub>25</sub>N<sub>2</sub>O<sub>3</sub>, 341.1965, observed: 341.1867.



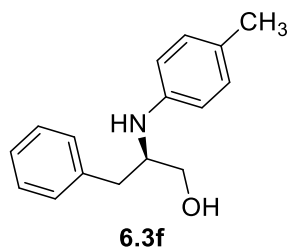
Colorless oil, 71% yield.

**$^1\text{H}$  NMR** (400 MHz, chloroform-*d*)  $\delta$  6.98 – 6.96 (comp, 2H), 6.50 – 6.48 (comp, 2H), 3.90 – 3.86 (comp, 1H), 2.49 – 2.32 (m, 2H), 2.23 (s, 3H), 1.82 – 1.78 (m, 2H), 0.90 – 0.82 (m, 3H);  **$^{13}\text{C}\{^1\text{H}\}$  NMR** (101 MHz, chloroform-*d*)  $\delta$  144.9, 129.7, 126.6, 113.3, 49.3, 31.3, 22.6, 20.4; **HRMS** (ESI) scaled for  $[\text{M}+\text{H}]^+$ :  $\text{C}_{11}\text{H}_{16}\text{N}$ , 162.1286, observed: 162.1286.



Colorless oil, 90% yield.

**$^1\text{H}$  NMR** (400 MHz, chloroform-*d*)  $\delta$  6.98 – 6.96 (comp, 2H), 6.61 – 6.47 (comp, 2H), 3.21 – 3.12 (comp, 1H), 2.23 (s, 3H), 2.15 – 2.08 (m, 2H), 1.77 – 1.70 (m, 2H), 1.13 – 1.02 (comp, 4H), 0.92 (d,  $J = 6.4$  Hz, 3H);  **$^{13}\text{C}\{^1\text{H}\}$  NMR** (101 MHz, chloroform-*d*)  $\delta$  145.0, 129.7, 126.3, 113.7, 52.6, 34.2, 33.6, 32.4, 22.3, 20.4; **HRMS** (ESI) scaled for  $[\text{M}+\text{H}]^+$ :  $\text{C}_{14}\text{H}_{22}\text{N}$ , 204.1752, observed: 204.1769.

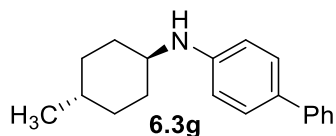


Colorless oil, 96% yield.

**$^1\text{H}$  NMR** (400 MHz, chloroform-*d*)  $\delta$  7.32 – 7.29 (comp, 2H), 7.26 – 7.17 (comp, 3H), 7.03 – 7.01 (comp, 2H), 6.64 – 6.62 (comp, 2H), 3.82 – 3.70 (m, 2H), 3.58 – 3.45 (m, 1H), 2.94 (dd,  $J = 13.6$ ,

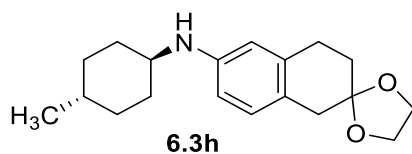


4.8 Hz, 1H), 2.84 (dd,  $J = 13.6, 7.6$  Hz, 1H), 2.27 (s, 3H);  $^{13}\text{C}\{^1\text{H}\}$  NMR (101 MHz, chloroform- $d$ )  $\delta$  144.8, 138.0, 130.0, 129.3, 128.6, 127.6, 126.5, 114.4, 63.3, 56.4, 37.4, 20.4; HRMS (ESI) scaled for  $[\text{M}+\text{H}]^+$ :  $\text{C}_{16}\text{H}_{20}\text{NO}$ , 242.1544, observed: 242.1548.



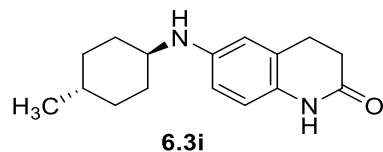
Colorless oil, 65% yield.

$^1\text{H}$  NMR (400 MHz, chloroform- $d$ )  $\delta$  7.54 – 7.52 (comp, 2H), 7.44 – 7.35 (comp, 4H), 7.23 (d,  $J = 7.6$  Hz, 1H), 6.66 (d,  $J = 7.6$  Hz, 2H), 3.26 – 3.19 (m, 1H), 2.16 – 2.12 (m, 2H), 1.80 – 1.71 (m, 2H), 1.42 – 1.39 (m, 1H), 1.17 – 1.06 (comp, 4H), 0.93 (d,  $J = 6.5$  Hz, 3H);  $^{13}\text{C}\{^1\text{H}\}$  NMR (101 MHz, chloroform- $d$ )  $\delta$  146.9, 141.339, 128.6, 127.9, 126.2, 125.9, 113.4, 52.2, 34.1, 33.6, 32.3, 29.7, 22.3; HRMS (ESI) scaled for  $[\text{M}+\text{H}]^+$ :  $\text{C}_{19}\text{H}_{24}\text{N}$ , 266.1908, observed: 266.1910.



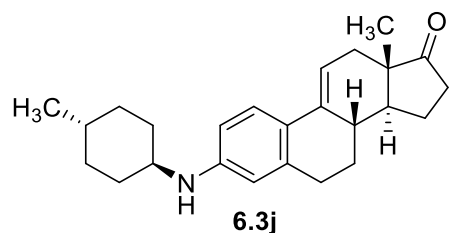
Colorless oil, 72% yield.

$^1\text{H}$  NMR (400 MHz, chloroform- $d$ )  $\delta$  6.83 (d,  $J = 8.4$  Hz, 1H), 6.40 (d,  $J = 8.4$  Hz, 1H), 6.35 (s, 1H), 4.04 – 3.89 (comp, 5H), 3.16 – 3.09 (m, 1H), 2.91 – 2.89 (m, 4H), 2.10 – 2.06 (m, 2H), 1.92 (t,  $J = 6.8$  Hz, 2H), 1.77 – 1.70 (m, 2H), 1.41 – 1.32 (comp, 1H), 1.13 – 1.00 (comp, 4H), 0.91 (d,  $J = 6.4$  Hz, 3H);  $^{13}\text{C}\{^1\text{H}\}$  NMR (101 MHz, chloroform- $d$ )  $\delta$  145.8, 135.9, 129.9, 122.8, 112.7, 112.1, 108.7, 64.4, 52.3, 38.2, 34.2, 33.6, 32.4, 31.9, 28.3, 22.3; HRMS (ESI) scaled for  $[\text{M}+\text{H}]^+$ :  $\text{C}_{19}\text{H}_{28}\text{NO}_2$ , 302.2120, observed: 302.2124.



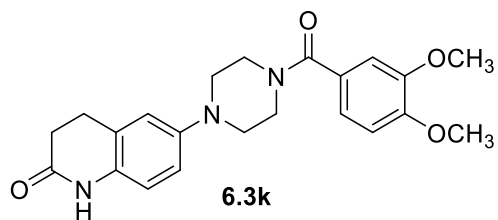
Colorless oil, 95% yield.

**<sup>1</sup>H NMR** (400 MHz, chloroform-*d*)  $\delta$  8.62 (s, 1H), 6.64 – 6.59 (m, 1H), 6.43 – 6.41 (comp, 2H), 3.47 (s, 1H), 3.14 – 3.07 (m, 1H), 2.86 (t,  $J = 7.6$  Hz, 2H), 2.57 (dd,  $J = 7.6$  Hz, 2H), 2.09 – 2.05 (m, 2H), 1.81 – 1.67 (m, 2H), 1.41 – 1.32 (m, 1H), 1.14 – 1.00 (comp, 4H), 0.91 (d,  $J = 6.6$  Hz, 3H); **<sup>13</sup>C{<sup>1</sup>H} NMR** (101 MHz, chloroform-*d*)  $\delta$  171.6, 143.3, 128.1, 125.0, 116.5, 113.3, 112.5, 52.9, 34.1, 33.5, 32.3, 30.8, 25.8, 22.2; **HRMS** (ESI) scaled for  $[M+H]^+$ : C<sub>16</sub>H<sub>23</sub>N<sub>2</sub>O, 259.1810, observed: 259.1813.



Colorless oil, 75% yield.

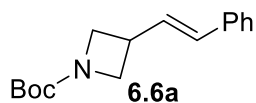
**<sup>1</sup>H NMR** (400 MHz, chloroform-*d*)  $\delta$  7.42 (d,  $J = 8.4$  Hz, 1H), 6.42 (dd,  $J = 8.4, 2.4$  Hz, 1H), 6.29 (d,  $J = 2.4$  Hz, 1H), 6.03 (dd,  $J = 5.2, 2.4$  Hz, 1H), 3.44 (s, 1H), 3.21 – 3.12 (m, 1H), 2.94 – 2.74 (m, 2H), 2.58 – 2.45 (m, 1H), 2.31 – 2.04 (comp, 8H), 1.80 – 1.70 (m, 2H), 1.71 – 1.60 (m, 2H), 1.48 – 1.35 (m, 2H), 1.16 – 1.01 (comp, 3H), 0.92 (s, 3H), 0.91 (s, 3H); **<sup>13</sup>C{<sup>1</sup>H} NMR** (101 MHz, chloroform-*d*)  $\delta$  222.0, 146.4, 137.2, 135.7, 125.1, 123.5, 114.4, 112.3, 112.2, 52.0, 47.9, 46.3, 38.4, 36.3, 34.1, 33.9, 33.6, 33.6, 32.3, 30.0, 28.0, 22.6, 22.3, 14.5. **HRMS** (ESI) scaled for  $[M+H]^+$ : C<sub>25</sub>H<sub>34</sub>NO, 364.2640, observed: 364.2640.



White solid, 85% yield.

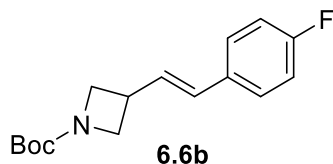
**<sup>1</sup>H NMR** (400 MHz, chloroform-*d*)  $\delta$  9.03 (s, 1H), 7.03 – 6.96 (comp, 2H), 6.86 (d,  $J = 8.0$  Hz, 1H), 6.77 – 6.69 (comp, 3H), 3.89 (s, 3H), 3.88 (s, 3H), 3.83 – 3.63 (comp, 4H), 3.16 – 3.01 (comp, 4H), 2.91 (t,  $J = 8.0$  Hz, 2H), 2.60 (t,  $J = 8.0$  Hz, 2H); **<sup>13</sup>C{<sup>1</sup>H} NMR** (101 MHz, chloroform-*d*)  $\delta$  171.7, 170.3, 150.4, 149.0, 147.1, 131.2, 127.8, 124.6, 120.2, 117.2, 116.2, 111.0, 110.5, 56.0, 50.6, 30.7, 25.8; **HRMS** (ESI) scaled for  $[M+H]^+$ : C<sub>22</sub>H<sub>26</sub>N<sub>3</sub>O<sub>4</sub>, 396.1923, observed: 396.1925.

**General procedure for Heck-type cross-coupling reactions between alkyl iodides and alkenes.** Alkyl iodide **4** (0.2 mmol, 1.0 equiv.), alkene **5** (0.6 mmol, 3.0 equiv.), Et<sub>3</sub>N (0.6 mmol, 3 equiv.) and Hf-Ir-Co-PPA (0.4  $\mu$ mol based on Co, 0.2 mol%; 0.6  $\mu$ mol based on Ir, 0.3 mol%) were mixed in dry DMF (2 mL). The resulting solution was stirred under blue LED irradiation at room temperature in an N<sub>2</sub> atmosphere for 24 h. After the reaction, brine (15 mL) and ethyl acetate (15 mL) were added and the mixture was shaken vigorously. The aqueous layer was extracted with ethyl acetate twice. The combined organic layers were washed with brine twice, dried over MgSO<sub>4</sub>, filtered and evaporated. The residue was purified by silica gel column chromatography using n-hexane and ethyl acetate as eluent to give the Heck-type cross-coupling products **6a - 6f**. Turnover number (TON) of the catalytic reaction is calculated based on Co catalyst: TON = (product amount) / (catalyst amount) = (yield)/(0.2%).



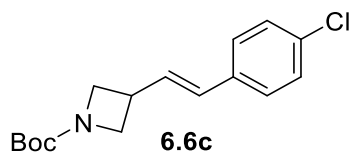
Colorless oil, 92% yield, >19:1 *E:Z*.

**<sup>1</sup>H NMR** (400 MHz, chloroform-*d*) δ 7.30 – 7.21 (comp, 4H), 7.18 – 7.14 (m, 1H), 6.39 – 6.22 (comp, 2H), 4.08 (t, *J* = 8.4 Hz, 2H), 3.75 (dd, *J* = 8.4, 6.0 Hz, 2H), 3.30 – 3.24 (m, 1H), 1.38 (s, 9H); **<sup>13</sup>C{<sup>1</sup>H} NMR** (101 MHz, chloroform-*d*) δ 156.4, 136.8, 131.1, 130.3, 128.6, 127.6, 126.2, 79.4, 55.0, 31.8, 28.4; **HRMS** (ESI) scaled for [M-Boc+H]<sup>+</sup>: C<sub>11</sub>H<sub>14</sub>N, 160.1126, observed: 160.1116.



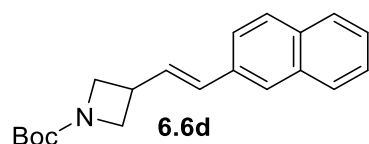
Colorless oil, 65% yield, >19:1 *E:Z*.

**<sup>1</sup>H NMR** (400 MHz, chloroform-*d*) δ 7.36 – 7.28 (comp, 2H), 7.03 – 6.96 (comp, 2H), 6.39 (d, *J* = 16.0 Hz, 1H), 6.27 (dd, *J* = 16.0, 8.0 Hz, 1H), 4.15 (t, *J* = 8.0 Hz, 2H), 3.81 (dd, *J* = 8.0, 6.0 Hz, 2H), 3.38 – 3.29 (m, 1H), 1.45 (s, 9H); **<sup>13</sup>C{<sup>1</sup>H} NMR** (101 MHz, chloroform-*d*) δ 163.5, 161.1, 156.3, 132.9, 132.9, 130.1, 130.1, 129.9, 127.7, 127.6, 115.6, 115.4, 79.5, 54.8, 31.8, 28.4; **<sup>19</sup>F NMR** (377 MHz, chloroform-*d*) δ -114.5; **HRMS** (ESI) scaled for [M-Boc+H]<sup>+</sup>: C<sub>11</sub>H<sub>23</sub>NF, 178.1032, observed: 178.1035.



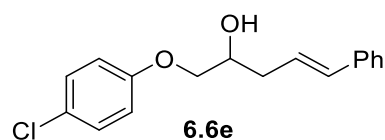
Colorless oil, 64% yield, >19:1 *E:Z*.

**<sup>1</sup>H NMR** (400 MHz, chloroform-*d*) δ 7.29 – 7.24 (comp, 4H), 6.43 – 6.30 (comp, 2H), 4.15 (t, *J* = 8.5 Hz, 2H), 3.81 (dd, *J* = 8.5, 6.0 Hz, 2H), 3.34 (ddt, *J* = 14.6, 8.5, 6.0 Hz, 1H), 1.45 (s, 9H); **<sup>13</sup>C{<sup>1</sup>H} NMR** (101 MHz, chloroform-*d*) δ 156.3, 135.2, 133.2, 131.0, 129.9, 128.8, 127.4, 79.5, 54.7, 31.8, 28.4; **HRMS** (ESI) scaled for [M-Boc+H]<sup>+</sup>: C<sub>11</sub>H<sub>13</sub>NCl, 194.0736, observed: 194.0753.



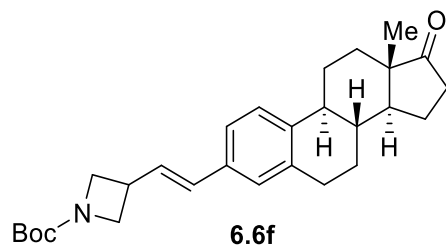
Colorless oil, 56% yield, >19:1 *E:Z*.

**<sup>1</sup>H NMR** (400 MHz, chloroform-*d*) δ 7.82 – 7.77 (comp, 3H), 7.71 (d, *J* = 1.6 Hz, 1H), 7.59 (dd, *J* = 8.4, 1.6 Hz, 1H), 7.48 – 7.42 (comp, 2H), 6.60 (d, *J* = 15.6 Hz, 1H), 6.50 (dd, *J* = 15.6, 8.0 Hz, 1H), 4.20 (t, *J* = 8.4 Hz, 2H), 3.88 (dd, *J* = 8.4, 6.0 Hz, 2H), 3.49 – 3.37 (m, 1H), 1.47 (s, 9H); **<sup>13</sup>C{<sup>1</sup>H} NMR** (101 MHz, chloroform-*d*) δ 156.4, 134.2, 133.6, 133.0, 131.2, 130.7, 128.3, 127.9, 127.7, 126.3, 126.1, 125.9, 123.4, 79.5, 54.9, 32.0, 28.4; **HRMS** (ESI) scaled for [M-tBu+2H]<sup>+</sup>: C<sub>15</sub>H<sub>16</sub>NO<sub>2</sub>, 254.1181, observed: 254.1181.



Colorless oil, 53% yield, 5:1 *E:Z*.

**<sup>1</sup>H NMR** (400 MHz, chloroform-*d*) δ 7.29 – 7.23 (comp, 3H), 7.18 – 7.12 (comp, 4H), 6.77 (d, *J* = 8.8 Hz, 2H), 6.44 (d, *J* = 16.0 Hz, 1H), 6.19 (dt, *J* = 16.0, 7.2 Hz, 1H), 4.05 (qt, *J* = 7.2, 4.4 Hz, 1H), 3.95 – 3.79 (comp, 2H), 2.52 – 2.40 (comp, 2H); **<sup>13</sup>C{<sup>1</sup>H} NMR** (101 MHz, chloroform-*d*) δ 156.1, 136.0, 132.4, 128.4, 128.3, 127.5, 126.4, 125.1, 124.0, 114.9, 114.8, 70.8, 68.6, 36.1; **HRMS** (ESI) scaled for [M-H<sub>2</sub>O+H]<sup>+</sup>: C<sub>17</sub>H<sub>16</sub>OCl, 271.0889, observed: 271.0883.



Colorless oil, 41% yield, 5:1 *E:Z*.

**<sup>1</sup>H NMR** (400 MHz, chloroform-*d*) δ 7.23 (s, 1H), 7.20 – 7.06 (comp, 2H), 6.40 – 6.27 (comp, 2H), 4.15 (t, *J* = 8.4 Hz, 2H), 3.80 (dd, *J* = 8.4, 6.0 Hz, 2H), 3.43 – 3.26 (m, 1H), 2.91 (dd, *J* = 9.2, 4.4 Hz, 2H), 2.55 – 2.48 (m, 1H), 2.46 – 2.38 (m, 1H), 2.32 – 2.25 (m, 1H), 2.20 – 2.13 (m, 1H), 2.10 – 1.95 (comp, 4H), 1.69 – 1.51 (comp, 6H), 1.45 (comp, *J* = 3.4 Hz, 12H); **<sup>13</sup>C{<sup>1</sup>H} NMR** (101 MHz, chloroform-*d*) δ 220.8, 156.4, 139.3, 136.7, 134.4, 130.8, 129.8, 126.8, 125.6, 123.7, 79.4, 50.5, 48.0, 44.4, 38.2, 35.9, 31.9, 31.6, 29.4, 28.4, 26.5, 25.7, 21.6, 13.9; **HRMS** (ESI) scaled for [M-tBu+2H]<sup>+</sup>: C<sub>23</sub>H<sub>30</sub>NO<sub>3</sub>, 380.2225, observed: 380.2227.

## 6.5 References

1. Zheng, H.; Fan, Y.; Song, Y.; Chen, J. S.; You, E.; Labalme, S.; Lin, W., Site Isolation in Metal–Organic Layers Enhances Photoredox Gold Catalysis. *J. Am. Chem. Soc.* **2022**, *144* (24), 10694-10699.
2. Drake, T.; Ji, P.; Lin, W., Site Isolation in Metal–Organic Frameworks Enables Novel Transition Metal Catalysis. *Acc. Chem. Res.* **2018**, *51* (9), 2129-2138.
3. Konnerth, H.; Matsagar, B. M.; Chen, S. S.; Pechtl, M. H. G.; Shieh, F.-K.; Wu, K. C. W., Metal-organic framework (MOF)-derived catalysts for fine chemical production. *Coord. Chem. Rev.* **2020**, *416*, 213319.
4. Lan, G.; Li, Z.; Veroneau, S. S.; Zhu, Y.-Y.; Xu, Z.; Wang, C.; Lin, W., Photosensitizing Metal–Organic Layers for Efficient Sunlight-Driven Carbon Dioxide Reduction. *J. Am. Chem. Soc.* **2018**, *140* (39), 12369-12373.
5. Lan, G.; Quan, Y.; Wang, M.; Nash, G. T.; You, E.; Song, Y.; Veroneau, S. S.; Jiang, X.; Lin, W., Metal–Organic Layers as Multifunctional Two-Dimensional Nanomaterials for Enhanced Photoredox Catalysis. *J. Am. Chem. Soc.* **2019**, *141* (40), 15767-15772.
6. Luo, T.; Fan, Y.; Mao, J.; Yuan, E.; You, E.; Xu, Z.; Lin, W., Dimensional Reduction Enhances Photodynamic Therapy of Metal–Organic Nanophotosensitizers. *J. Am. Chem. Soc.* **2022**, *144* (12), 5241-5246.
7. Zhao, M.; Wang, Y.; Ma, Q.; Huang, Y.; Zhang, X.; Ping, J.; Zhang, Z.; Lu, Q.; Yu, Y.; Xu, H.; Zhao, Y.; Zhang, H., Ultrathin 2D Metal–Organic Framework Nanosheets. *Adv. Mater.* **2015**, *27* (45), 7372-7378.
8. Jian, M.; Qiu, R.; Xia, Y.; Lu, J.; Chen, Y.; Gu, Q.; Liu, R.; Hu, C.; Qu, J.; Wang, H.; Zhang, X., Ultrathin water-stable metal-organic framework membranes for ion separation. *Science Advances* **6** (23), eaay3998.
9. Wei, R.-J.; You, P.-Y.; Duan, H.; Xie, M.; Xia, R.-Q.; Chen, X.; Zhao, X.; Ning, G.-H.; Cooper, A. I.; Li, D., Ultrathin Metal–Organic Framework Nanosheets Exhibiting Exceptional Catalytic Activity. *J. Am. Chem. Soc.* **2022**.
10. Dong, J.; Mo, Q.; Wang, Y.; Jiang, L.; Zhang, L.; Su, C.-Y., Ultrathin Two-Dimensional Metal–Organic Framework Nanosheets Based on a Halogen-Substituted Porphyrin Ligand:

Synthesis and Catalytic Application in CO<sub>2</sub> Reductive Amination. *Eur. J. Chem.* **2022**, *28* (41), e202200555.

11. Twilton, J.; Le, C.; Zhang, P.; Shaw, M. H.; Evans, R. W.; MacMillan, D. W. C., The merger of transition metal and photocatalysis. *Nature Reviews Chemistry* **2017**, *1* (7), 0052.
12. Skubi, K. L.; Blum, T. R.; Yoon, T. P., Dual Catalysis Strategies in Photochemical Synthesis. *Chem. Rev.* **2016**, *116* (17), 10035-10074.
13. Kojima, M.; Matsunaga, S., The Merger of Photoredox and Cobalt Catalysis. *Trends in Chemistry* **2020**, *2* (5), 410-426.
14. Zhang, G.; Liu, C.; Yi, H.; Meng, Q.; Bian, C.; Chen, H.; Jian, J.-X.; Wu, L.-Z.; Lei, A., External Oxidant-Free Oxidative Cross-Coupling: A Photoredox Cobalt-Catalyzed Aromatic C–H Thiolation for Constructing C–S Bonds. *Journal of the American Chemical Society* **2015**, *137* (29), 9273-9280.
15. Cao, H.; Jiang, H.; Feng, H.; Kwan, J. M. C.; Liu, X.; Wu, J., Photo-induced Decarboxylative Heck-Type Coupling of Unactivated Aliphatic Acids and Terminal Alkenes in the Absence of Sacrificial Hydrogen Acceptors. *Journal of the American Chemical Society* **2018**, *140* (47), 16360-16367.
16. Zhao, H.; McMillan, A. J.; Constantin, T.; Mykura, R. C.; Juliá, F.; Leonori, D., Merging Halogen-Atom Transfer (XAT) and Cobalt Catalysis to Override E2-Selectivity in the Elimination of Alkyl Halides: A Mild Route toward contra-Thermodynamic Olefins. *J. Am. Chem. Soc.* **2021**, *143* (36), 14806-14813.
17. Jia, Z.; Zhang, L.; Luo, S., Asymmetric C–H Dehydrogenative Allylic Alkylation by Ternary Photoredox-Cobalt-Chiral Primary Amine Catalysis under Visible Light. *J. Am. Chem. Soc.* **2022**, *144* (24), 10705-10710.
18. Occhialini, G.; Palani, V.; Wendlandt, A. E., Catalytic, contra-Thermodynamic Positional Alkene Isomerization. *J. Am. Chem. Soc.* **2022**, *144* (1), 145-152.
19. McManus, J. B.; Griffin, J. D.; White, A. R.; Nicewicz, D. A., Homobenzylic Oxygenation Enabled by Dual Organic Photoredox and Cobalt Catalysis. *J. Am. Chem. Soc.* **2020**, *142* (23), 10325-10330.
20. Thullen, S. M.; Rovis, T., A Mild Hydroaminoalkylation of Conjugated Dienes Using a Unified Cobalt and Photoredox Catalytic System. *J. Am. Chem. Soc.* **2017**, *139* (43), 15504-15508.
21. Wang, S.; Gao, Y.; Liu, Z.; Ren, D.; Sun, H.; Niu, L.; Yang, D.; Zhang, D.; Liang, X. a.; Shi, R.; Qi, X.; Lei, A., Site-selective amination towards tertiary aliphatic allylamines. *Nature Catalysis* **2022**, *5* (7), 642-651.
22. Liu, W.-Q.; Lei, T.; Zhou, S.; Yang, X.-L.; Li, J.; Chen, B.; Sivaguru, J.; Tung, C.-H.; Wu, L.-Z., Cobaloxime Catalysis: Selective Synthesis of Alkenylphosphine Oxides under Visible Light. *J. Am. Chem. Soc.* **2019**, *141* (35), 13941-13947.
23. Zhou, M.-J.; Zhang, L.; Liu, G.; Xu, C.; Huang, Z., Site-Selective Acceptorless Dehydrogenation of Aliphatics Enabled by Organophotoredox/Cobalt Dual Catalysis. *J. Am. Chem. Soc.* **2021**, *143* (40), 16470-16485.
24. Meng, Q.-Y.; Zhong, J.-J.; Liu, Q.; Gao, X.-W.; Zhang, H.-H.; Lei, T.; Li, Z.-J.; Feng, K.; Chen, B.; Tung, C.-H.; Wu, L.-Z., A Cascade Cross-Coupling Hydrogen Evolution Reaction by Visible Light Catalysis. *J. Am. Chem. Soc.* **2013**, *135* (51), 19052-19055.
25. U. Dighe, S.; Juliá, F.; Luridiana, A.; Douglas, J. J.; Leonori, D., A photochemical dehydrogenative strategy for aniline synthesis. *Nature* **2020**, *584* (7819), 75-81.

26. Constantin, T.; Zanini, M.; Regni, A.; Sheikh Nadeem, S.; Juliá, F.; Leonori, D., Aminoalkyl radicals as halogen-atom transfer agents for activation of alkyl and aryl halides. *Science* **2020**, *367* (6481), 1021-1026.
27. Lan, G.; Ni, K.; Veroneau, S. S.; Luo, T.; You, E.; Lin, W., Nanoscale Metal–Organic Framework Hierarchically Combines High-Z Components for Multifarious Radio-Enhancement. *J. Am. Chem. Soc.* **2019**, *141* (17), 6859-6863.
28. Zhao, W.; Sun, J., Triflimide (HNTf<sub>2</sub>) in Organic Synthesis. *Chem. Rev.* **2018**, *118* (20), 10349-10392.
29. Bhattacharya, S.; Snehalatha, K., Dialkylaminopyridine catalysed esterolysis of p-nitrophenyl alkanoates in different cationic microemulsions. *Journal of the Chemical Society, Perkin Transactions 2* **1996**, (9), 2021-2025.
30. Koshi, Y.; Nakata, E.; Miyagawa, M.; Tsukiji, S.; Ogawa, T.; Hamachi, I., Target-Specific Chemical Acylation of Lectins by Ligand-Tethered DMAP Catalysts. *J. Am. Chem. Soc.* **2008**, *130* (1), 245-251.
31. Quan, Y.; Lan, G.; Shi, W.; Xu, Z.; Fan, Y.; You, E.; Jiang, X.; Wang, C.; Lin, W., Metal–Organic Layers Hierarchically Integrate Three Synergistic Active Sites for Tandem Catalysis. *Angew. Chem. Int. Ed.* **2021**, *60* (6), 3115-3120.
32. Zhang, Z.-M.; Zhang, T.; Wang, C.; Lin, Z.; Long, L.-S.; Lin, W., Photosensitizing Metal–Organic Framework Enabling Visible-Light-Driven Proton Reduction by a Wells–Dawson-Type Polyoxometalate. *J. Am. Chem. Soc.* **2015**, *137* (9), 3197-3200.
33. Zhu, Y.-Y.; Lan, G.; Fan, Y.; Veroneau, S. S.; Song, Y.; Micheroni, D.; Lin, W., Merging Photoredox and Organometallic Catalysts in a Metal–Organic Framework Significantly Boosts Photocatalytic Activities. *Angew. Chem. Int. Ed.* **2018**, *57* (43), 14090-14094.



# Chapter 7. Biomimetic Active Sites on a Metal-Organic Layer for Artificial Photosynthesis

## 7.1 Introduction

In nature, enzymes rely upon active sites composed of precisely arranged metal centers, amino acids, and cofactors to efficiently catalyze chemical reactions. The reactivity and selectivity of metalloenzymes, for example, derives from a complex arrangement of metal ions coordinated to amino acid (AA) side chains and prosthetic groups, a secondary coordination sphere of additional proximal AA side chains, and cofactors (e.g., pigments, NAD(P)H, ATP) (**Figure 7-1a**).<sup>1</sup> Importantly, the secondary coordination sphere stabilizes transition states and reactive intermediates through non-covalent interactions while cofactors provide electrons, hydride equivalents, and other species to facilitate reactive pathways. Although a number of artificial systems, including metal-clusters,<sup>2-5</sup> metal and metal-oxide nanoparticles,<sup>6</sup> supermolecules, and polymers,<sup>7</sup> and MOFs,<sup>8-14</sup> have been developed to mimic the catalytic activity and selectivity of enzymes, current designs of artificial enzymes, however, predominately mimic the active metal centers of enzymes without secondary coordination or additional cofactors.<sup>15</sup> Thus, artificial enzyme systems are currently limited to catalyzing relatively simple reactions and lack the systematic tunability required to expand their scope. A general method to rationally design artificial enzymes with complex yet tunable active sites is needed to target increasingly challenging and relevant chemical transformations.

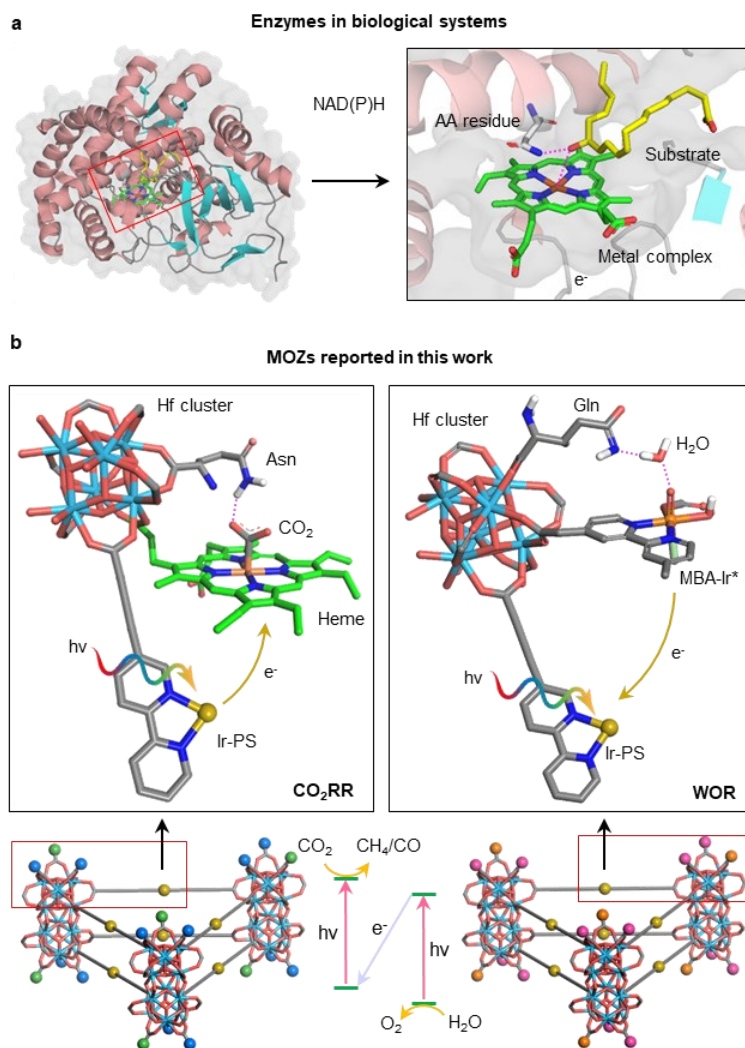


**Figure 7-1.** Design of biomimetic MOZs.(a) Schematic of the natural enzyme cytochrome P450 74A (PDB 3DSI) and its active site. (b) Schematic of representative MOZs reported in this work for CO<sub>2</sub>RR and WOR with their active sites. C atoms in haem are highlighted in green with all other atoms labeled as follows: H, white; C, grey; O, red; N, blue; Fe, orange in haemin; Hf, light blue; Ir, yellow in IrF-PS, orange in MBA-Ir\*.

In this chapter, we report a MOL-based artificial enzyme (metal-organic-zyme, MOZ) with precise arrangement of metal centers, amino acids, and pigments on a metal-organic monolayer to generate well-defined and complex active sites (**Figure 7-1b**). Further, the performance of MOZs

was systematically optimized through the following three steps (**Figure 7-2**): first, diversification and designing MOZ templates inspired by biocatalysts to create a library of MOZs through the incorporation of AAs; second, selection and screening of these MOZs for specific and enhanced activity; third, rational design of artificial ligands with increased functionality by leveraging the obtained mechanistic insights. Through these diversification, selection, and optimization processes, the optimized **MOZ-4** with pendant urea groups showed highly active and selective photocatalytic CO<sub>2</sub> reduction reaction (CO<sub>2</sub>RR) with TONs of 24740 and 10352 for CO and CH<sub>4</sub>, respectively, and a CO<sub>2</sub>RR selectivity of 98.0%, representing a 27-fold increase in activity over the homogeneous control. **MOZ-7** with pendant (*p*-chloro-phenyl)amide groups was similarly designed and optimized for photocatalytic water oxidation reaction (WOR) with a TON of 10213. Importantly, a combination of **MOZ-4** and **MOZ-7** with Co(bpy)<sub>3</sub><sup>2+</sup> as a redox mediator achieved total artificial photosynthesis of (1+n)CO<sub>2</sub> + 2H<sub>2</sub>O → CH<sub>4</sub> + nCO + (2+n/2)O<sub>2</sub> through a Z-scheme to afford a turnover frequency of 98.7 h<sup>-1</sup>, outperforming previously reported photocatalysts by over an order of magnitude.

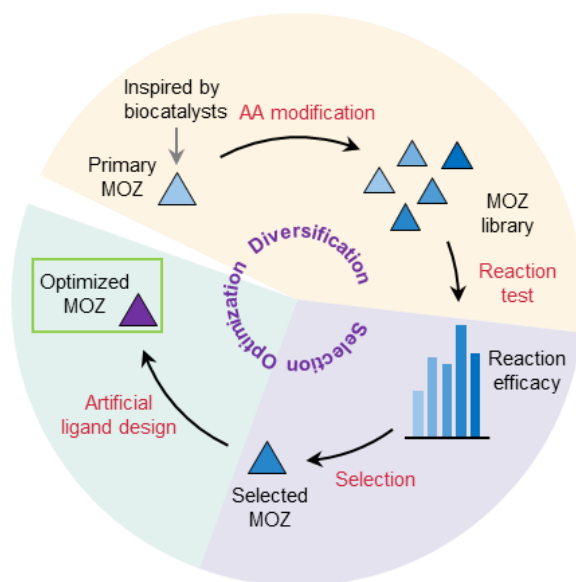


**Figure 7-2.** Schematic showing diversification, selection, and optimization of MOZs.

## 7.2 Results and Discussion

### 7.2.1 MOZs for Photocatalytic Carbon Dioxide Reduction

#### 7.2.1.1 Material Synthesis

We first designed a MOZ library for photocatalytic CO<sub>2</sub>RR (**Figure 7-3**). An underlying monolayer MOF (Hf-IrF) incorporating an Ir-based photosensitizer was first synthesized through a solvothermal reaction, which afforded the previously reported Hf<sub>12</sub> clusters<sup>16</sup> [Hf<sub>12</sub>(μ<sub>3</sub>-O)<sub>8</sub>(μ<sub>3</sub>-OH)<sub>8</sub>(μ<sub>2</sub>-OH)<sub>6</sub>] vertically capped by TFA and laterally connected by photosensitizing [Ir(DBB)(dF(CF<sub>3</sub>)ppy)<sub>2</sub>]<sup>+</sup> (IrF-PS) ligands. The crystalline two-dimensional network of the formula Hf<sub>12</sub>(μ<sub>3</sub>-O)<sub>8</sub>(μ<sub>3</sub>-OH)<sub>8</sub>(μ<sub>2</sub>-OH)<sub>6</sub>(IrF-PS)<sub>6</sub>(TFA)<sub>6</sub> is comprised of Hf<sub>12</sub> clusters capped with six labile TFA groups which can be exchanged for more strongly coordinating carboxylate groups to incorporate various functional groups onto these MOZs. Through carboxylate exchange, the ferric protoporphyrin hemin was installed onto Hf-IrF to afford a primary MOZ (**MOZ-1**) including an active Fe-based metal center.

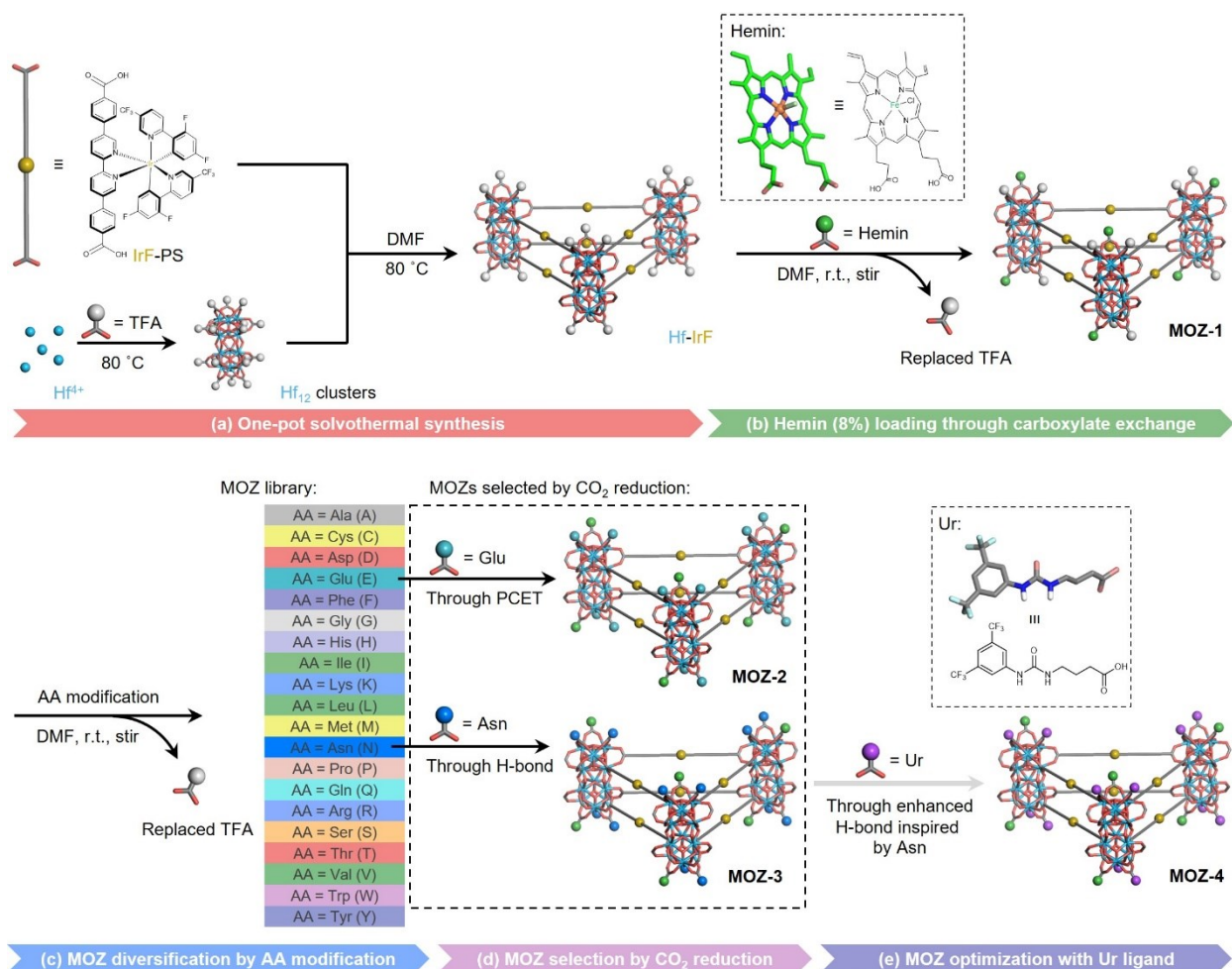


**Figure 7-3.** MOZ construction and optimization for CO<sub>2</sub>RR.

**MOZ-1** retained the monolayer morphology of Hf-IrF with a diameter of  $\sim 150$  nm and a thickness of  $\sim 2.1$  nm, as determined by TEM (**Figure 7-4a**) and AFM (**Figure 7-4d**), respectively. The  $\sim 0.5$  nm increase in thickness of **MOZ-1** over Hf-IrF corroborated the expected increase in the height for Hf<sub>12</sub>-clusters modified with flexible hemin groups. HRTEM (inset in **Figure 7-4a**) and high-angle annular dark-field (HAADF, **Figure 7-4b**) imaging of **MOZ-1** revealed a preserved six-fold **kgd** topological structure and the expected Hf<sub>12</sub>-Hf<sub>12</sub> distance of  $\sim 2.8$  nm. This topological structure of **MOZ-1** was further supported by comparing its PXRD pattern to that simulated from its model structure (**Figure 7-4f**). Energy-dispersive X-ray spectroscopy (EDS)

mapping showed homogenous distribution of hemin groups over the Hf- and Ir-based monolayer (**Figure 7-4c**). The loading of hemin was found to be  $\sim 8.0\%$  per IrF-PS based on UV-vis absorptions (**Figure 7-4e**) by deconvoluting the spectrum of digested **MOZ-1** into absorptions from hemin and IrF-PS, affording an empirical formula of  $\text{Hf}_{12}(\mu_3\text{-O})_8(\mu_3\text{-OH})_8(\mu_2\text{-OH})_6(\text{IrF-PS})_6(\text{hemin})_{0.48}(\text{TFA})_{5.52}$  for **MOZ-1**. The ratio of hemin to IrF-PS was designed to be  $<10\%$  so multiple electrons could be injected from IrF-PSs into hemin during a  $\text{CO}_2\text{RR}$  catalytic cycle. Moreover, the remaining TFA ( $\sim 90\%$ ) accommodated further modification of **MOZ-1** with AAs.

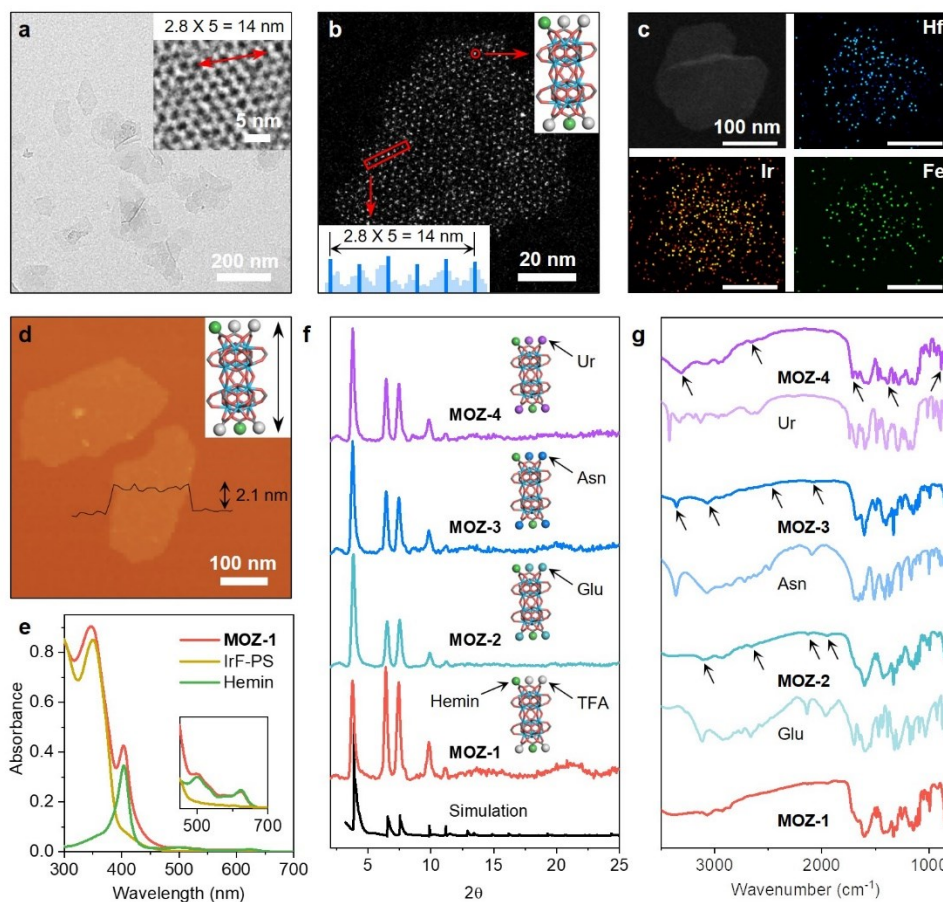


**Figure 7-4.** Characterization of MOZs. (a) TEM and HRTEM (inset) images, (b) HAADF image, (c) EDS maps, and (d) AFM topography of **MOZ-1**. (e) UV-vis spectrum of digested **MOZ-1**. (f) PXRD patterns of MOZs (g) IR spectra of MOZs compared to corresponding Glu, Asn, and Ur.



**MOZ-1** was subsequently diversified by replacing the remaining TFA groups with proteinogenic AAs to generate a library of MOZs (**Figure 7-3**). Prototypical Glu- and Asn-modified MOZs (denoted **MOZ-2** and **MOZ-3**, respectively) were specifically selected for comprehensive characterization. These MOZs again maintained the topological structure of **MOZ-1**, as revealed by PXRD (**Figure 7-4f**) and HRTEM imaging (**Figure 7-5**). Moreover, TEM, AFM, and dynamic light scattering (DLS) revealed a preserved monolayer morphology, with diameters of ~150 nm, thicknesses of 2.0-2.2 nm, and number-averaged sizes of 112-125 nm (**Figure 7-5**).

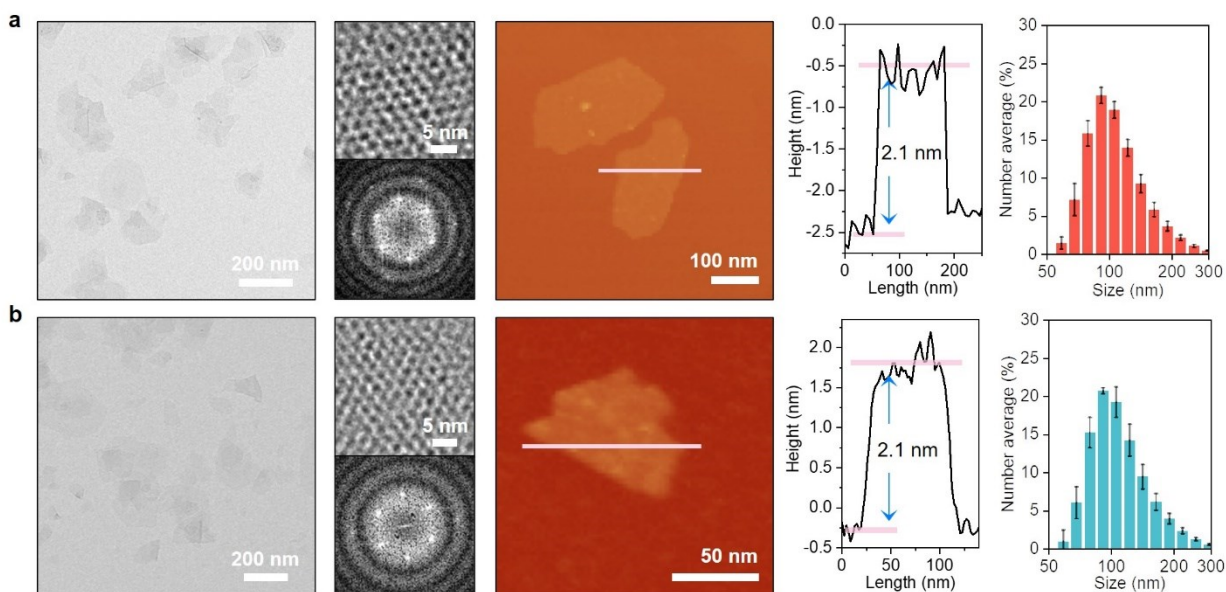


**Figure 7-5.** Morphology characterization of **MOZ-2** and **MOZ-3**. From left to right: TEM image, HRTEM image, AFM image, height profile, and DLS of **MOZ-2** (a) and **MOZ-3** (b).

The incorporation of Glu and Asn was confirmed by IR spectroscopy. The absorption peaks of **MOZ-1** were consistently observed and the unique spectroscopic features of Glu and Asn were only observed in **MOZ-2** and **MOZ-3**, respectively (**Figure 7-4g**). The exchange of TFA by Glu and Asn was confirmed by NMR analysis of digested hemin-free MOZ analogs, where no TFA signal was observed by  $^{19}\text{F}$  NMR and a near 1:1 ratio of AA to IrF-PS signal by  $^1\text{H}$  NMR (Note:

hemin-free analogs were used to avoid the influence of paramagnetic hemin, **Figure 7-6**). Thus, the weakly coordinating TFA groups were completely replaced by AAs while the strongly-coordinating hemin groups remained unchanged, as evidenced by preserved hemin to IrF-PS ratios of 7.8% and 8.0% in Glu- and Asn-modified MOZs, respectively. The empirical formulas of **MOZ-2** and **MOZ-3** were therefore determined to be  $\text{Hf}_{12}(\mu_3\text{-O})_8(\mu_3\text{-OH})_8(\mu_2\text{-OH})_6(\text{IrF-PS})_6(\text{hemin})_{0.47}(\text{Glu})_{5.53}$  and  $\text{Hf}_{12}(\mu_3\text{-O})_8(\mu_3\text{-OH})_8(\mu_2\text{-OH})_6(\text{IrF-PS})_6(\text{hemin})_{0.48}(\text{Asn})_{5.52}$ , respectively. The remaining proteinogenic amino acids are presumed to display similar compositions in their corresponding MOZs.

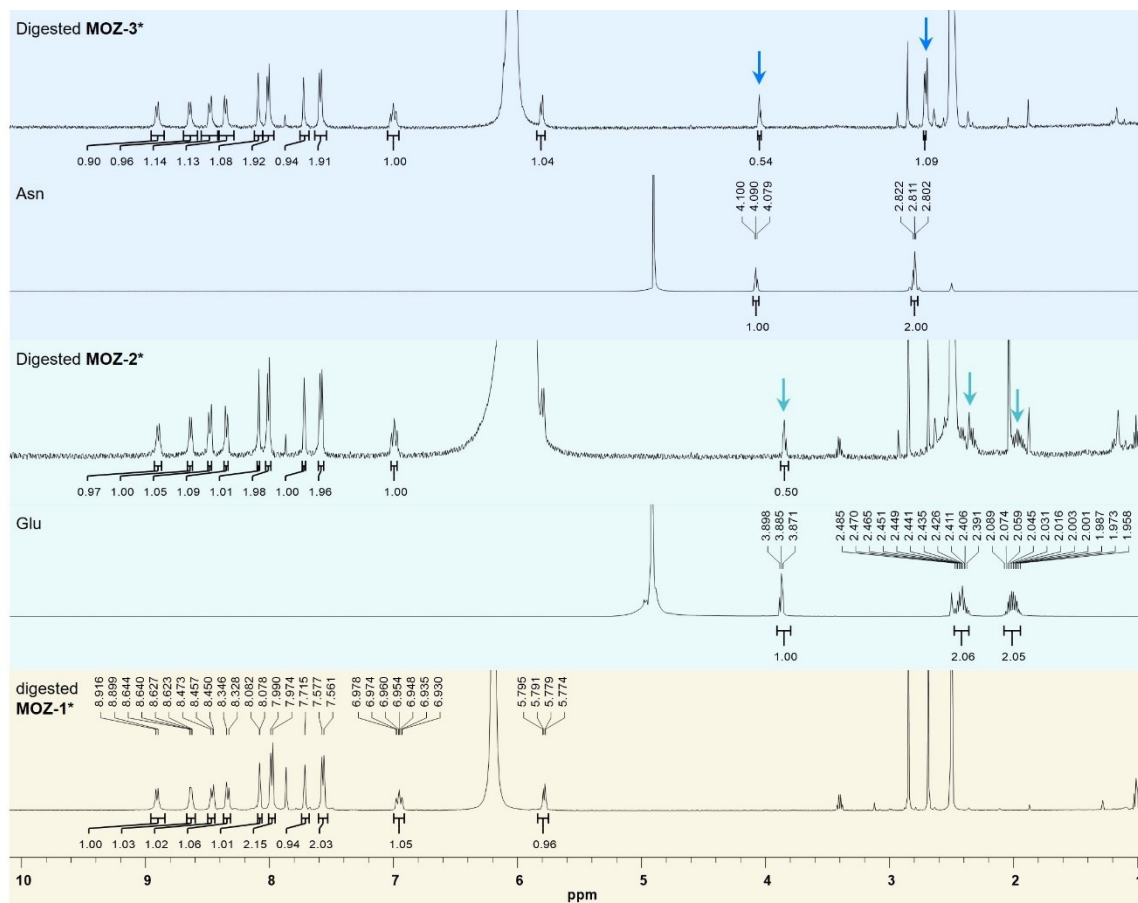


**Figure 7-6.**  $^1\text{H}$  NMR of digested MOZs.



### 7.2.1.2 AA Screening for CO<sub>2</sub>RR Optimization

The MOZs in this library were next selected for photocatalytic CO<sub>2</sub>RR.<sup>17-22</sup> The proximal arrangements of AAs and Fe-porphyrin centers (i.e., hemin) in each MOZ provided a unique active site on each Hf<sub>12</sub> cluster, with approximately two AAs (and their R-groups) within several Å of the Fe-centers. MOZs (0.1 μM based on hemin and 1.25 μM based on IrF-PS) were individually added to 1 mL DMA (providing good dispersity of MOZs) solutions of trifluoroethanol (TFE, 100 mM, as proton resource with a proper pK<sub>a</sub> of 12.5) and 1,3-dimethyl-2-phenyl-2,3-dihydro-1H-benzo[d]-imidazole (BIH, 50 mM, as sacrificial reductant) under 1 atm CO<sub>2</sub> and at room temperature, with visible-light irradiation for 6 h (Xenon lamp, λ > 300 nm). Upon irradiation, photoexcited IrF-PS ligands inject electrons into the active sites of each MOZ to drive CO<sub>2</sub>RR. MOZ-catalyzed CO<sub>2</sub>RR produces CO and CH<sub>4</sub> through two distinct steps: first, reduction of CO<sub>2</sub> to CO through a two-electron and two-proton process; second, reduction of CO to CH<sub>4</sub> through a six-electron and six-proton process (**Figure 7-7a**). The production of CO and CH<sub>4</sub> was detected by both gas chromatography (GC, **Figure 7-7b**) and gas chromatography-mass spectrometry (GC-MS, isotope labeling, **Figure 7-7c**). The only observed byproduct of this reaction is H<sub>2</sub>, which is proposed to proceed through a competing reaction pathway.<sup>17, 23</sup>

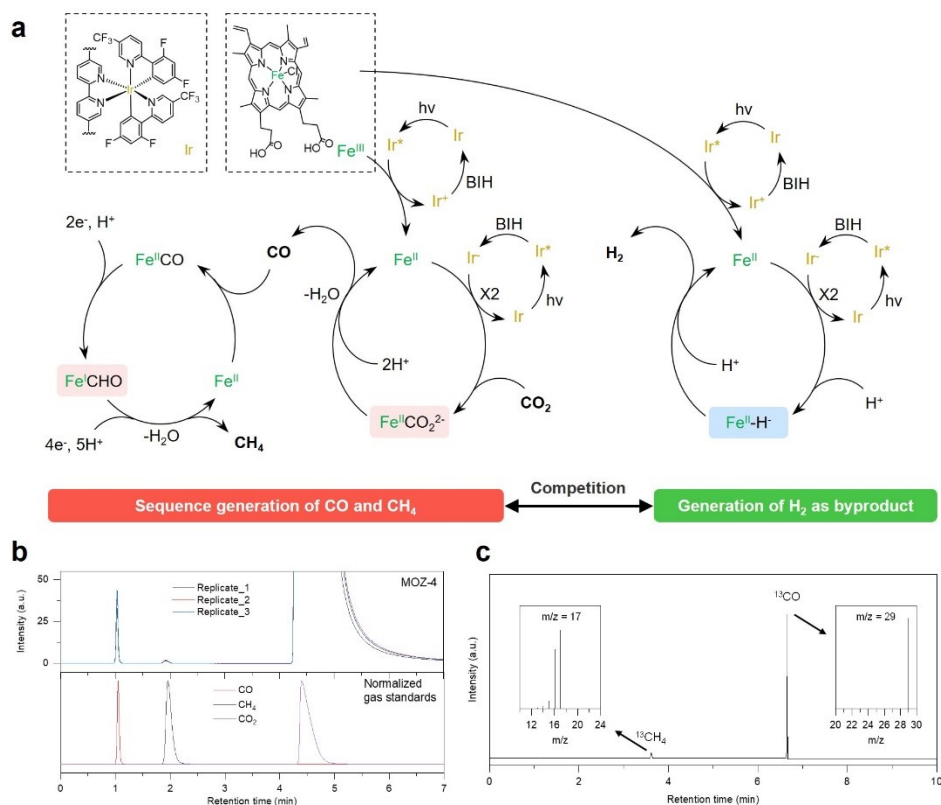


**Figure 7-7.** CO<sub>2</sub>RR product. (a) Proposed mechanistic cycles for CO<sub>2</sub>RR. (b) GC trace of gaseous mixture after CO<sub>2</sub>RR. (c) GC-MS trace and MS signal of gaseous mixture after CO<sub>2</sub>RR with <sup>13</sup>CO<sub>2</sub>.

The activity of each MOZ for CO<sub>2</sub>RR was evaluated by quantifying the generation of CO and CH<sub>4</sub>. **MOZ-1** showed a 7-fold increase in TON compared to the homogeneous control (a molar-equivalent mixture of hemin and IrF-PS) owing to accelerated electron transfer from excited IrF-PSs to the adjacent hemin (<2 nm distance). AA-modified MOZs, particularly **MOZ-2** and **MOZ-3**, further enhance these CO<sub>2</sub>RR activities. This enhancement is proposed to proceed through two distinct pathways: proton-coupled electron transfer (PCET) and H-bond stabilization (**Figure 7-8**).

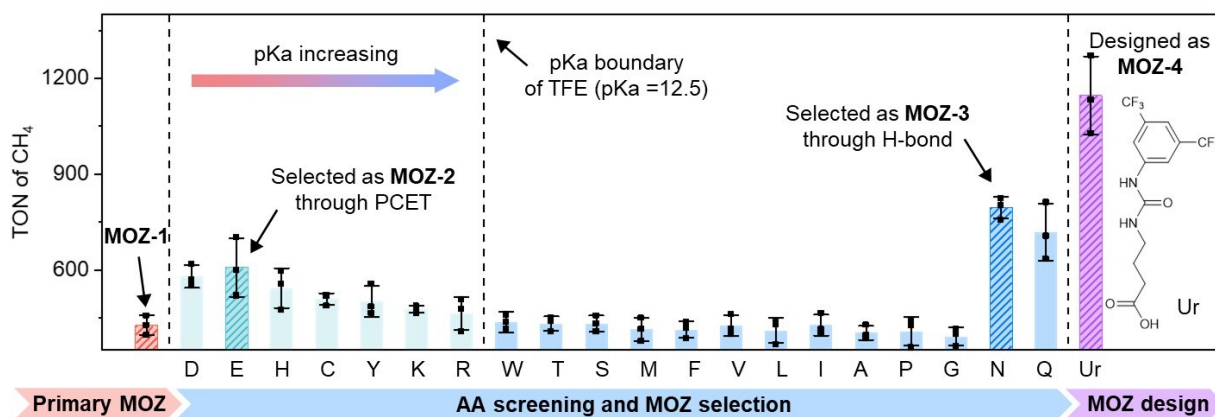


**Figure 7-8.** TONs for CH<sub>4</sub> of **MOZ-1**, AA-modified MOZs, and Ur-modified MOZ. Data are presented as mean  $\pm$  s.d. ( $n = 3$ ) with the error bars representing the s.d.; individual data points are shown as black dots.

First, as the generation of both CO and CH<sub>4</sub> requires protons and electrons, MOZs with R-groups more acidic (i.e., lower  $pK_a$ ) than the provided proton source (TFE,  $pK_a = 12.5$ ) may enhance catalytic activity through a PCET pathway.<sup>24</sup> The enhancement of CO<sub>2</sub>RR via this PCET pathway is maximized in Glu-modified **MOZ-2**, as Glu displays the lowest  $pK_a$  value among proteinogenic AAs. MOZs modified with AAs whose R-groups were less acidic than TFE were not expected to exhibit higher activity than **MOZ-1**, and so we were surprised to discover that Asn- and Gln-modified MOZs afforded much higher CO<sub>2</sub>RR activity over even **MOZ-2** (**Figure 7-8**). We propose this enhancement by Asn and Gln arises through H-bond stabilization, specifically through secondary-coordination sphere interactions between electron-deficient amide  $-NH_2$  fragments and Fe-bound reactive intermediates (**Figure 7-1b**).<sup>25</sup> This enhancement in CO<sub>2</sub>RR activity via H-bond stabilization is maximized in Asn-modified **MOZ-3**.

The H-bond stabilization by **MOZ-3** was elucidated by density functional theory (DFT) calculations. In the proposed two-step reduction of CO<sub>2</sub> and CO, Fe<sup>II</sup>CO<sub>2</sub><sup>2-</sup> and Fe<sup>I</sup>CHO are

proposed as crucial reactive intermediates (**Figure 7-9**). DFT calculations were thus performed on model compounds to investigate the possible geometries of  $\text{Fe}^{\text{II}}\text{CO}_2^{2-}$  and  $\text{Fe}^{\text{I}}\text{CHO}$ .<sup>26</sup> **MOZ-3** showed a moderate H-bond interaction between amide groups and Fe-bound  $\text{CO}_2$  in  $\text{Fe}^{\text{II}}\text{CO}_2^{2-}$  with an (N)H $\cdots$ O donor-acceptor distance of 1.96 Å and corresponding free enthalpy of stabilization ( $\Delta H_{\text{Stb}}$ ) of  $-14.1 \text{ kcal}\cdot\text{mol}^{-1}$ . **MOZ-3** showed an additional moderate H-bond interaction between amide groups and the Fe-bound CHO in  $\text{Fe}^{\text{I}}\text{CHO}$  with an (N)H $\cdots$ O donor-acceptor distance of 2.02 Å and a corresponding  $\Delta H_{\text{Stb}}$  of  $-9.1 \text{ kcal}\cdot\text{mol}^{-1}$ .

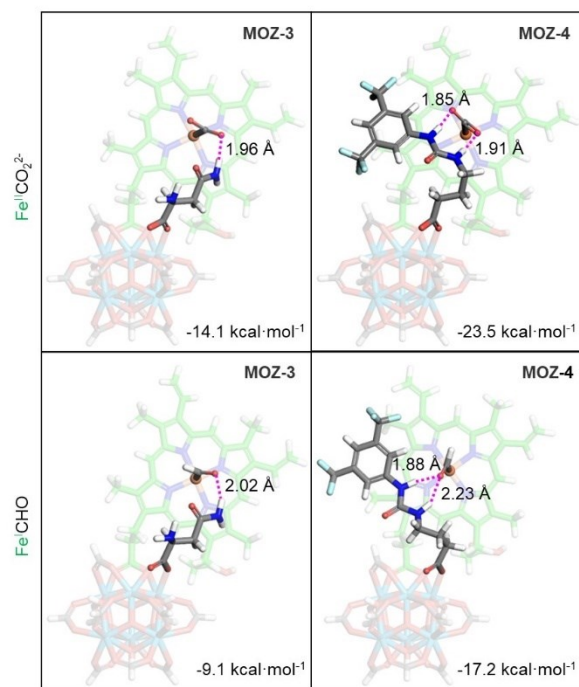


**Figure 7-9.** Representative model structures of  $\text{Fe}^{\text{II}}\text{CO}_2^{2-}$  and  $\text{Fe}^{\text{I}}\text{CHO}$  in **MOZ-3** and **MOZ-4**.

The activities of these MOZs were further evaluated in time-dependent reactions. Upon 72-h visible light irradiation, **MOZ-2** and **MOZ-3** significantly enhanced  $\text{CO}_2\text{RR}$  with the TONs for  $\text{CO}/\text{CH}_4$  reaching  $9530 \pm 753 / 4248 \pm 232$  and  $14620 \pm 995 / 5740 \pm 414$ , respectively, compared to  $3849 \pm 137 / 2213 \pm 26$  for **MOZ-1** and only  $955 \pm 262 / 373 \pm 47$  for the homogenous

control (**Figure 7-10a**). **MOZ-2**, however, was only moderately selective for CO<sub>2</sub>RR (80.9%), as the PCET pathway enabled by Glu also accelerated the generation of H<sub>2</sub> (**Figure 7-10b**). In contrast, **MOZ-3** accelerated the sequential generation of CO and CH<sub>4</sub> by stabilizing their reactive intermediates, leaving the H<sub>2</sub> generation pathway unaffected, thus leading to an enhanced selectivity of 97.4% (**Figure 7-10b**).

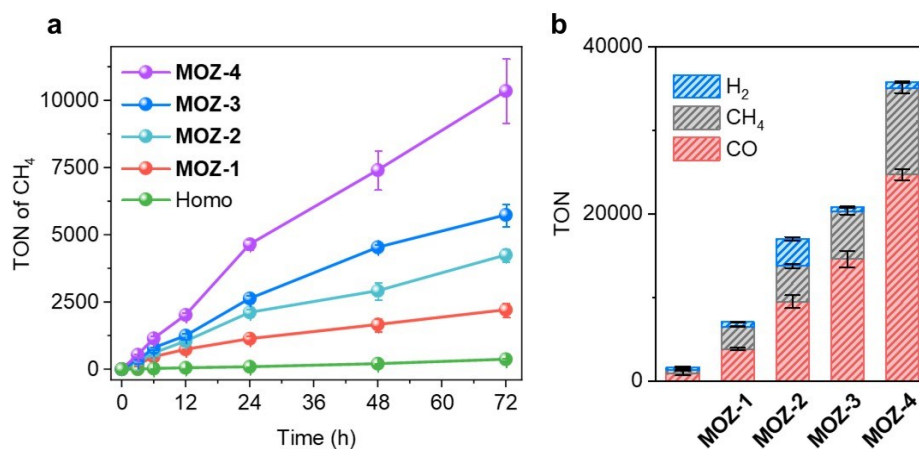


**Figure 7-10.** CO<sub>2</sub>RR reactivity of MOZs. (a) Time-dependent TONs of CH<sub>4</sub> for MOZs and homogeneous control (Homo) under visible-light irradiation. (b) TON summary of CO, CH<sub>4</sub>, and H<sub>2</sub> for MOZs and homogeneous control under 72 h visible-light irradiation. Data are presented as mean  $\pm$  s.d. (n = 3) with the error bars representing the s.d.

### 7.2.1.3 Artificial Ligands

The activity of this library in CO<sub>2</sub>RR was optimized by designing a urea-based ligand (Ur) to provide even stronger H-bond stabilization. This Ur ligand includes a phenyl ring bearing two electron-withdrawing -CF<sub>3</sub> groups to enhance the H-bond donor strength of the urea -NH fragment. Ur was modified onto **MOZ-1** in the same manner as above to afford **MOZ-4** and was similarly characterized to reveal a conserved morphology, topography, and structure, with the

empirical formula  $\text{Hf}_{12}(\mu_3\text{-O})_8(\mu_3\text{-OH})_8(\mu_2\text{-OH})_6(\text{IrF-PS})_6(\text{hemin})_{0.46}(\text{Ur})_{5.54}$ . As desired, **MOZ-4** further enhanced  $\text{CO}_2$  reduction with TONs for  $\text{CO}/\text{CH}_4$  of  $24740 \pm 649 / 10352 \pm 592$  and selectivity for  $\text{CO}_2\text{RR}$  of 98.0% over 72 h of visible-light irradiation, a 5-fold increase in activity over **MOZ-1** and 27-fold increase in activity over the homogeneous control (**Figure 7-10**).

The enhancement in activity of **MOZ-4** over **MOZ-3** is attributed to the designed stronger H-bond stabilization, as elucidated by DFT calculations (**Figure 7-9**). Two strong H-bonds to  $\text{Fe}^{\text{II}}\text{CO}_2^{2-}$  intermediate were modeled, with (N)H $\cdots$ O donor-acceptor distances of 1.85 Å and 1.91 Å, and a corresponding  $\Delta H_{\text{Stb}}$  of  $-23.5 \text{ kcal}\cdot\text{mol}^{-1}$ , whereas two strong/moderate H-bonds to  $\text{Fe}^{\text{I}}\text{CHO}$  intermediates were modeled, with (N)H $\cdots$ O donor-acceptor distances of 1.88 Å and 2.23 Å, and a corresponding  $\Delta H_{\text{Stb}}$  of  $-17.2 \text{ kcal}\cdot\text{mol}^{-1}$ . To confirm H-bond interaction from Ur in **MOZ-4**, we designed analogous ligands with either a single -NH fragment (Am-1) or no -NH fragment (Am-2) (**Figure 7-11a**). As expected, a MOZ modified with the Am-1 ligand showed comparable  $\text{CO}_2\text{RR}$  reactivity to **MOZ-3**, which also contained a single -NH fragment (**Figure 7-11b, 7-11c**). Moreover, a MOZ modified with the Am-2 ligand showed comparable  $\text{CO}_2\text{RR}$  reactivity to **MOZ-1**, which also was devoid of -NH fragments (**Figure 7-11b, 7-11c**).

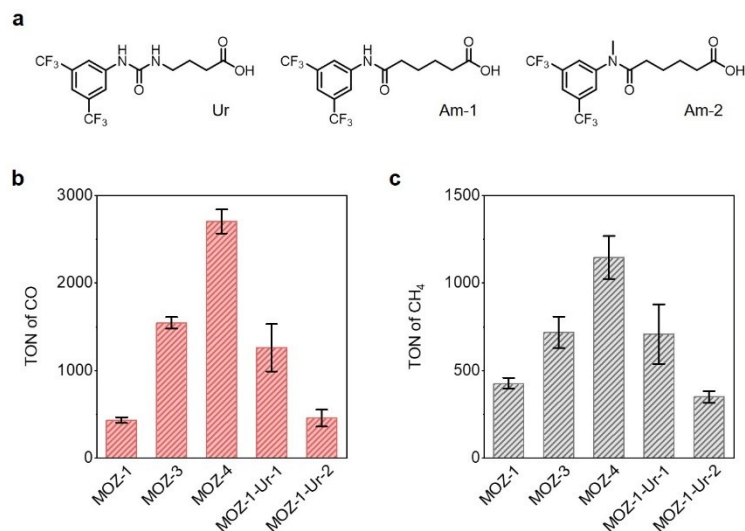


**Figure 7-11.** CO<sub>2</sub>RR by MOZs with artificial ligands.(a) Chemical structure of Ur, Am-1, and Am-2. TONs for (b) CO and (c) CH<sub>4</sub> in CO<sub>2</sub>RR catalyzed by **MOZ-4** and other control groups.

**MOZ-4** was examined for CO<sub>2</sub>RR with energy input from natural sunlight. These photocatalytic CO<sub>2</sub>RR studies were carried out under the same conditions as described above under natural sunlight for five consecutive days (**Figure 7-12a**). Reactivity was weather-dependent, but on a sunny day, **MOZ-4** catalyzed CH<sub>4</sub> generation with a TON of 904, a TOF of 150.7 h<sup>-1</sup>, a quantum yield of 1.8% at 350 nm, and a selectivity of over 99%. **MOZ-4** thus directly converted CO<sub>2</sub> to CH<sub>4</sub> with energy input from sunlight. The MOZs reported in this work showed orders-of-magnitude higher activity and selectivity than recently reported state-of-the-art photocatalysts, including small molecules,<sup>17, 23</sup> metal and metal oxide nanoparticles,<sup>27-30</sup> and MOFs,<sup>31</sup> and among others (**Figure 7-12b**). This stable, heterogeneous **MOZ-4** was recycled at least five times without apparent loss of activity (**Figure 7-12c**).

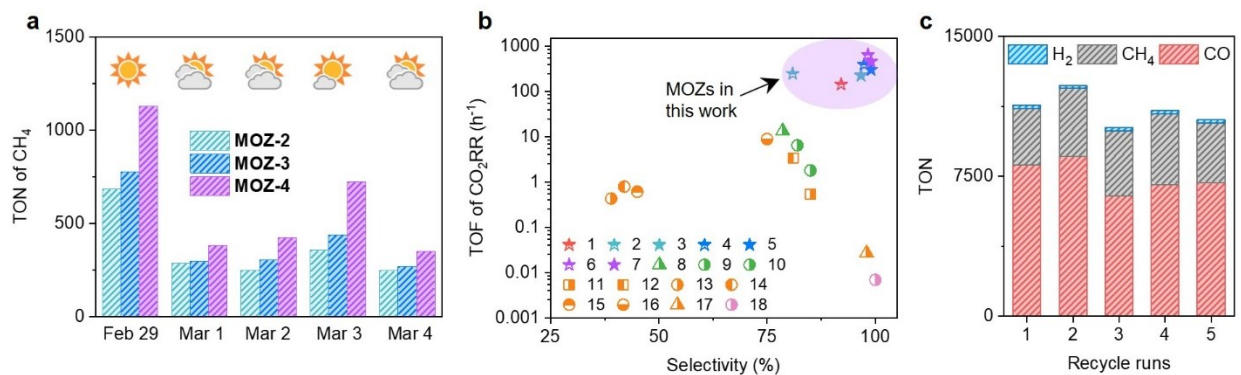


**Figure 7-12.** Sunlight-driven CO<sub>2</sub>RR and catalyst recycle. (a) TONs of CH<sub>4</sub> for **MOZ-2**, **MOZ-3** and **MOZ-4** over five consecutive days under direct sunlight. (b) Summary of activities for photocatalytic conversion of CO<sub>2</sub> to CH<sub>4</sub> by MOZs in this work compared to previously reported catalysts (see supplementary data **Table 7-1** for detail). (c) Summary of TONs of CO, CH<sub>4</sub>, and H<sub>2</sub> for recycled **MOZ-4** over five consecutive trials.

## 7.2.2 MOZs for Photocatalytic Water Oxidation

### 7.2.2.1 Material synthesis

A separate photocatalytic MOZ library for WOR was constructed and optimized through the same strategy (**Figure 7-13**).<sup>32</sup> A new primary MOZ was constructed from an identical Hf-IrF monolayer with the incorporation of an Ir-based active metal center (**MOZ-5**). This active catalyst, [Ir(H-MBA)Cp\*Cl]<sup>+</sup> (MBA-Ir, H-MBA = 2-(4'-methyl-[2,2'-bipyridin]-4-yl)acetic acid; Cp\* = pentamethylcyclopentadienyl), was loaded onto the surface of the underlying monolayer at an 8% ratio per IrF-PS (**Figure 7-14d**). **MOZ-5** retained the monolayer morphology of Hf-IrF with a diameter of ~150 nm, a thickness of ~2.1 nm, and a number-averaged size of 117.4 ± 8.1 nm, as determined by TEM, AFM, and DLS, respectively (**Figure 7-14a**). HRTEM imaging of **MOZ-5** revealed the 6-fold **k<sub>gd</sub>** topological structure and an expected Hf<sub>12</sub>-Hf<sub>12</sub> distance of ~2.8 nm. The topological structure of **MOZ-5** was further supported by the similarity of its PXRD pattern to that



simulated from its model structure (**Figure 7-14c**). **MOZ-5** had an empirical formula of  $\text{Hf}_{12}(\mu_3\text{-O})_8(\mu_2\text{-OH})_6(\text{IrF-PS})_6(\text{MBA-Ir})_{0.48}(\text{TFA})_{5.52}$ .

As previously reported,<sup>33</sup> MBA-Ir catalyzes WOR through two distinct steps: first, the generation of active WOR catalyst  $[\text{Ir}(\text{MBA})(\text{H}_2\text{O})_2(\text{CH}_3\text{COO})\text{Cl}]^+$  (MBA-Ir) via oxidation of the Cp\* group; second, the WOR catalyzed by MBA-Ir\* through an  $\text{Ir}^{\text{III}}/\text{Ir}^{\text{V}}$  cycle. Upon irradiation, photoexcited IrF-PS oxidize MBA-Ir to oxidize  $\text{H}_2\text{O}$  to  $\text{O}_2$  through a four-electron and four-proton process.

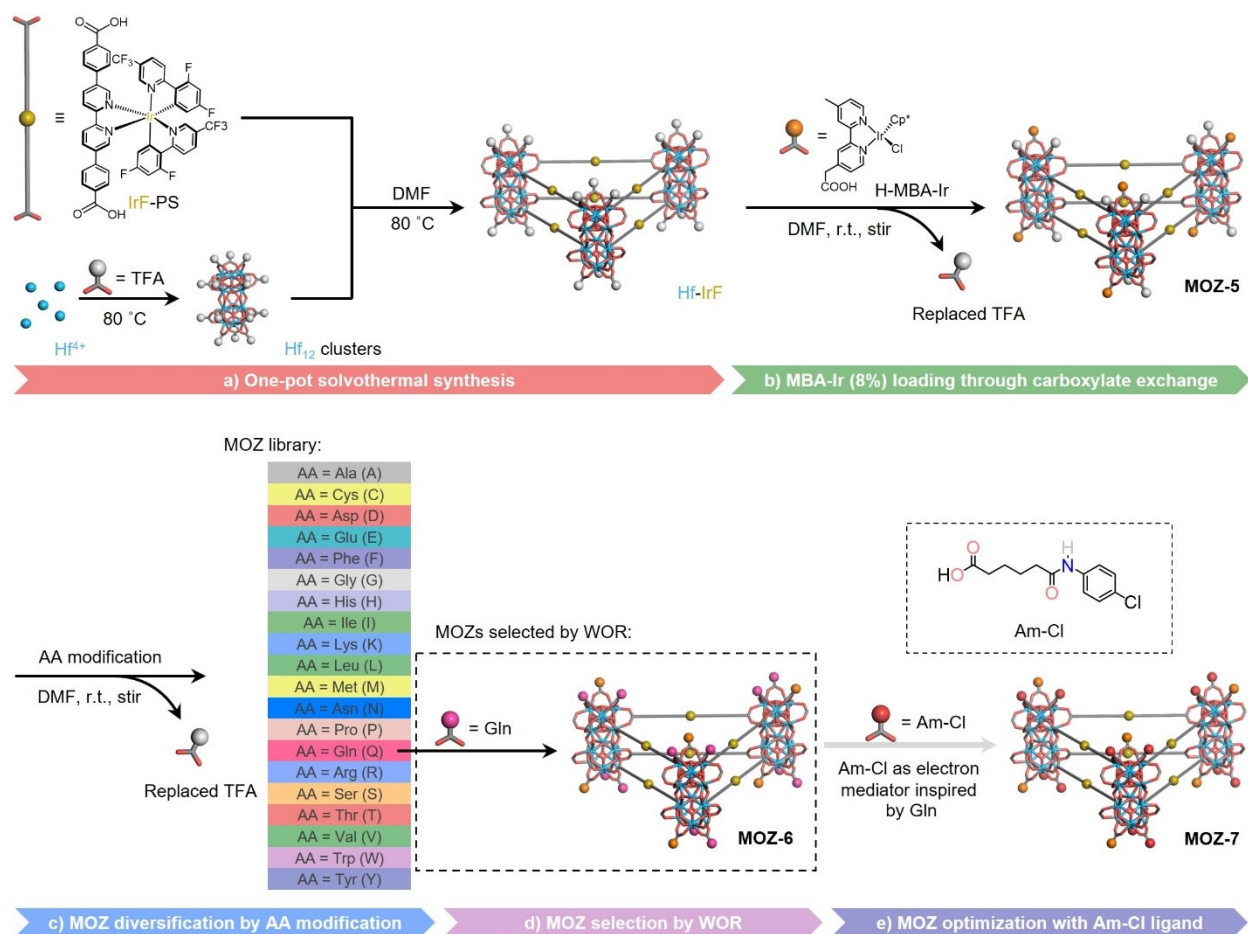


**Figure 7-13.** MOZ construction and optimization for WOR.

A library of MOZs was subsequently diversified by appending various proteinogenic AAs on **MOZ-5** and selected for photocatalytic WOR activity (**Figure 7-13**). The new MOZs were constructed by replacing the remaining TFA on **MOZ-5** with proteinogenic AAs through carboxylate exchange reactions. The resultant MOZ with Gln modification, denoted **MOZ-6**, was characterized by TEM, AFM, and DLS, revealing a preserved monolayer morphology, with diameters of ~150 nm, thicknesses of 2.1 nm, and number-averaged sizes of  $120.6 \pm 4.1$  nm (**Figure 7-14b**). **MOZ-6** also maintained the topological structure of **MOZ-5**, as revealed by PXRD (**Figure 7-14c**) and HRTEM imaging (**Figure 7-14b**). The incorporation of Gln in **MOZ-6** was confirmed by NMR analysis of digested **MOZ-6** with a near 1:1 ratio of Gln to IrF-PS signal (**Figure 7-14e**). While weakly coordinating TFA groups could be completely replaced by AAs, strongly coordinating MBA-Ir groups remained unchanged, affording a formulation of  $\text{Hf}_{12}(\mu_3\text{-O})_8(\mu_3\text{-OH})_8(\mu_2\text{-OH})_6(\text{IrF-PS})_6(\text{MBA-Ir})_{0.48}(\text{Gln})_{5.52}$  for **MOZ-6**.

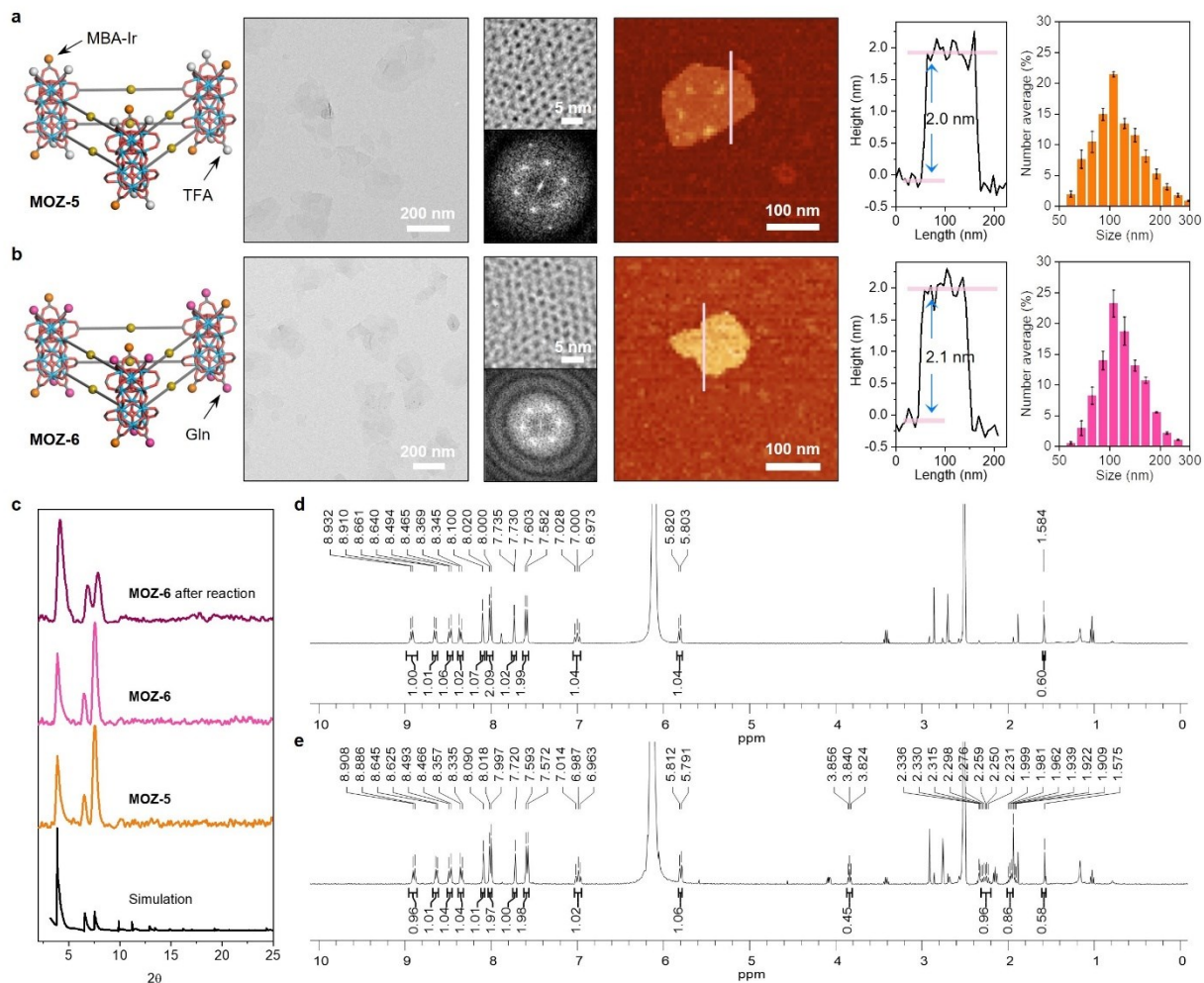


**Figure 7-14.** Characterization of **MOZ-5** and **MOZ-6**. Morphological characterization of (a) **MOZ-5** and (b) **MOZ-6**. For each, from left to right: modeled structure, TEM imaging, HRTEM imaging (top) and its FFT pattern (bottom), AFM topography, height profile, and number-averaged diameter as measured by DLS. (c) PXRD patterns of MOZs, freshly prepared or after reaction, compared to the simulated pattern based on the monolayered MOF structure. (d) NMR spectra of digested **MOZ-5**. (e) NMR spectra of digested **MOZ-6**.

### 7.2.1.2 AA Screening for WOR Optimization

Enhanced activities for WOR were achieved with AA-modified MOZs with cationic AA radicals ( $AA^{\bullet+}$ ) that exhibit oxidation potential between 1.24 and 1.77 V. This WOR activity enhancement was maximized in Gln-modified **MOZ-6** (**Figure 7-15a**) and a volcano-plot was obtained by plotting the WOR activity against the oxidation potential of  $AA^{\bullet+}/AA$ . These results suggest that here AAs may function as electron mediators for WOR via photo-oxidation of the proximal AA by IrF-PS to form  $AA^{\bullet+}$  through a PCET pathway followed by the oxidation of  $H_2O$ -bound  $MBA-Ir^*$  by  $AA^{\bullet+}$  through HAT. The proposed WOR mechanism of **MOZ-6** is shown in **Figure 7-15c** with its energy diagram calculated by DFT (**Figure 7-15d**). In this proposed mechanism, the rate-determining step of  $MBA-Ir^*$  catalyzed WOR is the formation of the oxygen-oxygen bond (corresponding to  $IM_2$  to  $IM_4$  in **Figure 7-15**), in which the activation energy drops from 48.7 kcal/mol in **MOZ-5** to 8.4 kcal/mol in **MOZ-6**. To further clarify the formation of the oxygen-oxygen bond, the geometry of  $TS_3$  in **MOZ-6** was optimized by DFT calculations (**Figure 7-15e**). These calculations revealed bound  $H_2O$  molecules could be stabilized by  $Gln^{\bullet+}$  through a H-bond interaction (1.92 Å) placing the oxygen atom within range (2.19 Å) for attack of proximal  $Ir^V=O$  moieties to form the oxygen-oxygen bond along with HAT from  $H_2O$  to  $Gln^{\bullet+}$ . As a result, **MOZ-6** significantly enhances WOR with a 72-h TON for  $O_2$  generation reaching  $8679 \pm 446$ , compared to  $4196 \pm 289$  for **MOZ-5** and only  $1006 \pm 171$  for the homogenous control (**Figure 7-15b**).

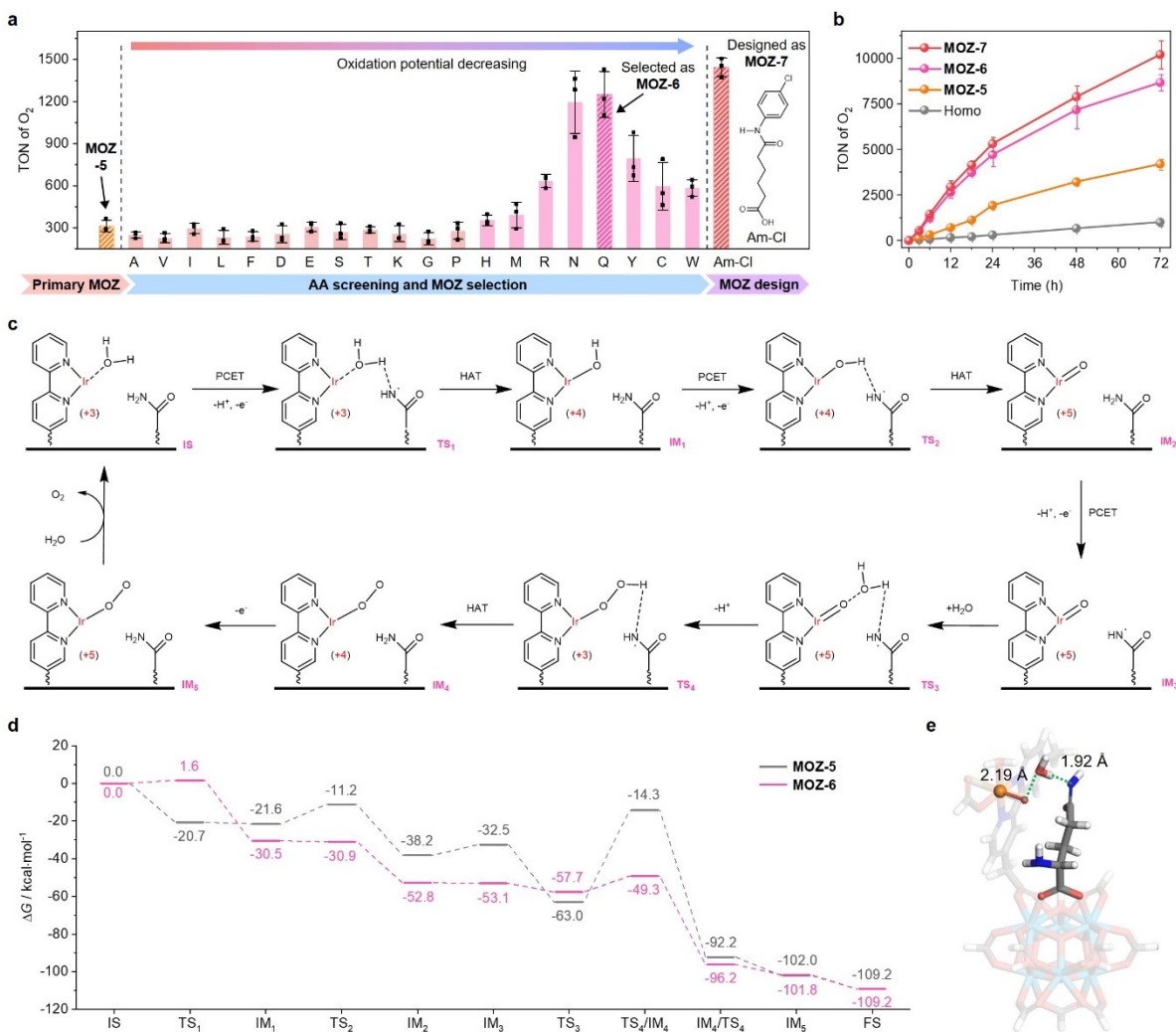


**Figure 7-15.** Photocatalytic WOR by MOZs. (a) TONs for O<sub>2</sub> of **MOZ-5**, AA-modified MOZs and Am-Cl-modified MOZ. (b) Time-dependent TONs of O<sub>2</sub> for MOZs and homogeneous control (Homo) under visible-light irradiation. Data are presented as mean ± s.d. (n = 3) with the error bars representing the s.d.; individual data points are shown as black dots. (c) Proposed mechanism for **MOZ-6**-catalyzed WOR. IS, initial state; TS, transitional state; IM, intermediate; FS, final state. (d) Energy diagram of MOZ-catalyzed WOR. e, Representative model structure of TS<sub>3</sub> of **MOZ-6**-catalyzed WOR. All atoms are labelled as follows: H, white; C, grey; O, red; N, blue; Ir, orange; Zr, light blue; Cl, light green. Ir-bound oxo, H<sub>2</sub>O and Gln are highlighted.

To further validate the proposed function of AAs as electron mediators in WOR, we designed a series of artificial ligands (Am-R) derived from 6-oxo-6-(phenylamino)hexanoic acid to optimize MOZ reactivity (**Figure 7-16a**). The Am-R ligands (R = OCH<sub>3</sub>, CH<sub>3</sub>, F, H, Cl, Br, or NO<sub>2</sub>) were composed of the same amide group but with oxidation potentials that could be tuned with the functional groups attached to the phenyl ring. By modifying **MOZ-5** with these artificial ligands, a similar volcano-plot as above was constructed by plotting the WOR activity against the oxidation potential. The WOR activity was optimized with Am-Cl (R = Cl) in **MOZ-7** (**Figure 7-16b**) with a 72-h TON of 10213 ± 758 (**Figure 7-16c**). **MOZ-7** showed higher photocatalytic WOR activity than many previously reported catalysts (**Table 7-2**).<sup>34-37</sup>

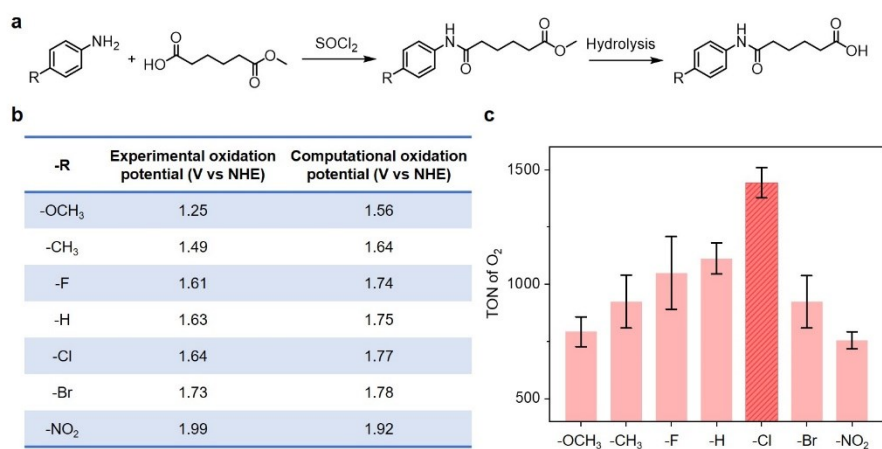


**Figure 7-16.** Am-R ligands for WOR.(a) Synthesis of 6-oxo-6-(phenylamino) hexanoic acid-derived Am-R ligands (R = OCH<sub>3</sub>, CH<sub>3</sub>, H, F, Cl, Br, or NO<sub>2</sub>) for photocatalytic WOR. (b) Summary of both experimental and computed oxidation potentials. (c) TON of O<sub>2</sub> for Am-R modified **MOZ-5** after 6-hour reactions under photocatalytic conditions. Data are presented as mean ± s.d. (n= 3) with the error bars representing the s.d.; individual data points are shown as black dots.

## 7.2.3 MOZs for Photocatalytic Total Carbon Dioxide Reduction

Combining these two libraries, photocatalytic total CO<sub>2</sub>RR was realized through a Z-scheme system relying upon **MOZ-4** and **MOZ-7** for CO<sub>2</sub>RR and WOR, respectively, with Co(bpy)<sub>3</sub><sup>2+</sup> as a redox mediator (**Figure 7-17a**). To improve reactivity, we first optimized the concentration of Co(bpy)<sub>3</sub><sup>2+</sup> as a redox mediator. Reactions were performed for 6 hours and the calculated TOF of CO<sub>2</sub>RR (CO + CH<sub>4</sub>) achieved a maximum of 18.4 h<sup>-1</sup> with 30 μM Co(bpy)<sub>3</sub><sup>2+</sup> (**Figure 7-17b**). We next optimized the ratio of **MOZ-4** and **MOZ-7** to match the reaction rate of both CO<sub>2</sub>RR and WOR for higher activity. The highest TOF of total CO<sub>2</sub>RR was found with a **MOZ-4** to **MOZ-7** ratio of 1:3 (**Figure 7-17c**).

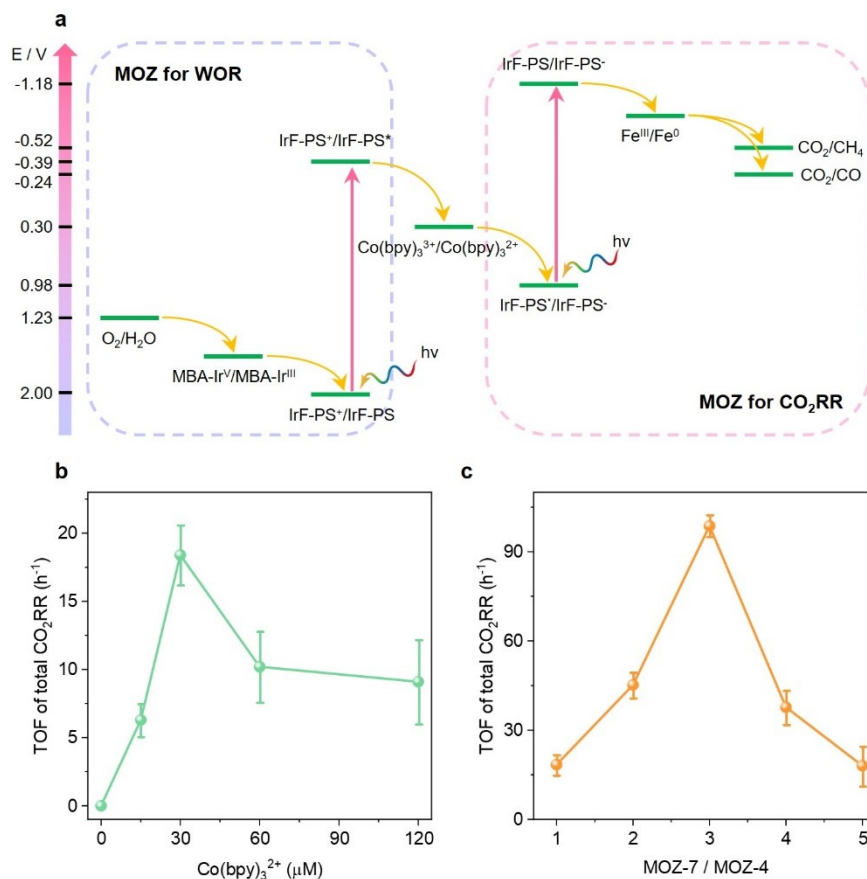


**Figure 7-17.** Photocatalytic total CO<sub>2</sub>RR. (a) Energy-level diagram of a Z-scheme system for photocatalytic total CO<sub>2</sub>RR by MOZs. (b) Optimization of electron shuttle for total CO<sub>2</sub>RR. (c) Optimization of catalyst ratios for total CO<sub>2</sub>RR. Data are presented as mean ± s.d. (n= 3) with the error bars representing the s.d.

In the absence of any sacrificial reagent, a combination of **MOZ-4** and **MOZ-7** in the optimized 1:3 ratio with 30 μM concentration of Co(bpy)<sub>3</sub><sup>2+</sup> competently catalyzed total photocatalytic CO<sub>2</sub> reduction to afford TONs of 4412 ± 147, 324 ± 69, and 1619 ± 96, for CO, CH<sub>4</sub>, and O<sub>2</sub>, respectively, during 48-hour reactions (**Figure 7-18a**). The quantum yield of MOZ-catalyzed photocatalytic total CO<sub>2</sub>RR was determined to be 1.1% at 350 nm. As a control, no obvious CO<sub>2</sub>RR or WOR products were detected in the homogeneous control (a molar-equivalent mixture of IrF-PS, hemin, Me-MBA-Ir, and Co(bpy)<sub>3</sub>Cl<sub>2</sub>) or without Co(bpy)<sub>3</sub>Cl<sub>2</sub> as mediator. This is likely because MOZs not only integrate CO<sub>2</sub>RR or WOR active sites but also isolate these two active sites into different MOZs to avoid mutual quenching. Co(bpy)<sub>3</sub>Cl<sub>2</sub> was selected as an electron shuttle between **MOZ-4** (IrF-PS\*/IrF-PS<sup>-</sup>, 0.98 V *vs* SHE) and **MOZ-7** (IrF-PS<sup>+</sup>/IrF-PS\*, -0.39 V *vs* SHE) due to its proper redox potential of [Co(bpy)<sub>3</sub>]<sup>3+</sup>/[Co(bpy)<sub>3</sub>]<sup>2+</sup> (0.30 V *vs* SHE). No obvious CO<sub>2</sub>RR or WOR products were detected in a mixture of **MOZ-4** and **MOZ-6** without Co(bpy)<sub>3</sub>Cl<sub>2</sub>. The photocatalytic CO<sub>2</sub>RR activity corresponded to a TOF for total artificial photosynthesis of 98.7 ± 3.7 h<sup>-1</sup>, outperforming previously reported photocatalysts (e.g. MOFs and metal-oxide nanoparticles) for complete artificial photosynthesis (i.e., converting water and CO<sub>2</sub> into O<sub>2</sub> and carbonaceous products using only light) by over an order of magnitude under similar reaction conditions (**Figure 7-18b**, **Table 7-3**).<sup>38-49</sup>



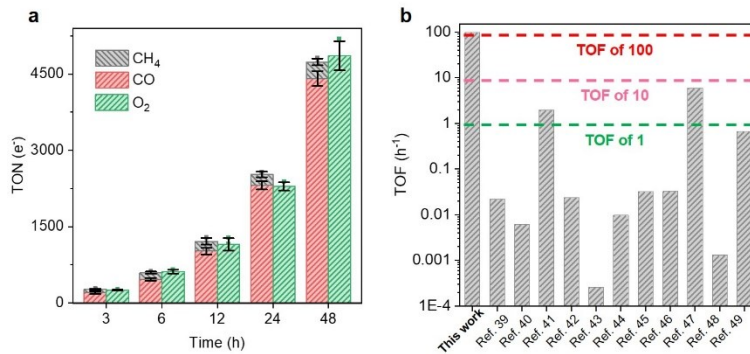


**Figure 7-18.** TONs of photocatalytic total CO<sub>2</sub>RR. (a) Time-dependent TONs of CO, CH<sub>4</sub> and O<sub>2</sub> for photocatalytic total CO<sub>2</sub>RR by a combination of **MOZ-4** and **MOZ-7**. (b) Comparison of photocatalytic total CO<sub>2</sub>RR activity in this work with that of previously reported catalysts.

### 7.3 Conclusion

In this chapter, we reported the rational design of a MOL-based artificial enzyme by integrating active metal centers, proximal amino acids, and other cofactors into tunable MOF monolayers. Through a diversification-selection-optimization strategy, two libraries of MOZs were developed for photocatalytic CO<sub>2</sub>RR and WOR, respectively. When combined into a single system, these MOZs realized efficient artificial photosynthesis in the presence of a catalytic amount of Co(bpy)<sub>3</sub><sup>2+</sup> redox mediator. We anticipate that the operating principles of our system can be leveraged to develop other MOZs for increasingly challenging reactions (e.g., N<sub>2</sub> reduction and complex molecule synthesis) by integrating diverse metal complexes, AAs, peptides, artificial ligands, and other cofactors into MOLs.

## 7.4 Methods

### 7.4.1 Material synthesis

**Synthesis of Hf-IrF.** Hf-IrF was synthesized according to a previously reported procedure in the literature.<sup>50</sup> 0.5 mL of HfCl<sub>4</sub> solution (2.0 mg/mL in DMF), 0.5 mL of IrF-PS solution (4.0mg/mL in DMF), 2  $\mu$ L of TFA, and 5 $\mu$ L of water were mixed in a 4.6 mL vial. The resultant reaction mixture was placed in an 80 °C oven for 24 hours. The yellow precipitate was isolated in 52% yield by centrifugation and washed with DMF and ethanol.

**Synthesis of MOZ-1.** To a 1 mL DMF suspension of Hf-IrF (4.1  $\mu$ mol based on Ir) was added 0.267 mg (0.41  $\mu$ mol) hemin. The reaction mixture was stirred for 3 hours at room temperature. The resultant dark yellow precipitate was collected by centrifugation and washed with DMF three times to quantitatively generate **MOZ-1**.

**Amino acid modification and synthesis of MOZ-2, MOZ-3, and MOZ-4.** To separate 1 mL DMF suspensions of **MOZ-1** (4.0  $\mu$ mol based on Ir) was added 3 equivalents (relative to iridium) of each AA or Ur. Each reaction mixture was stirred overnight at room temperature. The resultant dark yellow precipitates were collected by centrifugation and washed with DMF three times to give modified MOZs in quantitative yields. **MOZ-2** and **MOZ-3** were generated from Glu and Asn modification, respectively, and **MOZ-4** was generated from Ur modification.

**Synthesis of MOZ-5, MOZ-6, and MOZ-7.** To a 1 mL DMF suspension of Hf-IrF (4.1  $\mu$ mol based on Ir) was added 0.229 mg (0.41  $\mu$ mol) H-MBA-Ir. The reaction mixture was stirred for 3 hours at room temperature. The yellow precipitate was collected by centrifugation and washed with DMF three times to generate **MOZ-5**. To separate 1 mL DMF suspensions of **MOZ-5** (4.0  $\mu$ mol based on Ir) were added 3 equivalents relative to iridium of each AA or 6-oxo-6-(phenylamino) hexanoic acid-derived artificial ligands. Each reaction mixture was stirred

overnight at room temperature. The yellow precipitates were collected by centrifugation and washed with DMF three times to give modified MOZs. **MOZ-6** was generated from Gln modification, and **MOZ-7** was generated from modification Am-Cl.

#### 7.4.2 Catalytic Reactions

**MOZs for photocatalytic CO<sub>2</sub>RR.** To separate 4.6 mL vials were added 1 mL DMA, 11.2 mg BIH (50 mM, sacrificial reductant), 7.3 μL TFE (100 mM, proton source), and each modified MOZ (0.1 μM based on hemin and 1.25 μM based on IrF-PS). Each vial was sealed with a septum and degassed with CO<sub>2</sub> for 10 min before being stirred under visible-light irradiation (300 W Xenon lamp with 300-nm cutoff) at room temperature for 6 hours. 200 μL of gaseous products from each vial were collected in gas-tight syringes for GC analysis. Time-dependent photocatalytic CO<sub>2</sub>RR of **MOZ-1**, **MOZ-2**, **MOZ-3**, and **MOZ-4** were performed under the same condition, while the gaseous products from each vial were continuously collected at 3 h, 6 h, 12 h, 24 h, 48 h, and 72 h. All experiments were performed in triplicate.

**Selectivity of CO<sub>2</sub>RR.** CH<sub>4</sub>, CO, and H<sub>2</sub> were the only products detected in this work. Selectivity for CO<sub>2</sub>RR is therefore defined as:

$$\text{Selectivity} = \frac{\text{Number of CO} \times 2 + \text{Number of CH}_4 \times 8}{\text{Number of CO} \times 2 + \text{Number of CH}_4 \times 8 + \text{Number of H}_2 \times 2} \quad (1)$$

**Quantum yield (QY) calculation.** The quantum yields for the CO<sub>2</sub>RR products were determined by following equations:

$$QY_{\text{CO}_2\text{RR}} = \frac{\text{Number of generated CO} \times 2 + \text{Number of generated CH}_4 \times 8}{\text{Numbers of incident photons}} \quad (2)$$

The quantum yields for the WOR products were determined by following equations:

$$QY_{\text{WOR}} = \frac{\text{Number of generated O}_2 \text{ molecules} \times 4}{\text{Numbers of incident photons}} \quad (3)$$

The quantum yields for the artificial photosynthesis products were determined by following equations:

$$QY_{\text{total}} = \frac{\text{Number of generated CO} \times 2 + \text{Number of generated CH}_4 \times 8}{\text{Numbers of incident photons} / 2} \quad (4)$$

The number of incident photons were measured using  $\text{K}_3\text{Fe}(\text{C}_2\text{O}_4)_3$  as chemical actinometer irradiated with Xenon lamp or sunlight with  $350 \pm 10$  nm band-pass optical filter according to the literature<sup>51</sup> and known parameters.<sup>52</sup> The number of generated CO and  $\text{CH}_4$  or  $\text{O}_2$  was also measured under the same irradiation condition (Xenon lamp or sunlight with  $350 \pm 10$  nm band-pass optical filter).

**MOZs for sunlight driven  $\text{CO}_2\text{RR}$ .** To separate 4.6 mL vials were added 1 mL DMA, 11.2 mg BIH, and 7.3  $\mu\text{L}$  TFE. **MOZ-2**, **MOZ-3**, or **MOZ-4** (0.1  $\mu\text{M}$  based on hemin and 1.25  $\mu\text{M}$  based on IrF-PS) was added to each vial which was then sealed with a septum and degassed with  $\text{CO}_2$  for 10 min before being stirred under direct natural sunlight at room temperature from 10:00 to 16:00 between Feb. 29 and Mar. 4, 2020, in Chicago, Illinois. 200  $\mu\text{L}$  of gaseous products from each vial were collected on each day in gas-tight syringes for GC analysis.

**MOZs for photocatalytic WOR.** To separate 4.6 mL vials were added 0.5 mL MeCN, 0.5 mL  $\text{H}_2\text{O}$ , 27 mg  $\text{K}_2\text{S}_2\text{O}_8$  (100 mM, sacrificial oxidant), and each AA-modified MOZ (3.6  $\mu\text{M}$  based on MBA-Ir and 45  $\mu\text{M}$  based on IrF-PS). Each vial was sealed with a septum and degassed with  $\text{N}_2$  for 10 min before being stirred under visible-light irradiation (300 W Xenon lamp with 300-nm cutoff) at room temperature for 6 hours. 200  $\mu\text{L}$  of gaseous products from each vial were collected in gas-tight syringes for GC analysis. Time-dependent photocatalytic WOR of **MOZ-5**, **MOZ-6**, and **MOZ-7** were performed under the same condition, while the gaseous products from each vial were continuously collected at 3 h, 6 h, 12 h, 24 h, 48 h, and 72 h. All experiments were performed in triplicate.

**MOZs for photocatalytic total CO<sub>2</sub>RR.** To separate 23 mL vials were added 4 mL DMA, 1 mL H<sub>2</sub>O, 90 μg Co(bpy)<sub>3</sub>Cl<sub>2</sub> (30 μM), 36 μL TFE (100 mM), **MOZ-4** (0.3 μM based on hemin and 3.75 μM based on IrF-PS) and **MOZ-7** (0.9 μM based on MBA-Ir and 11.25 μM based on IrF-PS) or a homogeneous control (0.3 μM hemin, 0.9 μM Me-MBA-Ir, and 15 μM IrF-PS). Each vial was sealed with a septum and degassed with CO<sub>2</sub> for 20 min before being stirred under visible-light irradiation for 3 h, 6 h, 12 h, 24 h, and 48 h. 200 uL of gaseous products from each vial were collected at each time point in gas-tight syringes for GC analysis. All experiments were performed in triplicate.

## 7.5 Supplementary Data

**Table 7-1.** Summary of photocatalytic CO<sub>2</sub>RR with different catalytic systems.

Name	Reaction conditions	TOF <sub>CO</sub> ; TOF <sub>CH<sub>4</sub></sub> (h <sup>-1</sup> / μmol·g <sup>-1</sup> ·h <sup>-1</sup> ) with index in Figure 7-12b	References	
Homo control	Xe lamp; DMA; r.t.; 1 atm	8.7±1.8/6632±1403(299.2±63.3) <sup>a</sup> ; 4.8±1.4/924±261(41.7±11.8) <sup>a</sup> (8)	This work	
<b>MOZ-1</b>	Xe lamp; DMA; r.t.; 1 atm	72.5±5.2/55481.9±3953.9(2503±178) <sup>a</sup> ; 71.2±.2/13615.3±988.5(614.2±44.6) <sup>a</sup> (1)		
<b>MOZ-2</b>	Xe lamp; DMA; r.t.; 1 atm	146.5±11.8/112112±9056(5058±408) <sup>a</sup> ; 101.3±15.3/19386±2934(874.7±132.4) <sup>a</sup> (2)		
	Sunlight; DMA; r.t.; 1 atm	134.0/102027(3139.3) <sup>a</sup> ; 91.5/17417(535.9) <sup>a</sup> (3)		
<b>MOZ-3</b>	Xe lamp; DMA; r.t.; 1 atm	261.0±18.5/199734±14157(9011±638) <sup>a</sup> ; 132.7±5.6/ 25381±1084(1145±48) <sup>a</sup> (4)		
	sunlight; DMA; r.t.; 1 atm	199.3/151752(4707.2) <sup>a</sup> ; 103.8/19759(612.9) <sup>a</sup> (5)		
<b>MOZ-4</b>	Xe lamp; DMA; r.t.; 1 atm	450.8±22.8/345008±17473(15566±788) <sup>a</sup> ; 191.0±20.3/36541±3890(1648±175) <sup>a</sup> (6)		
	Sunlight; DMA; r.t.;1 atm	308.8/235327(6495.4) <sup>a</sup> ; 150.8/28730(793.0) <sup>a</sup> (7)		
Fe- <i>p</i> -TMA and Ir(ppy) <sub>3</sub>	AM 1.5 lamp; MeCN; r.t.; 1 atm	5.1/11133(142.8) <sup>a</sup> ; 1.4/764(9.8) <sup>a</sup> (9)		17
Fe- <i>p</i> -TMA and organic PS	AM 1.5 lamp; DMF; r.t.; 1 atm	1.5/700(10.0) <sup>a</sup> ; 0.30/35(0.5) <sup>a</sup> (10)		23
Cu/TiO <sub>2</sub>	UV lamp; H <sub>2</sub> O; r.t.; 1 atm	Not reported; N.A./0.18	53	

**Table 7-1 (cont.)**

Name	Reaction conditions	TOF <sub>CO</sub> ; TOF <sub>CH<sub>4</sub></sub> (h <sup>-1</sup> / μmol·g <sup>-1</sup> ·h <sup>-1</sup> ) with index in Figure 7-12b	References	
Cu <sub>0.33</sub> Pt <sub>0.67</sub> @TiO <sub>2</sub>	AM 1.5 lamp; N.A.; r.t.; no report.	Not reported; 8.6/134	54	
Pt@Cu <sub>2</sub> O/TiO <sub>2</sub>	Xe lamp; N.A.; 50; 0.2 MPa	0.032/8.3; 0.51/33 (11)	27 55 56 28 28 28 28 29	
Au/TiO <sub>2</sub>	UV lamp; N.A.; 75; 1 atm	Not reported; N.A./2.3		
Pt/N-doped TiO <sub>2</sub> (MgO,Pt)/TiO <sub>2</sub>	Xe lamp; N.A.; 45; 1 atm	Not reported; 4.5/5.7		
	Xe lamp; N.A.; 50; 0.2 MPa	0.0023/0.03; 3.4/11 (12)		
Ag/TiO <sub>2</sub> Pd/TiO <sub>2</sub>	Xe lamp; N.A.; 50; 0.2 MPa	0.073/1.7; 0.36/2.1 (13)		
	Xe lamp; N.A.; 50; 0.2 MPa	0.047/1.1; 0.74/4.3 (14)		
Rh/TiO <sub>2</sub> Pt/TiO <sub>2</sub>	Xe lamp; N.A.; 50; 0.2 MPa	0.026/0.62; 0.58/3.5 (15)		
	Xe lamp; N.A.; 80; 0.4 MPa	Not reported; 8.9/60 (16)		
In/TiO <sub>2</sub>	Hg lamp; N.A.; 100; 2 kPa	0.53/230; 6.2/675		57
TiO <sub>2</sub> /MWCNT	UV lamp; N.A.; r.t.; no report	Not reported; N.A./12		58
SEG-TiO <sub>2</sub>	Hg lamp; N.A.; r.t.; no report	Not reported; N.A./500	59	
(N <sub>3</sub> ,dye,Cu,Fe)/ TiO <sub>2</sub>	Hg lamp; N.A.; 75; 1 atm	Not reported; 0.040/0.85	60	
ZnPc/TiO <sub>2</sub>	W-Halogen lamp; H <sub>2</sub> O; no report; no report	23/201.3; 62/133	61	
Pd <sub>7</sub> Cu <sub>1</sub> /TiO <sub>2</sub>	Xe lamp; N.A.; no report; 0.2 MPa	Not reported; 0.027/19.6 (17)	30	
(NiO,In <sub>2</sub> O <sub>3</sub> )/TiO <sub>2</sub>	Hg lamp; N.A.; no report; 1 atm	0.49/60; 7.9/240	62	
WO <sub>3</sub>	Xe lamp; N.A.; r.t.; 1 atm	Not reported; N.A./1.0	51	
Zn <sub>2</sub> GeO <sub>4</sub>	Xe lamp; N.A.; r.t.; 1 atm	Not reported; N.A./1.5	63	
Pt/(g-C <sub>3</sub> N <sub>4</sub> /NaNbO <sub>3</sub> )	Xe lamp; N.A.; no report; 1 atm	Not reported; N.A./6.4	64	
SrNb <sub>2</sub> O <sub>6</sub>	Xe lamp; N.A.; 50; 0.2 MPa	N.A./1.7; N.A./0.33	65	
Cu <sub>3</sub> (BTC) <sub>2</sub> @TiO <sub>2</sub>	Xe lamp; N.A.; 40; 0.15 MPa	Not reported; 0.0069/2.63 (18)	31	
MOF-525-Co	Xe lamp; MeCN; no report; 80 kPa	0.43/200.6; 0.32/37	66	
CsPbBr <sub>3</sub> QD/GO	AM 1.5 lamp; EA; no report; no report	N.A./48.7; N.A./29.6	67	

<sup>a</sup> TOF<sub>1</sub>(TOF<sub>2</sub>), TOF<sub>1</sub> was calculated based on catalysts only; TOF<sub>2</sub> was calculated based on both catalysts and photosensitizers.

**Table 7-2.** Summary of photocatalytic WOR with different catalytic systems.

Name	Reaction conditions	TOF (h <sup>-1</sup> / μmol·g <sup>-1</sup> ·h <sup>-1</sup> )	References
Homo	Xe lamp; water and MeCN	10.5±0.3/1843±52(73.0±2.1) <sup>a</sup>	This work
<b>MOZ-5</b>	Xe lamp; water and MeCN	52.0±7.2/8798±1218(257.6±35.7) <sup>a</sup>	
<b>MOZ-6</b>	Xe lamp; water and MeCN	208.3±27.5/35224±4653(985.9±130.1) <sup>a</sup>	
<b>MOZ-7</b>	Xe lamp; water and MeCN	240.5±11.2/30222±1407(1138±53) <sup>a</sup>	
RuL(pic) <sub>2</sub> and Ru(bpy) <sub>3</sub> <sup>2+</sup>	Xe lamp; pH = 7 water	2200/1038715(66020) <sup>a</sup>	34
Di-Ru Complex and Ru-based PSS <sup>c</sup>	Xe lamp; pH = 7.2 water	1440/366943(2252) <sup>a</sup> 11088/2825458(14173) <sup>a</sup> 11952/3045623(12917) <sup>a</sup>	68
[IrClCp*(di-NHC)](PF <sub>6</sub> ) and Ru(bpy) <sub>3</sub> <sup>2+</sup>	LED at 450 nm; pH = 5.2 water	29/10264(1020) <sup>a</sup>	69
CoO <sub>x</sub> /MIL-101 and Ru(bpy) <sub>3</sub> <sup>2+</sup>	Xe lamp; pH = 9 water	173/24219(7683) <sup>a</sup>	35
Rh@Cr <sub>2</sub> O <sub>3</sub> /Ga <sub>1-x</sub> Zn <sub>x</sub> N <sub>1-x</sub> O	Xe lamp; pH=4.5 water	Not reported	36
Ta <sub>3</sub> N <sub>5</sub>	Xe lamp; neutral water	N.A./2100	70
Sm <sub>2</sub> Ti <sub>2</sub> S <sub>2</sub> O <sub>5</sub>	Xe lamp; pH = 8 water	N.A./18	71
IrO <sub>2</sub> -Ca(OH) <sub>2</sub> /Sm <sub>2</sub> Ti <sub>2</sub> S <sub>2</sub> O <sub>5</sub>	Xe lamp; pH = 8 water	17/47	71
IrO <sub>2</sub> /Y <sub>2</sub> Ti <sub>2</sub> O <sub>2</sub> S <sub>2</sub>	Xe lamp; pH = 8 water	8.3/93	37
RuO <sub>2</sub> /Bi <sub>4</sub> TaO <sub>8</sub> X (X = Cl, Br)	Xe lamp; neutral water	200/375	72
Pt/Bi <sub>4</sub> NbO <sub>8</sub> Cl	Xe lamp; pH = 2.5 water	62/400	73
Au, CoO <sub>x</sub> /BiVO <sub>4</sub>	Xe lamp; pH = 6.0 water	492/1640	74

<sup>a</sup> TOF<sub>1</sub>(TOF<sub>2</sub>), TOF<sub>1</sub> was calculated based on catalysts only; TOF<sub>1</sub> was calculated based on both catalysts and photosensitizers.

**Table 7-3.** Summary of photocatalytic total CO<sub>2</sub>RR with different catalytic systems.

Catalyst	Experimental Condition	Reduction Product	Oxidation Product	TOF of CO <sub>2</sub> RR (h <sup>-1</sup> )	Reference
<b>MOZ-4 + MOZ-7</b>	300 W Xe lamp (> 300 nm)	CO, CH <sub>4</sub>	O <sub>2</sub>	98.7 ± 3.7	This work
Bi <sub>2</sub> O <sub>2</sub> CO <sub>3</sub> /CoFe <sub>2</sub> O <sub>4</sub> /g-C <sub>3</sub> N <sub>4</sub>	800 W Xe lamp (> 400 nm),	CO, CH <sub>4</sub>	-	-	38
α-Fe <sub>2</sub> O <sub>3</sub> /g-C <sub>3</sub> N <sub>4</sub>	300 W Xe lamp (> 420 nm)	CO	-	0.022	39
Al bridged α-Fe <sub>2</sub> O <sub>3</sub> /g-C <sub>3</sub> N <sub>4</sub>	300 W Xe lamp, 2.6 bar CO <sub>2</sub>	CO, CH <sub>4</sub>	O <sub>2</sub>	6.2 × 10 <sup>-3</sup>	40
ZnO-Cu <sub>2</sub> O	300 W Xe lamp (>420 nm)	CH <sub>4</sub>	-	1.94	41
CdS/WO <sub>3</sub>	300 W Xe lamp (> 420 nm)	CH <sub>4</sub>	-	0.024	42
Cu <sub>2</sub> O/TiO <sub>2</sub>	1kW Hg lamp (> 305 nm)	CO	O <sub>2</sub>	2.6 × 10 <sup>-4</sup>	43
α-Fe <sub>2</sub> O <sub>3</sub> /g-C <sub>3</sub> N <sub>4</sub>	300 W Xe lamp	CO	O <sub>2</sub>	0.0097	44
ZnIn <sub>2</sub> S <sub>4</sub> /BiVO <sub>4</sub>	300 W Xe lamp	CO	O <sub>2</sub>	0.032	45
Bi <sub>2</sub> S <sub>3</sub> QDs/g-C <sub>3</sub> N <sub>4</sub>	300 W Xe lamp	CO, CH <sub>4</sub>	O <sub>2</sub>	0.0325	46
TiO <sub>2</sub> in MIL-101-Cr-NO <sub>2</sub>	300 W Xe lamp	CO, CH <sub>4</sub>	O <sub>2</sub>	5.9	47
WO <sub>3</sub>	40 W silicon nitride lamp (λ=800-1700 nm)	CO	O <sub>2</sub>	1.3 × 10 <sup>-3</sup>	48
MAPbI <sub>3</sub> @PCN-221(Fe0.2)	300 W Xe-lamp (>400 nm)	CO, CH <sub>4</sub>	O <sub>2</sub>	0.67	49
PCN-601	Xe-lamp (>410 nm)	CO, CH <sub>4</sub>	H <sub>2</sub> O <sub>2</sub>	0.23	75
ZrOCo <sup>II</sup> -IrO <sub>x</sub>	Laser (355 nm)	CO	O <sub>2</sub>	6.5 × 10 <sup>-4</sup>	76
ZrOCo <sup>II</sup> -Co <sub>3</sub> O <sub>4</sub>	480 mW Ar ion laser (476 nm)	CO	O <sub>2</sub>	-	77

## 7.6 References

- Lee, D.-S.; Nioche, P.; Hamberg, M.; Raman, C. S., Structural insights into the evolutionary paths of oxylipin biosynthetic enzymes. *Nature* **2008**, *455* (7211), 363-368.
- Berggren, G.; Adamska, A.; Lambertz, C.; Simmons, T. R.; Esselborn, J.; Atta, M.; Gambarelli, S.; Mouesca, J. M.; Reijerse, E.; Lubitz, W.; Happe, T.; Artero, V.; Fontecave, M., Biomimetic assembly and activation of [FeFe]-hydrogenases. *Nature* **2013**, *499* (7456), 66-69.
- Helm, M. L.; Stewart, M. P.; Bullock, R. M.; DuBois, M. R.; DuBois, D. L., A Synthetic Nickel Electrocatalyst with a Turnover Frequency Above 100,000 s<sup>-1</sup> for H<sub>2</sub> Production. *Science* **2011**, *333* (6044), 863-866.
- Camara, J. M.; Rauchfuss, T. B., Combining acid–base, redox and substrate binding functionalities to give a complete model for the [FeFe]-hydrogenase. *Nat. Chem.* **2012**, *4* (1), 26-30.
- Ott, S.; Kritikos, M.; Åkermark, B.; Sun, L.; Lomoth, R., A Biomimetic Pathway for Hydrogen Evolution from a Model of the Iron Hydrogenase Active Site. *Angew. Chem. Int. Ed.* **2004**, *43* (8), 1006-1009.
- Wu, J.; Wang, X.; Wang, Q.; Lou, Z.; Li, S.; Zhu, Y.; Qin, L.; Wei, H., Nanomaterials with enzyme-like characteristics (nanozymes): next-generation artificial enzymes (II). *Chem. Soc. Rev.* **2019**, *48* (4), 1004-1076.



7. Takezawa, H.; Shitozawa, K.; Fujita, M., Enhanced reactivity of twisted amides inside a molecular cage. *Nat. Chem.* **2020**.
8. Rabone, J.; Yue, Y. F.; Chong, S. Y.; Stylianou, K. C.; Bacsá, J.; Bradshaw, D.; Darling, G. R.; Berry, N. G.; Khimiyak, Y. Z.; Ganin, A. Y.; Wiper, P.; Claridge, J. B.; Rosseinsky, M. J., An Adaptable Peptide-Based Porous Material. *Science* **2010**, *329* (5995), 1053.
9. Deng, H.; Grunder, S.; Cordova, K. E.; Valente, C.; Furukawa, H.; Hmadeh, M.; Gándara, F.; Whalley, A. C.; Liu, Z.; Asahina, S.; Kazumori, H.; O’Keeffe, M.; Terasaki, O.; Stoddart, J. F.; Yaghi, O. M., Large-Pore Apertures in a Series of Metal-Organic Frameworks. *Science* **2012**, *336* (6084), 1018.
10. Xiao, D. J.; Bloch, E. D.; Mason, J. A.; Queen, W. L.; Hudson, M. R.; Planas, N.; Borycz, J.; Dzubak, A. L.; Verma, P.; Lee, K.; Bonino, F.; Crocellà, V.; Yano, J.; Bordiga, S.; Truhlar, D. G.; Gagliardi, L.; Brown, C. M.; Long, J. R., Oxidation of ethane to ethanol by N<sub>2</sub>O in a metal-organic framework with coordinatively unsaturated iron(II) sites. *Nat. Chem.* **2014**, *6* (7), 590-595.
11. Nath, I.; Chakraborty, J.; Verpoort, F., Metal organic frameworks mimicking natural enzymes: a structural and functional analogy. *Chem. Soc. Rev.* **2016**, *45* (15), 4127-4170.
12. Furukawa, H.; Cordova Kyle, E.; O’Keeffe, M.; Yaghi Omar, M., The Chemistry and Applications of Metal-Organic Frameworks. *Science* **2013**, *341* (6149), 1230444.
13. Li, L.; Lin, R.-B.; Krishna, R.; Li, H.; Xiang, S.; Wu, H.; Li, J.; Zhou, W.; Chen, B., Ethane/ethylene separation in a metal-organic framework with iron-peroxo sites. *Science* **2018**, *362* (6413), 443-446.
14. Ji, S.; Jiang, B.; Hao, H.; Chen, Y.; Dong, J.; Mao, Y.; Zhang, Z.; Gao, R.; Chen, W.; Zhang, R.; Liang, Q.; Li, H.; Liu, S.; Wang, Y.; Zhang, Q.; Gu, L.; Duan, D.; Liang, M.; Wang, D.; Yan, X.; Li, Y., Matching the kinetics of natural enzymes with a single-atom iron nanozyme. *Nat. Catal.* **2021**, *4* (5), 407-417.
15. Scott, S.; Zhao, H.; Dey, A.; Gunnoe, T. B., Nano-Apples and Orange-Zymes. *ACS Catal.* **2020**, *10* (23), 14315-14317.
16. Dai, R.; Peng, F.; Ji, P.; Lu, K.; Wang, C.; Sun, J.; Lin, W., Electron Crystallography Reveals Atomic Structures of Metal-Organic Nanoplates with M<sub>12</sub>(μ<sub>3</sub>-O)<sub>8</sub>(μ<sub>3</sub>-OH)<sub>8</sub>(μ<sub>2</sub>-OH)<sub>6</sub> (M = Zr, Hf) Secondary Building Units. *Inorg. Chem.* **2017**, *56* (14), 8128-8134.
17. Rao, H.; Schmidt, L. C.; Bonin, J.; Robert, M., Visible-light-driven methane formation from CO<sub>2</sub> with a molecular iron catalyst. *Nature* **2017**, *548* (7665), 74-77.
18. Mariano, R. G.; McKelvey, K.; White, H. S.; Kanan, M. W., Selective increase in CO<sub>2</sub> electroreduction activity at grain-boundary surface terminations. *Science* **2017**, *358* (6367), 1187.
19. García de Arquer, F. P.; Dinh, C.-T.; Ozden, A.; Wicks, J.; McCallum, C.; Kirmani, A. R.; Nam, D.-H.; Gabardo, C.; Seifitokaldani, A.; Wang, X.; Li, Y. C.; Li, F.; Edwards, J.; Richter, L. J.; Thorpe, S. J.; Sinton, D.; Sargent, E. H., CO<sub>2</sub> electrolysis to multicarbon products at activities greater than 1 A cm<sup>-2</sup>. *Science* **2020**, *367* (6478), 661-666.
20. Morales-Guio, C. G.; Cave, E. R.; Nitopi, S. A.; Feaster, J. T.; Wang, L.; Kuhl, K. P.; Jackson, A.; Johnson, N. C.; Abram, D. N.; Hatsukade, T.; Hahn, C.; Jaramillo, T. F., Improved CO<sub>2</sub> reduction activity towards C<sub>2+</sub> alcohols on a tandem gold on copper electrocatalyst. *Nat. Catal.* **2018**, *1* (10), 764-771.
21. Liu, C.; Colón, B. C.; Ziesack, M.; Silver, P. A.; Nocera, D. G., Water splitting-biosynthetic system with CO<sub>2</sub> reduction efficiencies exceeding photosynthesis. *Science* **2016**, *352* (6290), 1210.

22. Smith, P. T.; Kim, Y.; Benke, B. P.; Kim, K.; Chang, C. J., Supramolecular Tuning Enables Selective Oxygen Reduction Catalyzed by Cobalt Porphyrins for Direct Electrosynthesis of Hydrogen Peroxide. *Angew. Chem. Int. Ed.* **2020**, *59* (12), 4902-4907.
23. Rao, H.; Lim, C.-H.; Bonin, J.; Miyake, G. M.; Robert, M., Visible-Light-Driven Conversion of CO<sub>2</sub> to CH<sub>4</sub> with an Organic Sensitizer and an Iron Porphyrin Catalyst. *J. Am. Chem. Soc.* **2018**, *140* (51), 17830-17834.
24. Costentin, C.; Drouet, S.; Passard, G.; Robert, M.; Savéant, J.-M., Proton-Coupled Electron Transfer Cleavage of Heavy-Atom Bonds in Electrocatalytic Processes. Cleavage of a C–O Bond in the Catalyzed Electrochemical Reduction of CO<sub>2</sub>. *J. Am. Chem. Soc.* **2013**, *135* (24), 9023-9031.
25. Gotico, P.; Boitrel, B.; Guillot, R.; Sircoglou, M.; Quaranta, A.; Halime, Z.; Leibl, W.; Aukauloo, A., Second-Sphere Biomimetic Multipoint Hydrogen-Bonding Patterns to Boost CO<sub>2</sub> Reduction of Iron Porphyrins. *Angew. Chem. Int. Ed.* **2019**, *58* (14), 4504-4509.
26. Davethu, P. A.; de Visser, S. P., CO<sub>2</sub> Reduction on an Iron-Porphyrin Center: A Computational Study. *The Journal of Physical Chemistry A* **2019**, *123* (30), 6527-6535.
27. Zhai, Q.; Xie, S.; Fan, W.; Zhang, Q.; Wang, Y.; Deng, W.; Wang, Y., Photocatalytic Conversion of Carbon Dioxide with Water into Methane: Platinum and Copper(I) Oxide Co-catalysts with a Core–Shell Structure. *Angew. Chem. Int. Ed.* **2013**, *52* (22), 5776-5779.
28. Xie, S.; Wang, Y.; Zhang, Q.; Deng, W.; Wang, Y., MgO- and Pt-Promoted TiO<sub>2</sub> as an Efficient Photocatalyst for the Preferential Reduction of Carbon Dioxide in the Presence of Water. *ACS Catal.* **2014**, *4* (10), 3644-3653.
29. Wang, Y.; Lai, Q.; Zhang, F.; Shen, X.; Fan, M.; He, Y.; Ren, S., High efficiency photocatalytic conversion of CO<sub>2</sub> with H<sub>2</sub>O over Pt/TiO<sub>2</sub> nanoparticles. *RSC Advances* **2014**, *4* (84), 44442-44451.
30. Long, R.; Li, Y.; Liu, Y.; Chen, S.; Zheng, X.; Gao, C.; He, C.; Chen, N.; Qi, Z.; Song, L.; Jiang, J.; Zhu, J.; Xiong, Y., Isolation of Cu Atoms in Pd Lattice: Forming Highly Selective Sites for Photocatalytic Conversion of CO<sub>2</sub> to CH<sub>4</sub>. *J. Am. Chem. Soc.* **2017**, *139* (12), 4486-4492.
31. Li, R.; Hu, J.; Deng, M.; Wang, H.; Wang, X.; Hu, Y.; Jiang, H.-L.; Jiang, J.; Zhang, Q.; Xie, Y.; Xiong, Y., Integration of an Inorganic Semiconductor with a Metal–Organic Framework: A Platform for Enhanced Gaseous Photocatalytic Reactions. *Adv. Mater.* **2014**, *26* (28), 4783-4788.
32. Duan, L.; Bozoglian, F.; Mandal, S.; Stewart, B.; Privalov, T.; Llobet, A.; Sun, L., A molecular ruthenium catalyst with water-oxidation activity comparable to that of photosystem II. *Nat. Chem.* **2012**, *4* (5), 418-423.
33. Wang, C.; Wang, J.-L.; Lin, W., Elucidating Molecular Iridium Water Oxidation Catalysts Using Metal–Organic Frameworks: A Comprehensive Structural, Catalytic, Spectroscopic, and Kinetic Study. *J. Am. Chem. Soc.* **2012**, *134* (48), 19895-19908.
34. Duan, L.; Xu, Y.; Zhang, P.; Wang, M.; Sun, L., Visible Light-Driven Water Oxidation by a Molecular Ruthenium Catalyst in Homogeneous System. *Inorg. Chem.* **2010**, *49* (1), 209-215.
35. Han, J.; Wang, D.; Du, Y.; Xi, S.; Hong, J.; Yin, S.; Chen, Z.; Zhou, T.; Xu, R., Metal–organic framework immobilized cobalt oxide nanoparticles for efficient photocatalytic water oxidation. *Journal of Materials Chemistry A* **2015**, *3* (41), 20607-20613.
36. Maeda, K.; Teramura, K.; Lu, D.; Takata, T.; Saito, N.; Inoue, Y.; Domen, K., Photocatalyst releasing hydrogen from water. *Nature* **2006**, *440* (7082), 295-295.

37. Wang, Q.; Nakabayashi, M.; Hisatomi, T.; Sun, S.; Akiyama, S.; Wang, Z.; Pan, Z.; Xiao, X.; Watanabe, T.; Yamada, T.; Shibata, N.; Takata, T.; Domen, K., Oxysulfide photocatalyst for visible-light-driven overall water splitting. *Nature Materials* **2019**, *18* (8), 827-832.
38. Kumar, A.; Kumar, A.; Sharma, G.; Al-Muhtaseb, A. a. H.; Naushad, M.; Ghfar, A. A.; Guo, C.; Stadler, F. J., Biochar-templated g-C<sub>3</sub>N<sub>4</sub>/Bi<sub>2</sub>O<sub>2</sub>CO<sub>3</sub>/CoFe<sub>2</sub>O<sub>4</sub> nano-assembly for visible and solar assisted photo-degradation of paraquat, nitrophenol reduction and CO<sub>2</sub> conversion. *Chem. Eng. J.* **2018**, *339*, 393-410.
39. Jiang, Z.; Wan, W.; Li, H.; Yuan, S.; Zhao, H.; Wong, P. K., A Hierarchical Z-Scheme  $\alpha$ -Fe<sub>2</sub>O<sub>3</sub>/g-C<sub>3</sub>N<sub>4</sub> Hybrid for Enhanced Photocatalytic CO<sub>2</sub> Reduction. *Adv. Mater.* **2018**, *30* (10), 1706108.
40. Wang, J.; Qin, C.; Wang, H.; Chu, M.; Zada, A.; Zhang, X.; Li, J.; Raziq, F.; Qu, Y.; Jing, L., Exceptional photocatalytic activities for CO<sub>2</sub> conversion on AlO bridged g-C<sub>3</sub>N<sub>4</sub>/ $\alpha$ -Fe<sub>2</sub>O<sub>3</sub> z-scheme nanocomposites and mechanism insight with isotopesZ. *Applied Catalysis B: Environmental* **2018**, *221*, 459-466.
41. Bae, K.-L.; Kim, J.; Lim, C. K.; Nam, K. M.; Song, H., Colloidal zinc oxide-copper(I) oxide nanocatalysts for selective aqueous photocatalytic carbon dioxide conversion into methane. *Nat. Commun.* **2017**, *8* (1), 1156.
42. Jin, J.; Yu, J.; Guo, D.; Cui, C.; Ho, W., A Hierarchical Z-Scheme CdS–WO<sub>3</sub> Photocatalyst with Enhanced CO<sub>2</sub> Reduction Activity. *Small* **2015**, *11* (39), 5262-5271.
43. Aguirre, M. E.; Zhou, R.; Eugene, A. J.; Guzman, M. I.; Grela, M. A., Cu<sub>2</sub>O/TiO<sub>2</sub> heterostructures for CO<sub>2</sub> reduction through a direct Z-scheme: Protecting Cu<sub>2</sub>O from photocorrosion. *Applied Catalysis B: Environmental* **2017**, *217*, 485-493.
44. Shen, Y.; Han, Q.; Hu, J.; Gao, W.; Wang, L.; Yang, L.; Gao, C.; Shen, Q.; Wu, C.; Wang, X.; Zhou, X.; Zhou, Y.; Zou, Z., Artificial Trees for Artificial Photosynthesis: Construction of Dendrite-Structured  $\alpha$ -Fe<sub>2</sub>O<sub>3</sub>/g-C<sub>3</sub>N<sub>4</sub> Z-Scheme System for Efficient CO<sub>2</sub> Reduction into Solar Fuels. *ACS Applied Energy Materials* **2020**, *3* (7), 6561-6572.
45. Han, Q.; Li, L.; Gao, W.; Shen, Y.; Wang, L.; Zhang, Y.; Wang, X.; Shen, Q.; Xiong, Y.; Zhou, Y.; Zou, Z., Elegant Construction of ZnIn<sub>2</sub>S<sub>4</sub>/BiVO<sub>4</sub> Hierarchical Heterostructures as Direct Z-Scheme Photocatalysts for Efficient CO<sub>2</sub> Photoreduction. *ACS Applied Materials & Interfaces* **2021**, *13* (13), 15092-15100.
46. Guo, R.-t.; Liu, X.-y.; Qin, H.; Wang, Z.-y.; Shi, X.; Pan, W.-g.; Fu, Z.-g.; Tang, J.-y.; Jia, P.-y.; Miao, Y.-f.; Gu, J.-w., Photocatalytic reduction of CO<sub>2</sub> into CO over nanostructure Bi<sub>2</sub>S<sub>3</sub> quantum dots/g-C<sub>3</sub>N<sub>4</sub> composites with Z-scheme mechanism. *Appl. Surf. Sci.* **2020**, *500*, 144059.
47. Jiang, Z.; Xu, X.; Ma, Y.; Cho, H. S.; Ding, D.; Wang, C.; Wu, J.; Oleynikov, P.; Jia, M.; Cheng, J.; Zhou, Y.; Terasaki, O.; Peng, T.; Zan, L.; Deng, H., Filling metal–organic framework mesopores with TiO<sub>2</sub> for CO<sub>2</sub> photoreduction. *Nature* **2020**, *586* (7830), 549-554.
48. Liang, L.; Li, X.; Sun, Y.; Tan, Y.; Jiao, X.; Ju, H.; Qi, Z.; Zhu, J.; Xie, Y., Infrared Light-Driven CO<sub>2</sub> Overall Splitting at Room Temperature. *Joule* **2018**, *2* (5), 1004-1016.
49. Wu, L.-Y.; Mu, Y.-F.; Guo, X.-X.; Zhang, W.; Zhang, Z.-M.; Zhang, M.; Lu, T.-B., Encapsulating Perovskite Quantum Dots in Iron-Based Metal–Organic Frameworks (MOFs) for Efficient Photocatalytic CO<sub>2</sub> Reduction. *Angew. Chem. Int. Ed.* **2019**, *58* (28), 9491-9495.
50. Quan, Y.; Lan, G.; Fan, Y.; Shi, W.; You, E.; Lin, W., Metal–Organic Layers for Synergistic Lewis Acid and Photoredox Catalysis. *J. Am. Chem. Soc.* **2020**, *142* (4), 1746-1751.
51. Chen, X.; Zhou, Y.; Liu, Q.; Li, Z.; Liu, J.; Zou, Z., Ultrathin, Single-Crystal WO<sub>3</sub> Nanosheets by Two-Dimensional Oriented Attachment toward Enhanced Photocatalytic

Reduction of CO<sub>2</sub> into Hydrocarbon Fuels under Visible Light. *ACS Applied Materials & Interfaces* **2012**, *4* (7), 3372-3377.

52. Lide, D. R., *CRC handbook of chemistry and physics*. CRC press: 2004; Vol. 85.
53. Tan, J. Z. Y.; Fernández, Y.; Liu, D.; Maroto-Valer, M.; Bian, J.; Zhang, X., Photoreduction of CO<sub>2</sub> using copper-decorated TiO<sub>2</sub> nanorod films with localized surface plasmon behavior. *Chem. Phys. Lett.* **2012**, *531*, 149-154.
54. Zhang, X.; Han, F.; Shi, B.; Farsinezhad, S.; Dechaine, G. P.; Shankar, K., Photocatalytic Conversion of Diluted CO<sub>2</sub> into Light Hydrocarbons Using Periodically Modulated Multiwalled Nanotube Arrays. *Angewandte Chemie International Edition* **2012**, *51* (51), 12732-12735.
55. Hou, W.; Hung, W. H.; Pavaskar, P.; Goepfert, A.; Aykol, M.; Cronin, S. B., Photocatalytic Conversion of CO<sub>2</sub> to Hydrocarbon Fuels via Plasmon-Enhanced Absorption and Metallic Interband Transitions. *ACS Catalysis* **2011**, *1* (8), 929-936.
56. Li, X.; Zhuang, Z.; Li, W.; Pan, H., Photocatalytic reduction of CO<sub>2</sub> over noble metal-loaded and nitrogen-doped mesoporous TiO<sub>2</sub>. *Applied Catalysis A: General* **2012**, *429-430*, 31-38.
57. Tahir, M.; Amin, N. S., Indium-doped TiO<sub>2</sub> nanoparticles for photocatalytic CO<sub>2</sub> reduction with H<sub>2</sub>O vapors to CH<sub>4</sub>. *Applied Catalysis B: Environmental* **2015**, *162*, 98-109.
58. Xia, X.-H.; Jia, Z.-J.; Yu, Y.; Liang, Y.; Wang, Z.; Ma, L.-L., Preparation of multi-walled carbon nanotube supported TiO<sub>2</sub> and its photocatalytic activity in the reduction of CO<sub>2</sub> with H<sub>2</sub>O. *Carbon* **2007**, *45* (4), 717-721.
59. Liang, Y. T.; Vijayan, B. K.; Gray, K. A.; Hersam, M. C., Minimizing Graphene Defects Enhances Titania Nanocomposite-Based Photocatalytic Reduction of CO<sub>2</sub> for Improved Solar Fuel Production. *Nano Letters* **2011**, *11* (7), 2865-2870.
60. Nguyen, T.-V.; Wu, J. C. S.; Chiou, C.-H., Photoreduction of CO<sub>2</sub> over Ruthenium dye-sensitized TiO<sub>2</sub>-based catalysts under concentrated natural sunlight. *Catalysis Communications* **2008**, *9* (10), 2073-2076.
61. Zhao, Z.-H.; Fan, J.-M.; Wang, Z.-Z., Photo-catalytic CO<sub>2</sub> reduction using sol-gel derived titania-supported zinc-phthalocyanine. *Journal of Cleaner Production* **2007**, *15* (18), 1894-1897.
62. Tahir, M.; Tahir, B.; Amin, N. A. S.; Muhammad, A., Photocatalytic CO<sub>2</sub> methanation over NiO/In<sub>2</sub>O<sub>3</sub> promoted TiO<sub>2</sub> nanocatalysts using H<sub>2</sub>O and/or H<sub>2</sub> reductants. *Energy Conversion and Management* **2016**, *119*, 368-378.
63. Liu, Q.; Zhou, Y.; Kou, J.; Chen, X.; Tian, Z.; Gao, J.; Yan, S.; Zou, Z., High-Yield Synthesis of Ultralong and Ultrathin Zn<sub>2</sub>GeO<sub>4</sub> Nanoribbons toward Improved Photocatalytic Reduction of CO<sub>2</sub> into Renewable Hydrocarbon Fuel. *Journal of the American Chemical Society* **2010**, *132* (41), 14385-14387.
64. Shi, H.; Chen, G.; Zhang, C.; Zou, Z., Polymeric g-C<sub>3</sub>N<sub>4</sub> Coupled with NaNbO<sub>3</sub> Nanowires toward Enhanced Photocatalytic Reduction of CO<sub>2</sub> into Renewable Fuel. *ACS Catalysis* **2014**, *4* (10), 3637-3643.
65. Xie, S.; Wang, Y.; Zhang, Q.; Deng, W.; Wang, Y., SrNb<sub>2</sub>O<sub>6</sub> nanoplates as efficient photocatalysts for the preferential reduction of CO<sub>2</sub> in the presence of H<sub>2</sub>O. *Chemical Communications* **2015**, *51* (16), 3430-3433.
66. Zhang, H.; Wei, J.; Dong, J.; Liu, G.; Shi, L.; An, P.; Zhao, G.; Kong, J.; Wang, X.; Meng, X.; Zhang, J.; Ye, J., Efficient Visible-Light-Driven Carbon Dioxide Reduction by a Single-Atom Implanted Metal-Organic Framework. *Angewandte Chemie International Edition* **2016**, *55* (46), 14310-14314.

67. Xu, Y.-F.; Yang, M.-Z.; Chen, B.-X.; Wang, X.-D.; Chen, H.-Y.; Kuang, D.-B.; Su, C.-Y., A CsPbBr<sub>3</sub> Perovskite Quantum Dot/Graphene Oxide Composite for Photocatalytic CO<sub>2</sub> Reduction. *Journal of the American Chemical Society* **2017**, *139* (16), 5660-5663.
68. Xu, Y.; Fischer, A.; Duan, L.; Tong, L.; Gabrielsson, E.; Åkermark, B.; Sun, L., Chemical and Light-Driven Oxidation of Water Catalyzed by an Efficient Dinuclear Ruthenium Complex. *Angewandte Chemie International Edition* **2010**, *49* (47), 8934-8937.
69. Volpe, A.; Sartorel, A.; Tubaro, C.; Meneghini, L.; Di Valentin, M.; Graiff, C.; Bonchio, M., N-Heterocyclic Dicarbene Iridium(III) Catalysts Enabling Water Oxidation under Visible Light Irradiation. *European Journal of Inorganic Chemistry* **2014**, *2014* (4), 568-568.
70. Hitoki, G.; Ishikawa, A.; Takata, T.; Kondo, J. N.; Hara, M.; Domen, K., Ta<sub>3</sub>N<sub>5</sub> as a Novel Visible Light-Driven Photocatalyst ( $\lambda < 600$  nm). *Chemistry Letters* **2002**, *31* (7), 736-737.
71. Ishikawa, A.; Takata, T.; Kondo, J. N.; Hara, M.; Kobayashi, H.; Domen, K., Oxysulfide Sm<sub>2</sub>Ti<sub>2</sub>S<sub>2</sub>O<sub>5</sub> as a Stable Photocatalyst for Water Oxidation and Reduction under Visible Light Irradiation ( $\lambda \leq 650$  nm). *Journal of the American Chemical Society* **2002**, *124* (45), 13547-13553.
72. Tao, X.; Zhao, Y.; Mu, L.; Wang, S.; Li, R.; Li, C., Bismuth Tantalum Oxyhalogen: A Promising Candidate Photocatalyst for Solar Water Splitting. *Advanced Energy Materials* **2018**, *8* (1), 1701392.
73. Fujito, H.; Kunioku, H.; Kato, D.; Suzuki, H.; Higashi, M.; Kageyama, H.; Abe, R., Layered Perovskite Oxychloride Bi<sub>4</sub>NbO<sub>8</sub>Cl: A Stable Visible Light Responsive Photocatalyst for Water Splitting. *Journal of the American Chemical Society* **2016**, *138* (7), 2082-2085.
74. Qi, Y.; Zhao, Y.; Gao, Y.; Li, D.; Li, Z.; Zhang, F.; Li, C., Redox-Based Visible-Light-Driven Z-Scheme Overall Water Splitting with Apparent Quantum Efficiency Exceeding 10%. *Joule* **2018**, *2* (11), 2393-2402.
75. Fang, Z.-B.; Liu, T.-T.; Liu, J.; Jin, S.; Wu, X.-P.; Gong, X.-Q.; Wang, K.; Yin, Q.; Liu, T.-F.; Cao, R.; Zhou, H.-C., Boosting Interfacial Charge-Transfer Kinetics for Efficient Overall CO<sub>2</sub> Photoreduction via Rational Design of Coordination Spheres on Metal–Organic Frameworks. *J. Am. Chem. Soc.* **2020**, *142* (28), 12515-12523.
76. Kim, W.; Yuan, G.; McClure, B. A.; Frei, H., Light Induced Carbon Dioxide Reduction by Water at Binuclear ZrOCoII Unit Coupled to Ir Oxide Nanocluster Catalyst. *J. Am. Chem. Soc.* **2014**, *136* (31), 11034-11042.
77. Yuan, G.; Agiral, A.; Pellet, N.; Kim, W.; Frei, H., Inorganic core–shell assemblies for closing the artificial photosynthetic cycle. *Faraday Discuss.* **2014**, *176* (0), 233-249.

## Chapter 8. Energy Transfer in a Two-Dimensional Sp<sup>2</sup> Carbon Conjugated Covalent Organic Framework for Photo-Excited Nickel Catalysis

### 8.1 Introduction

Covalent organic frameworks constructed by robust periodic covalent bonds between organic building blocks are one of the promising classes of porous crystalline materials.<sup>1-3</sup> Owing to their permanent porosity, high structural stability, and tunable functionalities, COFs have been spotlighted and actively studied as new versatile materials in various applications including harmful gas removal, light-driven therapy, ion conduction, dynamic nuclear polarization, and catalysis.<sup>4-8</sup> To date, a diverse array of COFs have been reported, with linkages including boron-based, nitrogen-based, and carbon-based bridging bonds.<sup>9-10</sup> Particularly, COFs with long-range  $\pi$ -conjugation and organic photosensitizing moieties have been considered a promising cost-effective platform for photocatalysis in the absence of noble-metal photosensitizers.<sup>11</sup> Among them, sp<sup>2</sup> carbon-conjugated COFs,<sup>12</sup> have received broad interest since their inception in 2017, due to their excellent chemical stability and photoluminescence properties.<sup>13</sup>

To date, most COF-based photocatalysis has focused on small molecule activation, especially water splitting and carbon dioxide reduction.<sup>14</sup> Except for a few reports utilizing COFs in photo-oxidation or photoredox cross-coupling reactions of C-N, C-O, and C-S bonds,<sup>15-20</sup> COF-based photocatalysts are rarely explored in photocatalysis for fine chemical synthesis. The metallaphotoredox catalysis combining photosensitizers with transition metal catalysts is one of the crucial research areas in modern synthetic methodology for bond formations.<sup>21</sup> However, noble metal-based photosensitizers are usually required to achieve good performances in metallophotoredox catalysis. COF photocatalysts can potentially replace expensive precious

metal-based photocatalysts. Owing to the molecular nature of COFs, photophysical properties of conjugated COF materials can be modulated through ligand design, and different catalytic species can be introduced into COFs with chemically characterizable structures. These features offer opportunities in developing efficient COF photocatalysts for targeted reactions. However, COFs have rarely been examined in this area.

Ni is known for its ability to mediate radical-based cross-coupling reactions and has been widely explored in metallophotoredox catalysis and energy transfer catalysis.<sup>22-25</sup> The photophysics of Ni(II) complexes was comprehensively studied by the Doyle group through spectroscopic methods.<sup>26</sup> A <sup>3</sup>d-d excited state Ni(II) complex, that forms upon photoexcitation and can generate aryl radical, was proposed as the key intermediate in directly excited or energy transfer nickel catalysis. In recent works, through the design of photoactive ligands, various nickel-catalyzed cross-coupling reactions, including redox neutral C-C/C-X bond formation and reductive C-C/C-N bond formation, were achieved with a two-in-one nickel complex without the use of external photocatalysts.<sup>27</sup> Although the detailed mechanism was not elucidated for reactions catalyzed by the two-in-one nickel complex, we envision that the strategy can be applied to COF catalysis by introducing nickel into ligands connected to the conjugated networks of COFs with organic photosensitizing moieties. The conjugation between the photoactive component and the nickel complex may enable rapid energy transfer to excite the nickel complex to generate radicals for coupling reactions.

In this chapter, we designed and prepared a pyrene-based COF with sp<sup>2</sup>-carbon conjugation through Knoevenagel condensation (**Figure 8-1**). We successfully introduced a single Ni catalytic site using the bipyridine building blocks. Under light irradiation, pyrene building blocks in the framework act as photosensitizers and absorb energy from light. The energy is subsequently

transferred from pyrenes to Ni catalytic sites through the conjugated network. As a result, the COF functions as an excellent two-in-one photocatalyst to catalyze radical-based borylation and trifluoromethylation reactions of aryl halides. To the best of our knowledge, this is the first example of energy transfer catalysis catalyzed by COFs.

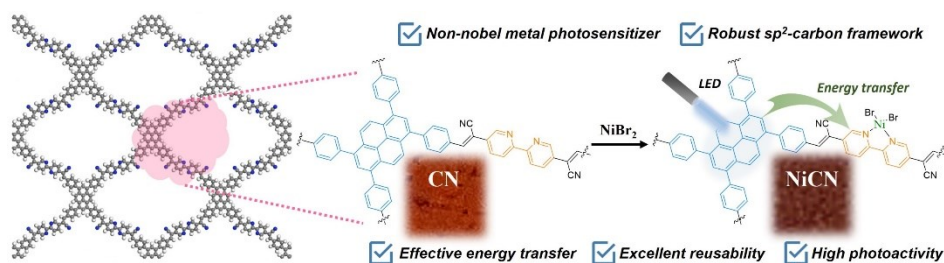


**Figure 8-1.** Schematics showing energy transfer catalysis by a sp<sup>2</sup>-carbon conjugated COF. Pyrene building blocks in the COF absorb light energy and the energy is rapidly transferred to Ni single catalytic sites to facilitate C-B and C-C bond formations.

## 8.2 Results and Discussion

### 8.2.1 Synthesis and Characterization of CN and NiCN

The 2D sp<sup>2</sup>-carbon conjugated COF (CN) was prepared via Knoevenagel reaction using 1,3,6,8-tetrakis(4-formylphenyl)pyrene (py-CHO) and 2,2'-([2,2'-bipyridine]-5,5'-diyl)diacetonitrile (bpy-CN) in *o*-dichlorobenzene and 1-butanol with a 6 M aqueous potassium hydroxide solution at 120 °C for 72 h (**Figure 8-2**). The COF was subsequently metalated with nickel(II) bromide ethylene glycol dimethyl ether complex (NiBr<sub>2</sub>·dme) in a 1:1 mixture of DMF and toluene at 60 °C for 24 h to prepare NiCN for catalytic reactions.



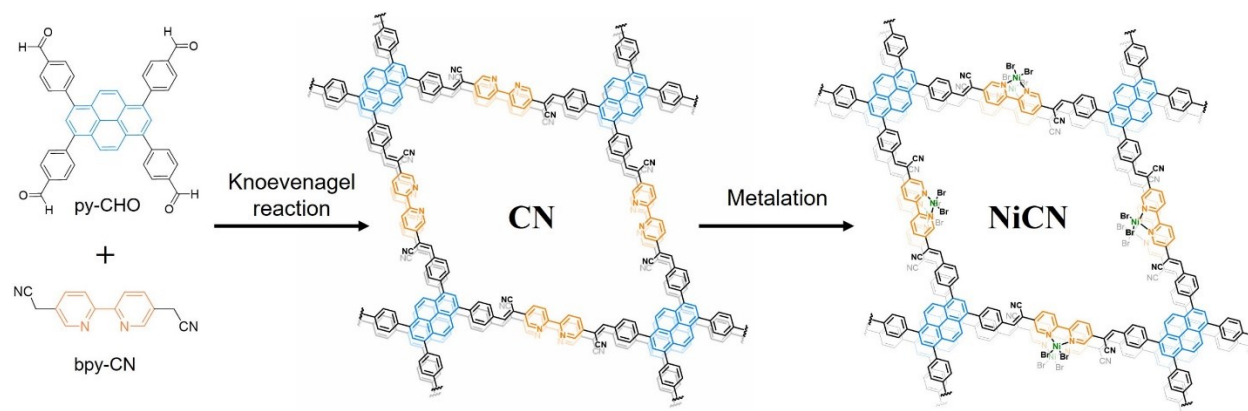


**Figure 8-2.** Synthetic scheme of NiCN.

IR spectrum of **CN** (**Figure 8-3a**) shows an absence of characteristic peaks from aldehyde C-H stretching ( $2718\text{ cm}^{-1}$  in py-CHO) and  $\text{C}\equiv\text{N}$  stretching ( $2256\text{ cm}^{-1}$  in bpy-CN). The distinct  $\text{C}=\text{O}$  stretching at  $1691\text{ cm}^{-1}$  decreased, while a peak corresponding to  $\text{C}=\text{C}$  stretching at  $1600\text{ cm}^{-1}$  increased. Additionally, new peaks appear around  $2215\text{ cm}^{-1}$  for both **CN** and **NiCN** (**Figure 8-3b**), assigned to vinyl nitrile group and confirmed by ssNMR (**Figure 8-3e**). These data demonstrate bond formation corresponding to Knoevenagel condensation and the establishment of a framework with an extended conjugated  $\pi$ -system.<sup>28</sup> The PXRD patterns and refinements of the materials were analyzed to assess their structures and crystallinity. The experimental pattern of **CN** matches the simulated pattern ( $R_p = 3.27\%$  and  $R_{wp} = 2.23\%$ ) from Rietveld refinement using a modeled structure, with eclipsed two-dimensional layer structure and one-dimensional channels within the framework (**Figure 8-3c**). **NiCN** showed a similar PXRD pattern to that of **CN**, confirming the preserved crystalline structure. The PXRD pattern of **NiCN** was also in agreement with the simulated pattern from Pawley refinement ( $R_p = 0.62\%$  and  $R_{wp} = 1.08\%$ ). Ni(II) and Br elements in **NiCN** were detected by X-ray photoelectron spectroscopy (XPS), demonstrating successful metalation (**Figure 8-3f**). To investigate the porosity of COFs, nitrogen isotherms were collected at 77 K after the COFs were degassed at  $120\text{ }^\circ\text{C}$  under vacuum for 10 h (**Figure 8-3d**).

The Brunauer–Emmett–Teller (BET) surface areas for CN and NiCN were calculated to be 364 m<sup>2</sup>g<sup>-1</sup> and 251 m<sup>2</sup>g<sup>-1</sup>, respectively, and the anticipated pore size (~2.5 nm) is comparable to the pore size distribution from the isotherm of CN. TEM revealed the rodlike morphologies of CN and NiCN with a diameter of approximately 0.2 μm (Figure 8-3g), in agreement with the literature reports.<sup>12</sup>

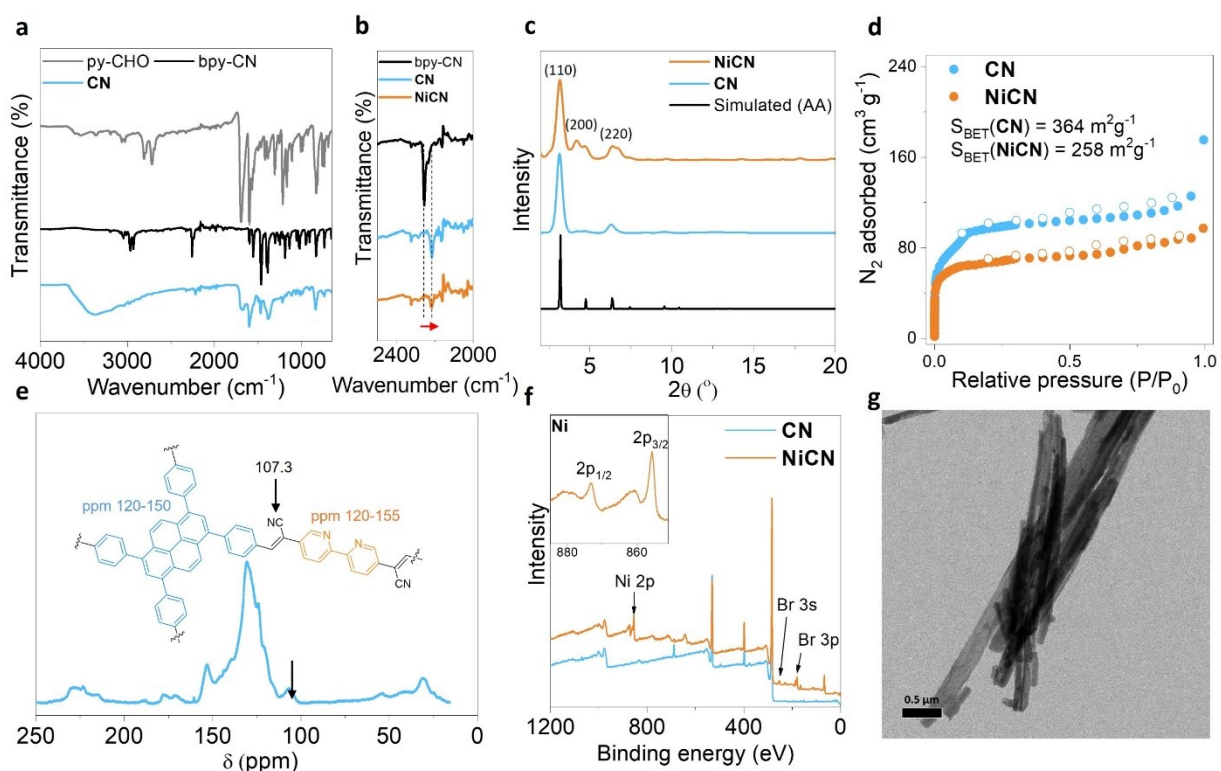


**Figure 8-3.** Characterization of CN. (a) IR spectra of py-CHO, bpy-CN and CN. (b) IR spectra of bpy-CN, CN, and NiCN in the C≡N triple bond stretching region. (c) PXRD patterns of CN, NiCN, and simulated pattern from structural model. (d) Nitrogen isotherms of CN and NiCN at 77 K. (e) ssNMR spectrum of CN. (f) XPS spectra of CN and NiCN. Inset shows the narrow scan of Ni 2p region. (g) TEM image of NiCN.

### 8.2.3 Borylation and Trifluoromethylation Reactions

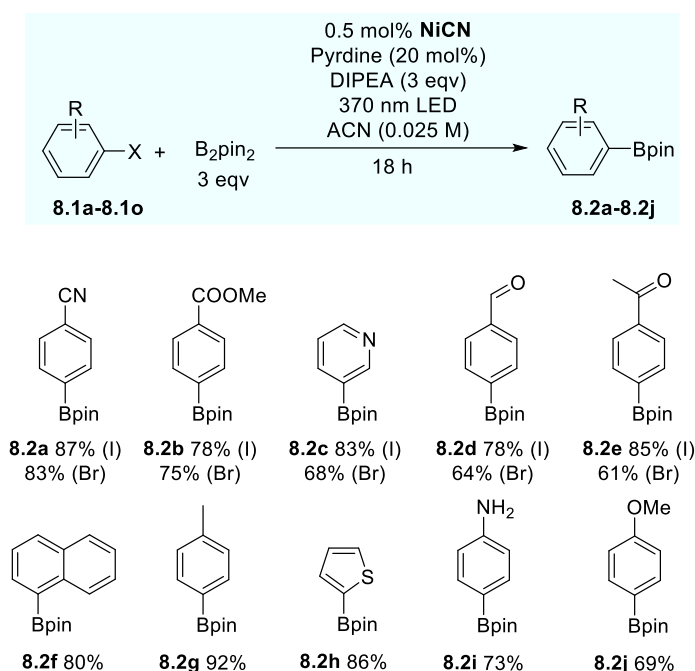
The reactivity of NiCN was first studied in energy-transfer mediated cross coupling reactions between 4-bromobenzonitrile/methyl 4-iodobenzoate and benzoic acid.<sup>24</sup> Despite intensive efforts in optimizing reaction conditions for the C-O coupling reactions, a large fraction of reactants were transformed into dehalogenation products, which was also observed in light-mediated reductive elimination from a Ni(II)-aryl complex.<sup>24</sup> When DMSO was used as solvent, a deoxygenated C-S cross-coupled product was observed, indicating the radical nature of the reactions. We, therefore, proposed that during the reactions, upon oxidative addition of Ni to the C-X bond in aryl halide, an efficient in-plane energy transfer in NiCN would facilitate the generation of aryl radicals from Ni-aryl complexes, leading to side products.

Realizing the radical nature of NiCN photocatalysis, we next examined radical-based borylation reactions and trifluoromethylation reactions of aryl halides. With diisopropylethylamine (DIPEA) as a base and pyridine as a nucleophile to activate boron agents,<sup>29</sup> methyl 4-bromobenzoate (**8.1b**) readily reacts with bis(pinacolato)diboron (B<sub>2</sub>pin<sub>2</sub>) in MeCN under 370 nm blue LED light irradiation for 16 hours to afford methyl 4-(4,4,5,5-tetramethyl-1,3,2-dioxaborolan-2-yl)benzoate (**8.2b**) in 78% yield. The corresponding homogeneous counterparts gave **8.2b** in only 29% yield under identical conditions (**Table 8-3**). In the presence of CuI and KF (as a base), NiCN also successfully catalyzed the trifluoromethylation of **8.1b** with TMSCF<sub>3</sub> in MeCN after 370 nm blue LED irradiation for 16 hours to yield methyl 4-trifluoromethyl benzoate (**8.3b**) in 88% yield. The homogeneous control gave a 21% yield under the same condition.

With optimized conditions in hand, we further explored the substrate scope for the borylation reactions of aryl halides. As shown in **Table 8-1**, aryl iodides with electron-withdrawing

groups (**8.1a**, **8.1c**, **8.1e**, **8.1g**, **8.1i**) of nitrile, ester, aldehyde, ketone, and pyridine groups reacted smoothly to yield products **8.2a-e** in 78-85% yields. Electron-deficient aryl bromides (**8.1b**, **8.1d**, **8.1f**, **8.1h**, **8.1j**) underwent the reactions with slightly lower yields of 61-83% compared to corresponding aryl iodides. Electron-rich aryl iodides, including 1-iodonaphthylene, 4-iodotoluene, 2-iodothiophene, 4-iodoaniline, and 4-iodoanisole (**8.1k-o**), were also tolerated in the reactions to give products **8.2f-j** in 69-92% yields. The TONs for borylation reactions ranged from 122 to 184.

**Table 8-1.** Substrate scope for NiCN-catalyzed borylation reactions.

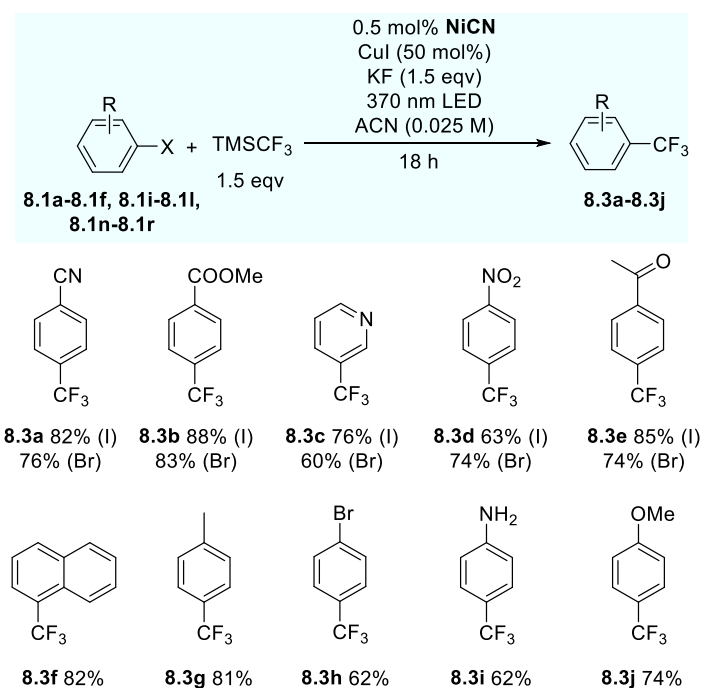


<sup>a</sup>‘I’ or ‘Br’ in parentheses stands for aryl iodide or aryl bromide used in the reactions. <sup>b</sup>Reactions were performed with **8.1** (0.1 mmol), B<sub>2</sub>pin<sub>2</sub> (0.3 mmol), pyridine (0.02 mmol), DIPEA (0.3 mmol) and 50 μmol NiCN in 4 mL acetonitrile under 370 nm irradiation for 18 hours.

The trifluoromethylation reactions showed a broad substrate scope as well (**Table 8-2**). Both electron-deficient aryl iodides (**8.1a**, **8.1c**, **8.1e**, **8.1p**, **8.1i**) and aryl bromides (**8.1b**, **8.1d**, **8.1f**, **8.1q**, **8.1j**) with nitrile, ester, pyridine, nitro and carbonyl groups successfully reacted with

TMSCF<sub>3</sub> to yield corresponding products **8.3a-e** in 60-88% yields. Electron-rich aryl iodides including 1-iodonaphthylene, 4-iodotoluene, 4-iodobromobenzene, 4-iodoaniline, and 4-iodoanisole (**8.1k-l**, **8.1n-o**, **8.1r**) also worked to afford products **8.3f-j** in 62-82% yields. The TONs for trifluoromethylation reactions reached 124-178. Electron-rich aryl bromides gave bad performances in both borylation and trifluoromethylation reactions, which was attributed to the weak oxidative addition ability of the electron-poor Ni center in NiCN. NiCN was successfully recycled by filtration in the borylation reaction of **8.1b** and reused in three consecutive cycles to synthesize **8.2b** without significant loss of reactivities and crystallinity (**Figure 8-4**), demonstrating the chemical stability and recyclability of the materials. A total TON of 436 was achieved in the recycle experiment.

**Table 8-2.** Substrate scope for NiCN-catalyzed trifluoromethylation reactions.



<sup>a</sup>‘I’ or ‘Br’ in parentheses stands for aryl iodide or aryl bromide used in reactions. <sup>c</sup>Reactions were performed with **8.1** (0.1 mmol), TMSCF<sub>3</sub> (0.15 mmol), CuI (0.05 mmol), KF (0.15 mmol) and 50 μmol NiCN in 4 mL acetonitrile under 370 nm irradiation for 18 hours.

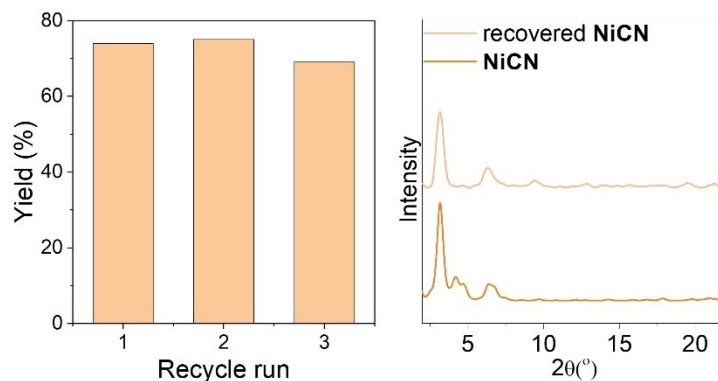


**Figure 8-4.** Catalyst recycle and reuse. Reaction yields of **8.1b** borylation in three consecutive runs (left) and PXRD pattern of the recycled **NiCN** (right).

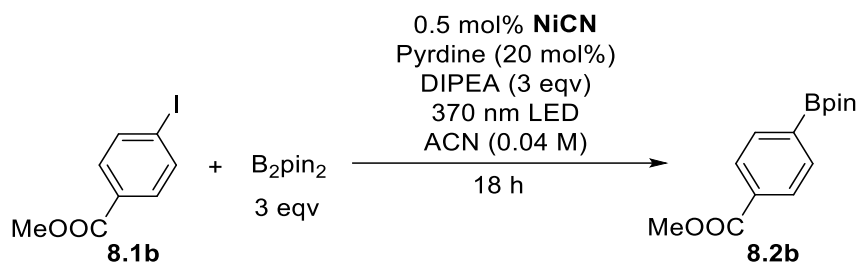
### 8.2.3 Mechanistic Studies

To study the mechanisms of **NiCN**-catalyzed borylation and trifluoromethylation reactions of aryl halides, several control experiments were performed (**Table 8-3**). As mentioned above, **NiCN** showed at least 2.5 times higher reactivities than the corresponding homogeneous catalysts. For both borylation and trifluoromethylation reactions, the addition of TEMPO severely decreased the reaction yields, and no product was observed in control groups without light. These results suggested a strong synergy between the pyrene moiety and the Ni catalytic site in **NiCN** and these reactions go through light-mediated radical pathways.

According to the literature precedents on excited states of Ni(II) complexes<sup>26</sup> and on photoredox borylation reactions,<sup>30</sup> we propose a plausible mechanism for **NiCN**-catalyzed borylation reactions by energy transfer in **Figure 8-4**. First, Ni(II) was photo-reduced by the pyrene moiety in **NiCN** using DIPEA as reductant. The resulting Ni(0) bipyridine complex undergoes oxidative addition of the C-X bond of aryl halide to form a Ni(II)-aryl complex. Upon excitation, the pyrene antenna absorbs light and transfers energy to the Ni(II)-aryl complex to

trigger the cleavage of Ni-C bond and generation of an aryl radical, which is captured by B<sub>2</sub>pin<sub>2</sub> to afford the borylation product. Another part of boron leaves as a boron radical anion which reduces Ni(I) species in the COF to Ni(0) to complete the reaction cycle.

**Table 8-3.** Control experiments for NiCN-catalyzed borylation reactions.



Entry	Deviation	Yield <sup>a</sup> (%)
1	No	78
2	0.25 mol% pyrene 0.5 mol% NiBr <sub>2</sub> (dtbbpy)	29
3	5 mol% pyrene 5 mol% NiBr <sub>2</sub> (dtbbpy)	63
4	No light	0
5	Add 1 eqv TEMPO	10

<sup>a</sup>Entry 1 indicates isolated yield. Entries 2-5 indicate GC-MS yields.

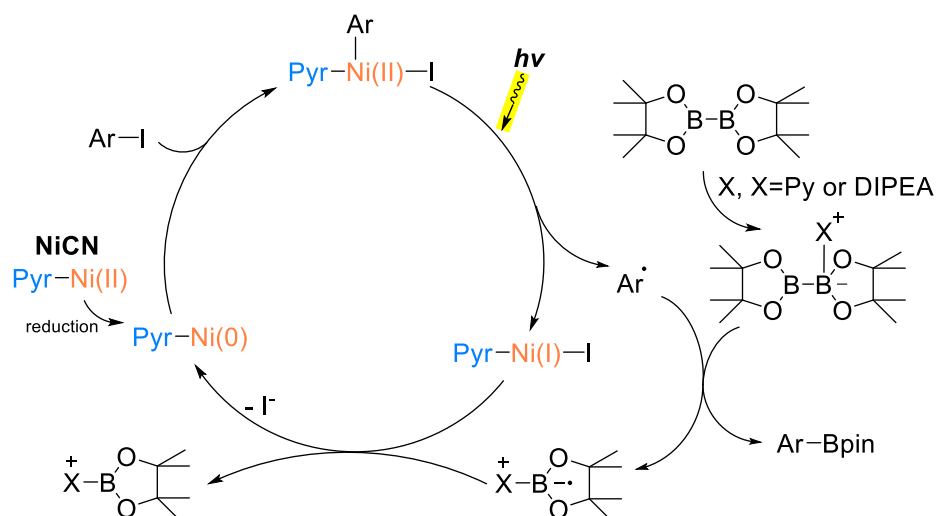


**Figure 8-5.** Proposed mechanism for NiCN-catalyzed borylation reactions.

CV experiments were performed to support the mechanism (**Figure 8-5a**). The reduction potential of pyrene was determined as  $-2.10$  V vs.  $\text{Fc}^+/\text{Fc}$ . The Ni(II) complex with 4,4'-di-tert-butyl-2,2'-dipyridyl (dtbbpy) ligand showed two reversible reductive peaks at  $-1.20$  V and  $-1.90$  V vs.  $\text{Fc}^+/\text{Fc}$ . With a proper reductive quencher (DIPEA in the borylation reaction), pyrene can reduce the Ni(II)-bipyridine complex to Ni(0) in a photoreduction reaction. Luminescence studies were performed to analyze the energy transfer in NiCN (**Figure 8-5b**). Ni(II)-aryl complex (**Int**) generated from oxidation addition of Ni(cod)(dtbbpy) into 4-bromobenzonitrile was synthesized,<sup>31</sup> and integrated into CN to synthesize CN-NiArBr with different nickel loadings. Stern-Völmer plots were fitted for quenching of CN-NiArBr and quenching of CN or pyrene by **Int**. The energy transfer efficiency of CN-NiArBr was calculated to be 220 times higher than that between CN and **Int**, and  $7.3 \times 10^5$  times faster than that between pyrene and **Int**. According to the properties of excited Ni(II)-aryl complexes,<sup>26</sup> the enhanced energy transfer in NiCN accelerates the generation of aryl radicals from Ni(II)-aryl complex, thereby improving the efficiency of radical borylation reactions.



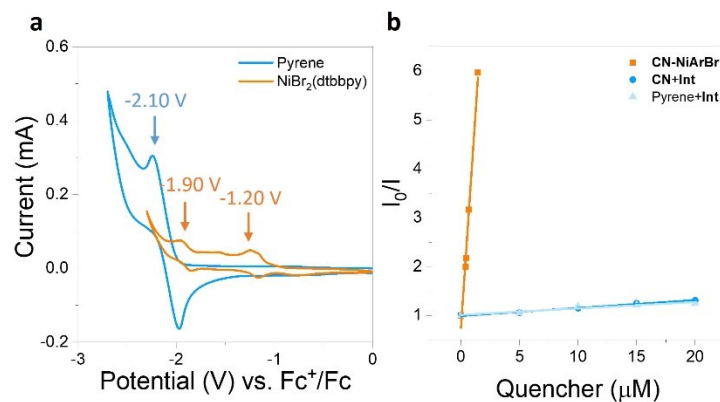


**Figure 8-6.** Mechanistic studies.(a) CV diagram of pyrene and NiBr<sub>2</sub>(dtbbpy). (b) Stern-Völmer plots for quenching of CN-NiArBr, CN, and pyrene.

### 8.3 Conclusion

In this chapter, we designed and prepared a sp<sup>2</sup> carbon conjugated COF that catalyzes the borylation and trifluoromethylation reactions of aryl halides through energy transfer catalysis. The highly crystalline porous materials were synthesized through Knoevenagel condensation between pyrene and bipyridine moieties and were conjugated throughout the covalent network via C=C bonds. Benefiting from a good in-plane  $\pi$ -electron delocalization, the COF, after metallated with Ni, has efficient energy transfer from the pyrene antenna to the catalytic Ni complex, which facilitates the generation of aryl radicals under photoexcitation conditions. Borylation and trifluoromethylation of aryl halides were successfully catalyzed by the COF with TONs of up to 184, and the COF was recycled and reused three times without loss of reactivity and crystallinity. This work shows the potential of photoactive COF in photocatalysis for organic reactions.

## 8.4 Methods

### 8.4.1 Material synthesis

**Synthesis of 1,3,6,8-tetrabromopyrene.** 1,3,6,8-tetrabromopyrene (py-Br) was synthesized according to reported method with slight modifications.<sup>32</sup> Bromine (16.2 g, 101.3 mmol) was slowly added into a nitrobenzene solution (150 mL) of pyrene (5.0 g, 24.7 mmol) with vigorous stirring at room temperature. After the addition was complete, the reaction temperature was heated at 160 °C for 6 h. After cooling to room temperature, the mixture was poured into acetone (500 mL) and the precipitate was collected by filtration and thoroughly washed with ethanol. The product was fully dried and used without further purification.

**Synthesis of 1,3,6,8-tetrakis(4-formylphenyl)pyrene.** Py-CHO was synthesized according to the reported method with slight modifications.<sup>33</sup> After a 250 mL round bottom flask containing py-Br (3.0 g, 5.8 mmol), 4-formylphenylboronic acid (6.0 g, 40.0 mmol), K<sub>2</sub>CO<sub>3</sub> (4.0 g, 29.0 mmol), and Pd(PPh<sub>3</sub>)<sub>4</sub> (600 mg, 0.52 mmol) was dried under vacuum for 3 h, dioxane (80 mL) and H<sub>2</sub>O (14 mL) were added into the flask and the mixture was refluxed under N<sub>2</sub> atmosphere for 3 days. Upon cooling to room temperature, the mixture was slowly transferred to a beaker containing 40 mL concentrated hydrochloric acid. The solid was filtered, washed with methanol and water, and dried in a 100 °C oven overnight. Chloroform (300 mL) was poured into the solid and stirred at 50 °C for 6 hours. After cooling to room temperature, the solid was separated by filtration and dried under vacuum to obtain py-CHO (2.0 g, 3.2 mmol, 55%). <sup>1</sup>H NMR (CDCl<sub>3</sub>, 400 MHz): δ 10.19 (s, 4H), 8.20 (s, 4H), 8.12 (d, J = 7.9 Hz, 8H), 8.07 (s, 2H), 7.88 (d, J = 7.8 Hz, 8H). HRMS m/z Calc. for C<sub>44</sub>H<sub>26</sub>O<sub>4</sub> ([M<sup>+</sup>]): 618.1831, Found: 618.1829.

**Synthesis of 5,5'-bis(bromomethyl)-2,2'-bipyridyl.** 5,5'-Bis(bromomethyl)-2,2'-bipyridyl (bpy-Br) was synthesized according to the reported method with slight modifications.<sup>33</sup>

After degassing with N<sub>2</sub> for 30 min, 300 mL CCl<sub>4</sub> was poured into a 500 mL round bottom flask containing 5,5'-dimethyl-2,2'-dipyridyl (5.0 g, 27.2 mmol), *N*-bromosuccinimide (9.8 g, 54.4 mmol), and azobisisobutyronitrile (0.1 g, 0.61 mmol). The mixture was refluxed under N<sub>2</sub> atmosphere for one day and hot filtered. After the filtrate was concentrated under vacuum, the crude solid was purified in methanol by sonication to afford a white powder (4.0 g, 11.7 mmol, 43%). <sup>1</sup>H NMR (CDCl<sub>3</sub>, 400 MHz): δ 8.61 (d, J = 2.1 Hz, 2H), 8.33 (d, J = 8.2 Hz, 2H), 7.79 (dd, J = 8.2, 2.3 Hz, 2H), 4.47 (s, 4H).

**Synthesis of 2,2'-([2,2'-bipyridine]-5,5'-diyl)diacetonitrile.** After bpy-Br (6.0 g, 17.54 mmol) and sodium cyanide (5.40 g, 110.20 mmol) were dissolved in DMSO (80 mL), the solution was stirred at 45 °C for 6 hours and then stirred at room temperature for 12 hours. The solution was heated to 80 °C and poured without cooling into deionized water (500 mL), filtered, and washed with deionized water several times. After the crude product was dried in a 100 °C oven, it was dissolved in methylene chloride and filtered using celite. The filtrate was concentrated and purified by silica gel column chromatography using methylene chloride/methanol (100/1) as eluent to obtain bpy-CN (2.37 g, 10.12 mmol, 57.68%) as a white powder. <sup>1</sup>H NMR (400 MHz, CDCl<sub>3</sub>): δ 8.67 (s, 2H), 8.49 (d, J = 8.2 Hz, 2H), 7.88 (dd, J = 8.2, 2.3 Hz, 2H), 3.87 (s, 4H). HRMS m/z Calc. for C<sub>14</sub>H<sub>11</sub>N<sub>4</sub> ([M+H<sup>+</sup>]): 235.0984, Found: 235.0989.

**Synthesis of CN.** A 10 mL Schlenk tube was charged with py-CHO (30 mg, 0.048 mmol), bpy-CN (23.1 mg, 0.099 mmol), 1,2-dichlorobenzene (2 mL), 1-butanol (2 mL) and aqueous KOH solution (0.1 mL, 4 M). The mixture was stirred for 3 min and then degassed through three freeze-pump-thaw cycles using a liquid nitrogen bath. The tube was sealed under vacuum, stirred for 1 min, and then heated at 120 °C for 3 days. After cooling to room temperature, the precipitate was washed with tetrahydrofuran and water. 300 mL chloroform was then poured into the solid and the

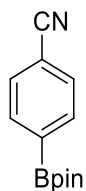
mixture was stirred at 60 °C for 12 hours. After filtration, the resulting powder was dried at 100 °C to obtain CN. Yield: 37 mg (75%).

**Synthesis of NiCN.** To 10 mL of CN dispersion (10 mg/mL) in 1:1 (v/v) mixture of DMF and toluene was added NiBr<sub>2</sub>·dme (15.4 mg, 50 μmol). The resulting solution was stirred at 60 °C for 24 hours. The precipitate was filtered and washed with DMF once and toluene once to yield NiCN in quantitative yield. The nickel loading was determined by ICP-MS analysis to be ~100 %.

#### 8.4.2 Catalytic Reactions

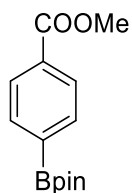
**General procedure for borylation of aryl halides.** Aryl halide (0.1 mmol, 1 equiv), B<sub>2</sub>pin<sub>2</sub> (0.3 mmol, 3 equiv.), pyridine (0.02 mmol, 1.6 μL, 20 mol%), and DIPEA (3 mmol, 52 μL) were mixed in 4 mL dry MeCN under nitrogen. NiCN (0.5 μmol based on pyrene, dispersion in MeCN) was then added and the resulting mixture was stirred under 370 nm blue LED irradiation for 18 hours. After the reaction, the solvent was removed under vacuum. The residue was subjected to column chromatography on silica gel using *n*-hexane and ethyl acetate as eluent to give cross-coupling products **2a-2o**.

**General procedure for trifluoromethylation of aryl halides.** Copper iodide (0.05 mmol, 9.5 mg, 50 mol%), potassium fluoride (0.15 mmol, 8.7 mg, 1.5 equiv) and TMSCF<sub>3</sub> (0.15 mmol, 22 μL, 1.5 equiv) were added to 1 mL dry MeCN under nitrogen. The solution was stirred for 10 mins. Aryl halide (0.1 mmol, 1 equiv) and NiCN (0.5 μmol based on pyrene, dispersion in MeCN) in 3 mL MeCN were then added and the resulting mixture was stirred under 370 nm blue LED irradiation for 18 hours. After the reaction, the solvent was removed under vacuum. The residue was subjected to column chromatography on silica gel using *n*-hexane and ethyl acetate as eluent to give cross-coupling products **8.3a-8.3o**.



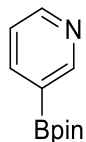
**8.2a**

White solid. 87% yield using 4-iodobenzointrile (**8.1a**) as the starting material. 83% yield using 4-bromobenzointrile (**8.1a'**) as the starting material.  $^1\text{H NMR}$  (400 MHz, chloroform-*d*):  $\delta$  7.89-7.86 (d,  $J = 8.3$  Hz, 2H), 7.62-7.60 (d,  $J = 8.3$  Hz, 2H), 1.34 (s, 12H);  $^{13}\text{C NMR}$  (101 MHz, chloroform-*d*):  $\delta$  135.1, 131.1, 118.8, 114.5, 84.5, 24.9; **HRMS** (ESI-TOF): calculated  $m/z$  for  $[\text{M}+\text{H}]^+$  ( $\text{C}_{13}\text{H}_{17}\text{BNO}_2$ ), 229.1274; observed, 229.1259. Characterization data matched those reported in the literature.<sup>30</sup>



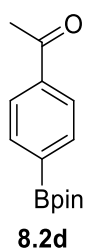
**8.2b**

White solid, 78% yield using methyl 4-iodobenzoate (**8.1b**) as the starting material. 75% yield using methyl 4-bromobenzoate (**8.1b'**) as the starting material.  $^1\text{H NMR}$  (400 MHz, chloroform-*d*):  $\delta$  8.00 (dd,  $J = 8.4, 2.1$  Hz, 2H), 7.85 (dd,  $J = 8.4, 2.0$  Hz, 2H), 3.91 (s, 3H), 1.34 (s, 12H);  $^{13}\text{C NMR}$  (101 MHz, chloroform-*d*):  $\delta$  167.1, 134.6, 132.3, 128.6, 84.1, 52.1, 24.9; **HRMS** (ESI-TOF): calculated  $m/z$  for  $[\text{M}+\text{H}]^+$  ( $\text{C}_{14}\text{H}_{20}\text{BNO}_4$ ), 263.1455; observed, 263.1450. Characterization data matched those reported in the literature.<sup>30</sup>

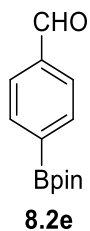


**8.2c**

Yellowish oil, 83% yield using 3-iodopyridine (**8.1c**) as the starting material. 68% yield using 3-bromopyridine (**8.1c'**) as the starting material. **<sup>1</sup>H NMR** (400 MHz, chloroform-*d*): δ 8.95 (s, 1H), 8.67 (d, *J* = 4.7 Hz, 1H), 8.09 – 8.06 (m, 1H), 7.31 (d, *J* = 7.4 Hz, 1H), 1.35 (s, 13H); **<sup>13</sup>C NMR** (101 MHz, chloroform-*d*): δ 154.9, 151.3, 142.7, 123.3, 84.3, 25.0; **HRMS** (ESI-TOF): calculated *m/z* for [M+H]<sup>+</sup> (C<sub>11</sub>H<sub>17</sub>BNO<sub>2</sub>), 206.1352; observed, 206.1353. Characterization data matched those reported in the literature.<sup>34</sup>

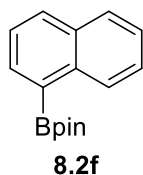


White solid, 85% yield using 4-iodoacetophenone (**8.1d**) as the starting material. 64% yield using 4-bromoacetophenone (**8.1d'**) as the starting material. **<sup>1</sup>H NMR** (400 MHz, chloroform-*d*): δ 7.93 (d, *J* = 8.4 Hz, 2H), 7.89 (d, *J* = 8.3 Hz, 2H), 2.62 (s, 3H), 1.36 (s, 12H); **<sup>13</sup>C NMR** (101 MHz, chloroform-*d*): δ 198.5, 139.0, 134.9, 127.3, 84.2, 26.8, 24.9; **HRMS** (ESI-TOF): calculated *m/z* for [M+H]<sup>+</sup> (C<sub>14</sub>H<sub>20</sub>BNO<sub>3</sub>), 247.1505; observed, 247.1505. Characterization data matched those reported in the literature.<sup>30</sup>

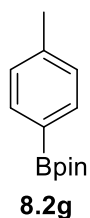


White solid, 78% yield using 4-iodobenzaldehyde (**8.1e**) as the starting material. 64% yield using 4-bromobenzaldehyde (**8.1e'**) as the starting material. **<sup>1</sup>H NMR** (400 MHz, chloroform-*d*): δ 10.02 (s, 1H), 7.94 (d, *J* = 8.2 Hz, 2H), 7.84 (d, *J* = 8.3 Hz, 2H), 1.34 (s, 12H).; **<sup>13</sup>C NMR** (101 MHz,

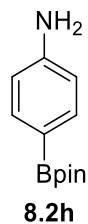
chloroform-*d*):  $\delta$  192.6, 138.1, 135.2, 128.7, 84.3, 24.9; **HRMS** (ESI-TOF): calculated  $m/z$  for  $[M+H]^+$  ( $C_{13}H_{18}BO_3$ ), 233.1349; observed, 233.1354. Characterization data matched those reported in the literature.<sup>30</sup>



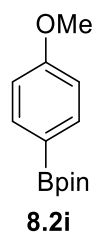
White solid, 80% yield using 1-iodonaphthalene (**8.1f**) as the starting material. **<sup>1</sup>H NMR** (400 MHz, chloroform-*d*):  $\delta$  8.77 (d,  $J = 8.4$  Hz, 1H), 8.09 (d,  $J = 6.9$ , 1H), 7.94 (d,  $J = 8.2$  Hz, 1H), 7.84 (d,  $J = 8.1$  Hz, 1H), 7.54 (t,  $J = 8.2$ , 1H), 7.48 (t,  $J = 7.5$  Hz, 2H), 1.43 (s, 13H). **<sup>13</sup>C NMR** (101 MHz, chloroform-*d*):  $\delta$  136.9, 135.7, 133.2, 131.6, 128.4, 128.4, 126.4, 125.5, 125.0, 83.8, 25.0; **HRMS** (ESI-TOF): calculated  $m/z$  for  $[M+K]^+$  ( $C_{16}H_{19}BO_2K$ ), 293.1115; observed, 293.1115. Characterization data matched those reported in the literature.<sup>30</sup>



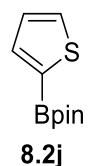
Yellowish oil, 92% yield using 4-iodotoluene (**8.1g**) as the starting material. **<sup>1</sup>H NMR** (400 MHz, chloroform-*d*):  $\delta$  7.71 (d,  $J = 7.7$  Hz, 2H), 7.19 (d,  $J = 7.7$  Hz, 2H), 2.37 (s, 3H), 1.34 (s, 12H); **<sup>13</sup>C NMR** (101 MHz, chloroform-*d*):  $\delta$  141.4, 134.8, 128.5, 83.7, 24.9, 21.7; **HRMS** (ESI-TOF): calculated  $m/z$  for  $[M+H]^+$  ( $C_{13}H_{20}BO_2$ ), 219.1556; observed, 219.1560. Characterization data matched those reported in the literature.<sup>30</sup>



White solid, 73% yield using 4-iodoaniline (**8.1h**) as the starting material. **<sup>1</sup>H NMR** (400 MHz, chloroform-*d*):  $\delta$  7.55 (d, *J* = 8.5 Hz, 2H), 6.60 (d, *J* = 8.5 Hz, 2H), 1.25 (s, 12H); **<sup>13</sup>C NMR** (101 MHz, chloroform-*d*):  $\delta$  149.0, 136.4, 114.2, 83.3, 24.9; **HRMS** (ESI-TOF): calculated *m/z* for [M+H]<sup>+</sup> (C<sub>12</sub>H<sub>19</sub>BNO<sub>2</sub>), 220.1509; observed, 220.1511. Characterization data matched those reported in the literature.<sup>35</sup>



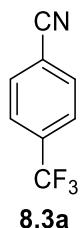
Yellowish oil, 69% yield using 4-iodoanisole (**8.1i**) as the starting material. **<sup>1</sup>H NMR** (400 MHz, chloroform-*d*):  $\delta$  7.75 (d, *J* = 8.8 Hz, 2H), 6.90 (d, *J* = 8.8 Hz, 2H), 3.83 (s, 3H), 1.33 (s, 12H); **<sup>13</sup>C NMR** (101 MHz, chloroform-*d*):  $\delta$  162.2, 136.5, 113.3, 83.6, 55.1, 24.9; **HRMS** (ESI-TOF): calculated *m/z* for [M+H]<sup>+</sup> (C<sub>13</sub>H<sub>20</sub>BO<sub>3</sub>), 235.1506; observed, 235.1506. Characterization data matched those reported in the literature.<sup>30</sup>



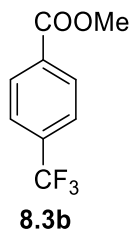
White solid, 86% yield using 2-iodothiophene (**8.1j**) as the starting material. **<sup>1</sup>H NMR** (400 MHz, chloroform-*d*):  $\delta$  7.68 – 7.59 (m, 2H), 7.19 – 7.17 (m, 1H), 1.34 (s, 12H); **<sup>13</sup>C NMR** (101 MHz,



chloroform-*d*):  $\delta$  137.1, 132.3, 128.2, 84.0, 24.7; **HRMS** (ESI-TOF): calculated  $m/z$  for  $[M+H]^+$  ( $C_{10}H_{16}BO_2S$ ), 211.0964; observed, 211.0962. Characterization data matched those reported in the literature.<sup>34</sup>

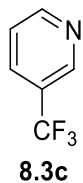


White solid, 82% yield using 4-iodobenzonitrile (**8.1a**) as the starting material, 76% yield using 4-bromobenzonitrile (**8.1a'**) as the starting material. **<sup>1</sup>H NMR** (400 MHz, chloroform-*d*):  $\delta$  7.66 (d,  $J = 8.7$  Hz, 1H), 7.55 (d,  $J = 8.7$  Hz, 1H); **<sup>19</sup>F NMR** (375 MHz, chloroform-*d*):  $\delta$  -63.5; **<sup>13</sup>C NMR** (101 MHz, chloroform-*d*):  $\delta$  134.6 (q,  $J^2 = 33.3$  Hz), 132.7, 126.2 (q,  $J^3 = 3.9$  Hz), 123.0 (q,  $J^1 = 274.1$  Hz), 117.4, 116.1. **HRMS** (ESI-TOF): calculated  $m/z$  for  $[M+H]^+$  ( $C_8H_5F_3N$ ), 172.0374; observed, 172.0380. Characterization data matched those reported in the literature.<sup>36</sup>

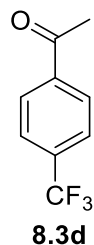


Colorless oil, 88% yield using methyl 4-iodobenzoate (**8.1b**) as the starting material, 83% yield using methyl 4-bromobenzoate (**8.1b'**) as the starting material. **<sup>1</sup>H NMR** (400 MHz, chloroform-*d*):  $\delta$  8.17 (d,  $J = 8.1$  Hz, 2H), 7.72 (d,  $J = 8.1$  Hz, 2H), 3.98 (s, 3H); **<sup>19</sup>F NMR** (375 MHz, chloroform-*d*):  $\delta$  -63.2; **<sup>13</sup>C NMR** (101 MHz, chloroform-*d*):  $\delta$  165.9, 134.4 (q,  $J^2 = 33.3$  Hz), 133.4, 130.0, 125.4 (q,  $J^3 = 4.0$  Hz), 123.6 (q,  $J^1 = 274.7$  Hz), 52.5. **HRMS** (ESI-TOF): calculated

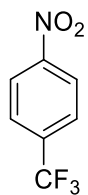
m/z for  $[M+H]^+$  ( $C_9H_8F_3O_2$ ), 205.0476; observed, 205.0480. Characterization data matched those reported in the literature.<sup>36</sup>



76% yield using 3-iodopyridine (**8.1c**) as the starting material, 60% yield using 3-bromopyridine (**8.1c'**) as the starting material. The yield was determined by GC-MS using benzotrifluoride as internal standard. **HRMS** (ESI-TOF): calculated m/z for  $[M+H]^+$  ( $C_6H_5F_3N$ ), 148.0374; observed, 148.0376.

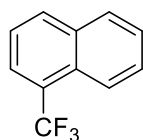


White solid, 85% yield using 4-iodoacetophenone (**8.1d**) as the starting material, 74% yield using 4-bromoacetophenone (**8.1d'**) as the starting material. **<sup>1</sup>H NMR** (400 MHz, chloroform-*d*):  $\delta$  8.07 (d,  $J = 8.3$  Hz, 2H), 7.75 (d,  $J = 8.3$  Hz, 2H), 2.67 (s, 3H); **<sup>19</sup>F NMR** (375 MHz, chloroform-*d*):  $\delta$  -63.2; **<sup>13</sup>C NMR** (101 MHz, chloroform-*d*):  $\delta$  197.0, 139.7, 134.4 (q,  $J^2 = 32.3$  Hz), 128.62, 125.7 (q,  $J^3 = 4.0$  Hz), 123.7 (q,  $J^1 = 274.7$  Hz), 26.77; **HRMS** (ESI-TOF): calculated m/z for  $[M+H]^+$  ( $C_9H_8F_3O$ ), 189.0527; observed, 189.0521. Characterization data matched those reported in the literature.<sup>37</sup>



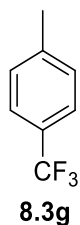
**8.3k**

White solid, 63% yield using 4-iodonitrobenzene (**8.1k**) as the starting material, 74% yield using 4-bromonitrobenzene (**8.1k'**) as the starting material. **<sup>1</sup>H NMR** (400 MHz, chloroform-*d*):  $\delta$  8.44 – 8.33 (d,  $J = 8.3$  Hz, 2H), 7.92 – 7.80 (d,  $J = 8.1$  Hz, 2H); **<sup>19</sup>F NMR** (375 MHz, chloroform-*d*):  $\delta$  -63.4; **<sup>13</sup>C NMR** (101 MHz, chloroform-*d*):  $\delta$  150.0, 136.1 (q,  $J^2 = 33.3$  Hz), 126.8 (q,  $J^3 = 4.0$  Hz), 124.1, 123.0 (q,  $J^1 = 274.7$  Hz); **HRMS** (ESI-TOF): calculated  $m/z$  for  $[M+H]^+$  ( $C_7H_5F_3NO_2$ ), 192.0272; observed, 192.0290. Characterization data matched those reported in the literature.<sup>38</sup>

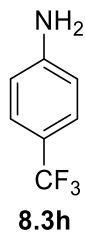


**8.3f**

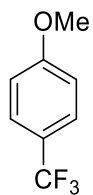
Yellowish oil, 82% yield using using 1-iodonaphthalene (**8.1f**) as the starting material. **<sup>1</sup>H NMR** (400 MHz, chloroform-*d*):  $\delta$  8.26 (d,  $J = 8.8$ , 1H), 8.05 (d,  $J = 8.4$  Hz, 1H), 7.96 (d,  $J = 8.1$ , 1H), 7.91 (d,  $J = 7.2$  Hz, 1H), 7.70-7.60 (dt,  $J = 8.6, 6.8$ , Hz, 2H), 7.54 (t,  $J = 7.7$  Hz, 1H); **<sup>19</sup>F NMR** (375 MHz, chloroform-*d*):  $\delta$  -59.7; **<sup>13</sup>C NMR** (101 MHz, chloroform-*d*):  $\delta$  133.9, 132.8, 129.0, 128.8, 127.7, 126.6, 126.1 (q,  $J^2 = 30.3$  Hz), 124.8 (q,  $J^1 = 273.7$  Hz), 124.7 (q,  $J^3 = 5.8$  Hz), 124.3 (q,  $J^3 = 2.7$  Hz), 124.2 ; **HRMS** (ESI-TOF): calculated  $m/z$  for  $[M+H]^+$  ( $C_{11}H_8F_3$ ), 197.0578; observed, 197.0580. Characterization data matched those reported in the literature.<sup>39</sup>



Colorless oil, 81% yield using 4-iodotoluene (**8.1g**) as the starting material. The product is volatile and was separated by column chromatography using hexane and ethyl ether as eluent. **<sup>1</sup>H NMR** (400 MHz, chloroform-*d*):  $\delta$  7.53 (d,  $J = 7.9$  Hz, 2H), 7.30 (d,  $J = 7.9$  Hz, 2H), 2.44 (s,  $J = 3.4$  Hz, 3H); **<sup>19</sup>F NMR** (375 MHz, chloroform-*d*):  $\delta$  -62.3; **<sup>13</sup>C NMR** (101 MHz, chloroform-*d*):  $\delta$  142.6, 129.3, 127.8 (q,  $J^2 = 32.5$  Hz), 125.1 (q,  $J^3 = 4.1$  Hz), 124.4 (q,  $J^1 = 272.6$  Hz), 21.4; **HRMS** (ESI-TOF): calculated  $m/z$  for  $[M+H]^+$  ( $C_{11}H_8F_3$ ), 197.0578; observed, 197.0581. Characterization data matched those reported in the literature.<sup>40</sup>

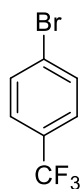


Colorless liquid, 62% yield using 4-iodoaniline (**8.1h**) as the starting material. **<sup>1</sup>H NMR** (400 MHz, chloroform-*d*):  $\delta$  7.42 (d,  $J = 8.3$  Hz, 2H), 6.71 (d,  $J = 8.3$  Hz, 2H), 3.97 (br, 2H); **<sup>19</sup>F NMR** (375 MHz, chloroform-*d*):  $\delta$  -62.8; **<sup>13</sup>C NMR** (101 MHz, chloroform-*d*):  $\delta$  149.4, 126.7 (q,  $J^3 = 4.0$  Hz), 124.8 (q,  $J^1 = 271.5$  Hz), 120.2 (q,  $J^2 = 32.9$  Hz), 114.2. **HRMS** (ESI-TOF): calculated  $m/z$  for  $[M+H]^+$  ( $C_7H_7F_3N$ ), 172.0531; observed, 172.0535. Characterization data matched those reported in the literature.<sup>41</sup>



**8.3i**

Yellowish liquid, 74% yield using 4-iodoanisole (**8.1i**) as the starting material. **<sup>1</sup>H NMR** (400 MHz, chloroform-*d*):  $\delta$  7.57 (d,  $J = 8.4$  Hz, 2H), 6.99 (d,  $J = 8.5$  Hz, 2H), 3.88 (s, 3H); **<sup>19</sup>F NMR** (375 MHz, chloroform-*d*):  $\delta$  -61.5; **<sup>13</sup>C NMR** (101 MHz, chloroform-*d*):  $\delta$  162.0, 126.9 (q,  $J^3 = 4.0$  Hz), 124.5 (q,  $J^1 = 271.9$  Hz), 122.9 (q,  $J^2 = 32.9$  Hz), 113.9, 55.4. **HRMS** (ESI-TOF): calculated  $m/z$  for  $[M+H]^+$  ( $C_8H_8F_3O$ ), 177.0527; observed, 177.0527. Characterization data matched those reported in the literature.<sup>36</sup>



**8.3l**

Colorless liquid, 62% yield using 4-iodobromobenzene (**8.1l**) as the starting material. **<sup>1</sup>H NMR** (400 MHz, chloroform-*d*):  $\delta$  7.66 (d,  $J = 8.7$  Hz, 2H), 7.52 (d,  $J = 8.8$  Hz, 2H); **<sup>19</sup>F NMR** (375 MHz, chloroform-*d*):  $\delta$  -62.8; **<sup>13</sup>C NMR** (101 MHz, chloroform-*d*):  $\delta$  132.1, 129.6 (q,  $J^2 = 33.3$  Hz), 126.9 (q,  $J^3 = 4.0$  Hz), 126.4, 123.9 (q,  $J^1 = 272.7$  Hz); **HRMS** (ESI-TOF): calculated  $m/z$  for  $[M+H]^+$  ( $C_7H_5BrF_3$ ), 224.9527; observed, 224.9521. Characterization data matched those reported in the literature.<sup>42</sup>

## 8.5 References

1. Jiang, J.; Zhao, Y.; Yaghi, O. M., Covalent Chemistry beyond Molecules. *J. Am. Chem. Soc.* **2016**, *138* (10), 3255-3265.
2. Geng, K.; He, T.; Liu, R.; Dalapati, S.; Tan, K. T.; Li, Z.; Tao, S.; Gong, Y.; Jiang, Q.; Jiang, D., Covalent Organic Frameworks: Design, Synthesis, and Functions. *Chem. Rev.* **2020**, *120* (16), 8814-8933.
3. Ma, T.; Kapustin, E. A.; Yin, S. X.; Liang, L.; Zhou, Z.; Niu, J.; Li, L.-H.; Wang, Y.; Su, J.; Li, J.; Wang, X.; Wang, W. D.; Wang, W.; Sun, J.; Yaghi, O. M., Single-crystal x-ray diffraction structures of covalent organic frameworks. *Science* **2018**, *361* (6397), 48-52.
4. Kang, D. W.; Ju, S. E.; Kim, D. W.; Kang, M.; Kim, H.; Hong, C. S., Emerging Porous Materials and Their Composites for NH<sub>3</sub> Gas Removal. *Adv. Sci.* **2020**, *7* (24), 2002142.
5. Kim, J. H.; Kang, D. W.; Yun, H.; Kang, M.; Singh, N.; Kim, J. S.; Hong, C. S., Post-synthetic modifications in porous organic polymers for biomedical and related applications. *Chem. Soc. Rev.* **2022**, *51* (1), 43-56.
6. Kang, D. W.; Kang, M.; Yun, H.; Park, H.; Hong, C. S., Emerging Porous Solid Electrolytes for Hydroxide Ion Transport. *Adv. Funct. Mater.* **2021**, *31* (19), 2100083.
7. Francis Kurisingal, J.; Kim, H.; Hyeak Choe, J.; Seop Hong, C., Covalent organic framework-based catalysts for efficient CO<sub>2</sub> utilization reactions. *Coord. Chem. Rev.* **2022**, *473*, 214835.
8. Cao, W.; Wang, W. D.; Xu, H.-S.; Sergeyev, I. V.; Struppe, J.; Wang, X.; Mentink-Vigier, F.; Gan, Z.; Xiao, M.-X.; Wang, L.-Y.; Chen, G.-P.; Ding, S.-Y.; Bai, S.; Wang, W., Exploring Applications of Covalent Organic Frameworks: Homogeneous Reticulation of Radicals for Dynamic Nuclear Polarization. *J. Am. Chem. Soc.* **2018**, *140* (22), 6969-6977.
9. Chen, X.; Geng, K.; Liu, R.; Tan, K. T.; Gong, Y.; Li, Z.; Tao, S.; Jiang, Q.; Jiang, D., Covalent Organic Frameworks: Chemical Approaches to Designer Structures and Built-In Functions. *Angew. Chem. Int. Ed.* **2020**, *59* (13), 5050-5091.
10. Li, L.-H.; Feng, X.-L.; Cui, X.-H.; Ma, Y.-X.; Ding, S.-Y.; Wang, W., Salen-Based Covalent Organic Framework. *J. Am. Chem. Soc.* **2017**, *139* (17), 6042-6045.
11. Guan, Q.; Zhou, L.-L.; Dong, Y.-B., Metalated covalent organic frameworks: from synthetic strategies to diverse applications. *Chem. Soc. Rev.* **2022**, *51* (15), 6307-6416.
12. Jin, E.; Asada, M.; Xu, Q.; Dalapati, S.; Addicoat, M. A.; Brady, M. A.; Xu, H.; Nakamura, T.; Heine, T.; Chen, Q.; Jiang, D., Two-dimensional sp<sup>2</sup> carbon-conjugated covalent organic frameworks. *Science* **2017**, *357* (6352), 673-676.
13. Li, X., sp<sup>2</sup> carbon-conjugated covalent organic frameworks: synthesis, properties, and applications. *Mater. Chem. Front.* **2021**, *5* (7), 2931-2949.
14. Wang, H.; Wang, H.; Wang, Z.; Tang, L.; Zeng, G.; Xu, P.; Chen, M.; Xiong, T.; Zhou, C.; Li, X.; Huang, D.; Zhu, Y.; Wang, Z.; Tang, J., Covalent organic framework photocatalysts: structures and applications. *Chem. Soc. Rev.* **2020**, *49* (12), 4135-4165.
15. Traxler, M.; Gisbertz, S.; Pachfule, P.; Schmidt, J.; Roeser, J.; Reischauer, S.; Rabeah, J.; Pieber, B.; Thomas, A., Acridine-Functionalized Covalent Organic Frameworks (COFs) as Photocatalysts for Metallaphotocatalytic C–N Cross-Coupling. *Angew. Chem. Int. Ed.* **2022**, *61* (21), e202117738.
16. Dong, W.; Yang, Y.; Xiang, Y.; Wang, S.; Wang, P.; Hu, J.; Rao, L.; Chen, H., A highly stable all-in-one photocatalyst for aryl etherification: the Ni<sup>III</sup> embedded covalent organic framework. *Green Chemistry* **2021**, *23* (16), 5797-5805.

17. Chen, H.; Liu, W.; Laemont, A.; Krishnaraj, C.; Feng, X.; Rohman, F.; Meledina, M.; Zhang, Q.; Van Deun, R.; Leus, K.; Van Der Voort, P., A Visible-Light-Harvesting Covalent Organic Framework Bearing Single Nickel Sites as a Highly Efficient Sulfur–Carbon Cross-Coupling Dual Catalyst. *Angew. Chem. Int. Ed.* **2021**, *60* (19), 10820-10827.
18. Kan, X.; Wang, J.-C.; Chen, Z.; Du, J.-Q.; Kan, J.-L.; Li, W.-Y.; Dong, Y.-B., Synthesis of Metal-Free Chiral Covalent Organic Framework for Visible-Light-Mediated Enantioselective Photooxidation in Water. *J. Am. Chem. Soc.* **2022**, *144* (15), 6681-6686.
19. Wu, C.-J.; Li, X.-Y.; Li, T.-R.; Shao, M.-Z.; Niu, L.-J.; Lu, X.-F.; Kan, J.-L.; Geng, Y.; Dong, Y.-B., Natural Sunlight Photocatalytic Synthesis of Benzoxazole-Bridged Covalent Organic Framework for Photocatalysis. *J. Am. Chem. Soc.* **2022**, *144* (41), 18750-18755.
20. Wang, X.; Dong, M.-J.; Wu, C.-D., Tuning the pore structures and photocatalytic properties of a 2D covalent organic framework with multi-branched photoactive moieties. *Nanoscale* **2020**, *12* (30), 16136-16142.
21. Chan, A. Y.; Perry, I. B.; Bissonnette, N. B.; Buksh, B. F.; Edwards, G. A.; Frye, L. I.; Garry, O. L.; Lavagnino, M. N.; Li, B. X.; Liang, Y.; Mao, E.; Millet, A.; Oakley, J. V.; Reed, N. L.; Sakai, H. A.; Seath, C. P.; MacMillan, D. W. C., Metallaphotoredox: The Merger of Photoredox and Transition Metal Catalysis. *Chem. Rev.* **2022**, *122* (2), 1485-1542.
22. Zuo, Z.; Ahneman, D. T.; Chu, L.; Terrett, J. A.; Doyle, A. G.; MacMillan, D. W. C., Merging photoredox with nickel catalysis: Coupling of  $\alpha$ -carboxyl sp<sup>3</sup>-carbons with aryl halides. *Science* **2014**, *345* (6195), 437-440.
23. Twilton, J.; Le, C.; Zhang, P.; Shaw, M. H.; Evans, R. W.; MacMillan, D. W. C., The merger of transition metal and photocatalysis. *Nature Reviews Chemistry* **2017**, *1* (7), 0052.
24. Welin, E. R.; Le, C.; Arias-Rotondo, D. M.; McCusker, J. K.; MacMillan, D. W. C., Photosensitized, energy transfer-mediated organometallic catalysis through electronically excited nickel(II). *Science* **2017**, *355* (6323), 380-385.
25. Kudisch, M.; Lim, C.-H.; Thordarson, P.; Miyake, G. M., Energy Transfer to Ni-Amine Complexes in Dual Catalytic, Light-Driven C–N Cross-Coupling Reactions. *J. Am. Chem. Soc.* **2019**, *141* (49), 19479-19486.
26. Ting, S. I.; Garakyaraghi, S.; Taliaferro, C. M.; Shields, B. J.; Scholes, G. D.; Castellano, F. N.; Doyle, A. G., 3d-d Excited States of Ni(II) Complexes Relevant to Photoredox Catalysis: Spectroscopic Identification and Mechanistic Implications. *J. Am. Chem. Soc.* **2020**, *142* (12), 5800-5810.
27. Li, J.; Huang, C.-Y.; Li, C.-J., Two-in-one metallaphotoredox cross-couplings enabled by a photoactive ligand. *Chem* **2022**, *8* (9), 2419-2431.
28. Bu, R.; Zhang, L.; Liu, X.-Y.; Yang, S.-L.; Li, G.; Gao, E.-Q., Synthesis and Acid-Responsive Properties of a Highly Porous Vinylene-Linked Covalent Organic Framework. *ACS Appl. Mater. Interfaces* **2021**, *13* (22), 26431-26440.
29. Zhang, L.; Jiao, L., Pyridine-Catalyzed Radical Borylation of Aryl Halides. *J. Am. Chem. Soc.* **2017**, *139* (2), 607-610.
30. Jiang, M.; Yang, H.; Fu, H., Visible-Light Photoredox Borylation of Aryl Halides and Subsequent Aerobic Oxidative Hydroxylation. *Org. Lett.* **2016**, *18* (20), 5248-5251.
31. Zhu, D.-L.; Xu, R.; Wu, Q.; Li, H.-Y.; Lang, J.-P.; Li, H.-X., Nickel-Catalyzed Sonogashira C(sp)–C(sp<sup>2</sup>) Coupling through Visible-Light Sensitization. *J. Org. Chem.* **2020**, *85* (14), 9201-9212.

32. Bernhardt, S.; Kastler, M.; Enkelmann, V.; Baumgarten, M.; Müllen, K., Pyrene as Chromophore and Electrophore: Encapsulation in a Rigid Polyphenylene Shell. *Eur. J. Chem.* **2006**, *12* (23), 6117-6128.
33. Xiang, Y.; Dong, W.; Wang, P.; Wang, S.; Ding, X.; Ichihara, F.; Wang, Z.; Wada, Y.; Jin, S.; Weng, Y.; Chen, H.; Ye, J., Constructing electron delocalization channels in covalent organic frameworks powering CO<sub>2</sub> photoreduction in water. *Appl. Catal., B* **2020**, *274*, 119096.
34. Lamola, J. L.; Moshapo, P. T.; Holzapfel, C. W.; Christopher Maumela, M., Palladium-catalyzed borylation of aryl bromides and chlorides using phosphatrioxa-adamantane ligands. *Tetrahedron Lett.* **2022**, *88*, 153572.
35. Jin, S.; Dang, H. T.; Haug, G. C.; He, R.; Nguyen, V. D.; Nguyen, V. T.; Arman, H. D.; Schanze, K. S.; Larionov, O. V., Visible Light-Induced Borylation of C–O, C–N, and C–X Bonds. *J. Am. Chem. Soc.* **2020**, *142* (3), 1603-1613.
36. Danoun, G.; Bayarmagnai, B.; Grünberg, M. F.; Gooßen, L. J., Sandmeyer Trifluoromethylation of Arenediazonium Tetrafluoroborates. *Angew. Chem. Int. Ed.* **2013**, *52* (31), 7972-7975.
37. Liu, J.; Hu, K.-F.; Qu, J.-P.; Kang, Y.-B., Organopromoted Selectivity-Switchable Synthesis of Polyketones. *Org. Lett.* **2017**, *19* (20), 5593-5596.
38. Zhang, K.; Budinská, A.; Passera, A.; Katayev, D., N-Nitroheterocycles: Bench-Stable Organic Reagents for Catalytic Ipso-Nitration of Aryl- and Heteroarylboronic Acids. *Org. Lett.* **2020**, *22* (7), 2714-2719.
39. Chen, M.; Buchwald, S. L., Rapid and Efficient Trifluoromethylation of Aromatic and Heteroaromatic Compounds Using Potassium Trifluoroacetate Enabled by a Flow System. *Angew. Chem. Int. Ed.* **2013**, *52* (44), 11628-11631.
40. Lin, X.; Hou, C.; Li, H.; Weng, Z., Decarboxylative Trifluoromethylating Reagent [Cu(O<sub>2</sub>CCF<sub>3</sub>)(phen)] and Difluorocarbene Precursor [Cu(phen)<sub>2</sub>][O<sub>2</sub>CCF<sub>2</sub>Cl]. *Eur. J. Chem.* **2016**, *22* (6), 2075-2084.
41. Yang, C.-T.; Fu, Y.; Huang, Y.-B.; Yi, J.; Guo, Q.-X.; Liu, L., Room-Temperature Copper-Catalyzed Carbon–Nitrogen Coupling of Aryl Iodides and Bromides Promoted by Organic Ionic Bases. *Angew. Chem. Int. Ed.* **2009**, *48* (40), 7398-7401.
42. Chu, L.; Qing, F.-L., Copper-Mediated Oxidative Trifluoromethylation of Boronic Acids. *Org. Lett.* **2010**, *12* (21), 5060-5063.



## Chapter 9. A Spirobifluorene-Based Covalent Organic Framework for Dual Photoredox and Nickel Catalysis

### 9.1 Introduction

COFs possess many desirable features such as robust structures, large surface areas, and well-defined pore environments<sup>1-8</sup> for potential applications in gas separation, conductivity, drug delivery, and catalysis.<sup>9-21</sup> As interlayer  $\pi$ - $\pi$  interactions provide an important driving force for COF synthesis,<sup>22</sup> most COFs have 2D structures with  $sp^2$  carbon linkages<sup>23-25</sup> and exhibit rapid exciton diffusion to quench excited states.<sup>26-29</sup>

In the previous chapter, we have discussed a photosensitizing 2D pyrene-based COF, **CN**, with long-range  $\pi$ -conjugation and eclipsed stacking of 2D networks.<sup>30</sup> **NiCN** shows fast energy transfer between pyrene units and Ni-bpy moieties to promote the generation of aryl radicals and catalyze photocatalytic borylation and trifluoromethylation of aryl halides, but exhibits low activity in dual photoredox and Ni-catalyzed reactions (e.g. C-O and C-N coupling reactions) due to rapid excited-state quenching and poor redox properties of the pyrene units.<sup>31</sup> We surmised that less efficient conjugation between the repeating units and staggered stacking between 2D networks would slow excited state quenching in 2D COFs.<sup>32-33</sup> Rational incorporation of photosensitizing units and Ni centers in such 2D COFs can facilitate dual photoredox and Ni catalysis (**Figure 9-1**).<sup>18</sup>

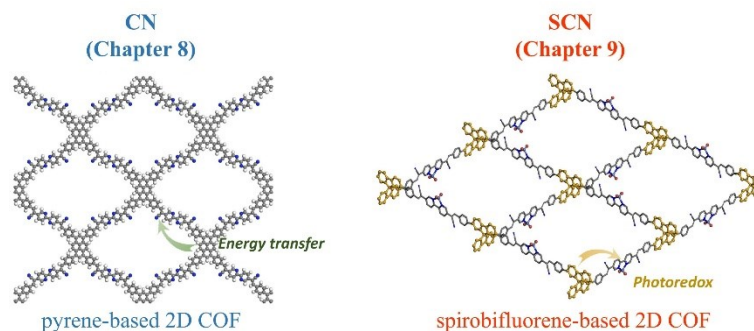


**Figure 9-1.** Schematic showing photocatalysis by CN (left) and NiSCN (right).

In this chapter, we report the first example of 2D COF based on spirobifluorene (sp) building blocks for dual photoredox and Ni catalysis. The sterically hindered  $sp^3$  carbon-based building blocks not only break the conjugation in 2D networks but also favor staggered stacking to prevent excited state quenching. The 2D COF with an  $sp^2$ -carbon linkage, SCN, was prepared via Knoevenagel condensation of 4,4',4'',4'''-(9,9'-Spirobi[fluorene]-2,2',7,7'-tetrayl) tetrabenzaldehyde (sp-CHO) and bpy-CN and then coordinated to Ni(II) centers via the bpy moieties to form NiSCN. Under light irradiation, the photoexcited sp units in NiSCN synergized with adjacent Ni(bpy)Br<sub>2</sub> centers to catalyze amination, etherification, and esterification of aryl bromides with 23 times higher efficiency than its homogeneous analogs.

## 9.2 Results and Discussion

### 9.2.1 Synthesis and Characterization of SCN and NiSCN

Based on the literature precedent of an imine-linked spirobifluorene COF,<sup>34-35</sup> we targeted the synthesis of SCN with a C=C linkage from sp-CHO and bpy-CN building blocks. The C=C linkages provide structural rigidity, improved stability, and enhanced energy/electron transfer.<sup>36</sup> Although imine-based COFs have generally shown high crystallinity, only a few  $sp^2$ -carbon

conjugated COFs with good crystallinity have been reported, due to the poor reversibility of C=C bonds.<sup>37-38</sup> Extensive screening of synthetic conditions led to the synthesis of **SCN** through a Knoevenagel reaction between sp-CHO and bpy-CN in 1,4-dioxane with a 4 M aqueous KOH solution at 100 °C (**Figure 9-2**). **NiSCN** was obtained by metalation of **SCN** with NiBr<sub>2</sub>·dme in DCM at 60 °C.

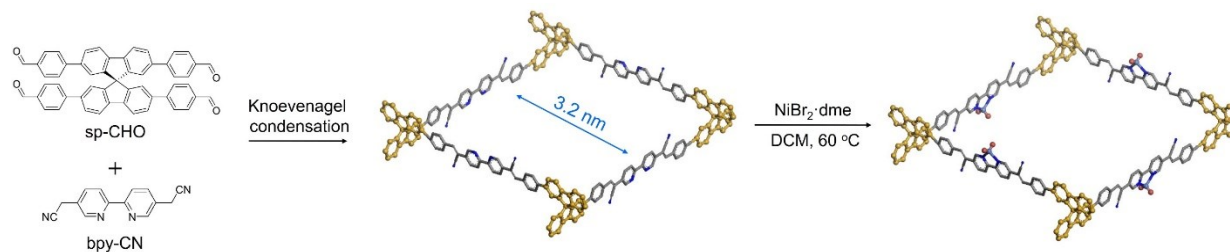


**Figure 9-2.** Synthetic scheme of **NiSCN**. Grey, C; blue, N; indigo, Ni; red, Br; sp units, yellow.

After the Knoevenagel condensation, the characteristic C=O stretching vibration of sp-CHO at 1690 cm<sup>-1</sup> significantly decreased in intensity in the IR spectrum of **SCN** (**Figure 9-3a**). The C=C stretching vibration at 1595 cm<sup>-1</sup> increased in intensity due to the formation of the vinyl linkage. The C≡N stretching vibration shifted from 2255 cm<sup>-1</sup> in bpy-CN to 2214 cm<sup>-1</sup> in **SCN** and 2216 cm<sup>-1</sup> in **NiSCN** (**Figure 9-3b**), indicating the formation of vinyl nitrile in **SCN** and **NiSCN**,<sup>39</sup> which was confirmed by ssNMR spectrum (**Figure 9-3d**).

PXRD studies showed that **SCN** and **NiSCN** exhibited 2D network structures with moderate crystallinity. Pawley refinement showed good agreement between the experimental and simulated PXRD patterns of **SCN** with R<sub>p</sub> = 0.81% and R<sub>wp</sub> = 1.24%. The non-planar **SCN** adopted staggered stacking, which disrupts interlayer π-π interaction (**Figure 9-3c**). Additionally, Pawley refinement of experimental PXRD pattern of **NiSCN** matched the simulated pattern, with R<sub>p</sub> = 1.85% and R<sub>wp</sub> = 2.65%. To our knowledge, **SCN** is the first sp<sup>2</sup>-carbon conjugated 2D COF with

staggered stacking.<sup>40</sup> The staggered stacking introduced disorder and reduced the crystallinity of **SCN**.<sup>35</sup>

The XPS spectrum of **NiSCN** exhibited Ni(II) with two distinct peaks at 872.85 and 875.44 eV, corresponding to 2p<sub>1/2</sub> and 2p<sub>3/2</sub> respectively. EXAFS analysis confirmed that the Ni centers in **NiSCN** adopted a similar tetrahedral coordination environment to that of Ni(bpy)Br<sub>2</sub> (**Figure 9-3e**), with two Ni-N bonds of 1.98 Å and two Ni-Br bonds of 2.35 Å. N<sub>2</sub> sorption isotherms demonstrated the porosity of **SCN** and **NiSCN**, with BET surface areas of 322 m<sup>2</sup>g<sup>-1</sup> and 69 m<sup>2</sup>g<sup>-1</sup>, respectively (**Figure 9-3f**). Based on the results, the pore sizes of **SCN** and **NiSCN** were calculated to be approximately 1.5 nm and 1.2 nm by DFT, respectively, matching the expected pore sizes obtained from structural models. TEM images of **SCN** and **NiSCN** revealed them as spherical nanoparticles with diameters of 100-200 nm.

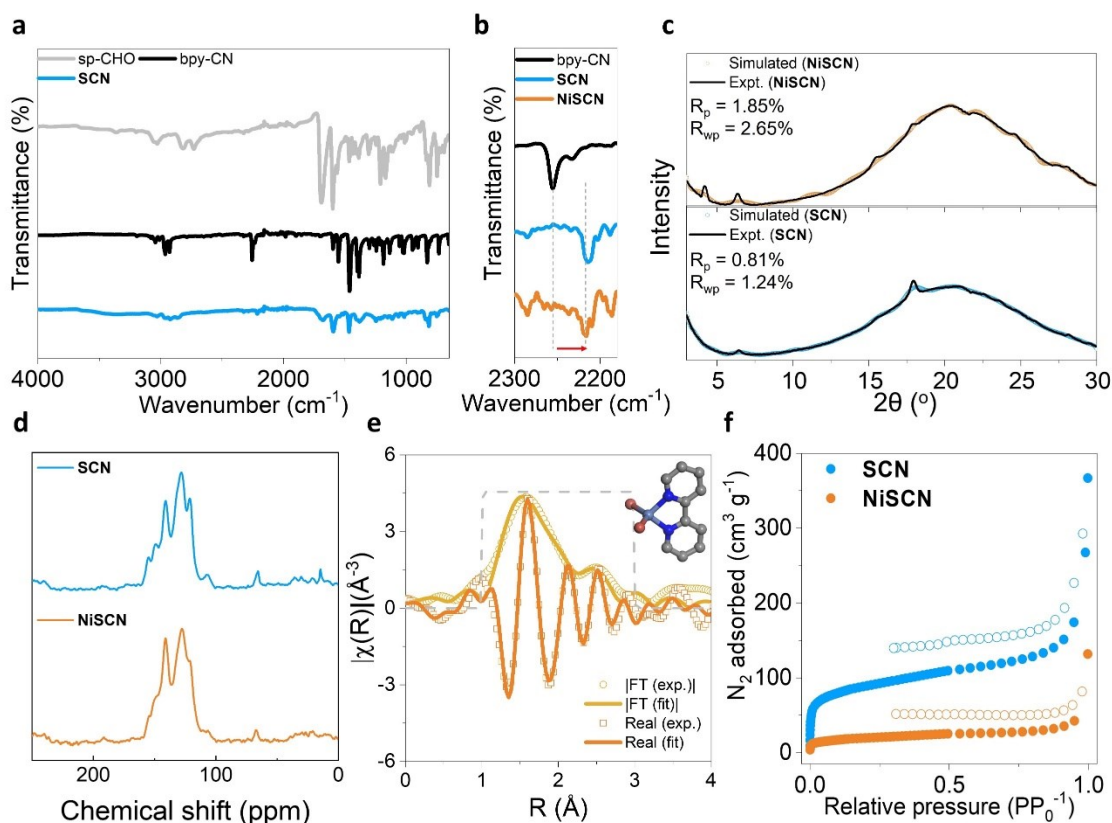


**Figure 9-3.** Characterization of SCN. (a) IR spectra of sp-CHO, bpy-CN, and SCN. (b) IR spectra of bpy-CN, SCN, and NiSCN in the C≡N triple bond stretching region. (c) PXRD patterns of SCN, NiSCN, and simulated pattern from structural model. (d) ssNMR spectrum of SCN and NiSCN. (e) EXAFS analysis of Ni in NiSCN. (f) Nitrogen isotherms of CN and NiCN at 77 K.

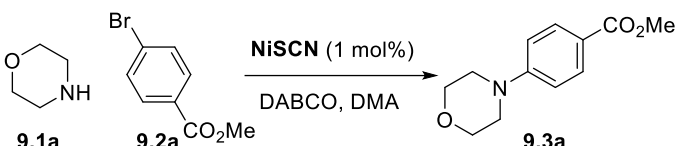
### 9.2.2 Sp<sup>2</sup> C-N and C-O Coupling Reactions and Mechanistic Studies

Nitrogen-containing compounds are of great significance due to their biological activities. C–N cross-coupling reactions provide a powerful synthetic method to amine molecules. We evaluated NiSCN in dual photoredox and Ni-catalyzed C-N coupling reactions. Under 440 nm irradiation, NiSCN efficiently catalyzed coupling of morpholine (**9.1a**) and methyl 4-bromobenzoate (**9.2a**) in DMA to afford **9.3a** in 91% yield.<sup>41-42</sup> A combination of sp and Ni(dtbbpy)Br<sub>2</sub> produced **9.3a** in 4% yield under identical conditions (**Table 9-1**, entry 2). Thus, NiSCN outperformed the corresponding homogenous analog by at least 23 times. Control reactions catalyzed by SCN or Ni(dtbbpy)Br<sub>2</sub> alone afforded **9.3a** in 0 and 7% yield, respectively (**Table 9-1**, entries 3, 4). A combination of SCN and Ni(dtbbpy)Br<sub>2</sub> gave **9.3a** in 9% yield (**Table 9-1**, entry 5). A control reaction with NiSCN in the absence of light irradiation did not produce **9.3a** (**Table 9-1**, entry 6). These results demonstrated the superiority of NiSCN in dual photoredox/Ni catalyzed amination of **9.2a** over homogeneous controls. In comparison, the NiCN (in Chapter 8) catalyzed the same reaction to give **9.3a** in 27% yield,<sup>30</sup> along with a large amount of dehalogenated product (45%).

The C-N coupling reaction can occur via a photoredox process or direct excitation of Ni complexes.<sup>41-42</sup> Ni complexes were reported to absorb around 425 nm.<sup>42</sup> However, we did not observe product formation with Ni(dtbbpy)Br<sub>2</sub> as catalyst under 440 nm irradiation (**Table 9-1**,

entry 5), likely due to the impact of the dtbbpy ligand on the photochemistry of Ni complexes. Based on these results, we propose that the reaction occurs via a photoredox process.

**Table 9-1.** Control experiments for NiSCN-catalyzed amination reactions.



entry	catalyst	yield of <b>9.3a</b> (%) <sup>a</sup>
1	<b>NiSCN</b> (1 mol%)	91
2	Sp (1 mol%) + NiBr <sub>2</sub> (dtbbpy) (1 mol%)	4
3	<b>SCN</b> (1 mol%)	0
4	NiBr <sub>2</sub> (dtbbpy) (1 mol%)	7
5	<b>SCN</b> (1 mol%) + NiBr <sub>2</sub> (dtbbpy) (1 mol%)	9
6 <sup>b</sup>	<b>NiSCN</b> (1 mol%)	0

<sup>a</sup>NMR yield. <sup>b</sup>Reaction was run in the dark.

As CV spectra of COFs typically show broad bands without distinct peaks, we measured the CV of sp and used its redox potential to approximate that of sp units in NiSCN. The CV of sp showed a reversible reduction peak at -1.08 V vs. Fc<sup>+</sup>/Fc and irreversible oxidation peaks above 0.5 V (**Figure 9-4a**). A potential of 1.34 V vs. Fc<sup>+</sup>/Fc was calculated as the photo-oxidation potential of sp units in NiSCN based on the emission maximum (465 nm, **Figure 9-4c**). The CV of Ni(bpy-CN)Br<sub>2</sub> showed Ni<sup>III/II</sup>, Ni<sup>II/I</sup>, and Ni<sup>I/0</sup> peaks at 0.62 V, -0.85 V, and -1.44 V vs. Fc<sup>+</sup>/Fc, respectively (**Figure 9-4b**).

We propose the mechanistic cycle for NiSCN-catalyzed C-N coupling of aryl bromides under light irradiation in **Figure 9-4e**. The catalytic cycle starts from two-electron reduction of NiSCN by photoexcited sp to generate Ni(I)-SCN<sup>•-</sup> (**A**), a Ni(I) species with a coordinated SCN radical anion. Amine substrates serve as a sacrificial reductant in this step. Next, aryl bromides oxidatively add to Ni(I)-SCN<sup>•-</sup> to form SCN-Ni(II)(Ar)(Br) (**B**), which undergoes ligand exchange between Br<sup>-</sup> and morpholine and deprotonation to form SCN-Ni(II)(Ar)[N(CH<sub>2</sub>CH<sub>2</sub>)<sub>2</sub>O] (**C**). The

oxidation power of photoexcited sp units (1.34 V) is higher than the oxidation potential of Ni(II) to Ni(III) (0.62 V). As a result, photo-excitation initiates electron transfer from Ni(II) to SCN to afford Ni(III)(Ar)[N(CH<sub>2</sub>CH<sub>2</sub>)<sub>2</sub>O] (**D**), facilitating reductive elimination to yield the product **3a** and regenerating the catalyst **A**.

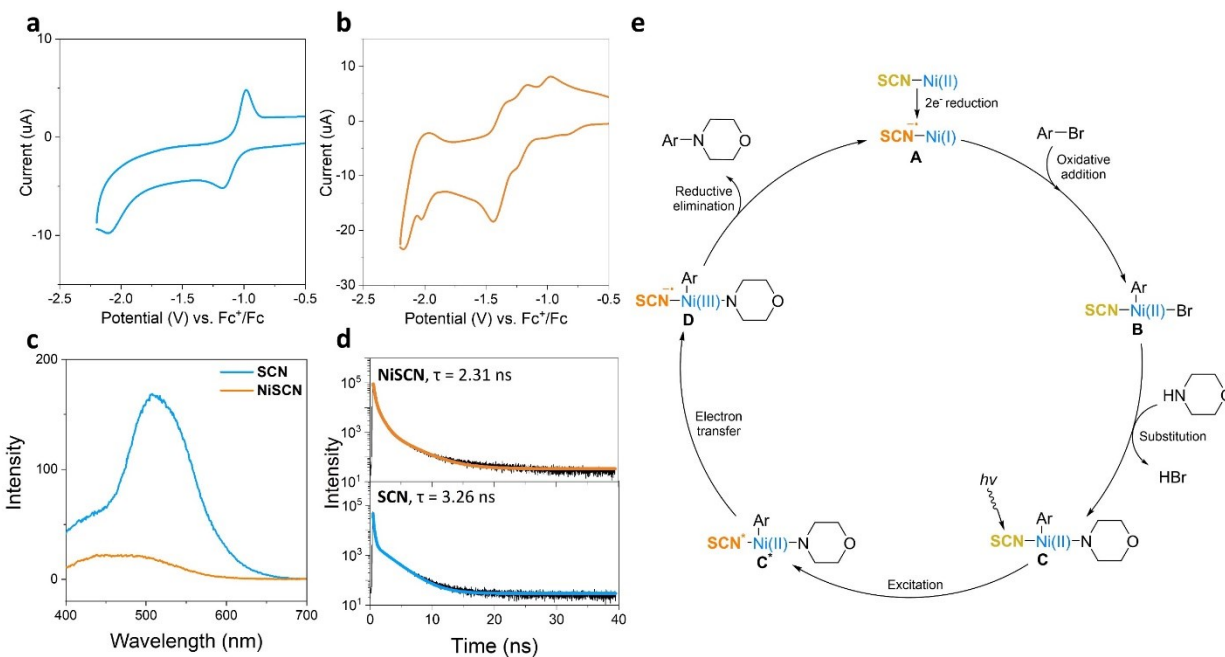


**Figure 9-4.** Mechanistic studies.(a) CV scan of sp. (b) CV scan of Ni(bpy-CN)Br<sub>2</sub>. (c) Emission spectra of SCN and NiSCN (ex: 370 nm). (d) TCSPC spectra of SCN and NiSCN. (e) Proposed mechanism for NiSCN-catalyzed amination reactions.

Compared to NiCN (Chapter 8),<sup>30</sup> the sp units in SCN exhibit a higher oxidation potential in the excited state to promote the reductive elimination step by single electron transfer. The sp units show the longest absorption at 309 nm in the ultraviolet region, while SCN and NiSCN can both be excited with blue light (**Figure 9-4c**). The luminescence lifetimes of SCN and NiSCN were determined via time-correlated single-photon counting (TCSPC) spectrum as 3.26 and 2.31 ns, respectively (**Figure 9-4d**), which are longer than the reported value for a spirobifluorene

analog (1.56 ns).<sup>43</sup> The increased excited state lifetime of NiSCN is in part responsible for its enhanced photocatalytic efficiency over the homogeneous counterparts.

### 9.2.3 Substrate Scope

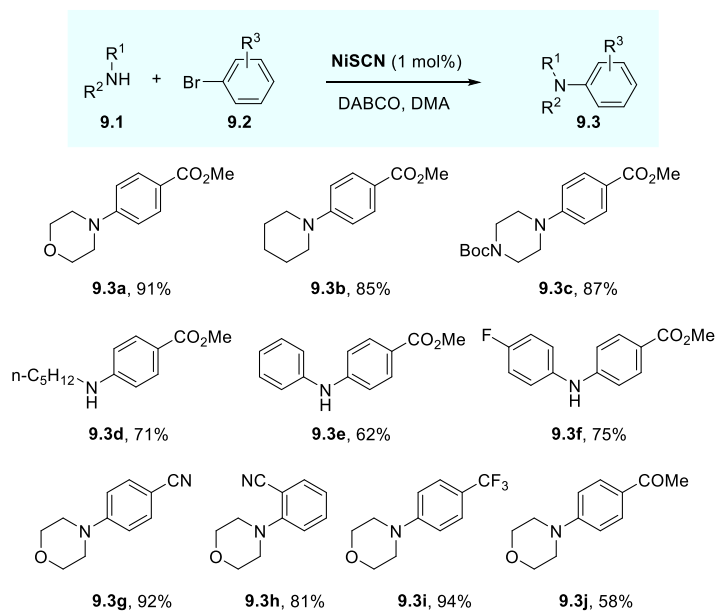
We next investigated the substrate scope of NiSCN-catalyzed C-N coupling reactions (**Table 9-2a**). Primary and secondary amines were tolerated to yield aniline derivatives **9.3a-d** in 91%, 85%, 87%, and 71% yields, respectively. With 10 mol% morpholine as the reductant to access the low-valent Ni complex, aniline and 4-fluoroaniline were successfully coupled with **9.2a** to give diphenylamines **9.3e** and **9.3f** in 62% and 75% yields, respectively. No morpholine-coupled products were observed in these reactions. Electron-deficient aryl bromides with nitrile, trifluoromethyl, and acetyl groups underwent coupling reactions to afford aniline **9.3g-j** in 92%, 81%, 94% and 58% yields, respectively.

As C-O coupling reactions are also synthetically useful, we tested NiSCN in dual photoredox/Ni catalyzed C-O coupling reactions (**Table 9-2b**). NiSCN efficiently catalyzed C-O coupling of aryl bromides in DMF. Carboxylic acids including acetic acid and benzoic acids were coupled with **9.2a** to afford phenol esters **9.5a**, **9.5e**, and **9.5f** in 65-70% yields. Water and methanol coupled with **9.2a** to afford phenol **9.5b** and anisole **9.5d** in 68% and 84% yield, respectively. Phenol also coupled with **9.2a** to produce diphenyl ether **9.5c** in 68% yield. Electron-withdrawing groups on the aryl bromides facilitated C-O coupling reactions. Aryl bromides with nitrile, ester, and acetyl groups underwent coupling reactions to give **9.5g-j** in 78%, 56%, 75%, and 85% yield, respectively.

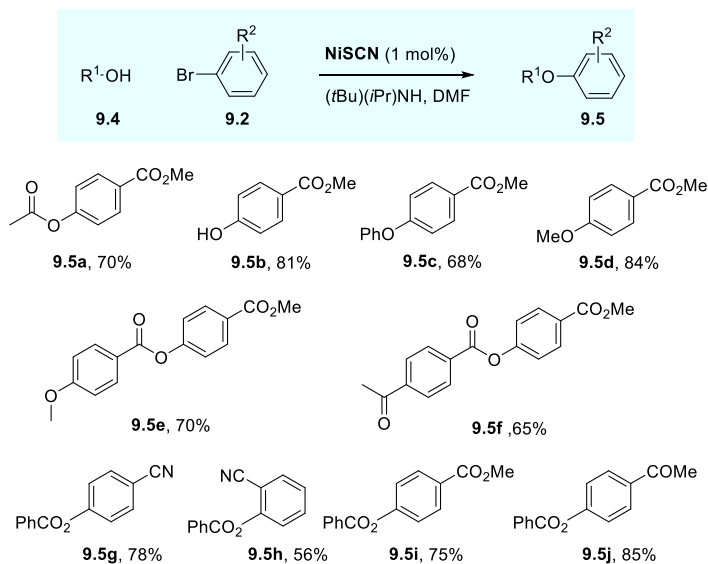


**Table 9-2.** Substrate scope of NiSCN-catalyzed sp<sup>2</sup> C-N and C-O coupling reactions.<sup>a</sup>

**a) C-N coupling<sup>b</sup>**



**b) C-O coupling<sup>c</sup>**



<sup>a</sup>Isolated yields. <sup>b</sup>9.1 (0.3 mmol), 9.2 (0.2 mmol), DABCO (0.2 mmol), and 2  $\mu$ mol NiSCN in 1 mL DMA under 440 nm irradiation for 18 hours. <sup>c</sup>9.4 (0.4 mmol), 9.2 (0.2 mmol), (tBu)(iPr)NH (0.4 mmol) and 2  $\mu$ mol NiSCN in 1 mL DMF under 440 nm irradiation for 18 hours.

Benzocaine was used in a late-stage functionalization by coupling with **9.2a** to give **9.3k** in 76% yield (**Figure 9-5a**). Ibuprofen also coupled with **9.2a** to give **9.5k** in 81% yield as an example of late-stage modification (**Figure 9-5a**). NiSCN has exhibited reactivities in  $sp^2$  C-S and C-C coupling reactions as well (**Figure 9-5b**). In coupling reactions between **9.2a** and **9.1a**, NiSCN was separated from the reaction mixture by filtration and used in 5 consecutive cycles without loss of catalytic activity (**Figure 9-5e**), demonstrating the stability of NiSCN under the catalytic conditions. Removal of NiSCN by filtration in the 6th run completely stopped the reaction with <1% Ni leaching in the filtrate as determined by ICP-MS. The PXRD pattern of the recovered NiSCN remained unchanged from those of the pristine NiSCN (**Figure 9-5d**).

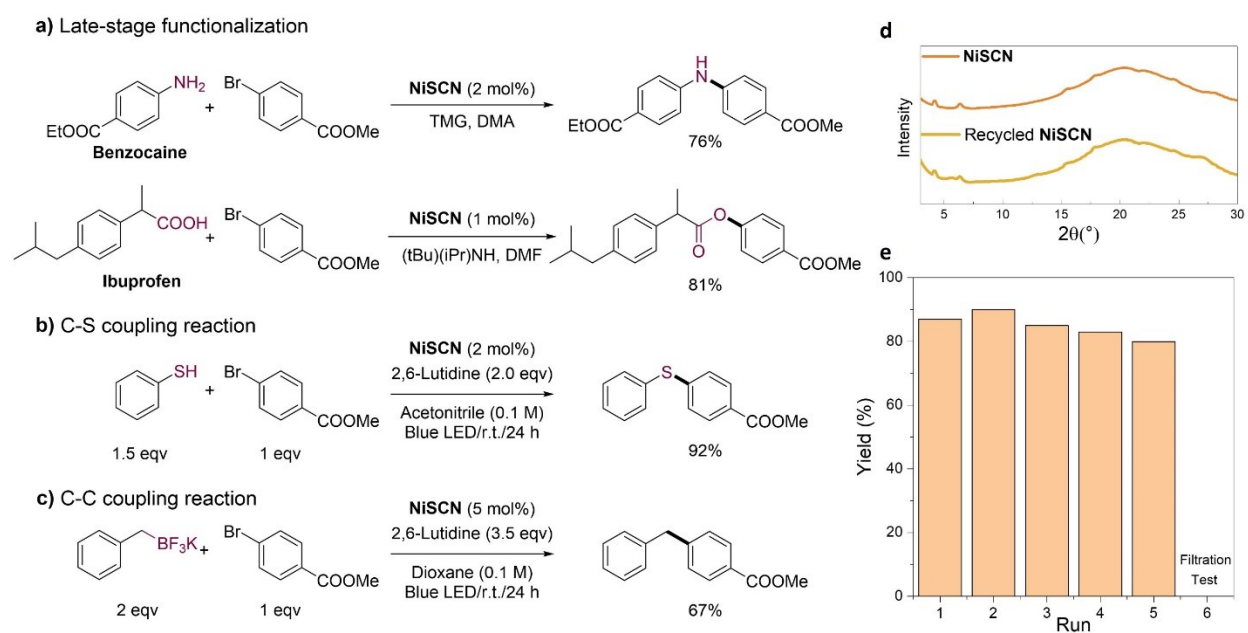


**Figure 9-5.** Synthetic application of NiSCN. (a) C-N coupling reaction of benzocaine and C-O coupling reaction of ibuprofen. (b)  $Sp^2$  C-S coupling reaction between thiophenol and **9.2a**. (c)  $Sp^2$  C-C coupling reaction between potassium benzyl trifluoroborate and **9.2a**. (d) PXRD pattern of recovered NiSCN in comparison with the original pattern. (e) Yields of **9.3a** in 5 consecutive runs of NiSCN-catalyzed C-N coupling reactions.

### 9.3 Conclusion

In this chapter, we designed a spirobifluorene-based COF for efficient photocatalytic amination and etherification/esterification of aryl bromides via dual photoredox/nickel catalysis. Constructed from spirobifluorene units and Ni-bpy linkers, **NiSCN** adopted a 2D structure with staggered stacking and reduced excited state quenching. The photoexcited spirobifluorene units not only efficiently reduced Ni(II) to Ni(I) for oxidative addition of aryl bromide to initiate the catalytic cycle but also oxidized the Ni(II) intermediate to Ni(III) for facile reductive elimination to yield the product and regenerate the catalyst. **NiSCN** successfully catalyzed C-N coupling and C-O coupling of aryl bromides and exhibited more than 23-fold higher catalytic efficiency than its homogeneous control. **NiSCN** was used in five consecutive reactions without loss of catalytic activity. This work uncovers a general strategy to construct multifunctional COFs for sustainable synergistic catalysis.

### 9.4 Methods

#### 9.4.1 Material synthesis

**Synthesis of sp-CHO.** A mixture of 2,2',7,7'-tetrabromo-9,9'-spirobifluorene (sp-Br, 3.67 g, 5.8 mmol), 4-formylphenylboronic acid (6.0 g, 40.0 mmol), K<sub>2</sub>CO<sub>3</sub> (4.0 g, 29.0 mmol), and Pd(PPh<sub>3</sub>)<sub>4</sub> (600 mg, 0.52 mmol) in a 250 mL round bottom flask was dried under vacuum for 3 h. Dioxane (80 mL) and H<sub>2</sub>O (14 mL) were added to the flask and the mixture was refluxed under N<sub>2</sub> atmosphere for 3 days. Upon cooling to room temperature, the mixture was slowly transferred to a beaker containing 40 mL concentrated hydrochloric acid. The solid was filtered, dried, and dissolved in DCM (200 mL). The solution was washed with water several times and dried over anhydrous MgSO<sub>4</sub>. The mixture was filtered, and the filtrate was dried under vacuum. The residue

was dissolved in methanol and sonicated for 5 min. The mixture was filtered, and the solvent was removed under vacuum. The solid residue was dried in a 100 °C oven overnight to obtain sp-CHO. (2.79 g, 3.77 mmol, 65%). <sup>1</sup>H NMR (CDCl<sub>3</sub>, 400 MHz): δ 9.90 (s, 4H), 7.97 (d, J = 8.0 Hz, 4H), 7.76 (d, J = 8.4 Hz, 8H), 7.68 (dd, J = 8.0, 1.6 Hz, 4H), 7.55 (d, J = 8.3 Hz, 8H), 7.19 (s, 4H), 7.01 (d, J = 1.3 Hz, 4H). HRMS m/z Calc. for C<sub>53</sub>H<sub>32</sub>O<sub>4</sub> ([M<sup>+</sup>]): 732.2301, Found: 732.2302.

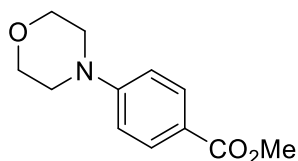
**Synthesis of bpy-CN.** Bpy-CN was prepared according to the published procedure.<sup>44</sup> Yield: 57.7%, white powder. <sup>1</sup>H NMR (400 MHz, CDCl<sub>3</sub>): δ 8.67 (s, 2H), 8.49 (d, J = 8.2 Hz, 2H), 7.88 (dd, J = 8.2, 2.3 Hz, 2H), 3.87 (s, 4H). HRMS m/z Calc. for C<sub>14</sub>H<sub>11</sub>N<sub>4</sub> ([M+H<sup>+</sup>]): 235.0984, Found: 235.0989.

**Synthesis of SCN.** A 10 mL Schlenk tube was charged with sp-CHO (35.16 mg, 0.048 mmol), bpy-CN (23.1 mg, 0.099 mmol), 1,4-dioxane (4 mL), aqueous KOH solution (0.1 mL, 4 M). The mixture was stirred for 3 min and then degassed through three freeze-pump-thaw cycles using a liquid nitrogen bath. The tube was sealed under vacuum, stirred for 1 min, and then heated at 100 °C for 3 days. After cooling to room temperature, the precipitate was washed with hot chloroform several times. 150 mL chloroform was then poured into the solid and the mixture was stirred at 90 °C for 24 hours. After filtration, the resulting powder was dried at 100 °C to obtain SCN. Yield: 30.90 mg (57%).

**Synthesis of Ni-coordinated COF.** To 10 mL of SCN dispersion (10 mg/mL) in DCM was added NiBr<sub>2</sub>·dme (15.4 mg, 50 μmol). The resulting dispersion was stirred at 60 °C for 24 hours. The precipitate was filtered and washed with DCM three times to yield NiSCN in quantitative yield. The nickel loading was determined by ICP-MS analysis and calculated to be 86 mol%.

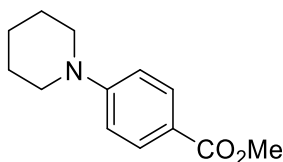
## 9.4.2 Catalytic Reactions

**General procedure for amination of aryl halides.** Aryl halide (0.2 mmol, 1 equiv), amine (0.3 mmol, 3 equiv.), DABCO (0.2 mmol, 22 mg, 1 equiv), and NiSCN (0.002 mmol, 3.2 mg, 1 mol%) were mixed in 1 mL dry DMA under nitrogen. The resulting mixture was sonicated and then stirred under 440 nm blue LED irradiation for 18 hours. After the reaction, 5 mL water was added. The aqueous phase was extracted with ethyl acetate three times (3 × 5 mL). The combined organic phase was washed with brine three times (3 × 5 mL) and dried over Na<sub>2</sub>SO<sub>4</sub>. The solvent was then removed, and the residue was subjected to column chromatography on silica gel using *n*-hexane and ethyl acetate as eluent to give cross-coupling products **9.3a-9.3j**.



**9.3a**, white solid, 91% yield.

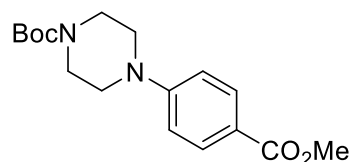
**<sup>1</sup>H NMR** (400 MHz, chloroform-*d*): δ 7.96 (d, *J* = 8.9 Hz, 2H), 6.89 (d, *J* = 8.9 Hz, 2H), 3.89 (s, 3H), 3.87 (t, *J* = 4.8 Hz, 4H), 3.31 (t, *J* = 4.8 Hz, 4H); **<sup>13</sup>C{<sup>1</sup>H} NMR** (101 MHz, chloroform-*d*): δ 167.1, 154.22, 131.2, 120.3, 113.5, 66.6, 51.7, 47.8; **HRMS** (ESI) calculated for [M+H]<sup>+</sup>: C<sub>12</sub>H<sub>16</sub>NO<sub>3</sub>, 222.1130, observed: 222.1130. Characterization data matched those reported in the literature.<sup>42</sup>



**9.3b**, white solid, 85% yield.

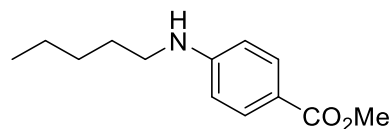
**<sup>1</sup>H NMR** (400 MHz, chloroform-*d*): δ 7.92 (d, *J* = 7.5 Hz, 2H), 6.89 (d, *J* = 7.8 Hz, 2H), 3.88 (s, 3H), 3.36 (m, 4H), 1.69 (m, 6H); **<sup>13</sup>C{<sup>1</sup>H} NMR** (101 MHz, chloroform-*d*): δ 167.2, 154.4, 131.3,

118.8, 113.7, 51.6, 48.9, 25.4, 24.4; **HRMS** (ESI) calculated for  $[M+H]^+$ :  $C_{13}H_{18}NO_2$ , 220.1137, observed: 220.1143. Characterization data matched those reported in the literature.<sup>45</sup>



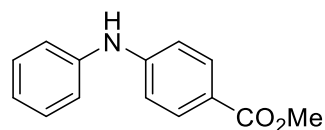
**9.3c**, white solid, 87% yield.

**$^1H$  NMR** (400 MHz, chloroform-*d*):  $\delta$  7.95 (d,  $J$  = 8.3 Hz, 2H), 6.88 (d,  $J$  = 8.4 Hz, 2H), 3.89 (s, 3H), 3.60 (s, 4H), 3.32 (s, 4H), 1.51 (s, 9H);  **$^{13}C\{^1H\}$  NMR** (101 MHz, chloroform-*d*):  $\delta$  167.0, 154.7, 154.0, 131.2, 120.2, 114.0, 80.1, 60.4, 51.7, 47.5, 28.4; **HRMS** (ESI) calculated for  $[M-tBuO+H_2]^+$ :  $C_{13}H_{17}N_2O_4$ , 265.1188, observed: 265.1187.



**9.3d**, yellowish oil, 71% yield.

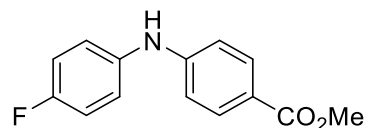
**$^1H$  NMR** (400 MHz, chloroform-*d*):  $\delta$  7.85 (dt,  $J$  = 8.8, 2.4 Hz, 2H), 6.54 (dt,  $J$  = 8.8, 2.4 Hz, 2H), 4.17 (s, 1H), 3.84 (s, 3H), 3.15 (t,  $J$  = 7.2 Hz, 2H), 1.68 – 1.58 (m, 2H), 1.43 – 1.32 (m, 4H), 0.92 (tt,  $J$  = 5.8, 2.3 Hz, 3H);  **$^{13}C\{^1H\}$  NMR** (101 MHz, chloroform-*d*):  $\delta$  167.4, 152.1, 131.6, 111.4, 76.7, 51.5, 43.4, 29.2, 29.0, 22.5, 14.0; **HRMS** (ESI) calculated for  $[M+H]^+$ :  $C_{13}H_{20}NO_2$ , 222.1494, observed: 222.1495.



**9.3e**, white solid, 62% yield.

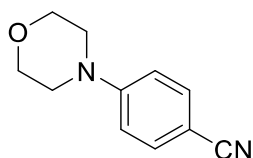
**$^1H$  NMR** (400 MHz, chloroform-*d*):  $\delta$  7.92 (d,  $J$  = 8.6 Hz, 2H), 7.34 (t,  $J$  = 7.8 Hz, 2H), 7.17 (d,  $J$  = 7.7 Hz, 2H), 7.07 (t,  $J$  = 7.4 Hz, 1H), 6.99 (d,  $J$  = 8.6 Hz, 2H), 6.05 (s, 1H), 3.88 (s, 3H);  **$^{13}C\{^1H\}$**

**NMR** (101 MHz, chloroform-*d*):  $\delta$  167.0, 148.1, 140.9, 131.5, 129.5, 123.1, 121.1, 120.5, 114.6, 51.8; **HRMS** (ESI) calculated for  $[M+H]^+$ : C<sub>14</sub>H<sub>14</sub>NO<sub>2</sub>, 228.1024, observed: 228.1027.



**9.3f**, white solid, 75% yield.

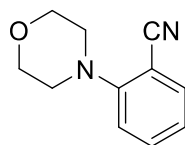
**<sup>1</sup>H NMR** (400 MHz, chloroform-*d*):  $\delta$  7.83 (dt,  $J$  = 8.8, 2.4 Hz, 2H), 7.08 (ddt,  $J$  = 9.0, 4.7, 2.4 Hz, 2H), 6.98 (tt,  $J$  = 8.6, 2.4 Hz, 2H), 6.81 (dt,  $J$  = 8.8, 2.4 Hz, 2H), 5.82 (s, 1H), 3.80 (s, 3H); **<sup>13</sup>C{<sup>1</sup>H} NMR** (101 MHz, chloroform-*d*):  $\delta$  167.0, 148.7, 136.7, 131.6, 123.5, 123.4, 121.0, 116.4, 116.2, 113.9, 51.7; **<sup>19</sup>F NMR** (377 MHz, chloroform-*d*)  $\delta$  -118.9; **HRMS** (ESI) calculated for  $[M+H]^+$ : C<sub>14</sub>H<sub>13</sub>FNO<sub>2</sub>, 246.0930, observed: 246.0930.



**9.3g**, white solid, 92% yield.

**<sup>1</sup>H NMR** (400 MHz, chloroform-*d*):  $\delta$  7.44 (d,  $J$  = 8.7 Hz, 2H), 6.79 (d,  $J$  = 8.7 Hz, 2H), 3.78 (t, 4H), 3.21 (t, 4H); **<sup>13</sup>C{<sup>1</sup>H} NMR** (101 MHz, chloroform-*d*):  $\delta$  153.5, 133.5, 120.0, 114.1, 100.9, 66.5, 47.3; **HRMS** (ESI) calculated for  $[M+H]^+$ : C<sub>11</sub>H<sub>13</sub>N<sub>2</sub>O, 189.1028, observed: 189.1027.

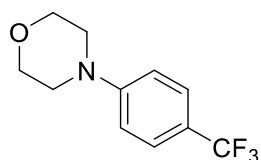
Characterization data matched those reported in the literature.<sup>42</sup>



**9.3h**, yellowish oil, 81% yield.

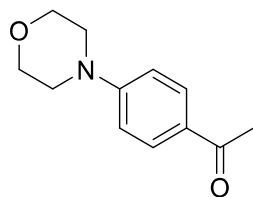
**<sup>1</sup>H NMR** (400 MHz, chloroform-*d*):  $\delta$  7.61 (d,  $J$  = 8.9 Hz, 1H), 7.53 (t,  $J$  = 7.9 Hz, 1H), 7.10 – 6.99 (m, 2H), 3.93 (t, 4H), 3.23 (t, 4H); **<sup>13</sup>C{<sup>1</sup>H} NMR** (101 MHz, chloroform-*d*):  $\delta$  155.5, 134.5,

133.9, 122.2, 118.5, 118.3, 106.2, 66.9, 51.8; **HRMS** (ESI) calculated for  $[M+H]^+$ :  $C_{11}H_{13}N_2O$ , 189.1028, observed: 189.1028.



**9.3i**, white solid, 94% yield.

**$^1H$  NMR** (400 MHz, chloroform-*d*):  $\delta$  7.50 (d,  $J$  = 8.2 Hz, 2H), 6.93 (d,  $J$  = 8.5 Hz, 2H), 3.87 (t, 4H), 3.24 (t, 4H);  **$^{13}C\{^1H\}$  NMR** (101 MHz, chloroform-*d*):  $\delta$  153.3, 126.5, 126.5, 126.4, 126.4, 126.0, 123.3, 121.3, 120.9, 114.4, 66.7, 48.2;  **$^{19}F$  NMR** (377 MHz, chloroform-*d*)  $\delta$  -61.44; **HRMS** (ESI) calculated for  $[M+H]^+$ :  $C_{11}H_{13}F_3NO$ , 232.0949, observed: 232.0952. Characterization data matched those reported in the literature.<sup>42</sup>



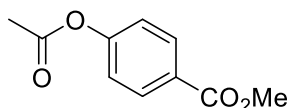
**9.3j**, white solid, 58% yield.

**$^1H$  NMR** (400 MHz, chloroform-*d*):  $\delta$  7.81 (d,  $J$  = 8.9 Hz, 2H), 6.79 (d,  $J$  = 8.9 Hz, 2H), 3.77 (t, 4H), 3.23 (t, 4H), 2.44 (s, 3H);  **$^{13}C\{^1H\}$  NMR** (101 MHz, chloroform-*d*):  $\delta$  197.3, 154.0, 130.6, 128.8, 114.1, 77.4, 77.1, 76.8, 67.1, 48.2, 26.6; **HRMS** (ESI) calculated for  $[M+H]^+$ :  $C_{12}H_{16}NO_2$ , 206.1181, observed: 206.1179. Characterization data matched those reported in the literature.<sup>42</sup>

**General procedure for etherification/esterification of aryl halides.** Aryl halide (0.2 mmol, 1 equiv), alcohol/carboxylic acid (0.4 mmol, 3 equiv.), *N-tert*-butylisopropylamine (0.4 mmol, 63.5  $\mu$ L, 4 equiv), and **NiSCN** (0.002 mmol, 3.2 mg, 1 mol%) were mixed in 1 mL dry DMF under nitrogen. The resulting mixture was sonicated and then stirred under 440 nm blue LED

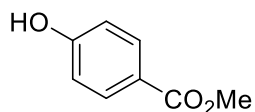


irradiation for 18 hours. After the reaction, 5 mL water was added. The aqueous phase was extracted with ethyl acetate three times ( $3 \times 5$  mL). The combined organic phase was washed with brine three times ( $3 \times 5$  mL) and dried over  $\text{Na}_2\text{SO}_4$ . The solvent was then removed, and the residue was subjected to column chromatography on silica gel using *n*-hexane and ethyl acetate as eluent to give cross-coupling products **9.5a-9.5j**.



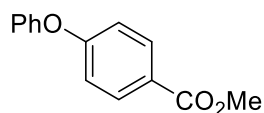
**9.5a**, white solid, 70% yield.

**$^1\text{H}$  NMR** (400 MHz, chloroform-*d*):  $\delta$  8.00 (d,  $J = 8.7$  Hz, 2H), 7.10 (d,  $J = 8.7$  Hz, 2H), 3.84 (s, 3H), 2.25 (s, 3H);  **$^{13}\text{C}\{^1\text{H}\}$  NMR** (101 MHz, chloroform-*d*):  $\delta$  168.8, 166.3, 154.3, 131.2, 127.7, 121.6, 77.3, 77.2, 77.0, 76.7, 52.2, 21.2; **HRMS** (ESI) calculated for  $[\text{M}+\text{H}]^+$ :  $\text{C}_{10}\text{H}_{11}\text{O}_4$ , 185.0657, observed: 185.0655. Characterization data matched those reported in the literature.<sup>46</sup>



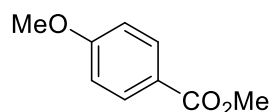
**9.5b**, white solid, 81% yield.

**$^1\text{H}$  NMR** (400 MHz, chloroform-*d*):  $\delta$  7.95 (d,  $J = 8.8$  Hz, 2H), 6.87 (d,  $J = 8.8$  Hz, 2H), 5.93 (s, 1H), 3.89 (s, 3H);  **$^{13}\text{C}\{^1\text{H}\}$  NMR** (101 MHz, chloroform-*d*):  $\delta$  167.1, 160.0, 131.9, 122.6, 115.2, 77.3, 77.2, 77.0, 76.7, 52.0; **HRMS** (ESI) calculated for  $[\text{M}+\text{H}]^+$ :  $\text{C}_8\text{H}_9\text{O}_3$ , 153.0552, observed: 153.0558.



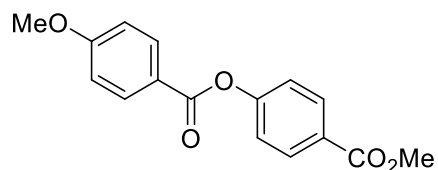
**9.5c**, white solid, 68% yield.

**<sup>1</sup>H NMR** (400 MHz, chloroform-*d*): δ 8.01 (d, *J* = 8.7 Hz, 2H), 7.39 (t, *J* = 7.9 Hz, 2H), 7.19 (t, *J* = 7.4 Hz, 1H), 7.07 (d, *J* = 7.8 Hz, 2H), 6.99 (d, *J* = 8.6 Hz, 2H), 3.90 (s, 3H); **<sup>13</sup>C{<sup>1</sup>H} NMR** (101 MHz, chloroform-*d*): δ 166.7, 161.8, 155.6, 131.7, 130.0, 124.5, 120.1, 117.3, 77.3, 52.0; **HRMS** (ESI) calculated for [M+H]<sup>+</sup>: C<sub>14</sub>H<sub>13</sub>O<sub>3</sub>, 229.0865, observed: 229.0867.



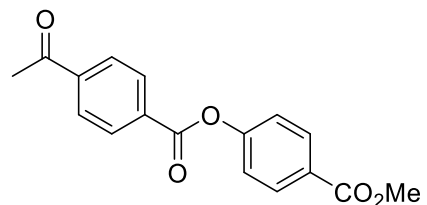
**9.5d**, white solid, 84% yield.

**<sup>1</sup>H NMR** (400 MHz, chloroform-*d*): δ 7.92 (d, *J* = 8.8 Hz, 2H), 6.84 (d, *J* = 8.8 Hz, 2H), 3.81 (s, 3H), 3.78 (s, 3H); **<sup>13</sup>C{<sup>1</sup>H} NMR** (101 MHz, chloroform-*d*): δ 166.9, 163.3, 131.6, 122.6, 113.6, 77.2, 55.4, 51.9; **HRMS** (ESI) calculated for [M+H]<sup>+</sup>: C<sub>9</sub>H<sub>11</sub>O<sub>3</sub>, 167.0708, observed: 167.0709.



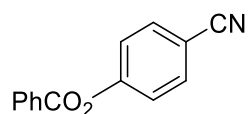
**9.5e**, white solid, 70% yield.

**<sup>1</sup>H NMR** (400 MHz, chloroform-*d*): δ 8.28 (d, *J* = 7.8 Hz, 2H), 8.13 (d, *J* = 8.2 Hz, 2H), 8.08 (d, *J* = 7.8 Hz, 2H), 7.32 (d, *J* = 8.2 Hz, 2H), 3.94 (s, 3H), 2.68 (s, 3H); **<sup>13</sup>C{<sup>1</sup>H} NMR** (101 MHz, chloroform-*d*): δ 166.4, 164.3, 164.1, 154.8, 132.4, 131.2, 127.6, 121.8, 121.4, 114.0, 77.4, 77.2, 77.0, 76.7, 55.6, 52.2; **HRMS** (ESI) calculated for [M+H]<sup>+</sup>: C<sub>16</sub>H<sub>15</sub>O<sub>5</sub>, 287.0920, observed: 287.0918. Characterization data matched those reported in the literature.<sup>46</sup>



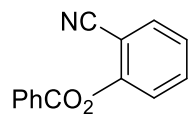
**9.5f**, white solid, 65% yield.

**<sup>1</sup>H NMR** (400 MHz, chloroform-*d*): δ 8.28 (d, *J* = 7.8 Hz, 2H), 8.13 (d, *J* = 8.2 Hz, 2H), 8.08 (d, *J* = 7.8 Hz, 2H), 7.32 (d, *J* = 8.2 Hz, 2H), 3.94 (s, 3H), 2.68 (s, 3H); **<sup>13</sup>C{<sup>1</sup>H} NMR** (101 MHz, chloroform-*d*): δ 197.8, 167.2, 163.9, 160.5, 154.4, 141.0, 132.9, 130.6, 121.8, 115.4, 77.5, 77.2, 76.8, 52.4, 27.1; **HRMS** (ESI) calculated for [M+H]<sup>+</sup>: C<sub>17</sub>H<sub>15</sub>O<sub>5</sub>, 299.0920, observed: 299.0914.



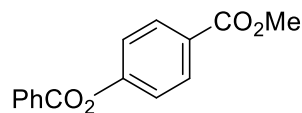
**9.5g**, white solid, 78% yield.

**<sup>1</sup>H NMR** (400 MHz, chloroform-*d*): δ 8.19 (d, *J* = 7.5 Hz, 2H), 7.74 (d, *J* = 8.5 Hz, 2H), 7.68 (t, *J* = 7.4 Hz, 1H), 7.54 (t, *J* = 7.7 Hz, 2H), 7.37 (d, *J* = 8.5 Hz, 2H); **<sup>13</sup>C{<sup>1</sup>H} NMR** (101 MHz, chloroform-*d*): δ 164.3, 154.3, 134.2, 130.3, 128.8, 128.7, 123.0, 118.3, 109.9, 77.3; **HRMS** (ESI) calculated for [M+H]<sup>+</sup>: C<sub>14</sub>H<sub>10</sub>NO<sub>2</sub>, 224.0712, observed: 224.0714.



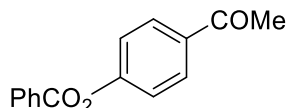
**9.5h**, white solid, 56% yield.

**<sup>1</sup>H NMR** (400 MHz, chloroform-*d*): δ 8.26 (d, *J* = 7.2 Hz, 2H), 7.74 (dd, *J* = 7.7, 1.3 Hz, 1H), 7.71 – 7.64 (m, 2H), 7.55 (d, *J* = 7.9 Hz, 1H), 7.51 (t, *J* = 7.4 Hz, 2H), 7.38 (t, *J* = 7.4 Hz, 1H); **<sup>13</sup>C{<sup>1</sup>H} NMR** (101 MHz, chloroform-*d*): δ 164.0, 152.6, 134.3, 134.1, 133.4, 130.5, 128.8, 128.3, 126.3, 123.3, 115.2, 107.1; **HRMS** (ESI) calculated for [M+H]<sup>+</sup>: C<sub>14</sub>H<sub>10</sub>NO<sub>2</sub>, 224.0712, observed: 224.0711.



**9.5i**, white solid, 75% yield.

**<sup>1</sup>H NMR** (400 MHz, chloroform-*d*): δ 8.20 (d, *J* = 7.1 Hz, 2H), 8.17 – 8.10 (m, 3H), 7.66 (t, *J* = 7.4 Hz, 1H), 7.53 (t, *J* = 7.7 Hz, 2H), 7.31 (d, *J* = 8.8 Hz, 2H), 3.93 (s, 3H); **<sup>13</sup>C{<sup>1</sup>H} NMR** (101 MHz, chloroform-*d*): δ 166.4, 164.7, 154.6, 133.9, 131.2, 130.3, 129.1, 128.7, 127.8, 121.8, 77.4, 77.0, 76.7, 52.2; **HRMS** (ESI) calculated for [M+H]<sup>+</sup>: C<sub>15</sub>H<sub>13</sub>O<sub>4</sub>, 257.0814, observed: 257.0811. Characterization data matched those reported in the literature.<sup>46</sup>



**9.5j**, white solid, 85% yield.

**<sup>1</sup>H NMR** (400 MHz, chloroform-*d*): δ 8.21 (d, *J* = 8.3 Hz, 2H), 8.05 (d, *J* = 8.6 Hz, 2H), 7.66 (t, *J* = 7.4 Hz, 1H), 7.53 (t, *J* = 7.7 Hz, 2H), 7.33 (d, *J* = 8.6 Hz, 2H), 2.62 (s, 3H); **<sup>13</sup>C{<sup>1</sup>H} NMR** (101 MHz, chloroform-*d*): δ 196.9, 164.6, 154.7, 134.8, 134.0, 130.3, 130.0, 129.1, 128.7, 121.97, 26.7; **HRMS** (ESI) calculated for [M+H]<sup>+</sup>: C<sub>15</sub>H<sub>13</sub>O<sub>3</sub>, 241.0865, observed: 241.0864. Characterization data matched those reported in the literature.<sup>46</sup>

## 9.5 References

1. Côté, A. P.; Benin, A. I.; Ockwig, N. W.; O'Keeffe, M.; Matzger, A. J.; Yaghi, O. M., Porous, Crystalline, Covalent Organic Frameworks. *Science* **2005**, *310* (5751), 1166-1170.
2. Li, L.-H.; Feng, X.-L.; Cui, X.-H.; Ma, Y.-X.; Ding, S.-Y.; Wang, W., Salen-Based Covalent Organic Framework. *J. Am. Chem. Soc.* **2017**, *139* (17), 6042-6045.
3. Ma, T.; Kapustin, E. A.; Yin, S. X.; Liang, L.; Zhou, Z.; Niu, J.; Li, L.-H.; Wang, Y.; Su, J.; Li, J.; Wang, X.; Wang, W. D.; Wang, W.; Sun, J.; Yaghi, O. M., Single-crystal x-ray diffraction structures of covalent organic frameworks. *Science* **2018**, *361* (6397), 48-52.
4. Diercks, C. S.; Yaghi, O. M., The atom, the molecule, and the covalent organic framework. *Science* **2017**, *355* (6328), eaal1585.
5. Kandambeth, S.; Mallick, A.; Lukose, B.; Mane, M. V.; Heine, T.; Banerjee, R., Construction of Crystalline 2D Covalent Organic Frameworks with Remarkable Chemical (Acid/Base) Stability via a Combined Reversible and Irreversible Route. *J. Am. Chem. Soc.* **2012**, *134* (48), 19524-19527.

6. Kang, F.; Wang, X.; Chen, C.; Lee, C.-S.; Han, Y.; Zhang, Q., Construction of Crystalline Nitrene-Linked Covalent Organic Frameworks Via Kröhnke Oxidation. *J. Am. Chem. Soc.* **2023**, *145* (28), 15465-15472.
7. Han, X.; Ma, T.; Nannenga, B. L.; Yao, X.; Neumann, S. E.; Kumar, P.; Kwon, J.; Rong, Z.; Wang, K.; Zhang, Y.; Navarro, J. A. R.; Ritchie, R. O.; Cui, Y.; Yaghi, O. M., Molecular weaving of chicken-wire covalent organic frameworks. *Chem* **2023**.
8. Qian, C.; Qi, Q.-Y.; Jiang, G.-F.; Cui, F.-Z.; Tian, Y.; Zhao, X., Toward Covalent Organic Frameworks Bearing Three Different Kinds of Pores: The Strategy for Construction and COF-to-COF Transformation via Heterogeneous Linker Exchange. *J. Am. Chem. Soc.* **2017**, *139* (19), 6736-6743.
9. Cao, W.; Wang, W. D.; Xu, H.-S.; Sergeev, I. V.; Struppe, J.; Wang, X.; Mentink-Vigier, F.; Gan, Z.; Xiao, M.-X.; Wang, L.-Y.; Chen, G.-P.; Ding, S.-Y.; Bai, S.; Wang, W., Exploring Applications of Covalent Organic Frameworks: Homogeneous Reticulation of Radicals for Dynamic Nuclear Polarization. *J. Am. Chem. Soc.* **2018**, *140* (22), 6969-6977.
10. Guo, J.; Jiang, D., Covalent Organic Frameworks for Heterogeneous Catalysis: Principle, Current Status, and Challenges. *ACS Cent. Sci.* **2020**, *6* (6), 869-879.
11. Kang, D. W.; Kang, M.; Yun, H.; Park, H.; Hong, C. S., Emerging Porous Solid Electrolytes for Hydroxide Ion Transport. *Adv. Funct. Mater.* **2021**, *31* (19), 2100083.
12. Kim, J. H.; Kang, D. W.; Yun, H.; Kang, M.; Singh, N.; Kim, J. S.; Hong, C. S., Post-synthetic modifications in porous organic polymers for biomedical and related applications. *Chem. Soc. Rev.* **2022**, *51* (1), 43-56.
13. Han, B.; Jin, Y.; Chen, B.; Zhou, W.; Yu, B.; Wei, C.; Wang, H.; Wang, K.; Chen, Y.; Chen, B.; Jiang, J., Maximizing Electroactive Sites in a Three-Dimensional Covalent Organic Framework for Significantly Improved Carbon Dioxide Reduction Electrocatalysis. *Angew. Chem. Int. Ed.* **2022**, *61* (1), e202114244.
14. Chen, Z.; Wang, K.; Tang, Y.; Li, L.; Hu, X.; Han, M.; Guo, Z.; Zhan, H.; Chen, B., Reticular Synthesis of One-Dimensional Covalent Organic Frameworks with 4-c sql Topology for Enhanced Fluorescence Emission. *Angew. Chem. Int. Ed.* **2023**, *62* (1), e202213268.
15. Kan, X.; Wang, J.-C.; Chen, Z.; Du, J.-Q.; Kan, J.-L.; Li, W.-Y.; Dong, Y.-B., Synthesis of Metal-Free Chiral Covalent Organic Framework for Visible-Light-Mediated Enantioselective Photooxidation in Water. *J. Am. Chem. Soc.* **2022**, *144* (15), 6681-6686.
16. Han, X.; Huang, J.; Yuan, C.; Liu, Y.; Cui, Y., Chiral 3D Covalent Organic Frameworks for High Performance Liquid Chromatographic Enantioseparation. *J. Am. Chem. Soc.* **2018**, *140* (3), 892-895.
17. Sun, T.; Xie, J.; Guo, W.; Li, D.-S.; Zhang, Q., Covalent–Organic Frameworks: Advanced Organic Electrode Materials for Rechargeable Batteries. *Advanced Energy Materials* **2020**, *10* (19), 1904199.
18. Jati, A.; Dey, K.; Nurhuda, M.; Addicoat, M. A.; Banerjee, R.; Maji, B., Dual Metalation in a Two-Dimensional Covalent Organic Framework for Photocatalytic C–N Cross-Coupling Reactions. *J. Am. Chem. Soc.* **2022**, *144* (17), 7822-7833.
19. Lin, W.; Lin, J.; Zhang, X.; Zhang, L.; Borse, R. A.; Wang, Y., Decoupled Artificial Photosynthesis via a Catalysis-Redox Coupled COF||BiVO<sub>4</sub> Photoelectrochemical Device. *J. Am. Chem. Soc.* **2023**, *145* (32), 18141-18147.
20. Duan, H.; Li, K.; Xie, M.; Chen, J.-M.; Zhou, H.-G.; Wu, X.; Ning, G.-H.; Cooper, A. I.; Li, D., Scalable Synthesis of Ultrathin Polyimide Covalent Organic Framework Nanosheets for High-Performance Lithium–Sulfur Batteries. *J. Am. Chem. Soc.* **2021**, *143* (46), 19446-19453.

21. Jati, A.; Dam, S.; Kumar, S.; Kumar, K.; Maji, B., A  $\pi$ -conjugated covalent organic framework enables interlocked nickel/photoredox catalysis for light-harvesting cross-coupling reactions. *Chem. Sci.* **2023**, *14* (32), 8624-8634.
22. Nguyen, V.; Grünwald, M., Microscopic Origins of Poor Crystallinity in the Synthesis of Covalent Organic Framework COF-5. *J. Am. Chem. Soc.* **2018**, *140* (9), 3306-3311.
23. Xu, S.; Richter, M.; Feng, X., Vinylene-Linked Two-Dimensional Covalent Organic Frameworks: Synthesis and Functions. *Acc. Mater. Res.* **2021**, *2* (4), 252-265.
24. Chandra, S.; Kandambeth, S.; Biswal, B. P.; Lukose, B.; Kunjir, S. M.; Chaudhary, M.; Babarao, R.; Heine, T.; Banerjee, R., Chemically Stable Multilayered Covalent Organic Nanosheets from Covalent Organic Frameworks via Mechanical Delamination. *J. Am. Chem. Soc.* **2013**, *135* (47), 17853-17861.
25. Waller, P. J.; Gándara, F.; Yaghi, O. M., Chemistry of Covalent Organic Frameworks. *Acc. Chem. Res.* **2015**, *48* (12), 3053-3063.
26. Meng, Y.; Luo, Y.; Shi, J. L.; Ding, H.; Lang, X.; Chen, W.; Zheng, A.; Sun, J.; Wang, C., 2D and 3D Porphyrinic Covalent Organic Frameworks: The Influence of Dimensionality on Functionality. *Angew. Chem. Int. Ed.* **2020**, *59* (9), 3624-3629.
27. Wang, G.-B.; Wang, Y.-J.; Kan, J.-L.; Xie, K.-H.; Xu, H.-P.; Zhao, F.; Wang, M.-C.; Geng, Y.; Dong, Y.-B., Construction of Covalent Organic Frameworks via a Visible-Light-Activated Photocatalytic Multicomponent Reaction. *J. Am. Chem. Soc.* **2023**, *145* (9), 4951-4956.
28. Zhang, X.; Geng, K.; Jiang, D.; Scholes, G. D., Exciton Diffusion and Annihilation in an sp<sup>2</sup> Carbon-Conjugated Covalent Organic Framework. *J. Am. Chem. Soc.* **2022**, *144* (36), 16423-16432.
29. Yuan, C.; Fu, S.; Yang, K.; Hou, B.; Liu, Y.; Jiang, J.; Cui, Y., Crystalline C—C and C=C Bond-Linked Chiral Covalent Organic Frameworks. *J. Am. Chem. Soc.* **2021**, *143* (1), 369-381.
30. Fan, Y.; Kang, D. W.; Labalme, S.; Li, J.; Lin, W., Enhanced Energy Transfer in A  $\pi$ -Conjugated Covalent Organic Framework Facilitates Excited-State Nickel Catalysis. *Angew. Chem. Int. Ed.* **2023**, *62* (11), e202218908.
31. Romero, N. A.; Nicewicz, D. A., Organic Photoredox Catalysis. *Chem. Rev.* **2016**, *116* (17), 10075-10166.
32. Lin, G.; Ding, H.; Yuan, D.; Wang, B.; Wang, C., A Pyrene-Based, Fluorescent Three-Dimensional Covalent Organic Framework. *J. Am. Chem. Soc.* **2016**, *138* (10), 3302-3305.
33. Yang, M.; Hanayama, H.; Fang, L.; Addicoat, M. A.; Guo, Y.; Graf, R.; Harano, K.; Kikkawa, J.; Jin, E.; Narita, A.; Müllen, K., Saturated Linkers in Two-Dimensional Covalent Organic Frameworks Boost Their Luminescence. *J. Am. Chem. Soc.* **2023**, *145* (26), 14417-14426.
34. Liu, Y. Y.; Li, X. C.; Wang, S.; Cheng, T.; Yang, H.; Liu, C.; Gong, Y.; Lai, W. Y.; Huang, W., Self-templated synthesis of uniform hollow spheres based on highly conjugated three-dimensional covalent organic frameworks. *Nat. Commun.* **2020**, *11* (1), 5561.
35. Zhao, J.; Xie, M.; Chen, X.; Jin, J.-K.; Zhao, W.; Luo, J.; Ning, G.-H.; Liu, J.; Li, D., A BODIPY-Based 1D Covalent Organic Framework for Photocatalytic Aerobic Oxidation. *Chem. Asian J.* **2023**, *18* (13), e202300328.
36. He, T.; Geng, K.; Jiang, D., All sp<sup>2</sup> carbon covalent organic frameworks. *Trends Chem.* **2021**, *3* (6), 431-444.
37. Li, X., sp<sup>2</sup>carbon-conjugated covalent organic frameworks: synthesis, properties, and applications. *Mater. Chem. Front.* **2021**, *5* (7), 2931-2949.
38. Xu, S.; Richter, M.; Feng, X., Vinylene-Linked Two-Dimensional Covalent Organic Frameworks: Synthesis and Functions. *Acc. Mater. Res.* **2021**, *2* (4), 252-265.

39. Bu, R.; Zhang, L.; Liu, X. Y.; Yang, S. L.; Li, G.; Gao, E. Q., Synthesis and Acid-Responsive Properties of a Highly Porous Vinylene-Linked Covalent Organic Framework. *ACS Appl. Mater. Interfaces* **2021**, *13* (22), 26431-26440.
40. Wang, S.; Li, X. X.; Da, L.; Wang, Y.; Xiang, Z.; Wang, W.; Zhang, Y. B.; Cao, D., A Three-Dimensional sp<sup>2</sup> Carbon-Conjugated Covalent Organic Framework. *J. Am. Chem. Soc.* **2021**, *143* (38), 15562-15566.
41. Corcoran, E. B.; Pirnot, M. T.; Lin, S.; Dreher, S. D.; DiRocco, D. A.; Davies, I. W.; Buchwald, S. L.; MacMillan, D. W. C., Aryl amination using ligand-free Ni(II) salts and photoredox catalysis. *Science* **2016**, *353* (6296), 279-283.
42. Lim, C.-H.; Kudisch, M.; Liu, B.; Miyake, G. M., C–N Cross-Coupling via Photoexcitation of Nickel–Amine Complexes. *J. Am. Chem. Soc.* **2018**, *140* (24), 7667-7673.
43. Thiery, S.; Tondelier, D.; Declairieux, C.; Geffroy, B.; Jeannin, O.; Métivier, R.; Rault-Berthelot, J.; Poriel, C., 4-Pyridyl-9,9'-spirobifluorenes as Host Materials for Green and Sky-Blue Phosphorescent OLEDs. *J. Phys. Chem. C* **2015**, *119* (11), 5790-5805.
44. Fan, Y.; Kang, D. W.; Labalme, S.; Li, J.; Lin, W., Enhanced Energy Transfer in A  $\pi$  - Conjugated Covalent Organic Framework Facilitates Excited - State Nickel Catalysis. *Angew. Chem. Int. Ed.* **2023**, *62* (11), e202218908.
45. Sun, R.; Qin, Y.; Nocera, D. G., General Paradigm in Photoredox Nickel-Catalyzed Cross-Coupling Allows for Light-Free Access to Reactivity. *Angew. Chem. Int. Ed.* **2020**, *59* (24), 9527-9533.
46. Welin, E. R.; Le, C.; Arias-Rotondo, D. M.; McCusker, J. K.; MacMillan, D. W. C., Photosensitized, energy transfer-mediated organometallic catalysis through electronically excited nickel(II). *Science* **2017**, *355* (6323), 380-385.